Author:
Saxby, Jennifer

Title:
From needles to plates

extreme volcanic ash shapes and implications for dispersion modelling

FROM NEEDLES TO PLATES: EXTREME VOLCANIC ASH SHAPES AND IMPLICATIONS FOR DISPERSION MODELLING

Jennifer Saxby

Supervisors: Katharine Cashman, Alison Rust, Frances Beckett

A dissertation submitted to the University of Bristol in accordance with the requirements for award of the degree of Doctor of Philosophy in the Faculty of Science

School of Earth Sciences

Word Count: 30636

ABSTRACT

Volcanic ash is hazardous to aircraft and can remain in the atmosphere for days or longer after an eruption. The rate of removal depends on meteorology and particle terminal fall velocity, which is sensitive to particle shape. However, most volcanic ash forecasts assume spherical particles; shape is difficult to quantify, and while the velocity of spheres can be determined analytically, modelling non-spheres relies on empirical drag laws. I assess the accuracy of drag laws for non-spheres for the range of flow regimes anticipated for volcanic ash falling in air, determine ash particle shape ranges, and assess the sensitivity of ash forecasts to shape.

Measurements of ash from Icelandic eruptions show that shape descriptors based on surface area are highly sensitive to imaging resolution and the particle size fraction used. I compare calculated terminal velocities to those measured in a settling column for volcanic ash and analogues; shape-dependent drag laws produce more accurate results than a spherical approximation. Particle shape also impacts the method of size measurement, as size for non-spherical particles can be measured in several ways.

Using the NAME model, I determine the sensitivity of ash forecasts to particle shape. Model particle trajectories are sensitive to shape where sedimentation velocities exceed atmospheric vertical velocities; a non-spherical 100 μm particle can travel 44% further than an equivalent-volume sphere. Therefore, the sensitivity of ash concentration forecasts to particle shape is dependent on the input particle size distribution.

I use these insights on measuring and modelling particle shape to discuss how best to parameterise shape in operational dispersion modelling systems; I identify drag laws which are accurate for the whole range of flow regimes expected for volcanic ash falling in air and compile particle shape data in order to recommend default values for use with these laws.

Author's Declaration

I declare that the work in this dissertation was carried out in accordance with the requirements of the University's Regulations and Code of Practice for Research Degree Programmes and that it has not been submitted for any other academic award. Except where indicated by specific reference in the text, the work is the candidate's own work. Work done in collaboration with, or with the assistance of, others, is indicated as such. Any views expressed in the dissertation are those of the author.

.....

Jennifer Saxby

September 18, 2019

Acknowledgments

Firstly I would like to thank my supervisors. Kathy Cashman, Alison Rust and Frances Beckett have provided a huge amount of advice, guidance and feedback over the last 4 years. I'd also like to thank my other co-authors, Elly Tennant and Hannah Rodger. Supervising your Master's projects was a highlight of my PhD work, so thank you for being so enthusiastic and a pleasure to work with.

Special thanks must go to Frances Boreham for camping and sharing a truck with me during 3 weeks of fieldwork in Iceland; her stream-fording skills are exceptional. Thanks also to Frances, Nick and David for the daily coffee breaks and general office fun over the last 4 years.

Thank you Tom Davies for all your help with X-ray tomography and data processing, and to Charles Clapham for your enthusiastic help with building lab equipment and for accommodating my sometimes last-minute requests.

Thank you to Stefan Wastegård and Simon Larsson from the University of Stockholm for showing Kathy and I around your wonderful city and for sharing your tephra. Thanks also to Jan Mangerud from the University of Bergen for taking the time to send me samples.

Finally I'd like to thank the whole Atmospheric Dispersion and Air Quality group at the Met Office for all of your invaluable help over the last 4 years and for being so welcoming whenever I visit - it's been a pleasure working with you all and I will miss it very much!

Contents

List of Figures

List of Tables

Chapter 1

Introduction

1.1 Motivations

Fine grained ash particles released into the atmosphere by large explosive eruptions can be transported hundreds or even thousands of km from the eruptive vent, and remain in the atmosphere for months or years (e.g., Gooding et al., 1983). Volcanic ash deposited on the ground poses a significant hazard to human respiratory health (Horwell, 2007; Horwell et al., 2010), can poison or starve livestock (Cronin et al., 1998), and damage infrastructure including electricity networks and wastewater disposal systems (Wilson et al., 2012). Ash suspended in the atmosphere is a danger to aircraft, as it can melt on contact with turbine components, disrupting air flow and causing engine failure (Giehl et al., 2017). From 1953 to 2009 there were at least 79 volcanic ash engine-damage incidents, of which nine resulted in engine failure; fortunately, in those cases at least one engine did not shut down or could be restarted, meaning there are no known crashes attributed to volcanic ash encounters (Guffanti et al., 2010). The costs of avoiding volcanic ash encounters can be high: the eruption of Eyjafjallajökull volcano in Iceland during April and May 2010 left 10.5 million people across Europe unable to travel due to airspace closure, and caused significant losses of revenue for the airline industry (Grant et al., 2012; Budd et al., 2011). The disruption caused by this incident prompted authorities to reassess recommendations to airlines, moving away from banning flight through visible ash clouds and towards a quantitative approach which defines safe thresholds (ICAO, 2012; Webster et al., 2012; Clarkson et al., 2016).

The use of safe thresholds creates a need to forecast both the location of the plume and ash concentrations. Forecasting is carried out by nine worldwide Volcanic Ash Advisory Centres (VAACs), which use atmospheric dispersion models to predict the expected location of ash in

the atmosphere. Forecasting air concentrations, in addition to the location of the plume, requires a sophisticated understanding of the aerodynamic behaviour of volcanic ash. This has motivated scientific enquiry into how we characterise physical particle properties, such as size, shape and density; and to what extent forecasts are sensitive to these properties.

The transport and dispersion of a volcanic ash cloud is dependent on meteorological variables (e.g. wind speed and direction) and the terminal fall velocity of the ash particles, defined as the velocity obtained when a particle's weight is balanced by air resistance such that it no longer accelerates. The dispersion of particles is highly sensitive to terminal velocity where it exceeds the vertical velocity of air motions such as wind advection and turbulent diffusion (Koyaguchi and Ohno, 2001). Terminal velocity of volcanic ash is a function of air density, air viscosity, and physical particle properties; of these, it is most sensitive to particle size, with density and shape having lesser but still significant impacts (Beckett et al., 2015). Drag of non-spherical particles can be many orders of magnitude higher than spheres, meaning that a non-spherical particle will have a lower terminal velocity than a sphere of equal volume and density. This allows non-spherical particles to travel further, and remain in the atmosphere longer, than spheres; it is therefore important that dispersion models can anticipate the velocity of non-spherical volcanic ash particles. While the drag of spheres can be determined analytically (Clift and Gauvin, 1971; White, 1974), empirical correlations are used for non-spheres, as there is no theory for the physics of flow around complex shapes. There are many empirical and semi-empirical drag laws for non-spherical particles, based on experiments using volcanic ash particles (Wilson and Huang, 1979; Dellino et al., 2005; Bagheri and Bonadonna, 2016b; Dioguardi et al., 2017, 2018) or analogues (Haider and Levenspiel, 1989; Ganser, 1993). These laws calculate terminal velocity as a function of one or more geometric shape descriptors, and they therefore require quantitative measurements of the shape of volcanic ash.

The physical properties of particles in an ash plume are difficult to quantify during an eruption: ground based sampling is not necessarily representative of the particles in the plume (Bonadonna et al., 2011), while in-plume sampling is limited to specialised research aircraft and the low-concentration margins of the plume (e.g., Cashman and Rust, 2016). Therefore, when models are used in an operational system, they are often initiated using a set of default particle properties based on measurements from past eruptions. In the case of shape, particles are often assumed to be spherical; of nine VAACs, six including the London VAAC assume spherical particles while three (Darwin, Buenos Aires and Tokyo) operationally model non-sphericity (Hort, 2016). To consider the use of a default particle shape in an operational system requires an assessment of (1) the most effective drag law in anticipating terminal velocity, (2) knowledge of the typical shape range of volcanic ash, to determine a value or range to use where no data are available,

and (3) model sensitivity analysis to determine the conditions under which forecasts are sensitive to particle shape.

The work presented here consists of measurements and experiments using individual volcanic ash particles. However, most volcanic ash particles $\leq$ 100 μm settle as aggregates, volcanic ash clusters with larger size and lower density than the individual particles of which they are composed (Sparks et al., 1997; Bonadonna and Phillips, 2003; Brown et al., 2012). Aggregation is caused by moist adhesion or hydrometeor formation in the presence of water, or electrostatic forces between fine-grained particles in its absence. Aggregate size and morphology vary with distance from the eruptive vent. Proximal ($\leq$ 15 km from source) aggregates are larger (up to cm in size) and often contain liquid water or ice, whereas distal aggregates are smaller (sub-mm) with often no evidence for the involvement of water (Brown et al., 2012). In this work we investigate the settling of single ash grains as most drag equations are calibrated using individual particles, and the majority of volcanic ash dispersion models do not explicitly parameterise ash aggregation; for forecasting of distal ash dispersion, it is often accounted for by adjusting the source term (e.g., Witham et al., 2017). This approach, however, assumes that aggregates fall out close enough to the vent to be unimportant in forecasting distal ash concentration. In reality, aggregation not only causes premature fallout of fine particles, but also delayed sedimentation of larger particles which have become coated with smaller particles, forming very low-density composites with high drag coefficients and low velocities in a process known as 'rafting'. These low-density composites can be deposited hundreds of km from the source (Schumacher, 1994; Bagheri et al., 2016). Therefore, there is a benefit to explicitly modelling aggregation or parameterising it by means of adjusting particle size, density and shape distributions in volcanic ash dispersion models, and a limitation of this work is that it does not include aggregates in the range of particle shapes investigated. However, since aggregates are non-spherical due to their high surface roughness (Lane et al., 1993; James et al., 2003) results presented here may also be relevant to the problem of modelling aggregation.

The aim of this thesis is to evaluate drag laws and shape descriptors for non-spherical particles. I assess different ways of quantifying ash particle shape, determine the sensitivity of atmospheric dispersion model outputs to shape, extend the literature database of volcanic ash shape measurements in order to constrain the shape range of volcanic ash and suggest default values for use in operational forecasts where no shape data are available. In doing this, I answer the following research questions:

- What is the shape range of volcanic ash?

- How well can current drag laws account for the aerodynamic behaviour of very non-spherical ash?
- How sensitive are ash concentration forecasts to particle shape?
- How should we parameterise particle shape in operational dispersion modelling systems?

1.2 Overview of research methods

The following sections give an overview of the field sampling, modelling and lab techniques used throughout this thesis. They provide additional context to the methods used where there is relevant information which has not been included in the background sections of individual chapters.

1.2.1 Field campaign

For three weeks during July and August 2016, I conducted a field campaign in order to collect samples of tephra from the SILK eruptions of Katla volcano, a series of distinctive light-coloured Holocene ash layers produced by large silicic eruptions. Katla is located in the southern part of Iceland's Eastern Volcanic Zone. It consists of a central caldera about 100 km^2 in area, covered by the 600 km^2 Myrdalsjökull ice cap, which is 400 – 700 m thick (Figure 1.1). Together the features are $\sim$ 80 km long from southwest to northeast (Larsen et al., 2001). The caldera is complex in structure, consisting of three distinct basins which each contain a crater: Kötlujökull, the easternmost, most frequently active and largest at 60 km^2; Sólheimajökull (19 km^2); and Entujökull (23 km^2).

For the last 1000 years, the average repose interval is 49 years, with a maximum repose of 200 years. The last large eruption was in 1918 (Elíasson, 2014). Pleistocene and Holocene Katla tephras are dominated by alkali basalts (Meyer et al., 1985); silicic eruptions are far less common. At least 12 SILK tephras were erupted between ca. 6600 and 1675 years BP, with volumes ranging from 0.05 to 0.3 km^3; isopach analysis of the six largest layers suggests an origin within the caldera (Larsen et al., 2001). SILK eruptions are far less regular than basaltic ones, with intervals of 100-1000 years; the current interval (1700 years since the last eruption at 270 $\pm$ 12 years A.D.) is the longest so far. The cause of this long interval is unknown, but possibilities include increased ice thickness or modifications to the magmatic system caused by large Quaternary events such as the Eldgjá fires (Larsen et al., 2001).

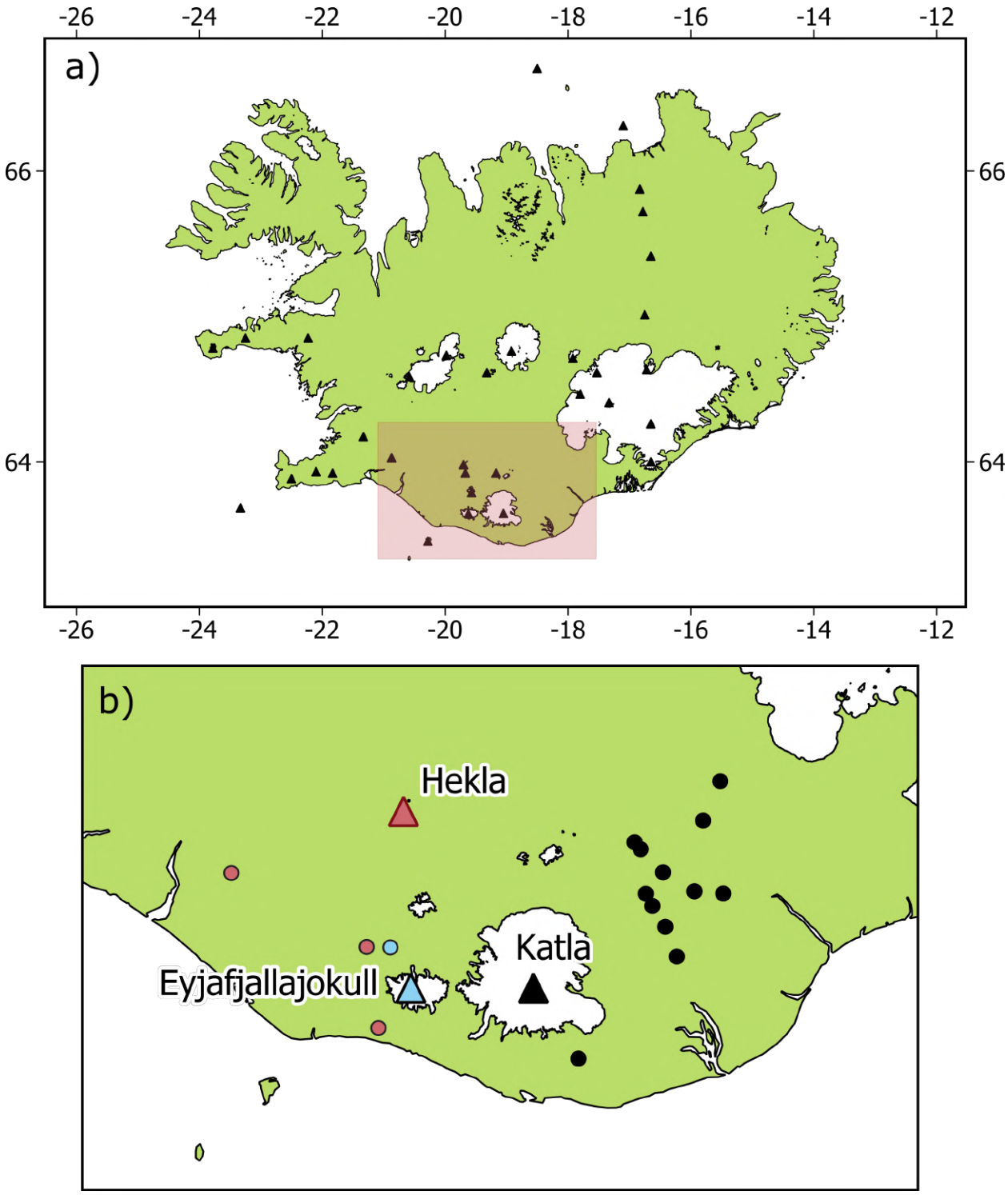

Figure 1.1: Sample locations for new samples of Icelandic tephra, showing Icelandic Holocene volcanoes (triangles), new sample locations (circles) and glaciers. Sample locations are coloured according to the tephra sampled. Shaded area in a) is enlarged in b).

Within the SILK tephras are three distinctive horizons known as the 'needle layers' for their abundance of elongated grains; I refer to them in this thesis as SILK-LN (lower needle layer), SILK-MN (middle needle layer) and SILK-UN (upper needle layer) after Larsen et al. (2001). The layers have compacted tephra volumes of 0.12 km^3, 0.03 km^3, and 0.16 km^3 respectively. The volumes suggest eruptions of VEI 3-4, lower magnitude than the largest basaltic eruptions. Narrow isopachs (Figure 1.2) indicate short-lived eruptions for SILK-LN and SILK-MN, although duration is poorly constrained as it is unknown whether only a part of each eruption broke through the ice cap, which is thought to have been present through most of the Holocene (Dugmore, 1989; Larsen et al., 2001).

I collected 24 samples of the SILK-LN, SILK-MN and SILK-UN tephra between 18.5 and 52.5 km from Katla caldera. For comparison, I also collected samples from two more tephras which are widespread over a similar area whenever they could be identified in a soil section: the 2010 eruption of Eyjafjallajökull and the 1947 eruption of Hekla. Sample locations are shown in Figure 1.1. The sampling strategy was initially based on GPS coordinates for the SILK-LN tephra reported by Thorsteinsdóttir (2015a), and isopach maps for the three SILK tephras from Larsen et al. (2001), which I used to identify areas with sufficient tephra thickness. Isopachs and sample locations for the three SILK eruptions are shown in Figure 1.2.

The SILK tephra layers are easily identifiable in the field due to their distinctive light greenish-grey colour and grain shapes (Figure 1.3). The grains can be divided into three types: elongated or fibrous vesicular grains (Figure 1.3b), equant vesicular grains, and poorly vesicular black scoriaceous grains. Among Icelandic tephras, the fibrous grains are unique to Katla. The deposits consist almost entirely of juvenile material; an absence of lithics could indicate either an absence in the erupted material or the very proximal fallout of large, dense lithic clasts, as there are no sections within 15 km of the caldera (Larsen et al., 2001).

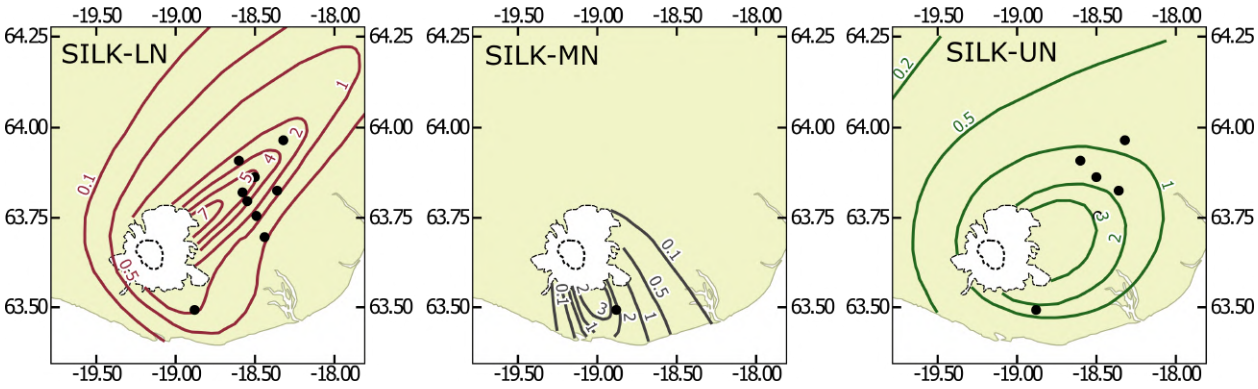

Figure 1.2: Isopach maps and sample locations for the SILK-LN, SILK-MN and SILK-UN tephras. Inner dashed line shows the Katla caldera; black dots show new sample locations; coloured lines show published isopachs after Larsen et al. (2001). All isopach values in cm.

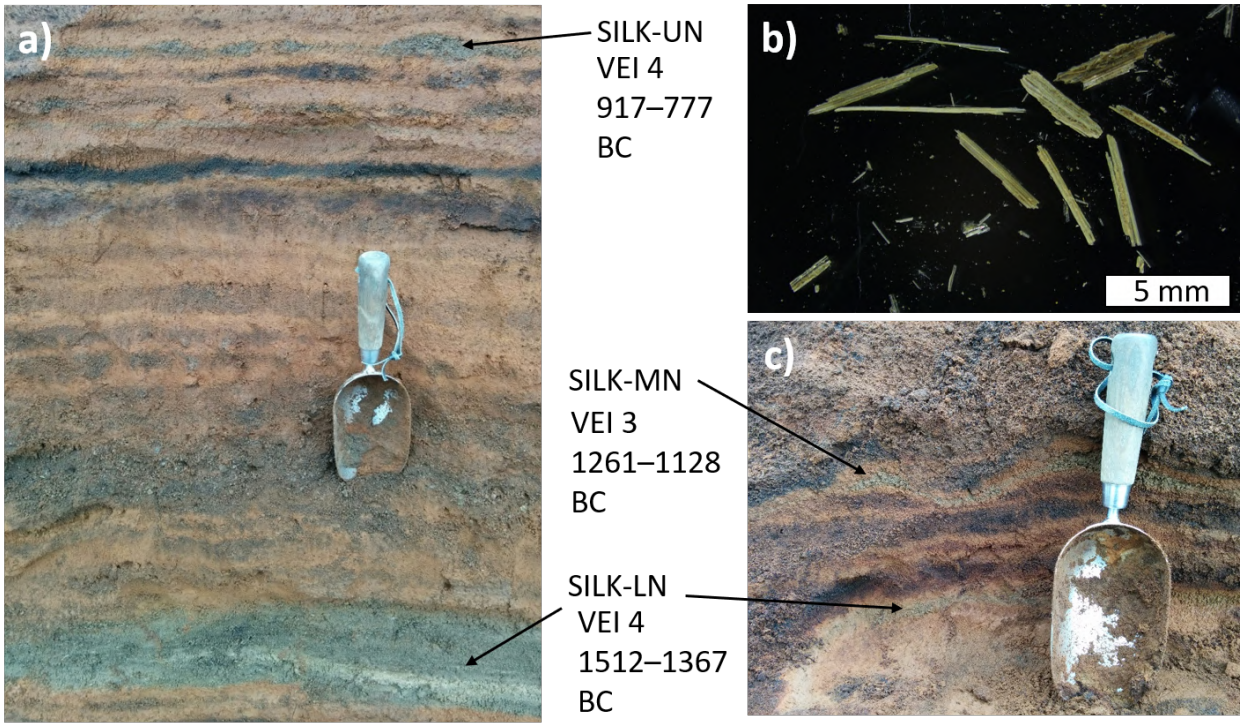

Figure 1.3: Katla SILK tephra in the field and lab: a, c) Example field sites showing the characteristic greenish-grey colour which allows identification in stratigraphic sections and b) photograph of characteristic large needle-shaped tube pumice fragments which also aided identification in the field.

1.2.2 Particle settling in the lab

To determine the impact of shape on settling velocity, I conducted experiments in a settling column using analogue particles, and also co-supervised two Master's projects which continued this line of enquiry. This section briefly details the lab setups along with some discussion of particle motions, an observation which is not covered in detail in any of the following chapters.

Lab setup

To assess the impact of shape on settling velocity, I first conducted lab experiments using smooth, simplified analogue particles (Figure 1.4). This allowed me to systematically vary particle shape, removing the difficulty in quantifying shape for irregular volcanic ash particles. It also meant I could replicate a Reynolds number (*Re*) range consistent with that of distal volcanic ash falling in air, by using a combination of material and fluid properties (summarised in Figure 1.5). Each analogue particle was dropped at least 5 times in a 40 $\times$ 40 $\times$ 70 cm clear Perspex tank (Figure 1.4b) filled with water, glycerine, or glucose syrup, and their trajectories were recorded using a high-speed camera using a variable frame rate based on settling velocity. A mirror was placed at 45° to the back of the tank, to allow simultaneous imaging from two perpendicular views from which the particle's horizontal position was determined.

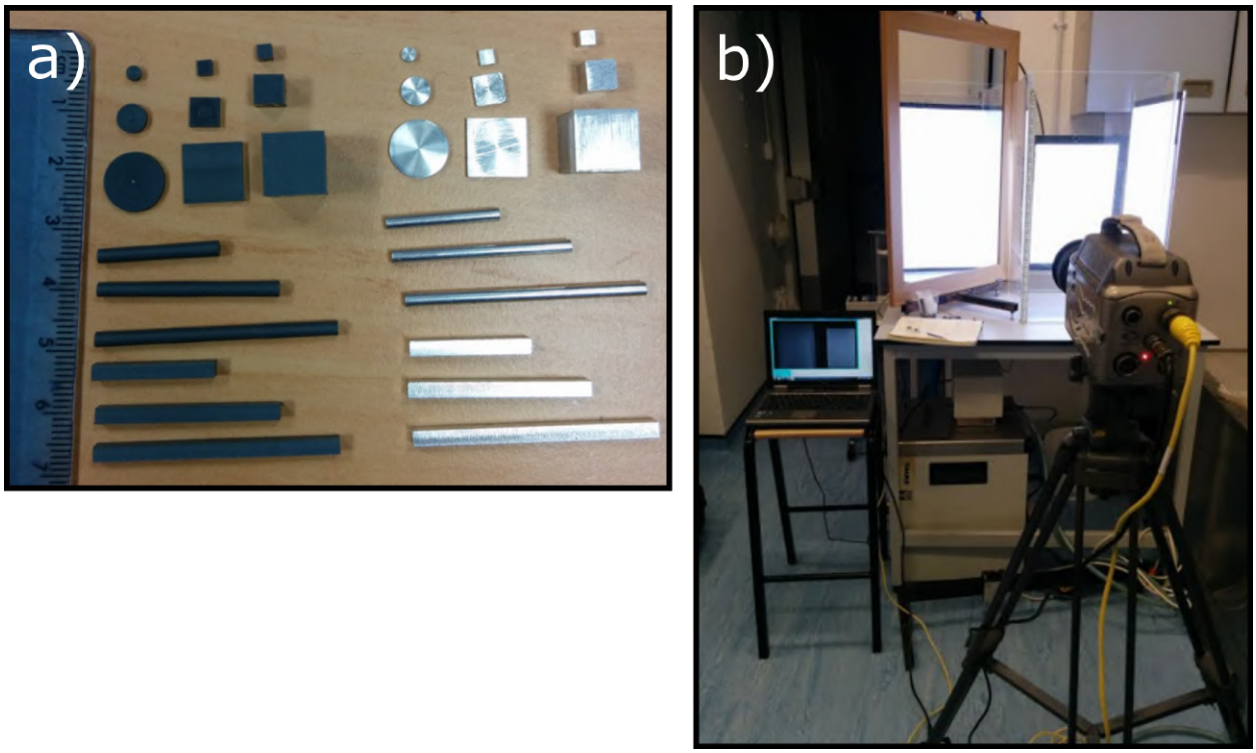

Figure 1.4: a) Ideal particle set, consisting of five particle shapes of three different sizes and two materials (PVC and aluminium) in order to systematically investigate the effect of shape over a wide range of *Re*; b) Photograph of settling tank and high speed camera.

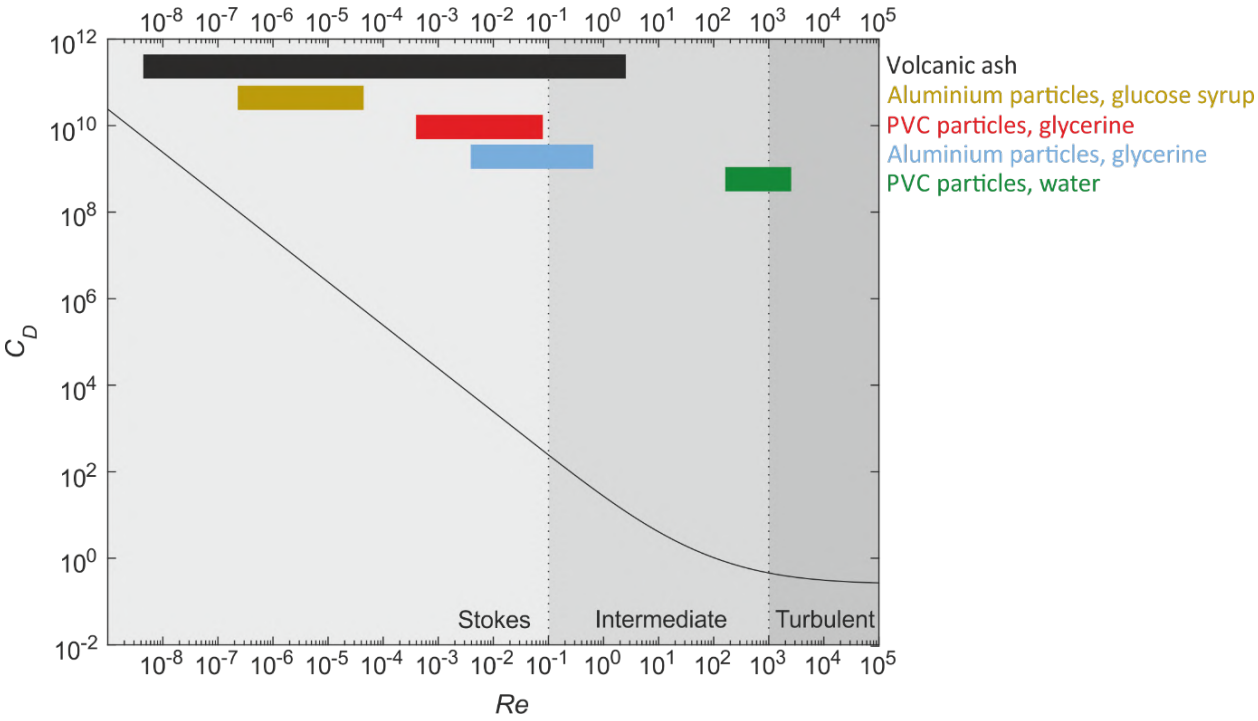

Figure 1.5: *Re* range of volcanic ash particles and particle-fluid combinations used in experimental setup. The *Re* range for volcanic ash particles (black bar) is calculated using the Ganser terminal velocity equations (Ganser, 1993) and the particle size distribution used as an operational default in NAME (0.1-100 µm; Witham et al. (2017)). Also plotted is the theoretical correlation between *Re* and C_D for spherical particles (black line) in the Stokes, intermediate and turbulent regimes (White, 1974).

Particle velocity and secondary motions

Non-spheres fall slower than spheres due to several effects which act to increase drag. The drag on any particle has two components: one third is form drag (pressure on the projected area of the particle in the direction of fall) and two thirds are friction drag (shear stresses over the total surface area of the particle; Leith (1987)). Irregular particles in stable fall will tend to have their maximum projected area in the direction of fall, creating a larger projected area over which to develop form drag; surface irregularities are likely to create a larger surface area over which to develop friction drag. In addition, irregular particles necessarily have regions of surface curvature greater than that of spheres, which can induce flow separation. Grain shape can also result in the development of rotations or oscillations perpendicular to the flow direction, an effect we observe in the intermediate *Re* regime in this study. For irregular shaped particles, it is unlikely that the centre of gravity will coincide with the geometric centre of the particle, and so motion produces a turning moment which can develop into a rotation (Wilson and Huang, 1979). The onset of instability varies between particle shapes; isometric particles begin to oscillate between $Re = 70$ and $Re = 300$

(Pettyjohn and Christiansen, 1948). Researchers using cylinders observe oscillation starting at $Re = 80$, while disks show instability at a wide range of Re with steady oscillations at $Re < 100$ and irregular motion at $Re > 100$ (Jayaweera and Mason, 1965; Willmarth et al., 1964). As well as being shape-dependent, secondary motions increase with increasing particle-fluid density ratio (Christiansen and Barker, 1965). In my lab experiments I observed a wide range of shape- and regime-dependent stable oscillations; examples are shown in Figure 1.6. Flattened particles (disks and squares) show incomplete rotations about the long axis which result in horizontal oscillation; isometric particles (cubes) exhibit a tumbling motion with rotation on all three principal axes; and elongate particles (square prisms and cylinders) rotate around their long axes as they fall. Square prisms additionally exhibit horizontal motion alongside rotation.

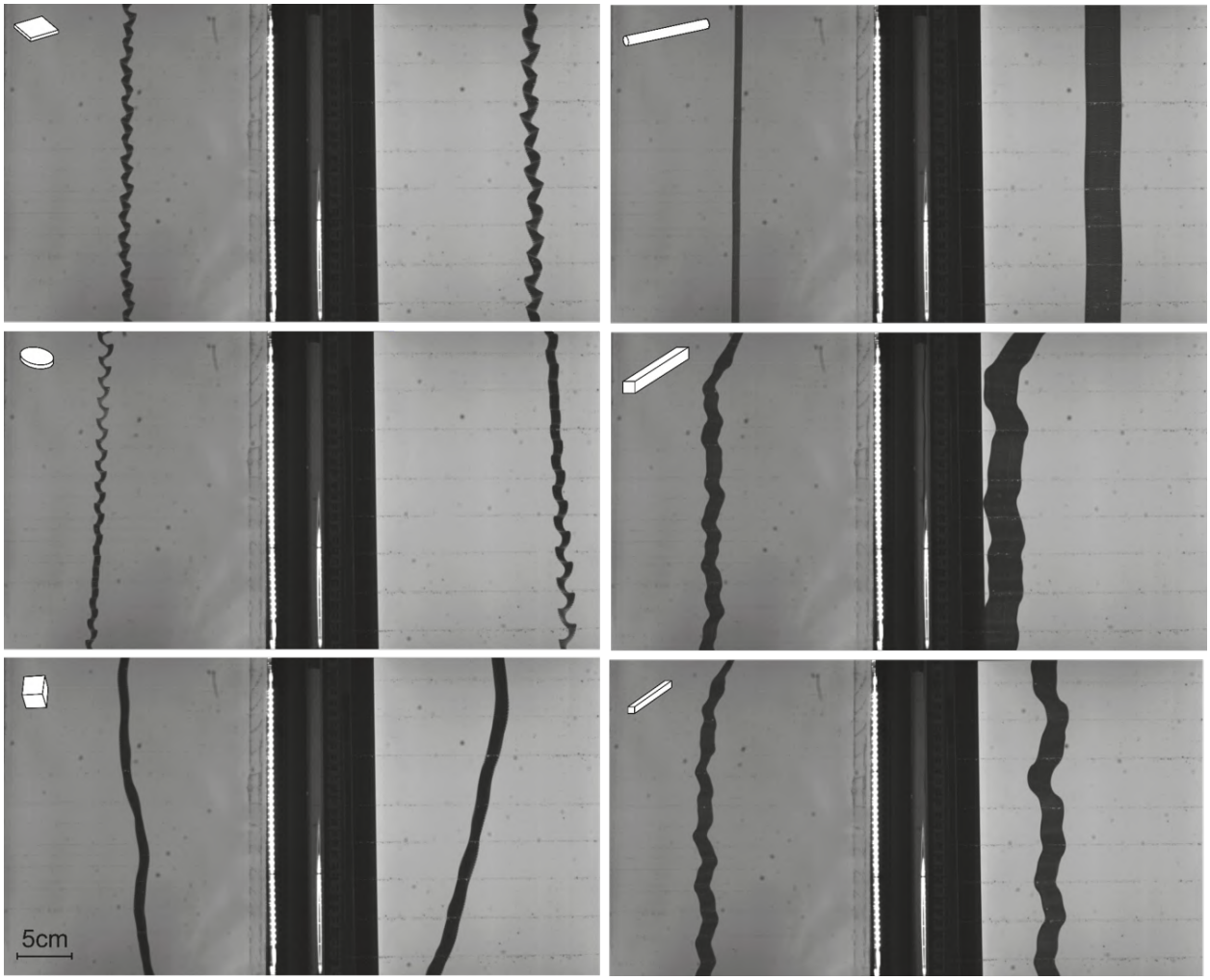

Figure 1.6: Particle trajectories gained by combining high-speed camera images of particles falling in the intermediate regime ($0.1 < Re < 1000$). For each particle trajectory the image shows both the direct view (right) and 90° reflected view using the mirror (left). Insets show particle shape.

Particle centre of mass

An interesting effect I observed is that secondary motions could be suppressed if a small bubble became attached to the particle during its fall. A flat square would usually fall with a regular horizontal fluttering motion in which the maximum projected area would be oriented in the direction of particle fall. However, the same particle with an air bubble attached to one corner would fall in a more irregular trajectory, with the bubble remaining at the top and a much smaller projected area in the direction of fall. Since natural volcanic ash particles contain bubbles and crystals, which like the air bubbles could modify a particle's centre of mass and theoretically impact secondary motions, in 2016-17 I co-supervised a Master's project to determine the relative impacts of shape and internal density distribution on settling velocity. The project (Tennant, 2017) used the same lab setup illustrated in Figure 1.4b, focused on the intermediate flow regime and used plastic particles and glycerine-water solutions. Tennant (2017) used analogue particles with enclosed air bubbles, as well as identical particles with no bubbles. The data therefore bridge the gap in *Re* between my experiments with water and those with glycerine. Data from Tennant (2017)'s experiments with solid (uniform density) particles are published alongside my own experiments with solid particles in Saxby et al. (2018) (Chapter 2 of this thesis).

In 2017-18 I designed another Master's project (Rodger, 2018) to extend the particle velocity dataset to include grains of volcanic ash settling in air at high *Re*. This project required a new, longer settling column which is illustrated in Figure 4.1, Chapter 4. Rodger (2018) investigated the aerodynamics of volcanic ash and related this to physical particle properties including shape, size, density and centre of mass to determine the impact of each property on settling velocity. In Chapter 4 I reanalyse velocity and shape data from Rodger (2018).

The unpublished results from Tennant (2017) and Rodger (2018) concerning particle centre of mass and its impact on secondary motions are summarised separately in Appendix E.

1.2.3 Ash dispersion modelling

The bulk of the modelling in this thesis uses the NAME model (Numerical Atmospheric-dispersion Modelling Environment; Jones et al. (2007)) which is developed by the Met Office, UK, and used to produce volcanic ash concentration forecasts which, along with satellite observations, inform London VAAC forecast products. I used NAME to investigate the sensitivity of ash dispersion models to particle shape; therefore, for other physical properties, I used London VAAC defaults in the absence of measurements. This section explains the origin of these modelling assumptions.

Table 1.1: Default ash particle size distribution used by the London VAAC to forecast the dispersion of volcanic ash in NAME (Witham et al., 2017).

μm	Mass fraction	Cumulative mass fraction
0.1-0.3	0.001	0.001
0.3-1.0	0.005	0.006
1.0-3.0	0.05	0.056
3.0-10.0	0.2	0.256
10.0-30.0	0.7	0.956
30.0-100.0	0.044	1.0

Eruption source parameters (ESPs) that can be specified in NAME are (Witham et al., 2017):

- Plume location
- Date, time, and duration of each eruptive phase
- Source geometry (NAME can accept point or spatially extended sources)
- Upper and lower plume heights, including temporal variations
- Mass eruption rate
- Vertical ash distribution
- Particle size distribution
- Ash density
- Ash shape

The physical particle properties currently used by the London VAAC are ash density and ash particle size distribution (PSD) (Witham et al., 2017); shape is assumed to be spherical. The default density for volcanic ash is 2300 kg m^{-3}, falling within observed values (e.g. Riley et al. (2003)). The default particle size distribution is given in Table 1.1; NAME continually accounts for a changing PSD by modelling sedimentation of large particles in the dry and wet deposition schemes (Beckett et al., 2014). Particles larger than 100 μm are assumed to fall out proximal to the volcano. The PSD is taken from Hobbs et al. (1991), who recorded ash size distributions from Mount St Helens, St Augustine, and Mount Redoubt. These defaults are generally used in the absence of any observations, but both input density and size distribution can be adjusted during an eruption to take new observations into account.

The London VAAC default is to release ash with a uniform distribution between the volcano's summit and the top of the plume, meaning that in the horizontal, a point source is used (Witham et al., 2017). The uniform vertical spread at source is used to account for uncertainties in plume height, and avoid forecasting the absence of ash at flight levels where it may be present (Webster et al., 2012; Webley et al., 2009). Vent and plume dynamics are not explicitly modelled (Witham et al., 2017). Instead the VAAC setup sums up near-source processes such as fallout, aggregation, and the effect of downdrafts by using an 'effective source' aimed at representing their net effect (Webster et al., 2012).

Mass eruption rate is based on a statistical relationship with plume height (Mastin et al., 2009):

$$H = 2.0V^{0.241} \tag{1.1}$$

where H = plume height above summit (km) and V = volumetric flow rate (m^3 DRE s^{-1}). The relationship is a correlation based on historical observations. Equation 1.1 gives the total volumetric flow rate, but it is expected that the majority of the total erupted mass will be particles larger than the maximum in the London VAAC's default PSD (Table 1.1) or aggregates of smaller particles. To account for this discrepancy it is assumed that most material falls out close to the vent, and the London VAAC accounts for this by multiplying the mass eruption rate by a 'distal fine ash fraction' of 5%. The proportion of total mass erupted included in the model does not affect forecasts of ash cloud extent but does affect the concentration of ash in the cloud.

1.3 Thesis overview

This thesis is formed of three papers which are either published or in revision; and a conclusions section including a description of ongoing and future work. In the overview below, I briefly describe the main outcomes of each section.

1.3.1 Chapter 2: The impact of particle shape on fall velocity: Implications for volcanic ash dispersion modelling

In this paper we investigated the sensitivity of volcanic ash terminal velocity, travel distance, and air concentration to particle shape. We used analogue experiments with non-spherical particles to examine the influence of shape and flow regime on drag and terminal velocity, alongside sensitivity analysis using the NAME dispersion model, which is used operationally by the London VAAC.

We found that the influence of shape on drag is highly dependent on flow regime and is greater at high Reynolds numbers (*Re*). In addition, the velocity of small, low-*Re* particles (volcanic ash of diameter $<$ 1-3 μm) is lower than typical atmospheric vertical velocities (advection and diffusion) and therefore transport is controlled by atmospheric processes; the relative influence of terminal velocity and therefore shape is greater as particles increase in size, and the transport of particles $>$ 100 μm is highly sensitive to shape. Therefore, the sensitivity of model outputs to shape is dependent on the input particle size distribution. For ash concentration forecasts, using a maximum particle size of 100 μm, we find that it is reasonable to use a spherical particle approximation as most VAACs currently do.

We also showed that the travel distance of large grains ($>$ 100 μm) is highly sensitive to shape, an important result for understanding the distal transport of tephra from large eruptions. Qualitative shape descriptions of particles in very distal ($>$ 1000 km) ash deposits preserved as non-visible (cryptotephra) layers reveal that these particles are usually very non-spherical winged or platy shards interpreted as large bubble wall fragments; there is little available quantitative shape data. There is a discrepancy between the measured and modelled transport distances of the largest cryptotephra shards; while most volcanic ash dispersion modellers assume that grains $>$ 100 μm fall out close to source, tephrochronologists regularly measure larger grain lengths in distal deposits. This discovery led me to research the influence of particle shape on the dispersion of the widespread Vedde cryptotephra, the project which forms the basis of Chapter 3.

1.3.2 Chapter 3: The importance of grain size and shape in controlling the dispersion of the Vedde cryptotephra

In this paper we assessed methods of measuring particle shape and size, and investigated the impact of the measurement method on the modelled travel distance of tephra from distal deposits. For this project we used samples of the Vedde cryptotephra from Katla volcano, Iceland, collected from proximal (Icelandic) and distal (Norwegian) deposits. Using optical microscopy and X-ray computed tomography (CT) scanning, we accurately measured particle size and shape using parameters by which atmospheric dispersion models are calibrated. The extreme anisotropy of distal particles compared to a proximal sample from the same eruption highlights the role of shape in atmospheric dispersion. We used our measured shape parameters and modern met data to initialise both a simple 2D atmospheric model written in MATLAB, and the NAME model. The results show that the transport of the largest grains (191 μm) in the Norwegian deposits is highly sensitive to shape over the distance from Katla volcano to the sample sites; only when we use a shape parameter can we explain the transport of large grains to distal sites ($>$ 1000 km).

We suggest that documenting ash shape and size is important for reconciling perspectives of the tephrochronology and physical volcanology communities, and we suggest some best practices for measuring the physical properties of cryptotephra particles. Collecting particle shape data for this chapter led to some critical evaluation of the X-ray CT method, a topic which is further explored in Chapter 4.

1.3.3 Chapter 4: How to measure the shape of volcanic ash, and recommendations for dispersion modelling

In this paper we assess the impact of the choice of shape descriptor and scan parameters on the results of measuring shape in 3D using X-ray CT. We use the resulting insights to assess the effectiveness of shape descriptors in anticipating terminal fall velocity, by measuring the velocity of particles in a settling column. We find that X-ray CT is an efficient and accurate method of obtaining bulk 3D shape parameters. Shape measures based on principal axis lengths are both less variable with particle size, and much less sensitive to imaging resolution, than shape measures based on surface area. We find that drag laws using the surface-area based shape factor sphericity are accurate when imaging resolution is between 10^2 and 10^5 voxels per particle; in addition, using the surface area of an equivalent scalene ellipsoid is a good approximation. We conclude that the shape-dependent drag laws of Ganser (1993), Bagheri and Bonadonna (2016b), and Dioguardi et al. (2018) produce more accurate terminal velocity estimates than a spherical approximation (White, 1974). Finally, we use these insights to present a database of shape descriptors for use with the above shape-dependent drag laws, which are valid for a wide range of flow regimes and therefore suitable for operationally modelling volcanic ash dispersion. The aim of this database is to provide average shape values which can be used to initialise dispersion models where no shape data are available, e.g. by VAACs during an eruption.

1.3.4 Chapter 5: Conclusions

In the conclusions section of this thesis, I assess the extent to which the preceding chapters have contributed towards answering the original research questions posed in the introduction. I also discuss the practical implications of the work in this thesis, including planned changes to the London VAAC operational volcanic ash forecasting system to parameterise the non-sphericity of volcanic ash. Finally, I suggest future work which would further contribute to the understanding of how 'extreme' volcanic ash shapes form and how best to model the transport of ash from large explosive volcanic eruptions.

Chapter 2

The impact of particle shape on fall velocity: implications for volcanic ash dispersion modelling

Author contributions and declaration: This chapter has been published in the Journal of Volcanology and Geothermal Research: Saxby, J., Beckett, F., Cashman, K., Rust, A., and Tennant, E. (2018), 'The impact of particle shape on fall velocity: Implications for volcanic ash dispersion modelling', Journal of Volcanology and Geothermal Research, 362, 32-48. Collection of ash samples was performed by Jennifer Saxby apart from the Vedde ash sample which was provided by Sigurður Reynir Gíslason. Analogue particles were made by Charles Clapham, who also helped build the velocity measurement setup. Shape measurement was performed by Jennifer Saxby with help and guidance from Tom Davies. Terminal velocity experiments were performed by Jennifer Saxby, apart from the experiments using a 70% glycerine solution which were performed by Eleanor Tennant as part of her Master's project which was supervised by Jennifer Saxby, Katharine Cashman and Alison Rust. Helen Webster provided valuable insights into the turbulence parameterisation in NAME. Frances Beckett, Dave Thomson, Claire Witham, Andrew Jones, and the Atmospheric Dispersion and Air Quality research group (Met Office, UK) provided support with dispersion modelling, and Matt Hort provided feedback on an earlier draft. During the publication process, reviews from Fabio Dioguardi and an anonymous reviewer greatly improved the manuscript.

Abstract

Modelling atmospheric volcanic ash dispersion is a critical tool in mitigating the impact of large explosive eruptions; it is also useful for understanding and reconstructing past events. Most atmospheric dispersion models include a sedimentation velocity term that is sensitive to the physical properties of the particle, but many do not use particle shape as an input parameter; instead particles are assumed to be spherical. There are many empirical and semi-empirical shape-dependent drag laws. We measure the velocity of scaled analogue particles over the range of flow conditions anticipated for volcanic ash dispersion to test published formulae against an independent dataset. We use a semi-empirical formula we determined to be accurate for non-spheres to investigate the sensitivity of the modelled transport of an ash cloud to particle shape, using the atmospheric dispersion model NAME and a shape parameter we measure for non-spherical ash particles from Katla volcano, Iceland. We find that model particle trajectories are sensitive to particle shape for particles >1–3 μm diameter; the sedimentation velocity of smaller particles is low compared to atmospheric vertical velocities. Sensitivity to shape increases with size such that 100 μm particles can travel 44% further from the source when they are highly non-spherical (sphericity = 0.5). Despite the sensitivity of the fall velocity of large particles to their shape, however, forecasts of distal ash concentration using particle size distributions of 0.1–100 μm and 0.1–250 μm show relatively good agreement between a spherical and non-spherical case for the first 36 h after an eruption. The vertical structure of an ash cloud is more sensitive to particle shape than the horizontal extent. Model particle trajectories are also sensitive to particle size, and we find a discrepancy between different particle size parameters for non-spherical ash: particle long axis L, used in cryptotephra studies, was on average twice the equivalent-volume sphere diameter d_v, used in dispersion modelling, for tephra samples from Katla volcano, Iceland. This discrepancy in size measurements could explain the observed travel distance of large distal cryptotephra shards.

2.1 Introduction

The ability to forecast the atmospheric transport of volcanic ash is crucial for mitigating the potential impact to aircraft, respiratory health, agriculture, and infrastructure (Stevenson et al., 2013; Giehl et al., 2017). Dispersion modelling can also aid in reconstructing past events: cryptotephra layers, distal and widespread volcanic ash deposits from large explosive eruptions, can be linked to their source volcano to provide an age framework for the host sediment (e.g., Wastegård, 2002). Dispersion modelling has the potential to constrain ash source regions for these eruptions. Modelling can also provide insights into the dynamics of past large eruptions in the absence of modern analogues, for example the $\sim$ 39 ka Campanian Ignimbrite (Italy; Costa et al. (2012)), the $\sim$ 74 ka Younger Toba Tuff (Indonesia) and the $\sim$ 340 ka Whakamaru eruption of Taupo (New Zealand; Matthews et al. (2012)).

To model the dispersion of an ash cloud the sedimentation of the particles must be represented. The fall velocity of a particle is governed by its physical properties, including its shape; for a given volume and density, non-spherical particles fall more slowly than spheres (e.g., Haider and Levenspiel, 1989). Eruptive processes produce a wide range of volcanic ash morphologies, making an accurate description of particle shape challenging (Liu et al., 2015). In addition, there are multiple empirical and semi-empirical correlations between shape and fall velocity for volcanic particles or analogues (Wilson and Huang, 1979; Haider and Levenspiel, 1989; Ganser, 1993; Dellino et al., 2005; Bagheri and Bonadonna, 2016b; Dioguardi et al., 2017, 2018), but little published literature compares the formulae or assesses their use in atmospheric dispersion models. An assessment of shape formulae for modelling particle travel distance is necessary because there is a recognised discrepancy in distal grain size data between the fields of volcanology (deposit sampling), dispersion modelling and satellite ash retrieval (Stevenson et al., 2015). Moreover, dispersion modelling has been unable to account for the observed travel distances of large, typically $>$80 μm, volcanic ash shards in cryptotephra deposits (Beckett et al., 2015; Stevenson et al., 2015; Watson et al., 2016). We hypothesise that particle shape may control tephra dispersion as very distal cryptotephra deposits from large explosive eruptions often contain abundant flat, platy shards (Mangerud et al., 1984; Blockley et al., 2007; Stevenson et al., 2015; Cashman and Rust, 2016).

We measure the velocity of scaled analogue particles to evaluate empirical shape formulae. In doing so we compare empirical schemes for estimating fall velocity using an independent dataset and use this to determine the most appropriate scheme for modelling the dispersion of non-spherical ash. We then measure the shape of ash particles from Katla volcano, Iceland, using 2D and 3D measurement techniques to compare the resulting shape data; we then use the data to investigate the sensitivity of the atmospheric dispersion model NAME (Numerical

Atmospheric-dispersion Modelling Environment; Jones et al. (2007)) to the formula we determine to be most accurate for non-spheres (Ganser, 1993), compared to an analytical solution for spheres (White, 1974). We assess both the sensitivity of maximum particle travel distance, important for understanding the distribution of cryptotephra particles (Stevenson et al., 2015), and distal atmospheric ash concentrations, with implications for ash forecasting. In this way we bring together the disciplines of physical volcanology and dispersion modelling to gain a greater understanding of the benefits and limitations of measuring particle shape and its uses as a dispersion model input parameter.

2.2 Background

Atmospheric dispersion models are numerical solutions describing physical and chemical processes within a suspended plume in response to atmospheric conditions (Holmes and Morawska, 2006). Models include a source term, which describes the location and magnitude of the source; source terms range from complex plume dynamics models to simple point sources. The particles are then dispersed according to meteorological (met) data from an atmospheric model, and processes such as sedimentation and deposition, which are controlled by a transport model. Eulerian transport models solve for particle concentration over a fixed computational grid (e.g. FALL3D; Costa et al. (2006)), whereas Lagrangian transport models calculate trajectories of model particles representing the mass of many real particles (e.g. HYSPLIT; Draxler and Hess (1997)). Both model types solve advection-diffusion equations, in which chemical or particulate pollutants are released from a source and dispersed passively (i.e. do not alter the flow conditions) according to wind velocity (advection) and atmospheric turbulence (diffusion). Heavy particulates, including volcanic ash, are also subject to sedimentation (gravitational settling).

In the Lagrangian model NAME (Jones et al., 2007), the behaviour of particulates in the vertical is determined by vertical velocity w:

$$w = w_a - w_{sed} + w' \tag{2.1}$$

where w_a is wind advection, w' is turbulent diffusion, and w_{sed} is sedimentation velocity. We can assume w_{sed} is equal to particle terminal velocity w_t, the velocity a particle obtains when its weight is balanced by air resistance such that the net force acting on the particle is zero and it no longer accelerates; fine grained particles reach terminal velocity in the atmosphere over distances that are negligible compared to plume height. Terminal velocity is a function of physical

particle properties including size, density and shape, as well as atmospheric density and viscosity, which vary with altitude (Jones et al., 2015). Particle removal processes can include impact on the ground surface (dry deposition; Webster and Thomson (2011)) and removal by precipitation (wet deposition; Webster and Thomson (2014)).

2.2.1 Modelling sedimentation

Scaling requires that terminal velocity be defined as a function of the dimensionless drag coefficient C_D. Terminal velocity w_t is calculated by:

$$w_t = (\frac{4}{3}\frac{d}{C_D}g\frac{\rho_P - \rho}{\rho})^{\frac{1}{2}} \tag{2.2}$$

where d is a characteristic particle dimension, g is gravitational acceleration (9.81 m s^{-1}), ρ is fluid density, and ρ_P is particle density. Parameters with a first order impact on C_D are shape and orientation (Bagheri and Bonadonna, 2016b), particle/fluid density ratio, and Reynolds number (Re), the ratio of inertial to viscous forces:

$$Re = \frac{\rho w_t d}{\mu} \tag{2.3}$$

where μ is the dynamic viscosity of the fluid. When Re is <0.1 such that there is no wake at the rear of a falling particle (Stokes flow), C_D for rigid spherical particles is well approximated by Stokes' Law:

$$C_D = \frac{24}{Re} \tag{2.4}$$

(Clift et al., 2005). At higher Re, the flow passes into a transitional state known as the intermediate regime. Between $Re = 20$ and $Re = 130$, an attached wake forms and increases in size downstream of the particle. From $Re \approx 1000$, the flow around a particle is fully turbulent (Clift and Gauvin, 1971). In this turbulent regime, C_D does not significantly change with Re; it can be considered a function of particle shape alone (Chhabra et al., 1999).

Irregular particles can have high surface curvature, a relatively large surface area over which to develop friction, and a tendency to display secondary oscillations during settling. All these factors mean that C_D of a highly irregular particle can be up to many orders of magnitude higher than that of a sphere (Dietrich, 1982). Variability in magma properties and fragmentation mechanisms

means that ash particles can have rough surfaces and low density (micropumice) or be extremely non-spherical (glass shards), making their terminal velocity difficult to anticipate (Dellino et al., 2005; Loth, 2008).

Analytical drag laws allow accurate velocity calculation for spheres (e.g., Clift and Gauvin, 1971; White, 1974) and a limited range of ellipsoidal shapes (e.g., Bagheri and Bonadonna, 2016b) over a wide *Re* range. Analytical solutions do not exist for flow around irregular particles; instead, empirical correlations are used. For meaningful comparison between particles, it is necessary to have a consistent definition for particle dimension d, although even with this condition C_D is sensitive to particle shape (Wilson and Huang, 1979). Since the drag coefficient of spheres can be determined analytically, most empirical sedimentation schemes define d as d_v, the diameter of a volume-equivalent sphere; C_D is then a function of one or more geometric ratios which compare the particle being described to a sphere (Clift et al., 2005). An example is sphericity ψ, the ratio of the surface area of a volume-equivalent sphere to the surface area of the particle (Wadell, 1933); a ψ of 1 indicates perfect sphericity and a ψ close to 0 indicates extreme non-sphericity. Particles with different shapes can have the same sphericity; this caveat is unavoidable if a small number of easily measurable shape descriptors are needed to describe an infinite number of possible morphologies (Clift et al., 2005). Another class of particle descriptors, termed form factors, use ratios between principal axis lengths (Wilson and Huang, 1979; Bagheri and Bonadonna, 2016b); these have the advantage of being simpler to measure than surface area for irregular particles, and they are less sensitive to image resolution (Liu et al., 2015). However, form factors do not describe small-scale surface roughness, which increases C_D (Achenbach, 1974). The most meaningful shape descriptor for any application is therefore dependent on the morphological variability of the particles. An important caveat of empirical correlations is that they are only valid within the *Re* range of the experiments on which the correlation is based.

2.2.2 Volcanic ash forecasting

Monitoring and operational forecasting of volcanic ash clouds is carried out worldwide by nine Volcanic Ash Advisory Centres (VAACs; ICAO (2012)), each responsible for a discrete region of airspace. VAACs use atmospheric dispersion models to forecast ash transport in the atmosphere following an eruption. The eruptive source can be characterised by its location, dimensions, vertical distribution of ash, plume phases (e.g. gas, particulates), and mass eruption rate (Hort, 2016). Most VAACs model volcanic ash as sedimenting particles, with the exception of the Montreal VAAC, which by default treats ash as a non-sedimenting particle (D'Amours et al., 2010). The remaining VAACs calculate particle terminal velocity as a function of physical particle

properties, including size (as a single value or particle size distribution), density, and shape. The Buenos Aires, Tokyo and Darwin VAACs operationally model non-sphericity (Hort, 2016). For example, the Buenos Aires VAAC uses the Fall3D dispersion model (Folch et al., 2009), which calculates sedimentation velocity using the Ganser (1993) sedimentation scheme with a default sphericity of 0.9 (Reckziegel et al., 2016), and the option to vary sphericity for each particle class if shape data are available.

In this study we focus on the operational setup of the London VAAC, which uses the NAME dispersion model. NAME is maintained and developed by the Met Office, UK, and has been used operationally to provide forecasts of pollutant dispersion for a wide range of applications, including for crises such as the 2005 Buncefield oil depot explosion (Webster et al., 2007) and the Fukushima power plant accident in 2011 (Leadbetter et al., 2015), as well as daily resuspended ash forecasts for southern Iceland (Liu et al., 2014; Beckett et al., 2017) and routine air quality forecasts for the UK (Jones, 2004). The London VAAC is responsible for providing forecasts of volcanic ash clouds for the domain covering Iceland, Scandinavia, the UK, and the north-eastern part of the North Atlantic. Most recently they provided forecasts for ash clouds from the eruptions of Eyjafjallajökull in 2010 and Grimsvötn in 2011 (Webster et al., 2012). For London VAAC forecasts (and by default where no scheme is specified), NAME calculates particle terminal velocity using the White (1974) analytical formula for spheres.

The main applications of volcanic ash forecasting are to prevent aircraft encounters with high concentrations of volcanic ash during or shortly after an eruption (Folch, 2012). The VAACs produce Volcanic Ash Graphics (VAGs) and accompanying text documents, Volcanic Ash Advisories (VAAs), which depict the forecast location of the ash cloud out to T + 18 h. However, also important is the long-term transport of ash particles and sulfate aerosols in the stratosphere, which can cause climate forcing by affecting the atmospheric radiative budget over months or years (e.g. Lacis et al. (1992)). Direct sampling of the El Chichón ash cloud, for example, has indicated that particles >5 μm can remain in the stratosphere for at least 6 months (Gooding et al., 1983); this may be due to slow settling of irregular shapes and low-density aggregates (Gooding et al., 1983; MacKinnon et al., 1984). Our conclusions on particle behaviour using NAME, however, are time-dependent and specific to the problem of forecasting volcanic ash concentration in the hours to days after an eruption.

In the absence of measurements of physical particle properties during an eruption, the London VAAC uses a default particle size distribution (PSD) based on grain size distributions from eruptions of Mount St Helens, Augustine, and Redoubt volcanoes (Hobbs et al., 1991), and assumes a density of 2300 kg m^{-3} (suitable for rhyolite glass). The setup considers particles from 0.1–100 μm, with larger particles assumed to fall out close to the volcano (Witham et al., 2017).

Importantly, the model sedimentation equations use volume-equivalent sphere diameter (d_v), while the Hobbs et al. (1991) PSD is determined from forward light scattering measurements by airborne instruments. The scattering properties of particles are dependent on particle shape, and therefore diameters determined by scattering coefficients are unlikely to be equal to d_v. Alternatively, PSDs from ground-based sampling studies are often determined by sieving the volcanic ash samples; although sieve size is also unlikely to be equivalent to d_v, especially for particles with very irregular shapes (Garboczi et al., 2017).

Beckett et al. (2015) found that NAME volcanic ash forecasts are sensitive to PSD, with density and shape having lesser but still signifcant impacts. They show, for example, that a d_v = 100 µm particle of ψ_R = 0.4 could travel up to 60% further than a spherical particle of equivalent volume. Here the shape descriptor ψ_R is a 2D measure of sphericity based on particle projected area and perimeter (Riley et al., 2003). 2D shape descriptors are often used as substitutes for 3D sphericity ψ due to the difficulty in obtaining surface area and volume measurements of fine ash particles. However, the sensitivity of the Ganser (1993) scheme to the method of sphericity measurement has not been evaluated.

2.2.3 The plume and ash cloud phases of ash transport and their representation in ash dispersion models

Tephra from an explosive eruption can be classified into several categories according to the conditions under which it falls out, which are linked to phases of plume development. Initially, an erupting plume rises convectively by buoyancy until the density of the plume is equal to the density of the atmosphere, at which height the plume spreads laterally as a gravity current (Koyaguchi and Ohno, 2001). Very coarse fragments are ejected from the lowest part of the column and follow ballistic trajectories (Bonadonna and Phillips, 2003); fragments with higher terminal velocity than the convective column rise velocity will not reach the umbrella cloud (Koyaguchi and Ohno, 2001). These classes of particles are often observed in proximal deposits as a pumice or scoria cone around the vent. Smaller particles (Class II fragments in the classification of Koyaguchi and Ohno (2001)) have terminal velocities lower than turbulent velocity in the umbrella cloud, but higher than atmospheric turbulence; these are mixed in the plume and fall out from the base of the umbrella cloud according to their terminal velocities. Particles with velocities lower than atmospheric turbulence and vertical advection (Class III fragments in the classification of Koyaguchi and Ohno (2001)) are most extensively dispersed in the atmosphere and can travel hundreds or thousands of km and remain in the atmosphere for months or years (e.g., Gooding et al., 1983). The grain size range of each class depends on eruption dynamics and atmospheric properties. Most atmospheric

dispersion models built for forecasting medial to distal ash clouds, such as NAME, do not explicitly parameterise near-source processes such as convection in the plume, and are instead designed to forecast the dispersion of particles in classes II and III (Koyaguchi and Ohno, 2001); the work presented here is focused on these smaller particles. In operational NAME forecasts, the fallout of larger particles from the convecting column is summed up by using an 'effective source' of 5% of the erupted mass, representing the distal fine ash fraction (Witham et al., 2017) which also accounts for other near-source processes such as enhanced fallout due to aggregation.

2.2.4 Quantifying ash morphology

To assess the discrepancy between ψ and ψ_R, and to provide a shape parameter for sensitivity analysis using NAME, we need to quantify the shape of volcanic ash; our samples are chosen for their unusual particle morphology and potential hazard impact. The main source of volcanic ash hazard to the UK and northern Europe is Iceland, with 124 explosive (>95% of magma erupted as tephra) eruptions since written records began around 870 CE (Thordarson and Larsen, 2007). Wind can transport ash from a short explosive eruption in Iceland to any country in Europe within 24 h, with most countries above 50°N subject to a >20% probability of airborne ash concentrations exceeding a 'safe' threshold (Leadbetter and Hort, 2011). Indeed, most cryptotephra layers in northern Europe have been identified by geochemical analysis to originate from Iceland (Lawson et al., 2012). Katla is an active subglacial volcano in Iceland's Eastern Volcanic Zone that is characterised in the Holocene by explosive basaltic eruptions, with over 300 in the last 8400 years (Óladóttir et al., 2005). The average repose interval from 1500 CE to present is 47 years (Larsen, 2000). Less common are eruptions of more evolved Katla (SILK) tephras; these take place with average repose intervals of 100–1000 years, although it is 1700 14C years since the last known SILK eruption (Larsen et al., 2001). We examine two samples of Katla tephra:

- The Vedde ash is found across northern Europe as a cryptotephra deposit and is thought to originate from an eruption of Katla around 12 ka BP (Wastegård et al., 1998; Lane et al., 2012). The Vedde has a bimodal composition consisting of both basaltic and rhyolitic ash, with SiO_2 contents of 45–58 and 72–76% respectively (Mangerud et al., 1984). It contains characteristic flat, platy rhyolitic glass shards that we interpret as bubble wall fragments (Figure 2.1).
- The SILK-LN ash is an intermediate composition ($\sim$ 65% SiO_2) tephra dated to $\sim$ 3.4 ka BP (Larsen et al., 2001; Óladóttir et al., 2005). It contains grains of variable morphology including distinctive 'needles' (Figure 2.1), which contain elongate bubbles in a glassy,

sparsely crystalline matrix. The SILK-LN tephra forms a widespread deposit in southern Iceland. Its volume on land of 0.12 km^3 DRE (Larsen et al., 2001) suggests an eruption of at least VEI 4 (Newhall and Self, 1982).

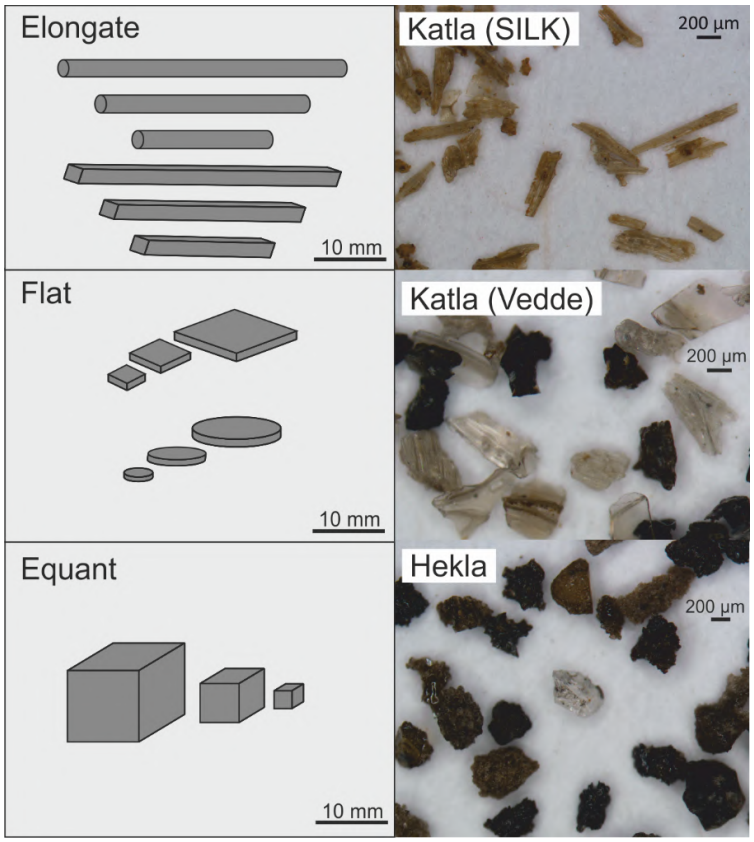

Figure 2.1: Particles used in scaled analogue experiments (left), and corresponding example ash morphologies from Katla and Hekla volcanoes, Iceland (right). SILK indicates the SILK-LN tephra layer ($\sim$ 3.4 ka BP; Larsen et al. (2001)); the Vedde ash has been dated to 12 ka BP (Wastegård et al., 1998); the Hekla sample is from the 1947 eruption.

Table 2.2: Physical properties of particles and fluids used in scaled analogue experiments.

Fluid	Fluid density ρ (at 17.5°C), kg m^{-3}	Fluid viscosity μ (at 17.5°C), Pa.s	Particles	Particle density ρ_P, kg m^{-3}	Reynolds number (*Re*) range	Flow regime(s)
Glucose syrup	1419.44	206.9	Aluminium	2707	$7.6 \times 10^{-7} < Re < 4.0 \times 10^{-5}$	Stokes
Glycerine	1262.6	1.7882	PVC	1431	$3.3 \times 10^{-4} < Re < 0.07$	Stokes
			Aluminium	2707	$3.3 \times 10^{-3} < Re < 0.09$	Stokes
70% glycerine 30% water	1194.6	0.040533	PVC	1431	$2 < Re < 56$	Intermediate
Water	998.51	0.0010696	PVC	1431	165 <Re< 2316	Intermediate, turbulent

2.3 Evaluation of sedimentation schemes and shape descriptors for non-spherical particles

Particle settling experiments with scaled analogue particles allowed us to systematically vary particle size, shape and density. We used analogue particles with ψ of 0.45 to 0.8 to represent end-member ash geometries (Figure 2.1). Geometries were simplified to allow accurate particle characterisation and measurement of multiple complex shape descriptors. Particle and fluid properties (Table 2.2) were adjusted to create flow conditions relevant to volcanic ash dispersion. The *Re* range of the experiments ($7.6 \times 10^{-7} > Re > 2316$) is characteristic of volcanic ash of about 0.6 - 2800 μm diameter falling in air (assuming spherical particles, a density of 2300 kg m^{-3}, atmospheric density of 1.225 kg m^{-3}, and atmospheric viscosity of 1.98×10^{-5} Pa.s). For comparison, most VAACs operationally model particles $\leq$ 100 μm (Hort, 2016); however, in large eruptions particles $>$ 100 μm comprise a substantial mass fraction of far-travelled deposits (Cashman and Rust, 2016). Extending our experiments to higher *Re* (i.e. higher equivalent ash diameter) also allowed us to assess the performance of sedimentation schemes in both Stokes and intermediate flow. As a caveat, we note that the particle-fluid density ratio also has an impact on C_D in the intermediate regime (Bagheri and Bonadonna, 2016b), and that the range of experimental particle-fluid density ratios ($\sim$ 1.1–2.1) is much lower than the density ratio expected for ash falling in air ($\sim$ 2000).

We recorded the velocity of analogue particles in a 40 × 40 × 70 cm clear Perspex tank filled with water, glycerine, a 70% volume glycerine-water solution, or glucose syrup. Particle trajectories were filmed using a Vision Research Phantom v9.1 high-speed video camera with a frame rate of 1000 fps. The video data were processed with Phantom Camera Control and ImageJ software. We recorded vertical velocity, but particles also moved laterally. For this reason, we placed a mirror at 45° to the edge of the tank to give an orthogonal view and allow trigonometric calculation of each particle's exact vertical position. Terminal velocity was calculated as the mean of five repeat measurements for each particle-fluid combination; we then calculated Re and C_D as a function of w_t. We ensured each particle reached terminal velocity by measuring velocity as a function of depth and only including data averaged over a depth range with constant velocity. The impact of boundary wall proximity on velocity was corrected using the approach of Chhabra et al. (1996) and Chhabra (1995); see Appendix A for details.

To compare measured w_t to published drag laws, we calculated theoretical w_t and Re using eqs. 2.2 and 2.3, and C_D using an analytical solution for spheres (White, 1974) and empirical solutions using one or more geometric shape descriptors (Wilson and Huang, 1979; Ganser, 1993; Bagheri and Bonadonna, 2016b; Dioguardi et al., 2017). These formulae are summarised in Table 2.4. For empirical correlations, the Re range of experiments is given. The schemes of Wilson and Huang (1979) and Dioguardi et al. (2017) are fully empirical in that they do not explicitly contain theoretical justification; the Ganser (1993) and Bagheri and Bonadonna (2016b) formulae incorporate an analytical solution for ellipsoids in Stokes flow (Oberbeck, 1876) and so can be considered semi-empirical. The resulting nonlinear equation systems were solved using a Matlab code which iterates to convergence, using w_t of an equivalent-volume sphere in Stokes flow as an initial guess. As all equations rely on an initial guessed Re, the solutions are locally convergent.

We calculated geometric shape descriptors (Table 2.4) using digital caliper measurements. Where it was necessary to use two-dimensional particle measures (e.g. area, perimeter), these were calculated for the particle's maximum projected area, as particles falling stably are often orientated with maximum area in the direction of fall (Christiansen and Barker, 1965; Dietrich, 1982). However, particles falling in the intermediate regime tend to change orientation as they fall (Willmarth et al., 1964; Wilson and Huang, 1979).

We used the parameterisation of Cheng (2008) to calculate density and viscosity of glycerine-water solutions from the volume fraction of glycerine and the temperature. The density and viscosity of glucose syrup were calculated from w_t of a metal sphere dropped in the fluid. Particle densities were calculated from mass and volume measurements and checked using relative weights in air

and water and Archimedes' principle of buoyancy.

To validate this procedure, Figure 2.2 shows theoretical and observed velocities for 2–10 mm diameter glass and metal spheres, for an *Re* range of 28–5600 using glycerine solutions of 30–70% by volume. Mean velocities deviate from the analytical solution (White, 1974) by a maximum of 8.2%. This is taken to represent the raw measurement error on the data. Standard errors are small (0.2–2.2%) and in many cases do not intersect with the analytical solution; we therefore assume that the main sources of error are the particle and fluid properties, e.g. ρ_P , rather than velocity measurement. We note that standard error for non-spherical particles in this study is higher (0.2–13.3%) as C_D depends on projected area in the direction of fall (Leith, 1987), such that non-spherical particles show a range of w_t dependent on orientation.

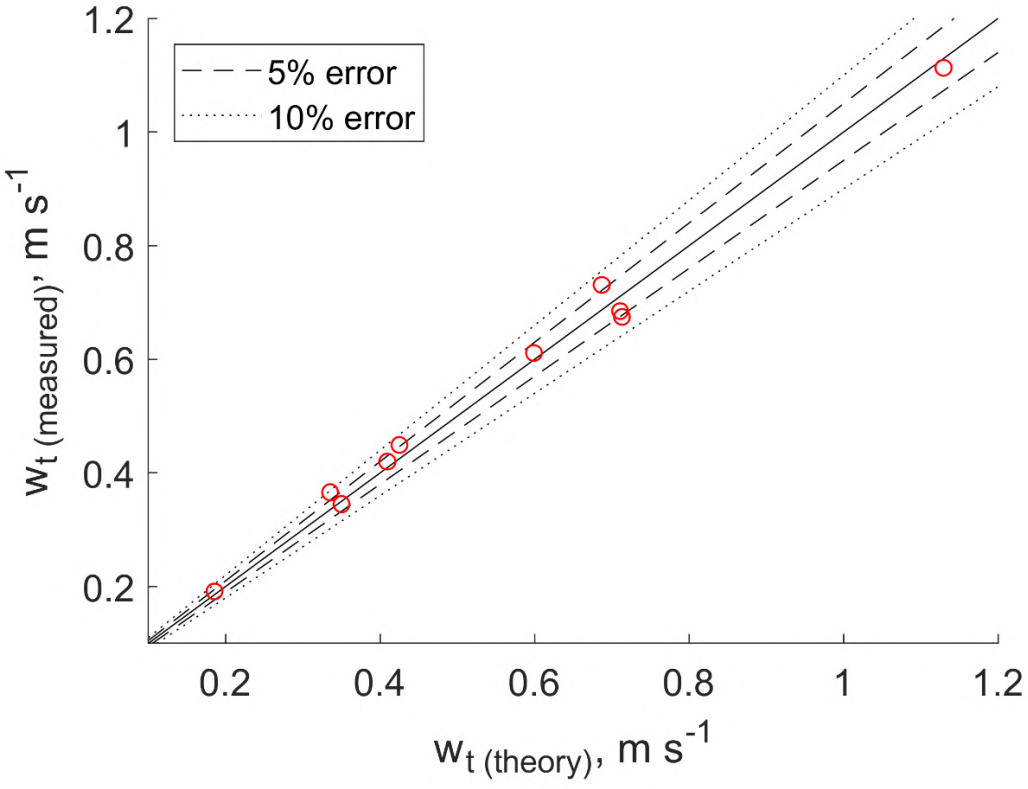

Figure 2.2: Measurements of w_t for spheres (this study), compared with the analytical solution of White (1974). The solid line indicates perfect agreement between $w_{t(theory)}$ and $w_{t(measured)}$. Symbols show the mean of 5 repeat measurements. Standard errors are smaller than markers.

Table 2.4: Mathematical description of drag calculations for the sedimentation schemes used in this study.

Sedimentation scheme	C_D definition	Shape descriptor	Experimental Re range
White (1974)	$C_D = C_1 + \frac{24}{Re} + \frac{C_2}{1+\sqrt{Re}}$ where $C_1 = 0.25$ and $C_2 = 6.0$ for $Re < 5 \times 10^3$.	None	-
Ganser (1993)	$C_D = \frac{24}{ReK_S}(1 + 0.1118[Re(K_S K_N)]^{0.6567}) + \frac{0.4305K_N}{1+\frac{3305}{ReK_S K_N}}$ where K_N is a correction factor for turbulent flow: $K_N = 10^{1.84148(-Log\psi)^{0.5743}}$ and K_S is a correction factor for laminar (Stokes) flow: $K_S = \frac{3}{1+2\psi^{-0.5}}$	Sphericity: $\psi = \frac{\pi^{\frac{1}{3}}(6V_P)^{\frac{2}{3}}}{A_P}$; Riley's sphericity (Riley et al., 2003): $\psi_R = \frac{4\pi A_{proj}}{P_P{}^2}$	$Re < 2.5 \times 10^4$
Wilson and Huang (1979)	$C_D = \frac{24}{Re}F^{-0.828} + 2\sqrt{1.07 - F}$	Form factor F: $F = (I+S)/2L$	$0.54 < Re < 79.1$
Bagheri and Bonadonna (2016b)	$C_D = \frac{24K_S}{Re}(1 + 0.125(ReK_N/K_S)^{\frac{2}{3}}) + \frac{0.46K_N}{1+5330/(ReK_N/K_S)}$ where: $K_S = (F_S^{\frac{1}{3}} + (F_S{}^{-\frac{1}{3}})/2$; $K_N = 10^{\alpha_2[-log(F_N)]\beta_2}$; $\alpha_2 = 0.45 + 10/exp(2.5log\rho' + 30)$; $\beta_2 = 1 - 37/exp(3log\rho' + 100)$; $F_S = fe^{1.3}(\frac{d_v^3}{LIS})$; $F_N = f^2e(\frac{d_v^3}{LIS})$	Flatness f: $f = S/I$; elongation e: $e = I/L$	$Re < 3 \times 10^5$
Dioguardi et al. (2017)	$C_D = \frac{4}{3}\frac{0.559C_{D,sphere}(Re^{4.18}\psi^{-Re^{-0.2}})^{0.5134}}{Re^2}$, where $C_{D,sphere}$ is calculated after Clift and Gauvin (1971): $C_{D,sphere} = \frac{24}{Re}(1 + 0.15Re^{0.687}) + \frac{0.42}{1+\frac{42500}{Re^{1.16}}}$	Sphericity: $\psi = \frac{\pi^{\frac{1}{3}}(6V_P)^{\frac{2}{3}}}{A_P}$	$0.03 < Re < 10^4$

2.3.1 Particle settling data

Results of settling experiments are shown in Figure 2.3 for the Stokes, intermediate and turbulent flow regimes. Velocity data are available in online supplementary information for the published version of this chapter. For a given Reynolds number *Re*, the drag coefficient C_D of a non-spherical particle is higher than for an analytical solution for spheres. The data show overlap with the C_D range in volcanic ash settling experiments by Dioguardi et al. (2017); this suggests that despite geometric differences between the particle shapes used and volcanic ash particles (e.g. the lack of small-scale surface irregularities on analogues) and differences in experimental setup, the drag coefficients obtained here are similar to those of volcanic ash particles. In the upper intermediate flow regime, however, flat and elongate analogue particles have higher C_D than volcanic ash particles of the same *Re* range (Dioguardi et al., 2017). Dynamic similarity between ash particles and analogues is lower in this regime due to the development of secondary tumbling or oscillating motions, which depend on shape (Christiansen and Barker, 1965; Wilson and Huang, 1979) and particle-fluid density ratio (Chow and Adams, 2011; Bagheri and Bonadonna, 2016b).

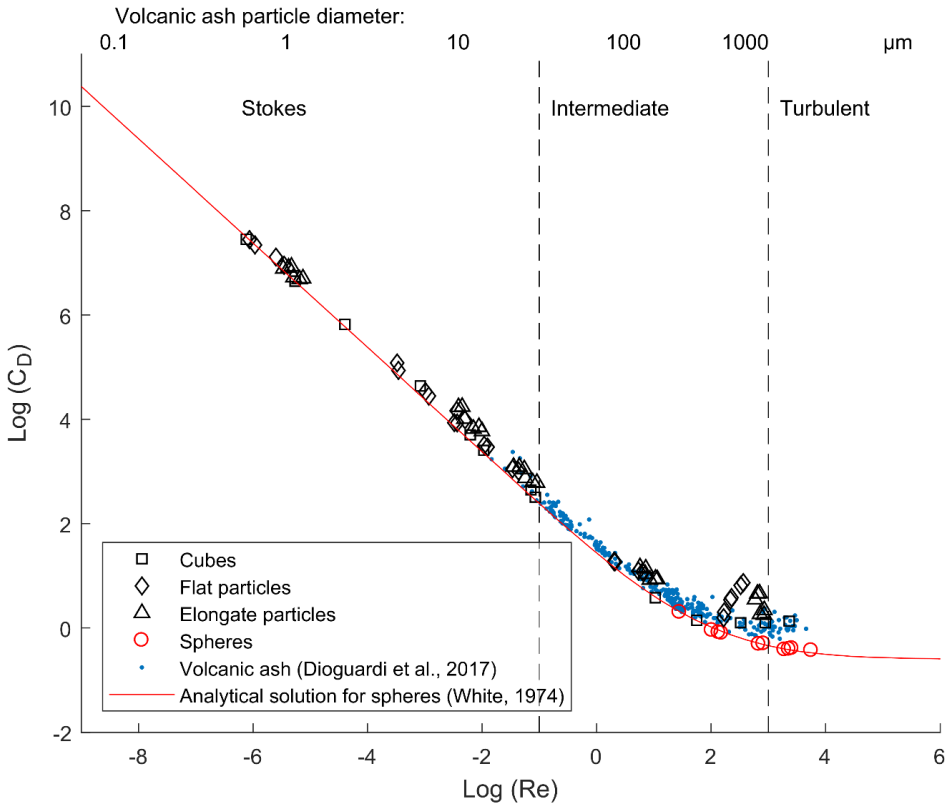

Figure 2.3: *Re* – drag relationship for spheres (red line = theory, open circles = analogue experiments) compared to non-spherical analogues (this study) and volcanic ash (Dioguardi et al., 2017). Flow regime boundaries are shown using dashed lines. The upper x axis shows volcanic ash diameters plotted at their approximate corresponding *Re*, calculated using the White (1974) scheme with particle density = 2300 kg m^{-3}, air density = 1.225 kg m^{-3} and air viscosity = 1.983 × 10^{-5} Pa·s.

High drag coefficients relative to spheres mean that our non-spherical analogues fell up to $\sim$ 75% slower (Figure 2.4) than an analytical solution for spheres (White, 1974). Deviation from sphere velocity is greater at higher *Re* and lower sphericity. There is no marked difference between flat and elongate particles of equivalent Re; however, equant particles are a better fit to a spherical solution than either elongate or flat particles. Some equant particles appear to fall faster than equivalent-volume spheres; this is likely to be a result of raw measurement error on the velocity data, which we estimate to be on the order of 8% of $w_{t(theory)}$ (Figure 2.2). The error is likely to be due to a combination of uncertainty on the measured particle positions in the settling column and uncertainty in $w_{t(theory)}$ due to errors in measuring particle and fluid properties.

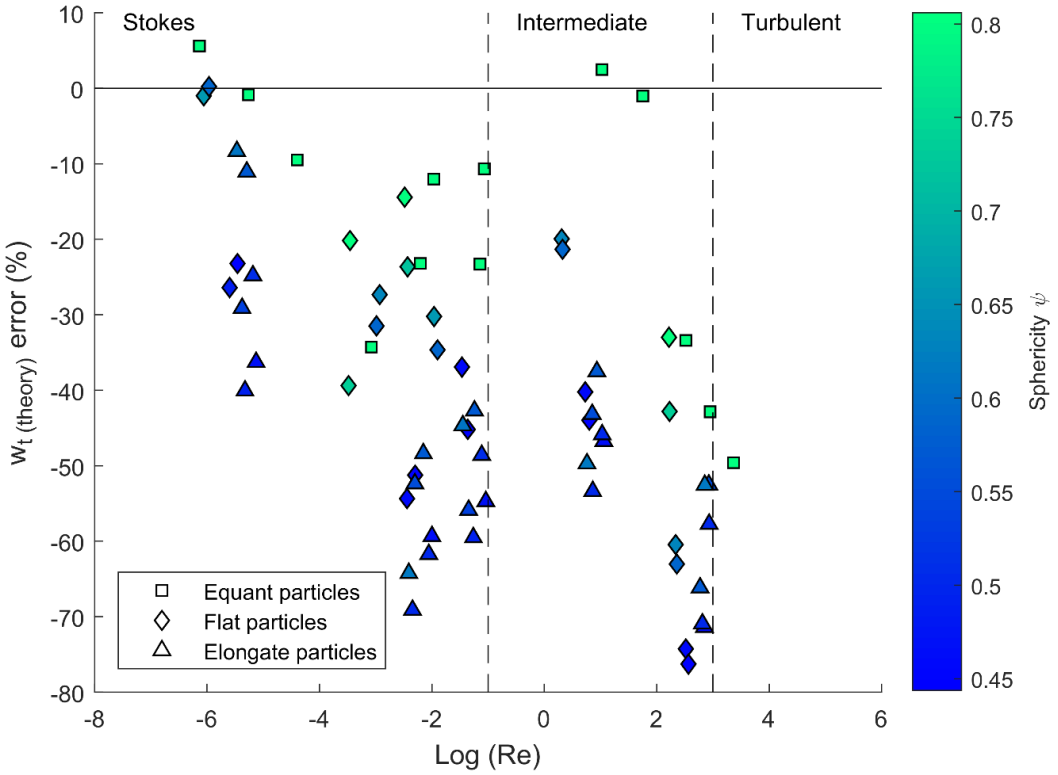

Figure 2.4: Error in predicted terminal fall velocity for the White (1974) analytical solution, as a function of *Re*. Symbols indicate particle shapes; colours indicate particle sphericity. Negative values of $w_{t(theory)}$ error indicate that the scheme has overestimated terminal velocity. $w_{t(theory)}$ error is calculated by: $\frac{w_{t(measured)} - w_{t(theory)}}{w_{t(theory)}} \times 100$.

Formulae in which C_D is derived as a function of one or more geometric shape descriptors (Wilson and Huang, 1979; Ganser, 1993; Bagheri and Bonadonna, 2016b; Dioguardi et al., 2017) in general provide a more accurate estimate of w_t (Figure 2.5), although the predictions are still, on average, slight overestimations. The exception is that elongated particles can fall $>$ 1.5 × faster than predicted by the w_t solution of Wilson and Huang (1979) within the *Re* range of their experiments, and $>$ 5.5 × faster in Stokes flow (Figure 2.5a).

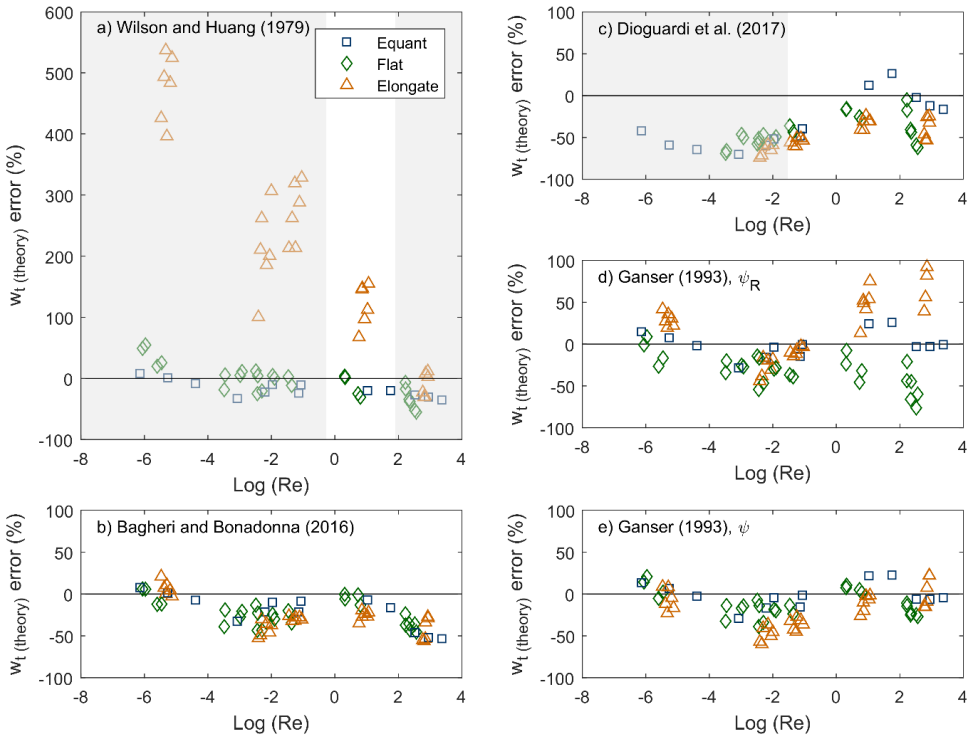

Figure 2.5: Error in predicted terminal fall velocity for the various sedimentation schemes investigated, as a function of *Re*. Mathematical descriptions of sedimentation schemes are given in Table 2.4. Negative values of $w_{t(theory)}$ error indicate that the scheme has over-predicted terminal velocity. $w_{t(theory)}$ error is calculated by: $\frac{w_{t(measured)} - w_{t(theory)}}{w_{t(theory)}} \times 100$. Greyed out areas indicate that measured *Re* is outside the range used to develop the correlation.

Using the Ganser (1993) sedimentation scheme with the shape descriptor ψ_R (2D sphericity; Riley et al. (2003)) in place of ψ (3D sphericity; Ganser (1993)) resulted in an increased range in error caused by an underestimation of terminal velocity for elongate particles and an overestimation for flat particles (Figure 2.5d). For our elongate analogue particles $\psi_R < \psi$; the converse is true for flat particles. For volcanic ash particles, the ratio of ψ to ψ_R is complicated by morphological factors other than elongation or flatness, such as small-scale surface roughness; it is therefore important to assess the impact of quantifying ash shape in 2D, and in Section 2.4 we report ψ and ψ_R for two samples of volcanic ash.

The Ganser (1993) sedimentation scheme (using ψ; Figure 2.5e) produced an overall mean absolute percentage error of 19%, which is comparable to the 16% error calculated from a larger compilation of data by Chhabra et al. (1999). We use the Ganser (1993) formula for the dispersion modelling in this study as it produces the lowest mean error of any scheme. However, we note that

the Bagheri and Bonadonna (2016b) formula produces similar results (mean absolute percentage error 26%, although less evenly distributed around zero) and is also valid for a wide *Re* range, due to the wide range of flow conditions and particle shapes used to produce the correlation and the semi-empirical construction of the formula.

2.4 Quantifying volcanic ash shape

We measured the shape of samples of SILK-LN and Vedde ash from Katla volcano, Iceland (Figure 2.1). Both samples are tephra fall deposits collected from soil sections in Iceland, and so cannot be classified as distal ash fall, which is the focus of this study; however, we sieved the samples to extract grains of 62.5–125 μm for shape analysis, to allow comparison between samples with different PSDs for a size fraction representative of distal ash (Stevenson et al., 2015), noting that ash shape in a single size class can vary with distance from source (Thorsteinsdóttir, 2015b).

2.4.1 2D shape analysis using scanning electron microscopy (SEM)

We measured ψ_R from 2D images taken at the University of Bristol using a Hitachi S-3500 N scanning electron microscope (SEM). We obtained backscattered electron (BSE) images using variable pressure (VP) mode at a pressure of 40 Pa. Grids of 49 images were acquired for each sample, giving 800–1600 grains. Grains were manually separated on the slides, and have a tendency to rest with the maximum projected area in view; however we cannot discount grain overlap and particle orientation as sources of error in this technique. Subsequent shape analysis was carried out using ImageJ. We used manual thresholding to create binary images, followed by the Analyse Particles plugin to output raw shape data such as particle perimeter (P_p) and projected area (A_{proj}). We excluded particles with $A_{proj} < 750$ pixels as lower pixel counts can reduce the accuracy of perimeter measurements and strongly alter the particle's apparent morphology (Liu et al., 2015). We then calculated ψ_R using $\psi_R = \frac{4\pi A_{proj}}{{P_p}^2}$ (Riley et al., 2003).

2.4.2 3D shape analysis using X-ray computed microtomography (CT)

We measured ψ using 3D volumes obtained by CT scans carried out using a Nikon XTH225ST scanner at the University of Bristol. We carried out scans at a voxel (volumetric pixel) edge length of 3.5 μm, a voltage of 100 kV and a current of 70 μA.

In CT analysis, samples are placed on a rotation table between an X-ray source and a detector. X-ray projections are taken as the sample is rotated from 0 to 360°; we used a rotation step of 0.11° giving 3141 projected images. The resulting images show density contrasts in the form of differing grey values in each voxel. To scan many particles efficiently, we encased the particles in epoxy resin, which ensured that particles were separated and did not move relative to each other during stage rotation. We filled 6 mm × 20 mm plastic cylinders with resin, waited 5–10 min for the resin to begin hardening, and then stirred in a weighed amount of ash sample, leaving the resin to completely set ($\sim$ 24 h) before scanning. The resin and plastic have lower X-ray attenuation coefficients than the ash, making it easy to segment the output 3D volume. In this way we were able to scan $>$ 100 particles for each sample in $\sim$ 2.5 h.

The raw data, in the form of 2D projections, were reconstructed to 3D volumes using CT Pro 3D reconstruction software. We carried out particle edge detection and surface reconstruction in Avizo 3D image analysis software based on voxel grey value contrasts. We calculated surface area A_p and volume V_p for each object using Avizo's Label Analysis module on the segmented volume. We then calculated ψ using $\psi = \frac{\pi^{\frac{1}{3}}(6V_P)^{\frac{2}{3}}}{A_P}$ (Ganser, 1993).

To validate this procedure, we conducted a sensitivity analysis to assess the impact of resolution on shape analysis. We used progressive downsampling of the dataset (e.g., Liu et al., 2015), to artificially decrease the resolution, followed by a repetition of the Label Analysis step. We found that mean sample ψ fluctuates significantly at $<$ 1200 voxels/particle. A voxel edge length of 3.5 µm gives a minimum of 2800 voxels/particle for the samples analysed, indicating that our imaging resolution is sufficient.

2.4.3 Volcanic ash shape data

The shape distributions of the SILK-LN and Vedde ash samples are shown in Figure 2.6. Both samples show a wide range of shapes within a single size class. Both ash samples are characterised by a low median ψ (0.53 for the SILK-LN ash and 0.52 for the Vedde ash), meaning that the particles are highly non-spherical. We used ψ = 0.5 for the dispersion modelling in the following section. Median ψ_R for both samples is within 0.1 of median ψ. ψ_R is lower than ψ for the SILK-LN ash at 0.44, and higher for the Vedde ash at 0.58. For both samples particle long axis L, from CT data, is on average twice the length of equivalent-volume sphere diameter d_v, with a median L/d_v of 2.1 for the SILK-LN ash and 2.0 for the Vedde ash.

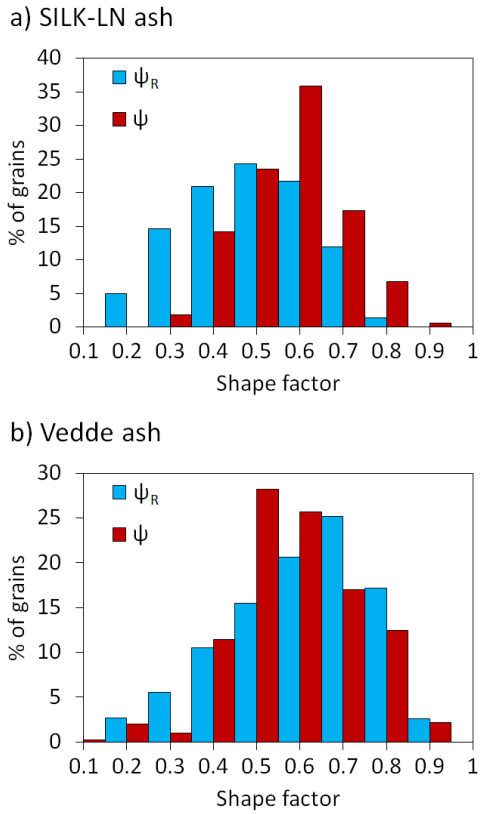

Figure 2.6: Grain shape distributions of ψ and ψ_R for two samples of ash of 62.5–125 µm (sieve mesh size) from Katla volcano, Iceland: a) the SILK-LN ash and b) the Vedde ash.

2.5 Sensitivity of dispersion model forecasts to particle shape

We used NAME to assess the sensitivity of ash dispersion forecasts to the shape factor assigned to the particles, using the median 3D sphericity of the SILK-LN and Vedde ash samples (ψ = 0.5). For all simulations we released ash from an eruptive source above the summit of Katla caldera, Iceland (63.6°N, 19.1°W) and used numerical weather prediction meteorological data from the Met Office's Unified Model (UM; Cullen (1993)) with a horizontal resolution of 25 km and a temporal resolution of 3 h. Model eruptions were initiated from 00:00 on 15th April 2010, when prevailing wind transported ash from Eyjafjallajökull volcano (24 km west of Katla) to northern Europe, causing major disruption to aviation (Budd et al., 2011). We modelled ash particles as spheres using the White (1974) analytical formula, and non-spheres using the Ganser (1993) empirical formula and ψ = 0.5. Note that for ψ = 0.5, particle size refers to equivalent-volume sphere diameter d_v. We assumed a plume height of 15 km, within the observed range for VEI 4 eruptions (Newhall and Self, 1982) and a particle density of 2300 kg m^{-3}. Additional model parameters are

detailed in the following sections.

2.5.1 Sensitivity of vertical velocity

The vertical velocity of particles in the atmosphere (w) is governed by sedimentation (w_{sed}) and atmospheric processes (w_a, w'); see equation 2.1. w_{sed} is sensitive to particle properties, including shape. Equation 2.1 therefore suggests that w will be sensitive to particle shape where $w_{sed} \gg w_a + w'$. We evaluated the relative contribution of atmospheric vertical velocities to determine the conditions under which vertical velocity is sensitive to shape.

To assess the likely range of vertical wind velocity across northern Europe, we extracted w_a from the UM data for a region extending from Iceland to the UK and Scandinavia for 59 vertical model levels at 3 h intervals throughout April 2010. For example, Figure 2.7 shows vertical air velocities at 6400 m asl. Vertical air velocities are mostly on the order of ± 0.001 to ± 0.1 m s^{-1}, with extremes around ± 1 m s^{-1} (where ± refers to up/down). UM vertical velocities are terrain following. However, to assess vertical velocities at altitude it is misleading to consider rate of change with respect to ground level, as the coordinate system will give a false impression of the terrain effect; we therefore present vertical velocities with respect to sea level.

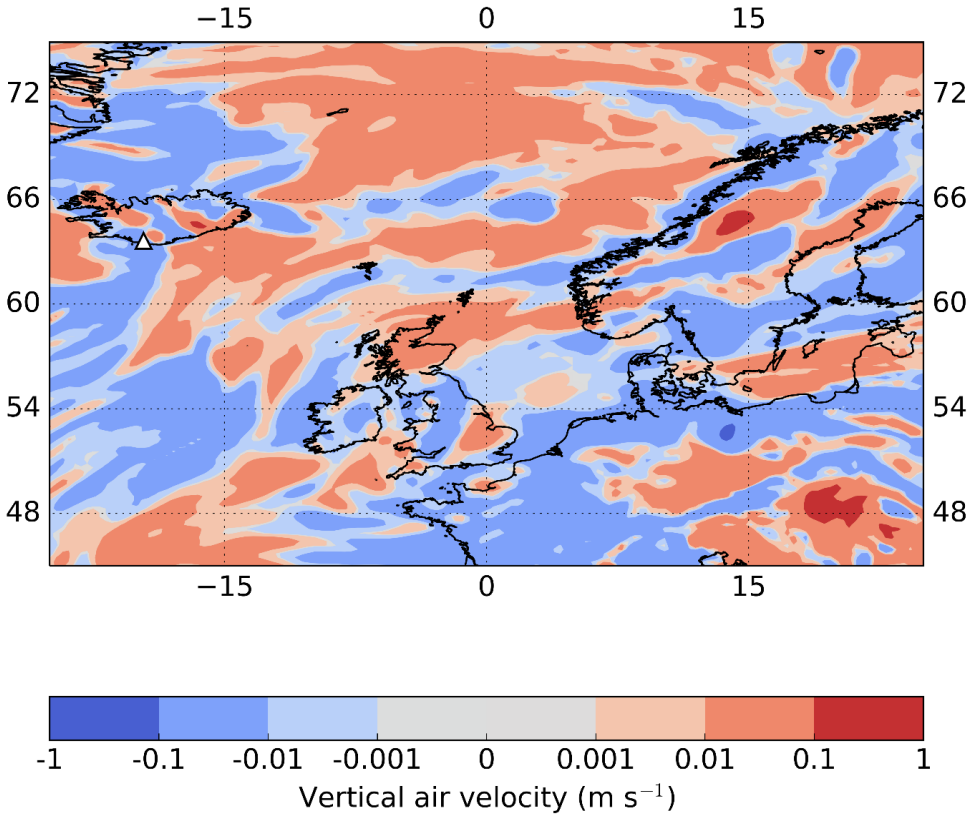

Figure 2.7: Vertical wind velocities at 06:00 on 2010/04/14 at Unified Model level 30 (altitude 6400 m, bounds = 6196.66, 6610.0). White triangle shows the position of Katla volcano in south Iceland.

Turbulence w' fluctuates at sub-grid spatial and temporal scales and is difficult to anticipate. Therefore, dispersion models often use probability distributions to parameterise unresolved turbulence. In NAME, the vertical component of turbulence is time-averaged and a function of the random component r:

$$w' = \sqrt{\frac{2\kappa}{\delta t}} r \tag{2.5}$$

where δt is the model timestep (s), κ is turbulent diffusivity, and r has a mean of 0 and a variance σ^2 of:

$$\sigma^2 = \frac{2\kappa}{\delta t} \tag{2.6}$$

Turbulent diffusity κ is calculated by $\sigma^2\tau$, where τ is the rate of dissipation of turbulent kinetic energy. Where sedimentation of heavy particles is modelled, κ is reduced according to settling

velocity to account for particles falling through turbulent eddies (Maryon et al., 1999) and can be calculated by:

$$\kappa = {\sigma_w *}^2 \, \tau_w * \tag{2.7}$$

where the subscript w denotes the vertical and

$$\tau_w * = \frac{\tau_w}{\sqrt{1 + \frac{w_t^2}{\sigma_w^2}}} \tag{2.8}$$

$$\sigma_w * = \frac{\sigma_w}{\sqrt{1 + \frac{T_p}{\tau_w *}}} \tag{2.9}$$

and T_p is the particle time constant (Maryon et al., 1999):

$$T_p = \frac{w_t}{g} \frac{\rho_P - \rho}{\rho_P} \tag{2.10}$$

In the free troposphere (above the boundary layer), vertical turbulence parameters are assumed to be constant at τ_w = 100 s and σ_w = 0.1 m s^{-1} (Jones et al., 2015).

As turbulence in NAME is timestep-dependent, we cannot directly compare w' and w_{sed}. We instead compared time for a particle to deposit due to sedimentation alone (T_{sed}) to time taken for the same particle to reach the ground through turbulent diffusion alone (T_{diff}), where:

$$T_{sed} = \frac{H}{w_t} \tag{2.11}$$

and H is plume height, and

$$T_{diff} = \frac{H^2}{\kappa} \tag{2.12}$$

We calculated the ratios w_{sed}/w_a and T_{diff}/T_{sed} for particles of 0.1–100 µm assuming ρ_P = 2300 kg m^{-3}, ρ = 1.225 kg m^{-3}, and μ = 1.98 × 10^{-5} Pa·s. We used NAME to simulate ash dispersal from an eruption of Katla volcano, Iceland, using a point source at 11490 m asl (10 km above summit and 5 km below our estimated plume height for the SILK-LN eruption).

Vertical velocity data

Ratios of particle sedimentation velocity to atmospheric velocity are shown in Figure 2.8. Sedimentation has a greater impact on velocity than vertical wind advection where $w_{sed} > w_a$, and this is the case for particles of $d_v > 3$ to 100 µm depending on w_a (Figure 2.8a). Sedimentation is more important than atmospheric turbulence where $T_{sed} < T_{diff}$. If we consider particle release heights between 5 and 25 km, $T_{sed} < T_{diff}$ for particles of minimum $d_v \sim 1$ µm (Figure 2.8b). We conclude that vertical velocity w is significantly modified by w_{sed}, a function of particle shape, for particles larger than $\sim$ 1–3 µm.

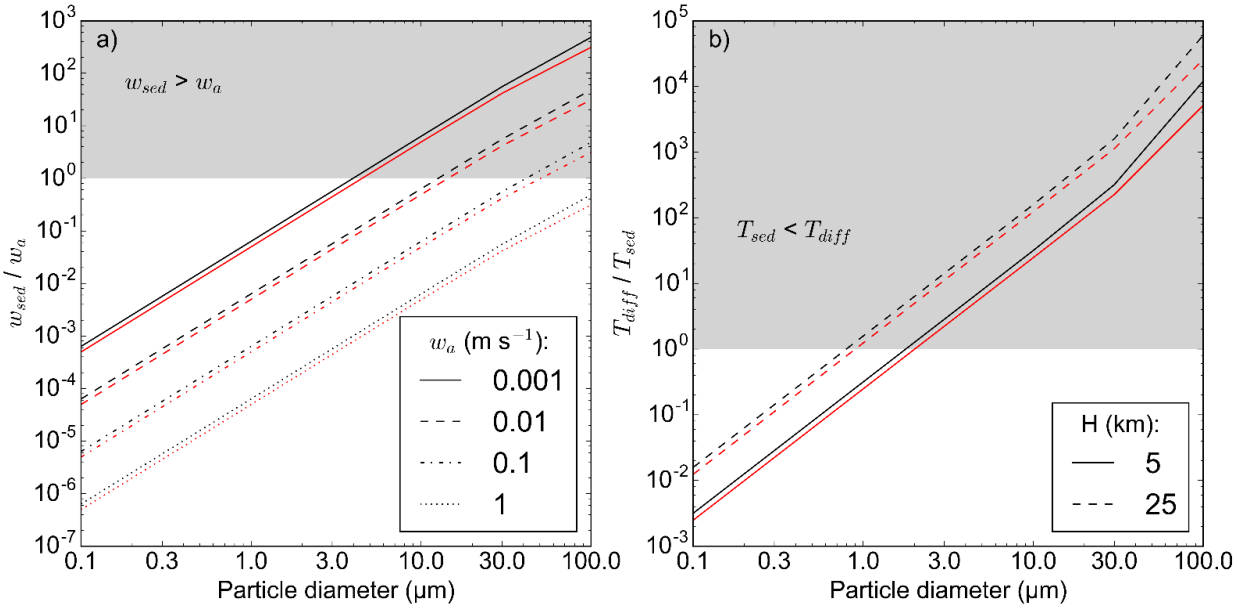

Figure 2.8: a) Velocity ratio w_{sed}/w_a, and b) time ratio T_{diff}/T_{sed}, as a function of particle diameter. Diameters here are equivalent-volume sphere diameters (d_v). Black lines indicate spheres and are calculated using the White (1974) sedimentation scheme; red lines indicate ψ = 0.5 and are calculated using the Ganser (1993) sedimentation scheme.

The results shown in Figure 2.8 neglect the impact of boundary layer turbulence (Jones, 2004; Stull, 2012) on particle transport, and consider advection data for a limited period; a longer analysis may have given a wider range of velocities. However, the results remain valid when using a full atmospheric model. For example, Figure 2.9 shows NAME modelled vertical trajectories of spherical and non-spherical particles of d_v = 1, 10 and 100 µm for the first 140 h after release. There is no discernible difference in the vertical trajectories of spherical and non-spherical particles of d_v = 1 µm. There is a significant vertical spread between individual trajectories, and particles move in both the positive and negative direction, suggesting transport is dominated by advection and

turbulent diffusion; sedimentation velocity is always positive. The vertical position of d_v = 10 µm particles is slightly sensitive to shape, but they still exhibit both upward and downward motion. For d_v = 100 µm particles there is a clear vertical separation between the trajectories of spherical and non-spherical particles and the time taken for particles to sediment is well predicted by T_{sed} alone, suggesting $w_{sed} > w_a + w'$. As w_{sed} is a function of shape, it is important to quantify shape for particles of d_v = 100 µm where we need an accurate assessment of particle travel time.

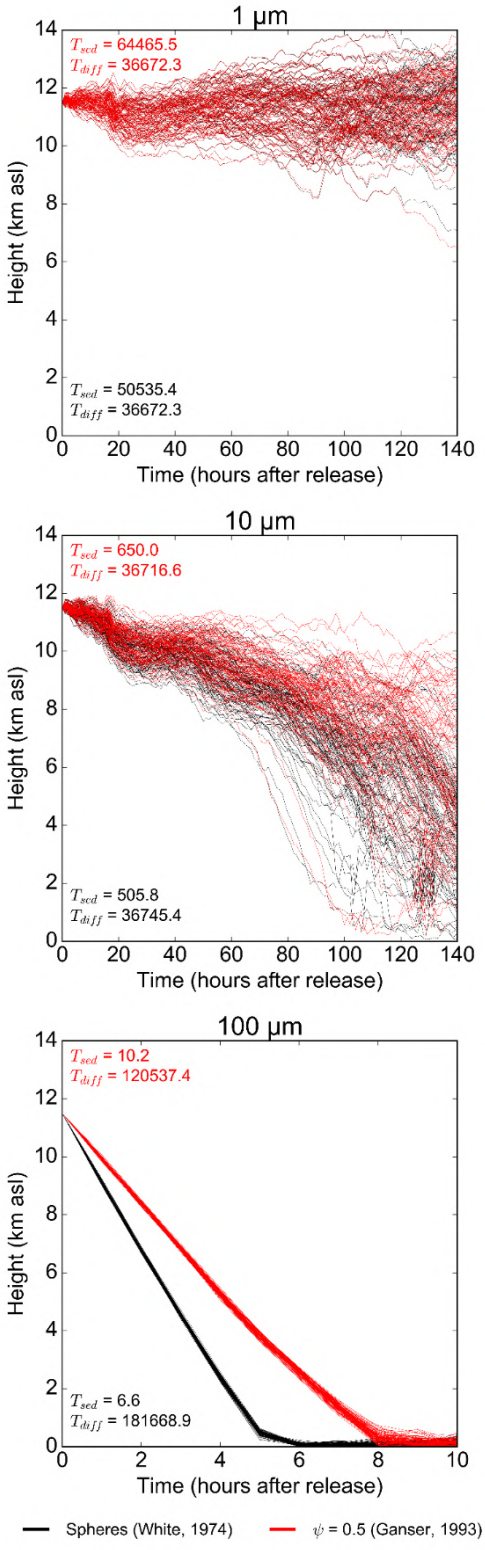

Figure 2.9: Calculated trajectories of spherical (black) and non-spherical (red) particles of 1, 10 and 100 µm. Diameters here are equivalent-volume sphere diameter (d_v). Diffusion time T_{diff} and sedimentation time T_{sed} are calculated using Equations 2.11 and 2.12.

2.5.2 Sensitivity of particle travel distance

To assess the maximum travel distance of individual particles, we carried out NAME runs with single particle sizes >100 μm, the maximum size used by the London VAAC. We used a 1D eruptive source based on a uniform distribution of particles from vent height to plume top.

Particle travel distance data

Maximum travel distance of particles >100 μm is sensitive to shape (2.10), with non-spherical particles travelling 44% further for a d_v = 100 μm particle and 87% further for a d_v = 500 μm particle. Although most VAACs assume that particles of $d_v > 100$ μm fall out close to source (Hort, 2016), in the meteorological conditions simulated here, a d_v = 200 μm and $\psi = 0.5$ particle can travel 528 km and a d_v = 300 μm particle of the same shape can travel 360 km from source. The travel distances for equivalent-volume spheres are 336 km and 216 km respectively.

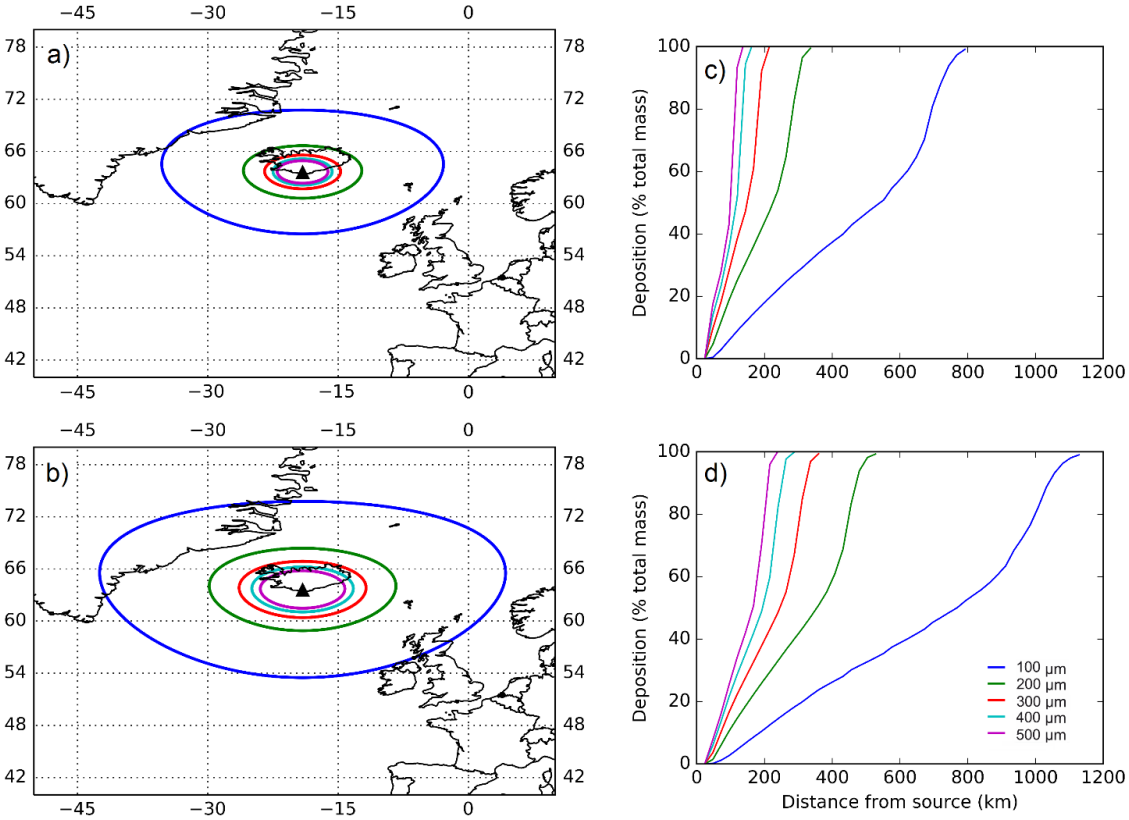

Figure 2.10: The maximum travel distances of particles from Katla volcano, Iceland (black triangle) represented as great circle distances from the volcano and percentage deposited as a function of distance. a) Maximum travel distance of spherical particles; b) maximum travel distance of non-spherical particles (ψ = 0.5); c) deposition versus distance for spherical particles; d) deposition versus distance for non-spherical particles (ψ = 0.5).

2.5.3 Sensitivity of atmospheric ash loading

We used NAME to model an eruption of Katla volcano using parameters estimated for the eruption of the SILK-LN tephra. To calculate mass flow rate and duration, we used the Mastin et al. (2009) correlation between plume height and erupted mass $H = 2V^{0.241}$, where H is plume height in km, V is volumetric flow rate in m^3 s^{-1} and volume is given as dense rock equivalent (DRE). An eruption duration of 7.8 h and a mass flow rate of 3.54×10^{13} g h^{-1} gives the total estimated tephra volume (0.12 km^3 DRE; Larsen et al. (2001)). We assumed that 95% of erupted mass is deposited close to source (Rose et al., 2000, 2001; Webster et al., 2012; Dacre et al., 2013), and multiplied the mass flow rate by a distal fine ash fraction of 5% to give an effective source of 1.77×10^{12} g h^{-1}. We distributed this mass over 15,000 model particles released per hour, the particle release rate used by the London VAAC (Witham et al., 2017).

As particles larger than the London VAAC's default maximum size of d_v = 100 μm can travel sufficiently far to be relevant for distal ash dispersal where shape is non-spherical (Figure 2.10), we used both the London VAAC default PSD (Maryon et al., 1999) and an additional coarser PSD, which we term the Katla SILK PSD (Figure 2.11). The Katla SILK PSD was derived from an average of 19 sieved and weighed samples of Katla SILK-LN tephra (data from Thorsteinsdóttir (2015b), which we normalised to a size range of 0.09–250 μm. The London VAAC default PSD uses grain sizes based on light scattering (Hobbs et al., 1991), and the Katla SILK PSD uses sieve mesh sizes (Thorsteinsdóttir, 2015b), whereas the sedimentation equations in NAME use d_v; we therefore make the simplifying assumption that scattering size ≈ sieve size ≈ d_v for the purpose of this sensitivity analysis.

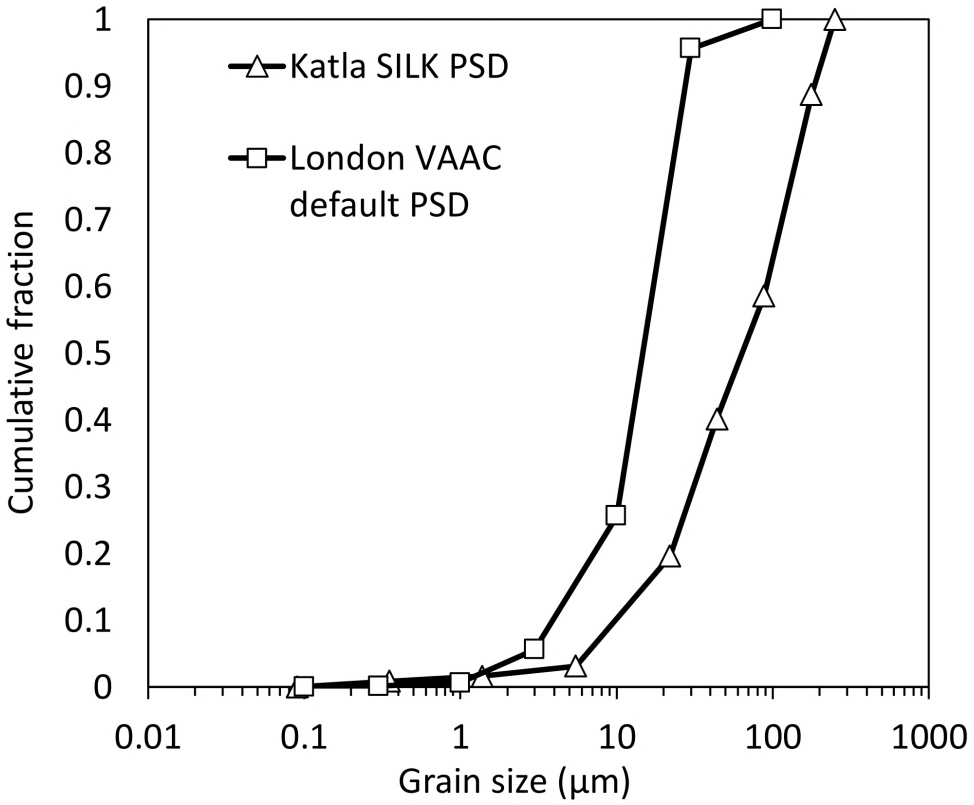

Figure 2.11: Particle size distributions used to assess the sensitivity of ash loading forecasts to shape: the London VAAC default PSD (Maryon et al., 1999) and the Katla SILK PSD (modified from Thorsteinsdóttir (2015b)).

To produce ash loading forecasts, we output volcanic ash air concentrations (g m^{-3}) at 22 vertical flight levels of 25 FL (2500 ft) depth and vertically integrated total column mass (g m^{-2}) over six 6 h averaged time periods. We then extracted the spatial extent of concentrations exceeding an 'unsafe to fly' threshold of $> 2 \times 10^{-3}$ g m^{-3} based on aircraft encounters with volcanic ash

(Clarkson et al., 2016). For total column mass we took an equivalent concentration of > 2 g m^{-2} to be 'unsafe' assuming the plume is 1 km thick, a reasonable value for moderate Icelandic eruptions (e.g., Dacre et al., 2013). We then assessed the percentage overlap of 'unsafe' concentrations for spherical and non-spherical cases. We limited our analysis to model levels and timesteps where at least 100 grid cells contain 'unsafe' concentrations. As a statistical measure, percentage overlap of a concentration contour has the advantage of reflecting differences in both the spatial position of the plume and the magnitude of the ash concentration values.

Ash loading forecast data

The percentage overlap between model ash concentrations of spherical and non-spherical (ψ = 0.5) particles decreases with time after the eruption start (Figure 2.12a). Modelled concentrations are more sensitive to sphericity when we use the coarser Katla SILK PSD: using the London VAAC default PSD, the mean percentage overlap for total column mass loading in the first 36 h after eruption is 95%, whereas for the Katla SILK PSD it is 87%. The lowest total column mass overlaps are 89% and 64%, respectively, representing good agreement between the spherical and non-spherical models even when using a coarser PSD (Figure 2.12c–d). Air concentrations are more sensitive to shape than total column mass loading (Figure 2.12b), suggesting that the vertical structure of the distal ash cloud is more sensitive to particle shape than the horizontal extent. Figure 2.12b shows the model timestep and vertical level which are most sensitive to shape (49% overlap); the mean for air concentration forecasts is much higher at 87%, meaning that the spherical and non-spherical models agree reasonably well for most vertical levels and timesteps.

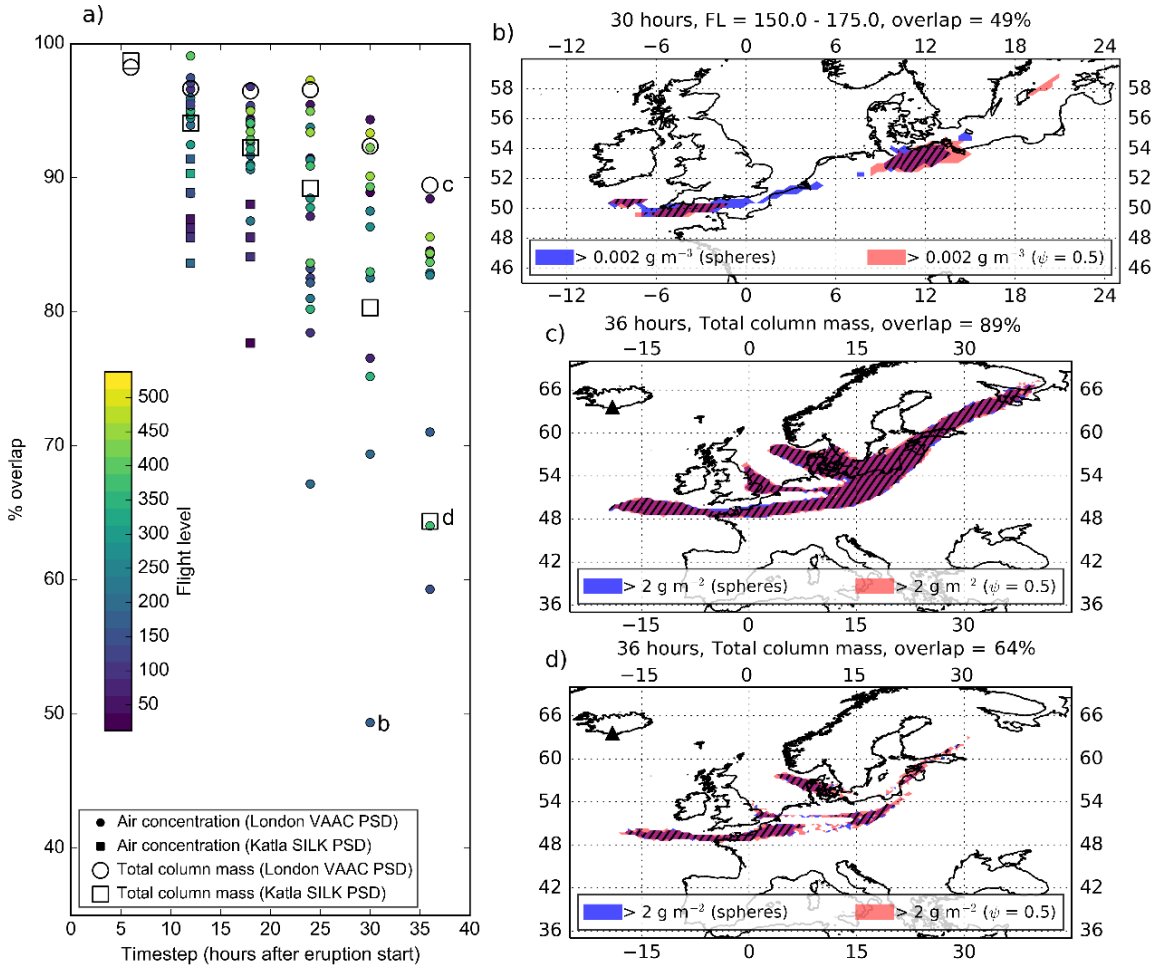

Figure 2.12: a) The impact of particle shape on atmospheric ash loading, given as percentage overlap of the modelled ash cloud with spherical and non-spherical (ψ = 0.5) particles. Results are given for individual air concentrations corresponding to flight levels of 25 FL depth, and for total column mass (vertically integrated). Results plotted in panels b), c) and d) correspond to the symbols labelled with letters in panel a). b) The vertical position of ash particles can be sensitive to sphericity. c) Total column mass loading is relatively insensitive to sphericity. d) Using a coarser PSD (up to 250 µm) still results in low sensitivity of total column mass to sphericity in the first 36 h after eruption. Hatched areas indicate overlap. Percent overlap is calculated by: $\frac{A_{overlap}}{(A_{spherical}+A_{non-spherical})-A_{overlap})} \times 100\%$ where $A_{overlap}$ is the area where the concentration contours overlap and $A_{spherical}$ and $A_{non-spherical}$ are the areas of the spherical particle and non-spherical particle ash cloud concentration contours, respectively. Black triangle indicates the source volcano (Katla, Iceland).

2.6 Discussion

Irregular shapes have higher drag coefficients (C_D) and lower terminal velocities (w_t) than equivalent-volume spheres. Our non-spherical analogue particles fall up to $\sim 75\%$ slower than an analytical solution for w_t of spheres (White, 1974). Empirical sedimentation schemes for non-spherical particles generally produce lower errors; the schemes of Ganser (1993) and Bagheri and Bonadonna (2016b) are particularly effective. The Ganser (1993) scheme is calibrated using 3D sphericity ψ but often used with 2D sphericity ψ_R; we find that $\psi > \psi_R$ for elongated grains and $\psi < \psi_R$ for platy grains. Both the Katla tephras (SILK-LN and Vedde) have a median $\psi \approx 0.5$; using this value as a shape parameter in the NAME atmospheric dispersion model causes particles to travel further than equivalent-volume spheres. However, the sensitivity of atmospheric dispersion predictions to shape is dependent on the particle size modelled, as the transport of particles with $d_v < 1$–3 μm is primarily governed by atmospheric vertical velocities (wind advection w_a and turbulence w') rather than sedimentation velocity w_{sed}, which is a function of shape. Particles of up to $d_v \approx 100$ μm are still affected by w_a and w', although to a lesser extent. Therefore, there is relatively good agreement between distal ash concentration forecasts using spherical and non-spherical particle models when a significant proportion of particles are $<$ 100 μm. However, it is necessary to use a shape parameter when modelling larger particles, for example proximal and medial tephra dispersion or tephra fallout applications.

In the following sections we discuss some of the implications and caveats of these conclusions. First we assess the use of scaled analogue particles as an experimental tool and discuss reasons for the relative success of the empirical sedimentation schemes and shape factors used to predict w_t. We then discuss ash shape data for the SILK-LN and Vedde samples with implications for how we measure volcanic ash shape, and how our particle size measurements also depend on shape. We conclude by discussing implications of the sensitivity of dispersion models to shape from points of view of both operational concentration forecasting and cryptotephra dispersal.

2.6.1 Shape and sedimentation schemes

The use of scaled analogue particles allows us to systematically vary *Re* and easily measure shape; however, the analogues we use are simplified versions of volcanic ash particles. Volcanic ash particles can contain many small bubbles and have rough surfaces. In the Stokes regime, C_D is insensitive to surface roughness (Loth, 2008). However, in the turbulent regime, increasing roughness results in higher C_D (Achenbach, 1974), although this effect is small compared to particle shape (Bagheri and Bonadonna, 2016b). If bubble size is large relative to particle size,

or the bubble content is high, volcanic particles may be better approximated by hollow rather than solid shapes. Hollow objects permit the flow of fluid inside the object as well as around it; Chhabra et al. (1999) found that the Ganser (1993) sedimentation scheme could not accurately predict the velocities of particles in experiments with hollow cylinders and agglomerates (e.g., Lasso and Weidman, 1986). Another effect of bubbles and phenocrysts in volcanic particles is to move the particle's centre of mass from its geometric centre. In a non-equant particle, removing the centre of mass from the geometric centre can have a major effect on particle orientation (Tennant, 2017), and therefore projected area in the direction of fall, which is an important indicator of C_D (Leith, 1987), especially for very non-spherical particles (Bagheri and Bonadonna, 2016b).

Empirical formulae for irregular particles generally produce more accurate estimates of w_t than analytical formulae for spheres. However, the shape formulae of Wilson and Huang (1979) and Dioguardi et al. (2017) should only be used within $0.54 < Re < 79.1$ and $0.03 < Re < 10^4$ respectively, due to the uncertainty inherent in extrapolating empirical formulae beyond the *Re* range of the experiments used to produce the correlation. This highlights a limitation of experiments using ash particles, which cannot replicate the flow conditions of the smallest (lowest *Re*) particles falling in air.

While Wilson and Huang (1979) and Dioguardi et al. (2017) use volcanic ash particles, Ganser (1993) and Bagheri and Bonadonna (2016b) use analogue particles. The schemes using analogue particles are calibrated over a much wider *Re* range but may not replicate the shape or particle-fluid density ratio of ash falling in air. The empirical scheme of Bagheri and Bonadonna (2016b) addresses this problem by combining analogue particle data with volcanic ash data and calibrating the results using a wide range of particle-fluid density ratios. Considering this context, the poorer performance of the Wilson and Huang (1979) and Dioguardi et al. (2017) drag laws, even within their experimental *Re* ranges, relative to Bagheri and Bonadonna (2016b) and Ganser (1993), can likely be explained by the differences in shape between the volcanic ash particles used to calibrate the laws and the smooth analogue particles of our database. The Dioguardi et al. (2017) experiments use ash particles with sphericity ψ of 0.07–0.732, whereas our analogues have ψ of 0.45–0.8. While the Dioguardi et al. (2017) scheme does not iterate to convergence for all particles outside their experimental *Re* range, the Wilson and Huang (1979) scheme iterates to convergence for all particles in this study but underestimates terminal velocity for elongate particles. We suggest that this is due to the shape descriptor used in the Wilson and Huang (1979) formula, given by $F = (I+S)/2L$, where L, I, and S are the long, intermediate and short particle axes respectively. The construction of the equation means F is very sensitive to the particle long axis L. For volcanic ash particles in Wilson and Huang (1979), F ranges from 0.13 to 0.86 with a mean of 0.41; for elongate analogues in this study, F ranges from 0.06–0.13. This highlights a difficulty

in extrapolating empirical sedimentation schemes beyond the shape range used to produce the correlation, as well as beyond the *Re* range.

We used the Ganser (1993) sedimentation scheme for dispersion modelling due to the low mean terminal velocity error of 19%. However, the Bagheri and Bonadonna (2016b) formula produces similar results (mean absolute percentage error 26%, a comparable result given our estimated $\sim$ 8% error on measured terminal velocities) and is valid for a wide *Re* range; moreover, it uses two fitting parameters (flatness f and elongation e; see Table 2.4) which are ratios of principal axis lengths and therefore less resolution-dependent than surface area-based measures such as ψ (Bagheri et al., 2015). Calculation of C_D using the Bagheri and Bonadonna (2016b) formula requires particle-fluid density ratio, but knowledge of these properties is also required for the w_t calculation. We recommend that the Bagheri and Bonadonna (2016b) scheme also be trialled as a volcanic ash dispersion modelling tool where it is more practical to obtain f and e rather than ψ.

2.6.2 Quantifying volcanic ash shape

The tephra layers sampled in this study were selected to examine the impact of characteristic non-equant particles (Larsen et al., 2001; Mangerud et al., 1984) on shape measurement and dispersion modelling. The SILK-LN and Vedde ash both have a median ψ of $\sim$ 0.5. In comparison, Alfano et al. (2011) analysed ash grains from eruptions of several volcanoes (Masaya, Nicaragua; Kilauea, USA; and Soufriere Hills, Montserrat) and found that ψ ranged from 0.7–0.9, while ψ of ash particles from Campi Flegrei, Italy, ranges from 0.2–0.5 (Mele and Dioguardi, 2018). Thus, although the Katla SILK-LN and Vedde ash have similar median ψ, ash from other volcanoes can be of very variable morphology. Additionally, both Katla samples have a large ψ range, indicating that a single value of sphericity is not valid for each size class (see also Alfano et al. (2011) and Mele and Dioguardi (2018)). Average sphericity is also sensitive to the measurement technique (Alfano et al. (2011); this study).

The low sphericity of the measured ash particles has implications for how we measure particle size. Most sedimentation schemes assume size = d_v. However, the cryptotephra community usually reports size as maximum grain lengths, while volcanologists report particle size distributions in terms of sieve mesh sizes. For a sphere, the three measures are equivalent. For simplicity, we assume that for a non-spherical particle, maximum grain length = long axis L and sieve mesh size = intermediate axis I, that is, all particles with $I <$ mesh size fall through the mesh. Figure 2.13 illustrates the discrepancy between L, I and d_v for non-spheres. We show theoretical L and I for particles of d_v = 1–500 μm assuming particles are cylinders with ψ = 0.5; there are two cylinders with ψ = 0.5 for each d_v, one corresponding to an elongate cylinder (rod) and one corresponding

to a flat cylinder (disk). The rod of d_v = 100 µm and ψ = 0.5 has L = 568 µm and I = 34.5 µm. The disk of d_v = 100 µm and ψ = 0.5 has L = 180 µm and I = 180 µm. Given the discrepancy between L and d_v, particle irregularity and the difference in size measurement conventions are likely to partially explain the inability of dispersion models to account for the travel distances of some large volcanic ash shards in cryptotephra deposits (Beckett et al., 2015; Stevenson et al., 2015; Watson et al., 2016), particularly given that volcanic ash travel distances are highly sensitive to particle size (Beckett et al., 2015). The maximum travel distance of a d_v = 100 µm and ψ = 0.4 particle, modelled using NAME, from the eruption of Eyjafjallajökull volcano in 2010 was 1375 km. Stevenson et al. (2012) describe a 100 µm particle from the same eruption in Lincolnshire, UK, 1646 km from source. However, (Stevenson et al., 2012) measure diameter as L while the NAME sedimentation equations use d_v. Figure 2.13 shows that for a cylindrical particle of ψ = 0.5 and L = 100 µm, d_v could be 18 or 55 µm. A NAME model ash particle with d_v = 30 µm, which lies between the two, can travel 4586 km from source (Beckett et al., 2015), further than the 1646 km travelled by the Lincolnshire particle. Although uncertainty in atmospheric, source, and other physical particle parameters could contribute to the discrepancy between observed and modelled particle travel distances, this suggests that the distance may be resolved solely by using a consistent size parameter from measurement to modelling.

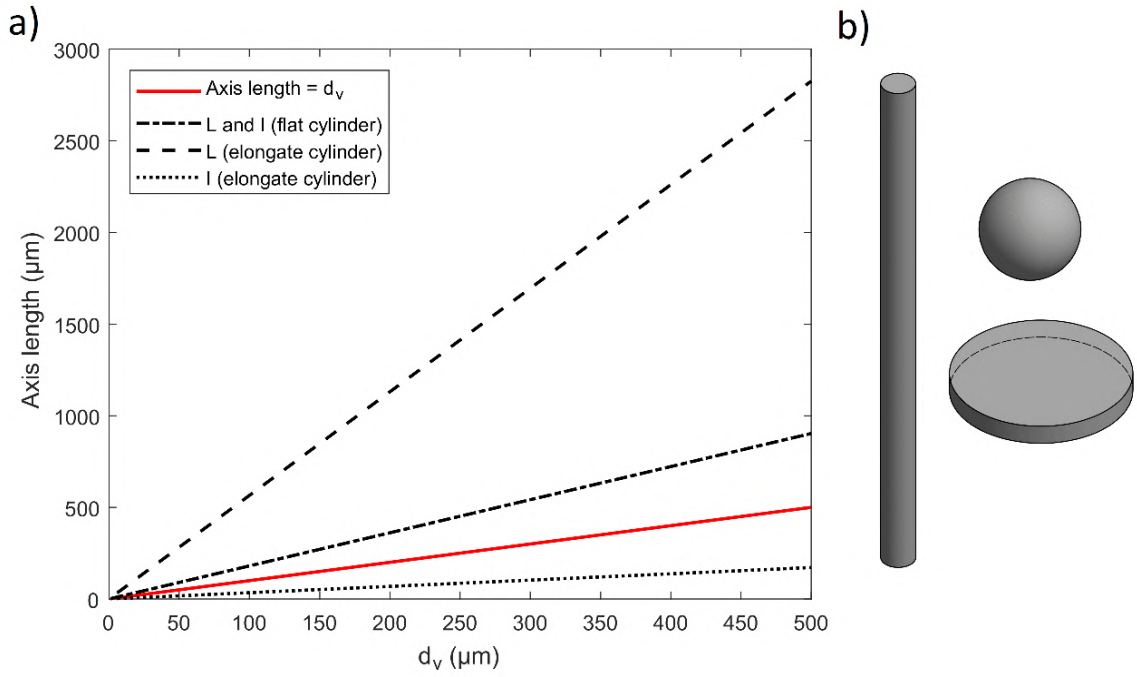

Figure 2.13: a) Theoretical relationship of equivalent-volume sphere diameter d_v to long axis L and intermediate axis I for a cylinder of sphericity ψ = 0.5. For each d_v there are two cylinders with ψ = 0.5; one a flat disk and one an elongate rod. b) Illustration showing a sphere and two cylinders of equivalent volume and ψ = 0.5.

2.6.3 Operational volcanic ash forecasting

Shape begins to influence particle trajectories at diameters between 1 and 100 μm, and becomes an important influence at $d_v > 100$ μm, the maximum diameter modelled by most VAACs (Hort, 2016). As non-spherical particles remain in the atmosphere longer than spheres, it is important to consider non-sphericity when assessing a suitable PSD for dispersion modelling. We show that a d_v = 200 μm non-spherical particle can travel > 500 km from source, meaning that these particles have the potential to be present in a large region of airspace even after a moderate eruption (Figure 2.10).

Despite the sensitivity of the travel distance of large particles to shape, we find that ash concentration forecasts for a model eruption of Katla volcano using NAME are relatively insensitive to shape even when we increase maximum d_v to 250 μm (Figure 2.12). The vertical structure of the plume, however, as indicated by outputs on relatively thin vertical layers (25 FL depth), is more sensitive to shape. The lower sensitivity of total column mass loading to shape (Figure 2.12c-d) is dependent on the input met data. If there is little vertical variation in wind speeds, different particle fall velocities will have less of an effect on horizontal dispersion than if winds at different altitudes are very different. Sensitivity to shape is also higher for larger particles, which is of concern for modelling proximal particle concentrations and tephra deposition. However, for operational scenarios, shape data are unlikely to be available in real-time. Currently, there are limited data on ash shape and how it varies with particle size, magma composition, eruption style or intensity, which makes it challenging to set defaults for a given volcano or eruption style. Therefore, in most cases the best option could be to assume a shape value which lies within the observed range for volcanic ash (as the Buenos Aires VAAC does), or to quantify uncertainty by using a non-spherical particle case as part of an ensemble forecast. The London VAAC uses a model setup with layers of 25 FL depth, enabling it to represent observations of very thin ash layers in the atmosphere (e.g., Schumann et al., 2011; Devenish et al., 2012). However, the vertical resolution of the met data, the uniform mass distribution at source between the vent and plume height, and the random components of turbulence and mesoscale motions mean that model plumes in NAME are usually thicker (Devenish et al., 2012). To account for unresolved high ash concentrations in thin plumes, concentrations in thin layers are multiplied by a 'peak-to-mean factor' of 10 and combined into thick layers (FL000 to FL200, FL200 to FL350, and FL350 to FL550) where the maximum thin layer value is taken as the value of the thick layer (Witham et al., 2017). In this way, the London VAAC setup accounts for differences in the height and thickness of the plume relative to the model output, and is likely to at least partially mask the impact of particle shape on vertical plume structure. Therefore in practice, the difference in operational products with and without a shape parameter may be smaller than those of the 25 FL depth outputs shown

here.

In the vertical, particle velocity in NAME is a function of the physical particle properties and meteorology. For the particle diameters considered by the London VAAC (0.1–100 μm), we expect the particle trajectories to follow the turbulent eddies, but inertial effects are not insignificant for larger particles. In NAME, the Lagrangian timescales and turbulent velocity variances are reduced according to settling velocity (Jones et al., 2015), to account for trajectory-crossing and inertial effects. By the particle drag coefficient we account for the impact of the flow on the particle, but not for the impact of the particle on the flow, a concept which is still poorly understood (Voth and Soldati, 2017). In addition, particles are assumed to disperse passively in the horizontal according to meteorological conditions. The extent to which particle shape might modify horizontal particle trajectories is unknown; non-spherical particles can fall according to trajectories which may be vertical but include particle rotation (Wilson and Huang, 1979) or have a horizontal component (Tennant, 2017).

Satellite retrieval constraints on volcanic ash transport can be used to validate and update dispersion model forecasts (Wilkins et al., 2016), retrieve physical particle properties (Francis et al., 2012) and determine ash emission rates to provide an updated source term (Stohl et al., 2011). The horizontal distribution of ash in a plume (i.e. total column mass) is relatively insensitive to shape (Figure 2.12), meaning particle shape is unlikely to be a significant source of discrepancy between plume positions in satellite retrievals and dispersion modelling. However, satellite retrievals could underestimate ash concentrations where ash is extremely non-spherical because many scattering formulae assume spherical particles (e.g., Kylling et al., 2014), and satellite retrievals can detect only a limited range of particle sizes (Stevenson et al., 2015).

2.6.4 Beyond the days after eruption

Volcanic ash dispersion modelling for operational purposes is concerned with high atmospheric concentrations of ash hours to days after eruption (Folch, 2012), and satellite retrievals have difficulty detecting low concentrations and thin layers after the first few days of an eruption (Gangale et al., 2010). Our ash concentration sensitivity analysis is limited to a short timeframe of 36 h from eruption start. However, low concentrations of fine grained ash can remain in the stratosphere, influencing the atmospheric radiative budget, for months or years (Lacis et al., 1992; Gooding et al., 1983; MacKinnon et al., 1984). Critically, small reductions in gravitational settling velocity due to particle non-sphericity add up to greater differences in particle height (Figure 2.9) and concentration (Figure 2.12) over longer timeframes. Therefore, we cannot rule out shape as an influence on stratospheric ash loading over longer timescales (months to years), although shape is

likely to be secondary to atmospheric controls on vertical velocity due to the small particle sizes (for example, a modal size of 2–5 μm and a maximum of 40 μm six months after the 1982 eruption of El Chichón; Gooding et al. (1983)).

Understanding the long-term transport of ash has the potential to improve our understanding of cryptotephra deposits. Widely dispersed tephra from large eruptions can provide a linked age framework, up to continental scales, for host sediment sequences (e.g., Davies, 2015). Cryptotephra layers are usually correlated and linked to their source volcano by major and/or trace element analysis of glass shards (e.g., Tomlinson et al., 2015). Volcanic ash dispersion modelling could help to constrain potential source regions by providing estimates of maximum potential travel distances of the largest cryptotephra shards found in a site. We show that by using the same particle size parameter for ground-based sampling and dispersion modelling, we can better account for the particle sizes and travel distances reported in the two disciplines. We also show that to forecast the transport distances of very large distal ash shards requires a shape parameterisation: the maximum dispersal distance of ash shards with $d_v > 100$ μm is highly sensitive to shape (Figure 2.10). We note that using ψ_R as a shape descriptor can significantly alter predicted analogue particle velocities compared to using ψ (Figure 2.5). Therefore, by using consistent size and shape parameters to calibrate sedimentation schemes and measure volcanic ash shards, we can reduce the error in dispersion model predictions of particle travel distance.

Chapter 3

The importance of grain size and shape in controlling the dispersion of the Vedde cryptotephra

This work is in press for the Journal of Quaternary Science as Saxby, J., Cashman, K., Rust, A., and Beckett, F., 'The importance of grain size and shape in controlling the dispersion of the Vedde cryptotephra' (submitted March 2019; revised and resubmitted September 2019; accepted October 2019). The Norwegian Vedde ash samples were provided by Jan Mangerud, Stefan Wastegård and Simon Larsson, with whom we also had many useful discussions about cryptotephra transport. The Icelandic Vedde ash sample was provided by Sigurður Reynir Gíslason. Jennifer Saxby obtained and analysed published data on the Vedde ash and meteorological data. Shape and size measurement was performed by Jennifer Saxby with help and guidance from Thomas Davies (X-ray CT) and Katharine Cashman (optical microscopy). Modelling in Matlab was performed by Jennifer Saxby. Modelling in NAME was performed by Jennifer Saxby with guidance from Frances Beckett. Claire Witham provided feedback on an earlier draft.

Abstract

Volcanic ash is dispersed in the atmosphere according to meteorology and particle properties, including size and shape. However, the multiple definitions of size and shape for non-spherical particles affect our ability to use physical particle properties to understand tephra transport. Moreover, although particles $>$ 100 μm are often excluded from operational ash dispersion model setups, ash in tephra deposits $>$ 1000 km from source can exceed 100 μm. Here we measure the shape and size of samples of Vedde ash from Iceland, an exceptionally widespread tephra layer in Europe, collected in Iceland and Norway. Using X-ray computed tomography (CT) and optical microscopy, we show that distal ash is more anisotropic than proximal samples, suggesting that shape exerts an important control on tephra dispersion. Shape also impacts particle size measurements. Particle long axis, a parameter often reported by tephrochronologists, is on average 2.4 $\times$ greater than geometric size, used by dispersion modellers. By using geometric size and quantifying shape, we can explain the transport of Vedde ash particles $\leq$ 190 μm more than 1200 km from source. We define a set of best practices for measuring the size and shape of cryptotephra shards and discuss the benefits and limitations of using physical particle properties to understand cryptotephra transport.

3.1 Introduction

The ejection of fine grained ash (defined by Rose and Durant (2009) as diameters < 1000 μm, which fall in the intermediate flow regime) into the atmosphere from large volcanic eruptions can result in widespread dispersal of tephra. Distal ash deposits (here > 1000 km from source) are often preserved as non-visible (crypto-) tephra layers comprising low concentrations of ash shards preserved in peat or lake sediments or ice cores. Shards can be identified by their characteristic translucent glassy appearance and bubbly or platy morphologies and are linked to tectonic regions or specific volcanoes by geochemical analysis (Tomlinson et al., 2015). By linking the ash to an eruption of known age, cryptotephra deposits provide continental-scale age frameworks for their host sediment sequences. Cryptotephra studies can also improve understanding of volcanic processes, constrain eruptive histories (Wastegård, 2002; Lawson et al., 2012), and when combined with dispersion modelling can be used to assess past atmospheric conditions (Lacasse, 2001; Lacasse and van den Bogaard, 2002) and ash transport mechanisms (Stevenson et al., 2012, 2013, 2015; Watson et al., 2016; Dunbar et al., 2017). When particle size distributions (PSDs) and ash shard concentrations are reported, these data can improve constraints on total eruptive volumes, which are usually only calculated from proximal tephra (Ponomareva et al., 2015).

Many cryptotephra layers originating from Iceland can be found in northern Europe (Lawson et al., 2012); these distal deposits provide a valuable record of eruptions in Iceland during the Quaternary, for which proximal deposits are scarce due to glaciation (Lane et al., 2012). However, dispersion modellers have been unable to account for the travel distances of the largest grains (typically > 80 μm) in such deposits (Lacasse, 2001; Stevenson et al., 2015; Beckett et al., 2015; Watson et al., 2016). Numerical models show that dispersion distance is sensitive to particle size and shape for cryptotephra-sized grains (Beckett et al., 2015; Saxby et al., 2018). Cryptotephra studies often report size as maximum grain length L (the greatest distance between two parallel tangents on the grain), and do not report shape, while models use the geometric size d_v (diameter of a volume-equivalent sphere) and can include a shape parameter. For very non-spherical particles, L and d_v can differ significantly (Saxby et al., 2018).

We explore whether particle shape is one of the contributing factors in long-distance ash transport, using proximal and distal samples of the 12.1 ka BP Vedde tephra from Katla volcano, Iceland. We quantify the shape and size of ash shards and use these data to model their transport. We show that by quantifying geometric size and particle shape, we can explain the dispersion of the largest shards (< 191 μm) of the Vedde tephra to sites in Norway, a distance of > 1200 km, given a plume height of > 20 km above ground level (agl). Travel distance is sensitive to particle shape, and the method of size measurement; we can only account for the significant travel distance of

some large cryptotephra shards by using consistent size and shape parameters from measurement to modelling. We also assess different measures of particle size and determine the dependence of shard size on the amount of material sampled.

3.1.1 Particle shape and tephra transport

Far from the vent, where the influence of plume dynamics is negligible, volcanic ash dispersion is controlled by meteorological conditions (e.g. wind advection and turbulent diffusion) and the sedimentation velocity of the particles. In dry conditions, sedimentation velocity is controlled by terminal fall velocity, which is sensitive to air density, air viscosity, and particle size, shape and density (Folch, 2012; Beckett et al., 2015). Non-spherical volcanic ash particles have a lower terminal velocity than equivalent-volume spheres (Riley et al., 2003). Therefore, to understand the dispersion of cryptotephra it is essential to constrain particle properties. The influence of shape on cryptotephra dispersion distance, however, has not been examined.

Cryptotephra are typically characterised by ash grains of $L = 25$-80 μm (Blockley et al., 2005). However, grain size is not often reported. Where sizes are given, they are often modal or maximum sizes, and the amount of material required to accurately constrain these parameters is unclear. In addition, the process of extracting cryptotephra from sediment often involves the mechanical removal of larger and/or smaller sediment particles by sieving (e.g., Turney, 1998; Blockley et al., 2005), limiting the range of observed sizes. Descriptions of cryptotephra morphology are often qualitative, with ash particles characterised by glassy bubble wall fragments with winged, platy or fluted morphologies (e.g., Mangerud et al., 1984; Stevenson et al., 2013). Although this suggests a link between ash morphology and distal transport, shape measurements are scarce and, where given, are often ratios between particle axis lengths measured in 2D (e.g., Watson et al., 2016). Shape-dependent particle terminal velocity equations used in dispersion models, in contrast, are calibrated using 3D shape measures (e.g., Wilson and Huang, 1979; Ganser, 1993; Bagheri and Bonadonna, 2016b). By measuring the 3D shape of distal tephra particles we can better determine the sensitivity of travel distance to particle shape using dispersion modelling.

3.1.2 The Vedde ash

The Vedde ash, dated to 12.1 ka BP (Rasmussen et al., 2007) is an exceptionally widespread event horizon that is described in > 60 terrestrial and ice sequences and > 30 marine deposits throughout Europe and the North Atlantic, as distally as the Ural Mountains, Siberia (Haflidason et al., 2018), making it an important marker for the correlation of Quaternary sequences (Lane et al., 2012).

Few proximal outcrops are described, probably due to the extensive glaciation of Iceland during the Younger Dryas at 12.6 – 12.0 ka BP (Ingólfsson and Norðdahl, 2010). The Vedde ash, with a bimodal composition (45 – 58% and 72 – 76% SiO_2), has been geochemically linked to Katla volcano, Iceland (Mangerud et al., 1984). Distally it is characterised by cuspate, winged or platy shards (Figure 3.1) interpreted as thin bubble wall structures (Norðdahl and Haflidason, 1992). It is unclear to what extent these particle shapes influenced distal transport.

Although the Vedde ash mostly occurs as cryptotephra, there are several lake and peat bog sites in the Ålesund and Nordfjord areas of western Norway (Figure 3.2, inset) with exceptionally thick ($\leq$ 50 cm) deposits, created by drainage into palaeolakes from larger catchment areas (Mangerud et al., 1984). We examine six Vedde ash samples from visible deposits (thickness 0.5 – 21 cm) in Norway as well as one proximal sample from Iceland (Figure 3.2; Table 3.2). The deposits provide large sample sizes, allowing us to accurately quantify maximum and modal shard size and determine the number of shards necessary for accurate measurement. The reworked ash in Norway is in both marine and lacustrine sediments, ruling out ocean circulation or ice rafting as a transport mechanism (Mangerud et al., 1984), and so we can assume the ash was transported to the lake catchments by atmospheric circulation. The distance over which the ash has been transported after deposition is therefore negligible compared to the distance it was transported before deposition.

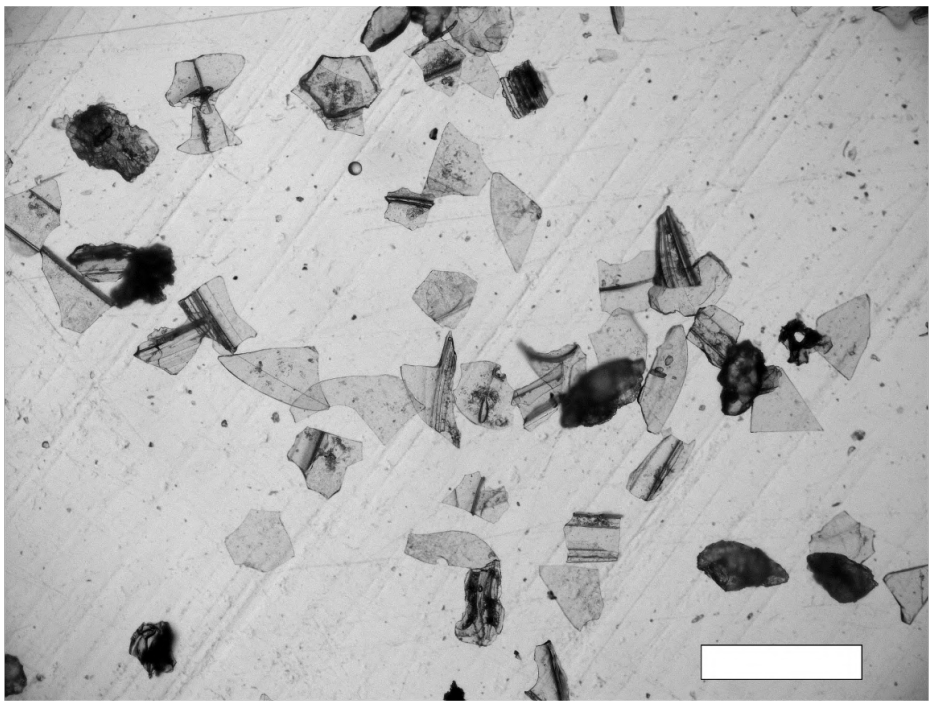

Figure 3.1: Vedde ash shards from western Norway (sample KV1). 125-180 μm sieve fraction. Scale bar = 500 μm.

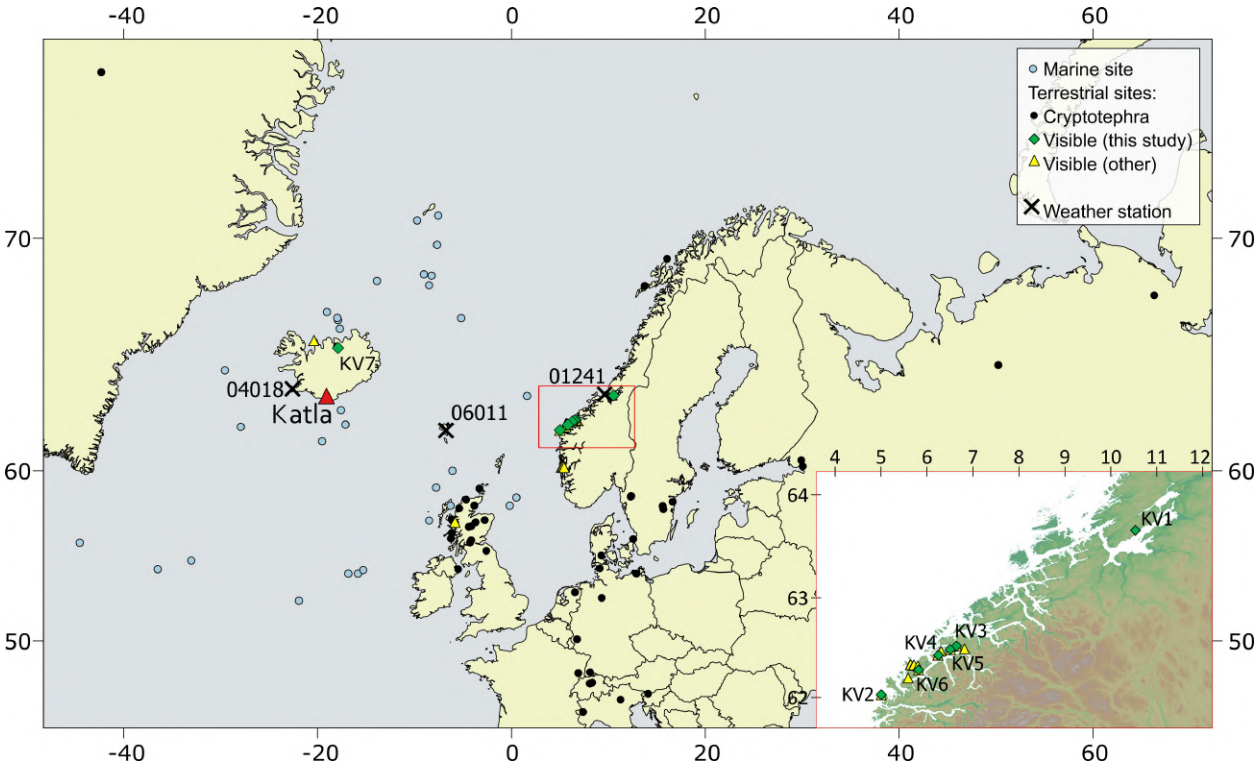

Figure 3.2: Documented occurrences of the Vedde ash in terrestrial and marine sites. All data sources are given in supplementary material for the submitted paper version of this chapter. Sites labelled KV are the source of samples described in this study. Area in red is enlarged in inset to show locations of samples from Norway. Numbered black crosses denote weather stations in the North Atlantic region from which we analyse wind velocity data.

3.2 Methods

3.2.1 Determining particle size, shape and density

We sieved all samples at half-φ intervals, apart from sample KV5 which was sieved to > 62.5 µm prior to this study. We manually picked ~ 10 of the largest ash shards from each Norwegian sample and mounted them on tape with maximum projected area in view. Maximum projected area A_{max}, perimeter P, and maximum axis length L were obtained through optical microscopy images analysed with ImageJ software. Grain depth D was estimated by focusing down through the translucent particles using a dial with increments of 1 µm; we estimated volume by $V = A_{max}D$ and surface area by $A_{surf} = 2A_{max} + PD$. This approximation does not consider surface roughness,

Table 3.2: Sample codes and locations for samples of the Icelandic Vedde ash used in this study. Latitude and longitude are in decimal degrees (WGS84).

Sample	Latitude	Longitude	Site	Country	Core type	Distance from source (km)	Reference
KV1	63.65914	10.53415	Rørtjønna	Norway	Lake	1454	
KV2	62.02756	5.004157	Kråkenes	Norway	Lake	1232	Mangerud et al. (1984); Lohne et al. (2014)
KV3	62.52116	6.641243	Stettetjøn	Norway	Bog	1296	Mangerud et al. (1984)
KV4	62.48559	6.506024	Slettebakktjønn	Norway	Lake	1291	Mangerud et al. (1984)
KV5	62.42842	6.249304	Gjølvatn	Norway	Lake	1280	Mangerud et al. (1984)
KV6	62.27965	5.817248	Litletjørn/ Litlevatn	Norway	Lake	1264	Svendsen and Mangerud (1987)
KV7	65.74995	17.89799	Fnjóskadalur	Iceland	Palaeolake	240	Norðdahl and Haflidason (1992)

which is a reasonable simplification as the particles examined are smooth-sided bubble wall shards. We calculated sphericity as a function of volume and surface area:

$$\psi = \frac{\pi^{\frac{1}{3}}(6V)^{\frac{2}{3}}}{A_{surf}} \tag{3.1}$$

(Ganser, 1993). With this definition, a sphere has $\psi = 1$ and the value decreases towards zero with increasing difference from a spherical shape; for example, an oblate spheroid with a ratio between semi-major and semi-minor axes of 2:1 has a sphericity of 0.91. We obtained d_v by solving for the diameter of a volume-equivalent sphere. We averaged the 5 particles with the largest d_v as representative of maximum d_v (d_{v5}) and L (L_5) for each sample.

To obtain bulk shape descriptors, and determine the impact of sample size on measurements, we also scanned $>$ 300 particles from the 62.5 – 125 μm (3 – 4 φ) sieve fraction of each sample, using X-ray microcomputed tomography (CT). We used a single size fraction, where the proximal and distal PSDs overlap, as particle shape can be size-dependent (e.g., Mele and Dioguardi, 2018). To separate particles, we encased them in epoxy resin within 6 mm diameter, 20 mm long plastic cylinders. X-ray projections were taken as the cylinders were rotated 360°. The resolution of 3.5 μm voxel edge length gave $>$ 2800 voxels/particle; a minimum of 1200 voxels/particle gives an

accurate mean ψ (Saxby et al., 2018). A 3D volume, constructed from 2D image slices using CT Pro 3D, allowed segmentation of the particles from the much less dense epoxy according to greyscale values, and the surfaces of the particles were reconstructed with Avizo software. We employed the Label Analysis module to calculate V, A_{surf}, and the three principal axis lengths L, I, and S (long, intermediate and short axes, respectively) of each particle. Using these axis lengths we calculated form factor F:

$$F = \frac{I+S}{2L} \tag{3.2}$$

(Wilson and Huang, 1979), elongation e:

$$e = \frac{I}{L} \tag{3.3}$$

and flatness f:

$$f = \frac{S}{I} \tag{3.4}$$

(Bagheri and Bonadonna, 2016b). We calculated ψ using equation 3.1.

For the largest shards we estimated a density of 2456 kg m^{-3}, based on glass composition (Iacovino, 2017; Lange and Carmichael, 1990; Ochs and Lange, 1999). We used the average composition of the rhyolitic component of the Vedde ash from Mangerud et al. (1984) and assumed there are no internal bubbles; in reality $\sim$20% of the selected shards contain 1-2 visible bubbles, but these are small relative to the grain size. The density is consistent with observations by Turney (1998) who extracted the Vedde ash from sediment using liquids with densities of 2400-2500 kg m^{-3}.

3.2.2 Dispersion modelling

To test the hypothesis that particle shape is an important factor in distal ash transport we used NAME (Numerical Atmospheric-dispersion Modelling Environment; Jones et al. (2007)). NAME is a Lagrangian atmospheric dispersion model, in which model particles are advected by 3D meteorological fields and dispersed using a random walk scheme which includes parameterisations for sub-grid scale atmospheric turbulence and mesoscale motions (Thomson et al., 2009; Webster et al., 2018). NAME also includes parameterisations for wet and dry deposition, with sedimentation schemes for both spherical and non-spherical particles (Webster and Thomson, 2011, 2014; Beckett et al., 2015).

To initialize NAME to model the transport and dispersion of a volcanic ash cloud the following parameters must be provided: the source location, the eruption start and end times, the plume height, the source strength (mass eruption rate, MER) and the particle characteristics (size, density and shape).

To consider the eruption and meteorological conditions conducive to transport the ash to Norway we first ran a 2D stratified model in MATLAB; full details are given in Appendix B. This allowed us to test multiple plume height and wind speed scenarios and determine the sensitivity of travel distance to physical particle properties.

We analysed modern meteorological (met) archive data to provide realistic bounds on atmospheric conditions at the time of the Vedde eruption. Single-site met data were obtained from the Wyoming Soundings archive (http://weather.uwyo.edu/upperair/sounding.html). We downloaded soundings from radiosonde ascents for the weather stations at Keflavík, Iceland (site code 04018); Tórshavn, Faroe Islands (06011); and Ørland, Norway (01241; see Figure 3.2 for locations), for the period 1973 - 2018. Data are collected twice daily to measure atmospheric parameters including wind speed, direction, temperature and relative humidity as a function of altitude ($<\sim 30$ km). Monthly average horizontal wind velocities and exceptional records are shown in Figure 3.3. In our analysis, we included only single wind speed records containing ≥ 20 discrete height records, with the highest > 25 km. In the winter, stratospheric winds over Iceland are generally westerly, with monthly average wind speeds up to ~ 40 m s^{-1} in the stratosphere (Figure 3.3; Lacasse (2001)). Several individual records show mean velocities of > 80 m s^{-1} (averaged over 0 – 25 km).

We found that, assuming a constant wind field in our simple modelling setup, to explain the transport of the largest Vedde ash shards we needed:

- A high plume (> 20 km).
- Wind speeds higher than the stratospheric monthly averages shown in Figure 3.3.

Travel distance was more sensitive to size than shape, in agreement with Beckett et al. (2015). Uncertainties on particle density translate into differences in travel distances which are small compared to the differences due to size and shape, suggesting our measurement methods are robust. A full description of the model setup, our calculation of uncertainties and their propagation into travel distance is given in Appendix B.

We then ran NAME using 3D analysis meteorology from the Unified Model (UM; Cullen (1993)). The UM met data are from 2011 to present, have a horizontal resolution of between 17 and 25 km, a temporal resolution of 3 h, and include wind speed and direction as well as other

meteorological parameters such as cloud water and ice, precipitation, and boundary layer height (Thomson et al., 2009; Webster and Thomson, 2011; Witham et al., 2017). As our initial sensitivity analysis determined that wind speeds higher than any monthly average were necessary, we used the radiosonde dataset (Figure 3.3) to identify dates with favourable conditions for ash transport from Iceland to Norway. Dates (dd/mm/yy) where mean wind speed from 0 – 25 km was > 40 m s^{-1} and the mean wind direction from 0 – 25 km was between 220 and 320° for at least two sites out of three North Atlantic weather stations (Figure 3.2) are: 07/03/11, 08/03/11, 23/03/11, 10/03/14, 16/03/14, 26/01/15, 11/02/15, and 28/12/16. NAME runs for these 8 dates used UM data from 59 pressure levels to ~ 29 km altitude; the meteorological conditions higher in the stratosphere were taken to be the same as at 29 km. A full description of this 'persisted met' approach is given in Appendix B. Particles were released in a uniform distribution from the vent height to the plume top at 35 km agl over an 8 hour period from 00:00 to 08:00 on each day and tracked for 48 hours to ensure deposition of at least 99% of the mass released. Dates specified are the first day of the run, and the simulations were continued for the following two days using reanalysis data for those dates. As we are interested in particle travel distance rather than deposit thickness, we plot deposition as the fraction of total mass in each grid cell, using a minimum contour of 10^{-20}. The chosen mass eruption rate (MER) is therefore arbitrary; we use 2×10^{12} g hr^{-1}.

Plume height can be constrained using empirical fits to mass eruption rate (Mastin et al., 2009), or maximum clast size in very proximal deposits (within tens of km; Burden et al. (2011)) but this is not feasible for the Vedde eruption due to the near-absence of proximal deposits. Maximum plume height estimates for recent Icelandic eruptions range from 10 – 20 km (e.g., Biass et al., 2014; Leadbetter and Hort, 2011), but our initial analysis (Appendix B) indicated a plume > 20 km was needed. Carey et al. (2010) estimated a maximum plume height of 34 km for the 1875 explosive eruption of Askja volcano using the method of Carey and Sparks (1986). Sharma et al. (2008) estimated a plume height of 30 – 34 km for the 1362 eruption of Öræfajökull, using maximum clast size data. Both eruptions transported ash to Scandinavia (Pilcher et al., 2005; Carey et al., 2010). Based on these estimates we use 35 km agl as an upper bound.

We calculated terminal velocity w_t using the drag laws of White (1974) for spherical particles and Ganser (1993) for non-spherical particles; full details of the drag laws are given in Appendix B. For the particle size, we used 191 μm, d_{v5} of sample KV4, as a maximum; runs with a shape parameter use $\psi = 0.55$, the mean ψ of those particles. We chose sample KV4 as these particles had the highest w_t of the Norwegian samples according to preliminary calculations using Ganser's (1993) drag law, allowing us to constrain the minimum conditions necessary for transport.

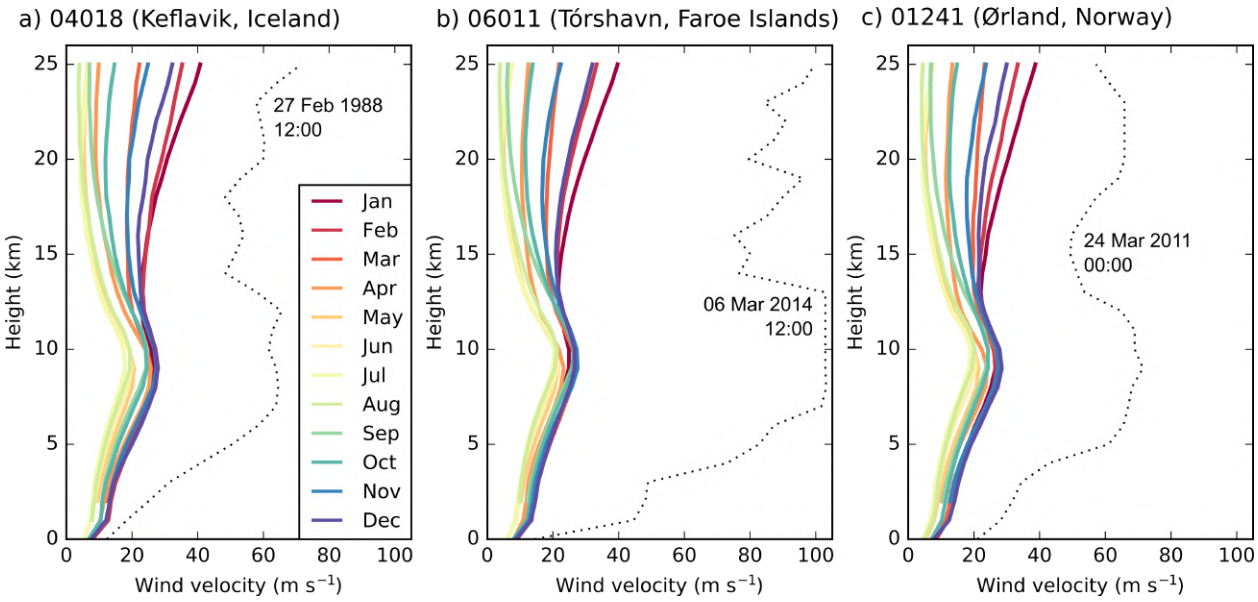

Figure 3.3: Balloon-borne radiosonde data for the weather stations at a) Keflavík, Iceland, b) Tórshavn, Faroe Islands, and c) Ørland, Norway. Station codes correspond to locations in Figure 3.2. Coloured lines show monthly mean speed at each height for the period 1973 – 2018. Dashed lines show individual records for days with extremely high winds, with the day and time chosen based on the highest (height-averaged mean) wind velocities.

3.3 Results

3.3.1 Particle size and shape

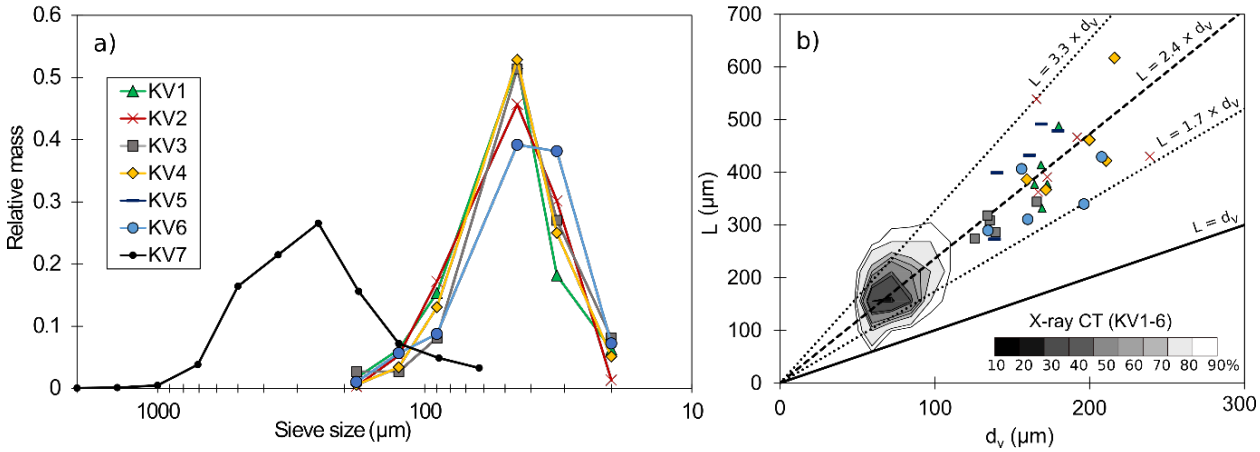

Figure 3.4: Vedde ash particle size. a) Sieve size distributions for samples KV1-6 (Norway; excluding KV5 which was sieved to $>$ 63 µm prior to this study) and KV7 (Iceland). b) Particle long axis L and geometric size d_v for the 5 largest particles in each of the samples KV1-6, measured using optical microscopy. L ranges from 1.7 to 3.3 $\times d_v$. For comparison X-ray CT data from 5241 ash particles are contoured for the same samples.

The Vedde ash sample collected in Iceland, KV7, has a single modal sieve size of 250-354 µm with the largest grains $>$ 1 mm; grain sizes in the Norway samples (KV1-6) are smaller (Figure 3.4a), as anticipated (e.g., Carey and Sparks, 1986; Folch, 2012). Samples KV1-6 have a single common mode of 45 - 90 µm, despite a range of geographical settings and distances from source (Table 3.2). Optical microscopy measurements of the size parameters d_{v5} and L_5 are $>$100 µm in all distal samples, with KV4 having the largest d_{v5} and L_5 of 191 µm and 451 µm, respectively. All data are presented in supplementary material for the submitted paper version of this chapter.

The standard size parameter for ash dispersal modelling is d_v but L is more commonly measured. L/d_v for samples KV1-6 ranges from 1.7 to 3.3 with a mean of 2.3 (Figure 3.4b). 81% of the CT data for the 90-125 µm sieve fraction from these samples are in this L/d_v range (contours in Figure 3.4b), although the minimum L/d_v is close to 1, the value for a sphere, and the maximum L/d_v = 10.9. The range of L/d_v ratios we observe is similar to the range of L/I ratios measured by Mangerud et al. (1984) for the Vedde ash.

We obtained bulk shape descriptors from CT scans of the 62.5 – 125 µm sieve size fraction of each

sample (Figure 3.5). The proximal and distal samples do not differ significantly in form factor F (Equation 3.2), although the Iceland sample has the highest mean F (0.58). Mean flatness f (Equation 3.4) and elongation e (Equation 3.3) are similar. KV1-5, however, have higher e than f, indicating shards are generally flatter (ratio of short to intermediate axis) than they are elongated (ratio of intermediate to longest axis). Sample KV6, in contrast, has equal mean e and mean f (0.65). Distal samples KV1-6 have flatter shards (mean f of 0.60 to 0.66; Figure 3.5c) than proximal sample KV7 (mean f = 0.74). Differences between proximal and distal ash are most pronounced in the surface-area based shape factor sphericity (ψ), which ranges from a mean of ψ = 0.56, with 50% of the data between 0.45 and 0.67, in the Iceland sample KV7 to a mean ψ of 0.37 to 0.43 for distal samples KV1-6. Sphericities of larger shards measured by optical microscopy fall within the range of values observed using tomography (Figure 3.5a) but are generally higher than the mean. This could be explained by a variation in particle size, but the difference may also be due to the differing measurement methods: the optical microscopy method approximates particles as smooth flat plates, and so may result in lower surface areas, and higher sphericity, than the CT method which measures roughness on a scale only limited by imaging resolution.

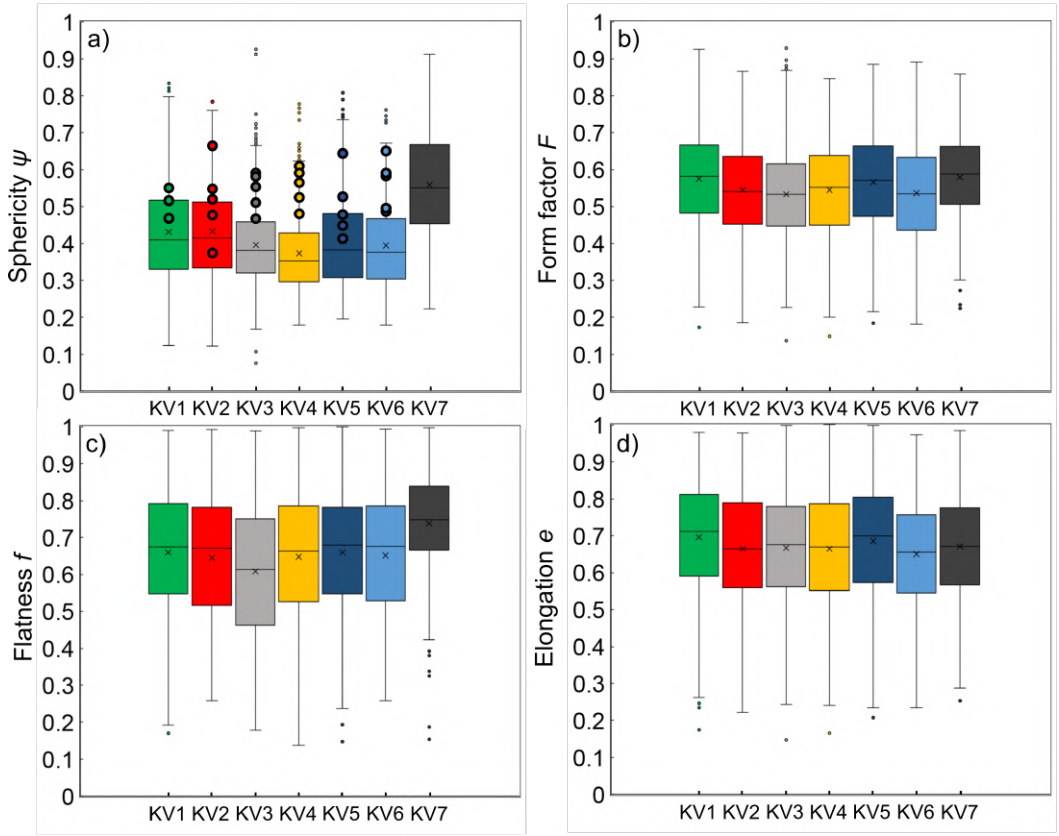

Figure 3.5: 3D shape data for the 62.5 – 125 µm sieve size fraction, Vedde samples KV1-7, measured using X-ray CT; a) sphericity ψ (Ganser, 1993), b) form factor F (Wilson and Huang, 1979), c) Flatness f (Bagheri and Bonadonna, 2016b), d) Elongation e (Bagheri and Bonadonna, 2016b). Crosses indicate the mean value; lines show the median and lower and upper quartiles. For all shape factors, a value of 1 indicates an equant particle (in the case of ψ, a sphere; in the case of e and f, a particle with at least two axes of equal length; for F, three axes of equal length). Small markers show outliers; large markers in plot a) indicate sphericity of the 5 largest shards in samples KV1-6 measured using optical microscopy.

3.3.2 Modelled travel distance

Preliminary analysis (Appendix B) suggested that measuring L_5 could not explain the transport of the largest Vedde shards even assuming extreme idealised conditions (plume height of 35 km and a constant wind speed of 80 m s^{-1} for the entire particle trajectory, which is unlikely). Modelling using NAME confirms the discrepancy in travel distance between runs with L_5 of sample KV4 (451 µm; Figure 3.6a,b) and d_{v5} (191 µm; Figure 3.6c,d).

Even using d_{v5}, we must model particles as non-spheres using Ganser's (1993) drag law and our measured ψ of 0.55 to explain the transport of the largest Vedde ash shards to Norway. In one

NAME simulation using particle size = 191 μm and ψ = 0.55 (23/03/11), five of the six sites fall within the great circle distance enclosing 95% of erupted mass deposition (Figure 3.6d). For the other dates we modelled, sites KV1-6 fall outside this distance, but the results show that a small amount of mass ($< 5\%$) can travel the distance required for deposition in western Norway. Simulations for the other seven days for which we ran NAME are given in Appendix B. In all simulations using spheres with d_v = 191 μm, 95% of the mass is deposited within 880 km of the source and no mass travels to the Norwegian sites (minimum distance of 1232 km, Figure 3.6c; Appendix B), indicating that particle shape exerts an important control on distal dispersion of the largest Vedde ash shards.

Modelling transport of the modal size fraction (45-90 μm) shows that its maximum travel distance is less sensitive to shape (Figure 3.6e,f) than the largest grains, and that deposition of a single size fraction can occur over a wide area.

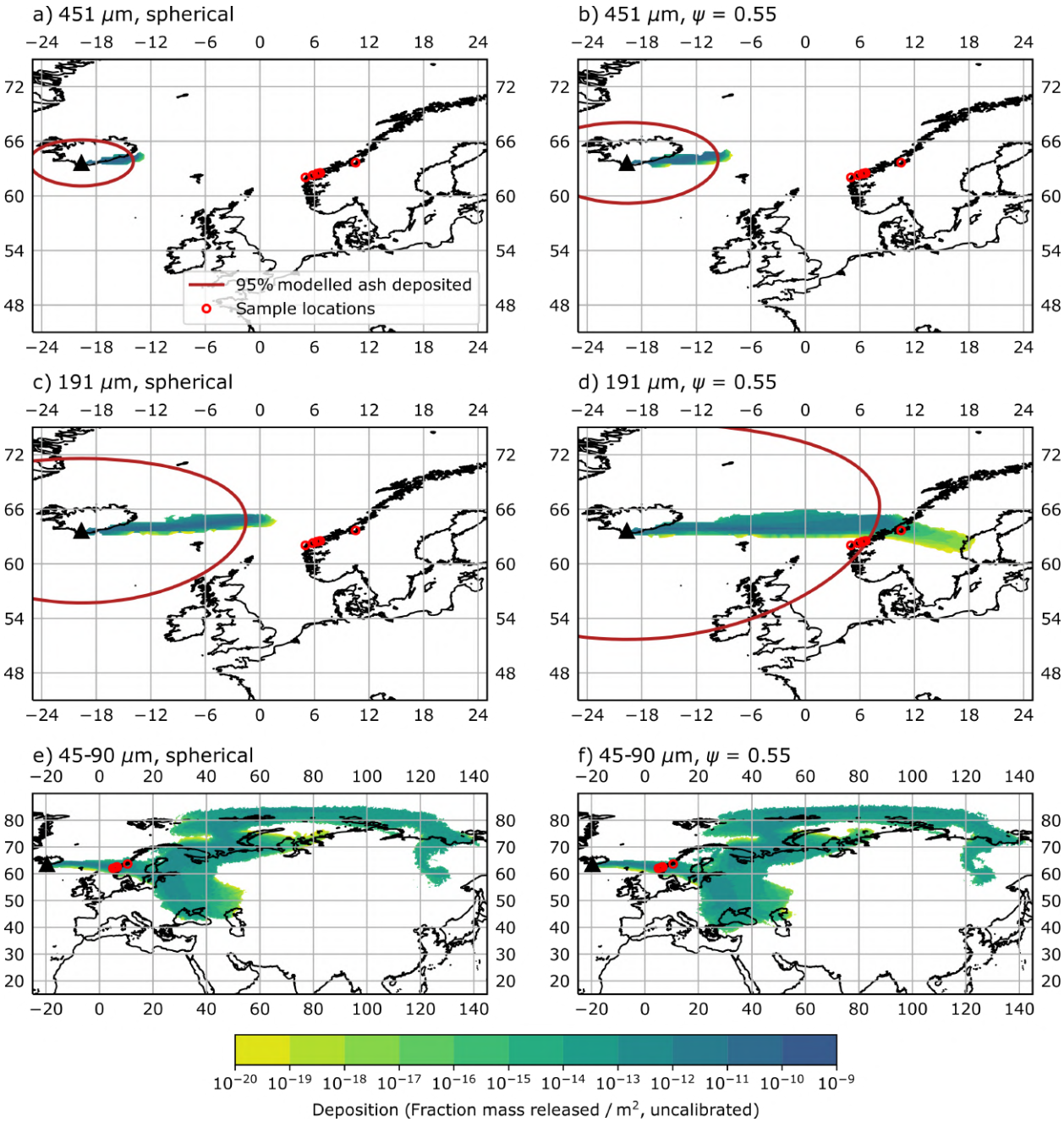

Figure 3.6: Simulated isomass maps for a Vedde-like eruption of Katla volcano (black triangle) on 23/03/2011 using a 35 km agl plume height. Sample locations are given for sites KV1-6 to provide a reference for observed particle travel distances. The red line indicates the great circle distance from the source at which 95% of the erupted mass has been deposited. 451 μm is L_5 of sample KV4; 191 μm is d_{v5} of sample KV4; 45-90 μm is the modal sieve fraction for all western Norway samples.

3.3.3 Cryptotephra sampling strategies

The discrepancy between modelled travel distances of the largest Vedde ash shards for different methods of quantifying size and shape (Figure 3.6, Supplementary Figure B.5) illustrates the need for accurate measurements of maximum particle size and shape. Consideration must be given, therefore, to sampling strategy (Bonadonna, 2006).

The Norwegian Vedde ash deposits KV1-6 are thicker (Figure 3.7a) than other samples collected at a similar distance from the source. Mangerud et al. (1984) calculated the original thicknesses in the Ålesund area of western Norway, the location of Vedde samples KV3-5, to be about 2-3 mm (compacted thickness) based on a regression between the lake area to catchment area ratio and the Vedde ash thickness observed; even these corrected thicknesses are anomalous relative to other locations in Scandinavia. The narrow geographical distribution of visible tephra (Figure 3.2) suggests that the western Norway Vedde sites could be on-axis (in line with the prevailing wind direction). On-axis transport may also explain the higher maximum shard size of the visible tephra layers (Figure 3.7b), where maximum shards are $140 < d_{v5} < 191$ μm and $306 < L_5 < 451$ μm. As western Norway has mountainous topography, orographic effects could also explain the greater fallout of ash in this region (e.g., Watt et al., 2015).

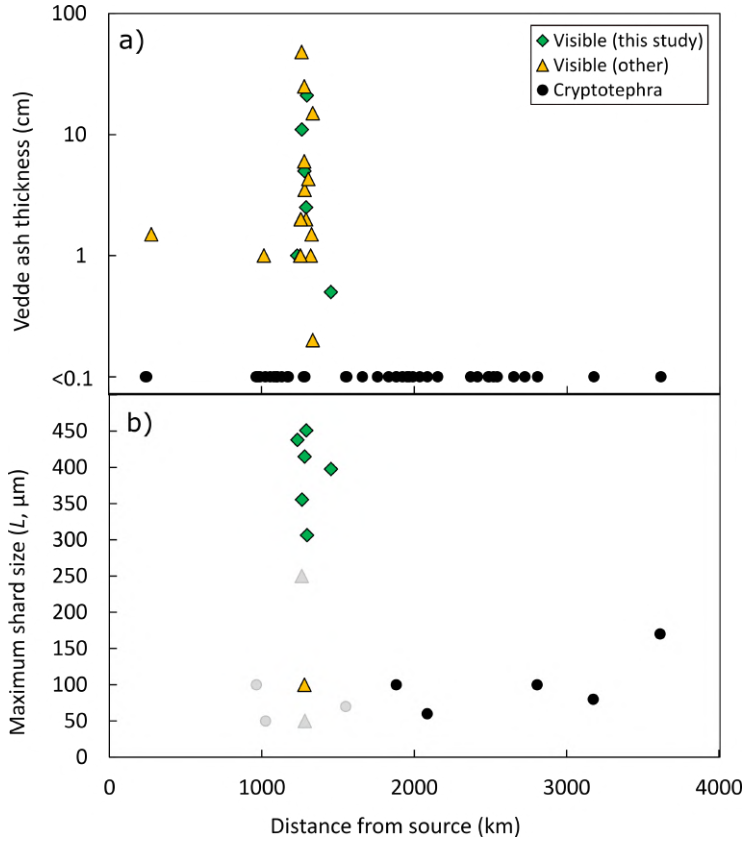

Figure 3.7: Published measurements of a) tephra layer thickness and b) maximum shard size with distance from vent. All data sources are given in supplementary material for the submitted paper version of this chapter; size data from this study are L_5 and from other studies are L. We include data from studies which do not specify the size parameter measured as greyed out symbols of the same shape.

To determine whether the large maximum ash size is a function of the large available sample, we progressively subsampled the X-ray CT dataset for the 62.5 – 125 µm sieve fraction of sample KV3, the largest CT dataset. Our results show that the method of size measurement (L or d_v) has more of an impact on results than the number of particles averaged or the choice of mean or median as an averaging technique (Figure 3.8a), in agreement with observations using much coarser proximal tephra deposits (Bonadonna, 2006). For example, a sample of > 1000 particles is required to obtain a consistent maximum size d_{v5} (Figure 3.8b), which suggests that measurements of maximum shard size are not accurate where only a few shards are available, as in very distal cryptotephra deposits. Accurate calculation of mean size, in contrast, requires only about 50 shards (Figure 3.8b).

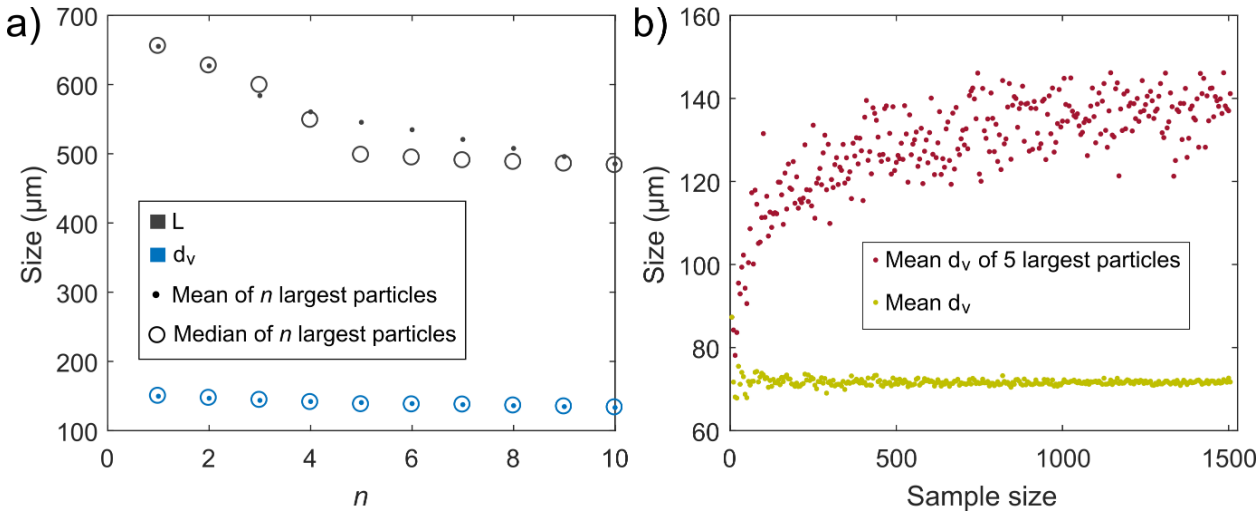

Figure 3.8: The effect of a) the size parameter measured, and the averaging technique (mean or median, and the number of largest particles averaged n) on the maximum size observed in a sample of 1507 particles; and b) by randomly subsampling the same dataset, the effect of sample size on measurement of maximum shard size. Data are for sample KV3, 62.5 – 125 μm sieve fraction.

3.4 Discussion

We show that particle shape, and conversion to size, is one of the major contributing factors in the distal transport of the Vedde ash. Importantly, particle shape affects size measurements (e.g., $d_v < L$); our results suggest that the discrepancy in methods of size measurement between the dispersion modelling and cryptotephra communities can explain much of the reported discrepancy between observed and modelled travel distances (Lacasse, 2001; Stevenson et al., 2015; Beckett et al., 2015; Watson et al., 2016).

Quantitative size and shape data for distal tephra are scarce, but important for understanding eruptions for which proximal data are unavailable (Lane et al., 2012), and for the validation of dispersion models (Witham et al., 2007). Distal Vedde ash samples are not only finer grained but also less spherical on average than the proximal sample: the distal samples have a modal sieve size 45 – 90 μm and mean ψ of 0.37 – 0.43; the proximal sample has a modal sieve size of 250 – 354 μm and mean ψ = 0.56 (sphericity values are for sieve size 62.5 – 125 μm). This indicates that physical particle properties are a strong control on distal tephra dispersion.

The difference in shape between proximal and distal samples is most pronounced when we measure ψ, which may be because ψ, as a surface area-based measure, is sensitive to surface roughness. Proximal and distal samples also differ in flatness f. In contrast, all samples have similar mean

values for elongation e and form factor F, suggesting a narrower range of these shape measures produced by fragmentation at source, and/or that flatness and surface roughness have a greater impact on terminal velocity.

The influence of shape and size on travel distance is confirmed by dispersion modelling, by which we can explain the travel distance of the largest grains in Vedde sites KV1-6 only if we quantify size as d_v and model particles as non-spheres with sphericity calculated by Equation 3.1 and using the drag law of Ganser (1993) (Figure 3.6; Supplementary Figure B.5). To be confident in this conclusion also requires consideration of uncertainty in the model physics and the associated sensitivity of NAME output. Of 6 eruption source parameters and 12 internal model parameters, Harvey et al. (2018) found that NAME outputs are most sensitive to plume height, MER, the precipitation threshold for wet deposition, and free tropospheric turbulence. We suggest uncertainty due to the model physics is less than the uncertainty in source parameters. The particles we modelled are sufficiently large to be unaffected by turbulence as their terminal velocities are much greater than turbulent vertical velocities (Saxby et al., 2018). We normalise our model results to be independent of MER and take a maximum likely plume height for Icelandic eruptions. Even using a maximum plume height and extreme wind conditions we show that it is necessary to evoke particle non-sphericity to explain transport distance.

Particle size measured for distal deposits has implications for PSDs used to forecast ash concentrations in the atmosphere. Of nine worldwide VAACs (Volcanic Ash Advisory Centres), only one (Buenos Aires) considers particles > 100 μm by default for forecasting ash dispersion (Hort, 2016). We show that although the bulk of ash in distal deposits is < 100 μm, $d_{v5} > 100$ μm in all samples (Figure 3.4), meaning that particles > 100 μm can travel > 1000 km from source.

We can explain transport of the largest Vedde ash shards (d_v = 191 μm and ψ = 0.55) to Norway assuming a plume height of 20 – 35 km agl (Figure 3.6, Supplementary Figure B.5). Comparison with minimum eruption volume estimates of 2.8 – 3.3 km^3 (Lacasse et al., 1995) for the marine ash deposit North Atlantic Ash Zone 1 (NAAZ1), which is correlated to the Vedde ash (Lacasse et al., 1996), suggests a VEI ≥ 5; eruptions of this magnitude are associated with plumes > 25 km (Newhall and Self, 1982) and so it is reasonable to invoke a high plume for the Vedde eruption.

Modelling results rely on accurate measurement of maximum grain size, which we assume provides constraints on maximum transport distance. The terminal velocity of very fine grained particles is low compared to atmospheric vertical velocities (advection and diffusion) meaning that travel distance does not strongly depend on their physical properties; the residence time of particles with $d_v = 10$ μm is insensitive to shape while for particles with $d_v = 100$ μm it is highly sensitive to shape (Saxby et al., 2018). The exact size at which terminal velocity becomes dominant depends

on atmospheric velocities, particle shape and density. The influence of atmospheric velocity partly explains why grains of a single size fraction (45 – 90 μm) can deposit over a range of distances (Figure 3.6); this is also due to the vertical spread of ash in the plume and spatial variation in depositional processes such as removal by precipitation (Webster and Thomson, 2014), aggregation (Bagheri et al., 2016), topographic effects (Watt et al., 2015), and gravitational instabilities in the proximal ash cloud (Manzella et al., 2015). Aggregation causes both early fallout of fine grained particles and delayed sedimentation of larger particles due to coating with finer grained particles, forming low density composites in a process known as 'rafting' (Bagheri et al., 2016). All these factors may explain the poor correlation between modal cryptotephra shard size and distance (Watson et al., 2016), and explain why a range of ash particle sizes are found in any given sample location.

We therefore suggest that modelling transport distance as a function of terminal velocity is only meaningful when the largest shards of a sample can be accurately identified, meaning a sample of 500 and ideally $>$ 1000 shards, and those shards have d_{v5} on the order of 100 μm. However, measurements of smaller or fewer shards are useful in other volcanological applications: shard size can inform estimations of total grain size distribution, eruptive style and magnitude (Cashman and Rust, this volume).

The Vedde ash was selected for this study of the impact of size and shape on travel distance due to its characteristic platy shard morphology (Mangerud et al., 1984) and its abundance in European sediment sequences (Lane et al., 2012). However, it is important to note that the samples are from deposits that have been reworked. Ash particles can undergo sorting by size and shape due to fluvial processes; for example, Watson et al. (2016) found that cryptotephra shards were larger in lakes than in neighbouring peat bogs. However, despite differences in deposit thickness and drainage basin size, we find no significant difference in the particle shape and size distributions for the 6 Norwegian sites studied, suggesting that our observations of shard size and shape are representative of the primary air fall deposit.

We present a method of assessing the transport of ash from an eruption at a time for which no meteorological data are available, by setting upper limits on plume height and wind speed based on modern met data. Tephra may have been able to travel further in the Pleistocene, however, due to stronger atmospheric circulation (Sigurdsson, 1990). Additionally, changes in atmospheric temperature during cold stadials, and the resulting atmospheric density increase, could increase the neutral buoyancy height of the plume (Lacasse, 2001). Our results should therefore be interpreted as maximum possible dispersion distances under ideal modern conditions. Furthermore, controls on tephra transport (e.g. plume height, meteorology) can change during an eruption and so another major assumption in linking ash transport models to deposit characteristics is that all samples are

from the same eruptive phase. This is particularly relevant when studying cryptotephra deposits for which the eruption chronology is unknown. The Vedde ash has been tentatively linked to the Sólheimar ignimbrite in Iceland (Lacasse et al., 1995), raising the possibility of additional atmospheric ash injection via a co-ignimbrite plume, which could have been subject to different meteorological conditions. In fact, although our model runs can account for the transport of ash from Iceland to Norway, they cannot account simultaneously for deposition of the Vedde ash to the north and west of the vent (northern Iceland and Greenland; Figure 3.2). A change of wind direction during the eruption, or vertical inhomogeneity in the wind field, may be necessary to explain these deposits.

Finally, our results suggest additions to cryptotephra sampling and measuring techniques for volcanological applications. Ideally maximum shard size should be measured, although this requires a sample of at least 500 and optimally > 1000 shards (Figure 3.8). Measurements taken from smaller samples are still useful as the mean shard size can be accurately quantified using fewer (~ 50) shards; the number measured should be noted. Also important is calculation of the size parameter d_v, the parameter most often used in dispersion models; estimates can be obtained rapidly for translucent shards using an optical microscope. It is useful to report particle sphericity ψ where surface area can be measured. For eruptions where ψ is not available, it is reasonable to assume a non-spherical shape (Dunbar et al., 2017). If there is a relationship between maximum shard size, particle shape, and transport distance, as shown here, modelling of cryptotephra transport could be used to estimate eruption parameters (Watson et al., 2016); inverting for plume height (mass eruption rate) and wind speed from proximal deposits is already common (e.g., Carey and Sparks, 1986). Note that plume height and wind speed constraints will be minima because of uncertainties in defining particle size and the modelling assumption that samples are collected on-axis. For most cryptotephra deposits, the plume axis is poorly constrained, and particles are unlikely to have followed the shortest path from source to deposit.

Chapter 4

How to measure the shape of volcanic ash, and recommendations for dispersion modelling

This work has been submitted to Earth and Planetary Science Letters as Saxby, J., Rust, A., Beckett, F., Cashman, K., and Rodger, H., 'How to measure the shape of volcanic ash, and recommendations for dispersion modelling' (submitted July 2019, revised and resubmitted November 2019). The Vedde ash sample was collected by Sigurður Reynir Gíslason; the other ash samples were collected by Jennifer Saxby with help from Frances Boreham during a field campaign in Iceland in summer 2016. Morphological analysis using X-ray CT and reconstructions were carried out by Jennifer Saxby with assistance in using the scanner from Tom Davies. Density analyses were performed by Jennifer Saxby. Particle velocity lab experiments were carried out by Hannah Rodger as part of her Master's project which was supervised by Jennifer Saxby, Katharine Cashman and Alison Rust. Jennifer Saxby analysed video data from these lab experiments to calculate terminal fall velocities. Claire Witham provided feedback on an earlier draft of this paper.

Abstract

The sedimentation rate of volcanic ash through the atmosphere influences its travel distance, with important implications for aviation and human health. The fall velocity of a particle depends on its size and density, but also shape, and volcanic ash is not spherical. To capture the sedimentation of non-spherical ash, atmospheric dispersion models use empirical drag laws calibrated using geometric shape descriptors. However, particle shape data are scarce and there is no standard method of shape measurement. In addition, shape measurements are not always available during an eruption, when dispersion models are used operationally to forecast ash hazard. We assess the variability in the shape of volcanic ash from Icelandic eruptions using X-ray computed tomography. We then assess the effectiveness of the shape descriptors by comparing terminal velocities calculated using drag laws with our measured shape parameters to their terminal velocity measured in a settling column. We find that shape-dependent drag laws produce more accurate results than a spherical approximation. However, accurate drag calculations based on the shape descriptor sphericity, which is a function of surface area, require the imaging resolution to be within the range of 10^2 - 10^5 voxels per particle. Shape descriptors based on ratios between principal axis lengths are more robust as they are less variable among particle size classes and much less sensitive to imaging resolution. Finally, we compile particle shape data from this study and literature sources and make recommendations on default values for use with atmospheric dispersion models where no shape data are available.

4.1 Introduction

Volcanic ash (tephra particles with diameters < 2 mm) can remain in the atmosphere from minutes to days or longer after a large explosive eruption (Durant et al., 2010); the rate of removal from the atmosphere depends on meteorological processes and particle terminal fall velocity. Accurate calculation of terminal velocity requires a parameterisation of particle shape (e.g., Riley et al., 2003; Bagheri and Bonadonna, 2016b,a). This means that models used for forecasting volcanic ash dispersion can be sensitive to the shape parameter assigned to the model particles (Scollo et al., 2008; Beckett et al., 2015; Saxby et al., 2018). In addition, the shape of volcanic ash particles can provide information on componentry (Buckland et al., 2018), eruptive style (Liu et al., 2015, 2017), transport mechanisms (Rose and Chesner, 1987), emplacement conditions (Dufek and Manga, 2008; Buckland et al., 2018), and tephra layer identification (Liu et al., 2016).

The question of how to measure, and model, particle shape is relevant in many other disciplines. Many atmospheric particulates are non-spherical, meaning that shape is an important parameter in understanding the transport of nuclear fallout (Rolph et al., 2014), ice crystals (Westbrook and Sephton, 2017), pollen (Schwendemann et al., 2007), wildfire embers (Anthenien et al., 2006) and desert dust (Chou et al., 2008). The hydrodynamic behaviour of particles settling in water is also a function of shape; for example, assemblages of marine species such as foraminifera, which are used to estimate palaeodepth (e.g., Speijer et al., 2008; Jorry et al., 2006). Particle shape is also an important factor in understanding the drag of non-spherical particles in streams (Komar and Reimers, 1978) and understanding particle sorting (Oakey et al., 2005); shape has an impact on crystal settling velocities in magma, with implications for magma rheology (Higgins and Roberge, 2003).

For all these applications, particle size is as important, and generally more important than shape; however, particle shape can influence the results of grain size measurement. Particles passing through a sieve mesh may have one dimension larger than the mesh aperture, and so the results of sieving are dependent on the shape of the particle (Arason et al., 2011), and particle shape affects the results of particle size distributions calculated from 2D images (Higgins and Roberge, 2003). Although particle volume is a shape-independent measure of size, it is not straightforward to measure for irregular particles.

Volcanic eruptions produce a wide variety of particle shapes, related to the kinetics of vesiculation and crystallization during magma ascent, and the fragmentation mechanism. Ash types include vesicular pumice clasts, smooth crystals, platy bubble wall shards, and needle-like fragments of tube pumice. Describing shape using one or more quantitative geometric shape descriptors

reduces operator bias and allows comparison between datasets; however, the most useful shape descriptor will depend on the textural variability of the sample and the purpose of the research, meaning there is no 'standard' way to measure shape. In addition, the results strongly depend on measurement parameters such as the resolution of the images used (Alfano et al., 2011; Liu et al., 2015; Dioguardi et al., 2017). Most shape descriptors applied to volcanic ash particles can be measured from projections of particle surfaces via 2D image analysis (e.g., Riley et al., 2003). However, recent advances in the use of optical and electron microscopy (Ersoy et al., 2010; Bagheri et al., 2015; Vonlanthen et al., 2015) and X-ray computed tomography (CT; Ersoy et al. (2010); Dioguardi et al. (2017); Mele and Dioguardi (2018)) mean it is now easy to construct high-resolution 3D models of volcanic ash particle surfaces.

This study provides an assessment of the techniques used for measuring 3D shape parameters for the purpose of understanding the aerodynamic behaviour of volcanic ash. We assess the shape range of volcanic ash and consider how best to measure shape for the purpose of calculating the terminal velocity of volcanic ash in an atmospheric dispersion model. We measure multiple 3D geometric shape descriptors using the X-ray CT method. To assess the effectiveness of the shape descriptors in anticipating particle fall velocity, we also measure the terminal velocity of our volcanic ash samples in a settling column and compare the results to calculated terminal velocities using empirical drag laws with our measured shape parameters. Our reference datasets include ash samples from Icelandic volcanoes (Katla, Hekla and Eyjafjallajökull) spanning a wide range of composition, eruptive style, and morphology; this allows us to assess the variation in the shape of volcanic ash between eruptions and between size fractions, and the sensitivity of 3D shape descriptors to the CT scan parameters. We use the resulting insights to present a database of shape descriptors for use with semi-empirical drag laws (Ganser, 1993; Bagheri and Bonadonna, 2016b; Dioguardi et al., 2018) which are valid for a wide range of flow conditions and therefore suitable for modelling the sedimentation of volcanic ash in the atmosphere.

4.2 Modelling the terminal velocity of non-spherical ash

Particle terminal velocity (w_t) is defined as the velocity a falling object reaches when the drag force is equal to the gravitational force and so acceleration is zero; volcanic ash particles reach terminal velocity in the atmosphere over distances which are small compared to the distance required to sediment from a plume, and so it is reasonable to neglect acceleration in modelling. Terminal

velocity can be calculated as a function of drag:

$$w_t = \left(\frac{4}{3} \frac{d}{C_D} g \frac{\rho_P - \rho}{\rho} \right)^{\frac{1}{2}} \tag{4.1}$$

where d is the particle size (for a sphere, diameter), g is gravitational acceleration, ρ is fluid density, ρ_P is particle density, and C_D is the drag coefficient, a dimensionless coefficient which is a function of particle shape and flow regime. Volcanic ash falling in air can be subject to several flow regimes, defined by the dimensionless Reynolds number Re; the flow around a particle is classed as laminar when $Re < 0.1$ and turbulent at $Re > 1000$. The drag of spheres can be calculated analytically with high accuracy for all flow regimes (e.g., White, 1974). A spherical particle approximation is appropriate for small (less than $\sim$ 30 μm diameter) volcanic ash particles in the laminar regime (Alfano et al., 2011; Saxby et al., 2018), but shape begins to influence particle sedimentation and transport distance at particle diameters between $\sim$ 30 and 100 μm, with particles $\geq$ 100 μm being highly sensitive to shape (Beckett et al. (2015); Saxby et al. (2018), Saxby et al. (in revision; Chapter 3 of this thesis)). Solutions for non-spherical particles, which are characterised by higher C_D than spheres of equivalent size and density, are generally empirical or semi-empirical correlations which relate C_D to one or more geometric shape descriptors. Therefore, such correlations are valid for finite Re and particle shape ranges which are limited by the experimental conditions and the formulation used.

4.3 Tephra samples

We use tephra samples from fall deposits of three Icelandic volcanoes, spanning five eruptions, and collected between 10 and 242 km from vent, to investigate a range of clast types, morphologies, and compositions. The samples consist of deposits from three eruptions of Katla volcano: the Vedde eruption (KVE) of $\sim$ 12 ka BP (Wastegård et al., 1998), and two silicic Katla (SILK) tephra samples, SILK-MN (KSM) and SILK-UN (KSU), dated to 2975±12 a BP and 2660±50 a BP, respectively (Larsen et al., 2001). We also use tephra samples from the 1947 eruption of Hekla volcano (HEK) and the 2010 eruption of Eyjafjallajökull (EYJ). The Katla SILK deposits are noted for their distinctive 'needles', that are elongated tube pumice fragments containing sparse microlites and numerous elongated bubbles in a glassy matrix (Larsen et al., 2001), while the Katla Vedde deposits are flat, platy bubble wall shards (Mangerud et al., 1984). The Eyjafjallajökull 2010 sample is characterised by blocky or angular glassy particles with a wide range of vesicularity (Gislason et al., 2011) and the Hekla sample is characterised by blocky vesicular particles. The samples also span a range of compositions. The Vedde sample is bimodal (45-58 % and 72-76 %

Table 4.2: Summary of samples and methods used in this study.

Sample set	No. of particles	Eruptions	Volume-equivalent sphere diameter d_v (mm)	Measurement methods
1	46	KVE, KSM, HEK, EYJ	1.0 – 2.6	Morphological analysis using X-ray CT; density; terminal velocity
2	19557	KVE, KSU, HEK	0.025 – 3.6	Morphological analysis using X-ray CT

SiO_2; Mangerud et al. (1984)) and the Hekla 1947 and Eyjafjallajökull 2010 samples are andesitic (with $\sim$ 62 % SiO_2 and 58 % SiO_2, respectively; Larsen et al. (1999); Gislason et al. (2011)). The SILK-MN and SILK-UN samples are dacitic (65 % and 64 % SiO_2, respectively; Larsen et al. (2001)).

4.4 Measurements

A summary of the measurements obtained is given in Table 4.2. Prior to analysis, all samples were manually dry sieved at 1 φ intervals using sieve mesh diameters of 4 to -1 φ (62.5 to 2000 μm), apart from sample KVE which was sieved at half-φ intervals using sieve mesh diameters of 3.5 to -0.5 φ (88 to 1414 μm). We selected 46 individual particles from the 0 φ and -0.5 φ sieve fractions of the KVE, KSM, HEK and EYJ samples for detailed analysis including terminal velocity measurements; grains were selected to include a wide range of shapes.

4.4.1 Particle velocities

Particle velocities were measured using a settling column and high-speed imaging based on the method of Bagheri and Bonadonna (2016b). The 1.5 m high and 0.15 m diameter glass settling column ensures that particles fall a sufficient distance to reach terminal velocity. At the top of the column is a guiding tube to ensure particles fall approximately in the centre to minimise errors associated with the particle's position in the column; the settling column setup is illustrated in Figure 4.1. A Vision Research Phantom v9.1 high speed camera was positioned 0.1 m from the

bottom of the apparatus, where particles fall from the settling column into a flat-sided glass box. A measure with precision of 1 mm was placed at the back of the box. To focus the camera prior to the experiments, a thread with a weight attached to the end was lowered down the guiding tube into this box, which was illuminated with two external LED lamps. Each grain of ash was then released individually into the guiding tube and filmed at a sample rate of 1400 fps and an exposure of 711.25 µs. Phantom 675.2 Camera Control software was used to output individual video frames in jpeg format including a time stamp from which terminal velocity could be calculated from 5 to 8 cm sections of each particle's trajectory. The error arising from the relative positioning of the camera, particle, and ruler was corrected assuming that each particle was falling in the centre of the 15 cm main settling column. Each particle velocity measurement presented here represents the median of 5 repeat measurements. Repeat data could not be collected for particles which broke upon landing and so those experiments are not reported. This creates a potential bias against measuring the fall velocity of particles with certain shapes and densities. Velocity data are available in supplementary material for the submitted paper version of this chapter.

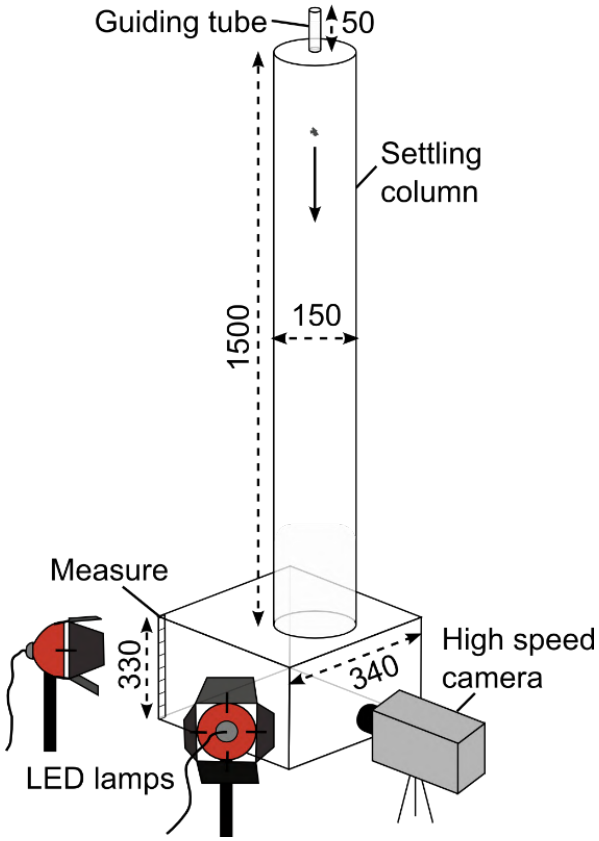

Figure 4.1: Schematic diagram of the settling column setup. All dimensions are in mm.

4.4.2 Density

We calculated particle density using volumes from CT scans and particle mass measured on a balance with a precision of 0.0001 g. Particle dimensions calculated using Avizo CT software were checked using digital calipers. Densities calculated based on composition (Mangerud et al., 1984; Larsen et al., 1999, 2001; Gislason et al., 2011), using a glass density calculator (Iacovino, 2017) and correcting for bubble volumes, were similar to measured densities.

4.4.3 Particle dimensions using X-ray computed micro-tomography

Scans of individual large particles (Sample Set 1, Table 4.2) were carried out on a Nikon XTH225ST scanner using a voltage of 120 kV and a current of 58 µA. Particles were mounted individually in florist's foam or cotton wool within plastic pipettes. Of the 46 particles in Sample Set 1, 16 were scanned at the maximum instrument resolution (voxel edge length = 3 µm). We used this high-resolution dataset to examine the sensitivity of X-ray CT volumes and shape descriptors to imaging resolution by progressively downsampling the datasets to give resolutions of 2, 4, 8, 16 and 32 times the original voxel edge lengths. The remaining 30 particles were scanned at the lower resolution of voxel edge length = 96 µm (32 times the voxel edge length of the high-resolution scans). We also carried out CT scans of ash from all sieve fractions of the KVE, KSU and HEK samples (Sample Set 2, Table 4.2) to obtain bulk shape descriptors. For these scans we used a voltage of 100 kV and a current of 70 µA. Particles smaller than 4 φ (62.5 µm) were not used due to constraints on imaging resolution. The voxel size was varied to maintain a minimum resolution of between 4728 and 20,000 voxels per particle, in order to obtain size-independent shape parameters; within this range we find no correlation between resolution and shape. Samples were encased in epoxy resin to ensure good particle separation and allow simultaneous imaging of up to several hundred particles, as discussed in Saxby et al. (2018). Despite this preparation, particles from several coarser sieve fractions tended to float to the top of the sample container before the epoxy hardened; these particles were touching in the resulting segmented 3D volumes and were separated using a watershed algorithm (Avizo Separate Objects module), which first detects object centres and then simulates flooding from these regions to the edges of 3D 'catchments' defined according to the greyscale value gradient. We reconstructed 3D volumes using CT Pro 3D software and segmented the volumes in Avizo. From the resulting particle surfaces, we obtained particle surface area (A_{surf}), volume (V), and three orthogonal principal axis lengths: long axis L, intermediate axis I and short axis S.

4.4.4 Morphological parameters

We compare observed terminal fall velocities with calculations based on the drag laws of Ganser (1993), Bagheri and Bonadonna (2016b) and Dioguardi et al. (2018). The three drag laws chosen are all applicable for the range of flow regimes expected for volcanic ash falling in air and are all calibrated using geometric shape descriptors which we can obtain from CT scan data. We calculate w_t using equation 4.1; all the drag laws use the diameter of a volume-equivalent sphere, d_v, for the particle size parameter d. C_D is calculated as a function of one or more geometric shape descriptors, given below; for the corresponding C_D equations, see Appendix C. Since the drag of spheres can be determined analytically to high accuracy, a popular approach in defining shape descriptors is to use a ratio of a particle parameter to that of a volume-equivalent sphere. The Ganser (1993) drag law, for example, uses sphericity (ψ_G), the ratio of A_{surf} of a volume-equivalent sphere to A_{surf} of the particle being described:

$$\psi_G = \frac{\pi^{\frac{1}{3}} (6V)^{\frac{2}{3}}}{A_{\text{surf}}} \tag{4.2}$$

where A_{surf} is a measure of 3D surface area and therefore an effective descriptor of roughness at all scales, limited only by imaging resolution. Difficulty in measuring the 3D surface area of irregular particles has meant that studies have often calculated sphericity using approximate surface area of a smooth scalene ellipsoid A_e (Dellino et al., 2005; Mele et al., 2011), with equal principal axes to the particle:

$$A_e = 4\pi \left(\frac{\left(\frac{L}{2}\right)^z \left(\frac{I}{2}\right)^z + \left(\frac{L}{2}\right)^z \left(\frac{S}{2}\right)^z + \left(\frac{I}{2}\right)^z \left(\frac{S}{2}\right)^z}{3} \right)^{\frac{1}{z}} \tag{4.3}$$

where z = 1.6075. The Dioguardi et al. (2018) drag law is calibrated using an ellipsoid approximation; their shape descriptor Ψ_D is the ratio of 3D sphericity to 2D circularity:

$$\Psi_D = \psi_e / X \tag{4.4}$$

(Dellino et al., 2005), where:

$$\psi_e = \frac{\pi^{\frac{1}{3}} (6V)^{\frac{2}{3}}}{A_e} \tag{4.5}$$

and

$$X = \frac{P_{\text{proj}}}{P_c} \tag{4.6}$$

where P_{proj} = maximum projected perimeter and P_c = the perimeter of a circle with equal projected area to the particle being described. In this study we focus on 3D shape measurement and do not measure X, as this 2D parameter is a function of particle perimeter, one of the 2D parameters most

sensitive to imaging resolution (Liu et al., 2015). When calculating Ψ_D we use the Dioguardi et al. (2018) recommended best fit approximation:

$$\Psi_D \approx 0.83\psi_e \tag{4.7}$$

Another class of particle shape descriptor, termed form factors, consists of combinations of L, I and S; these measure the form of the particle but are insensitive to small-scale surface roughness (Bagheri and Bonadonna, 2016b) and are therefore less sensitive to imaging resolution. These include the two shape factors defined by Bagheri and Bonadonna (2016b), elongation e and flatness f, where

$$e = \frac{I}{L} \tag{4.8}$$

and

$$f = \frac{S}{I}. \tag{4.9}$$

The shape descriptors ψ_G, Ψ_D, e, and f are all scaled between 0 and 1 where 1 = an equant particle; this allows for easy comparison between parameters.

4.5 Results

4.5.1 Sensitivity of shape descriptors to X-ray computed micro-tomography scan and reconstruction parameters

Greyscale threshold

Particle surfaces are reconstructed from raw CT data by separating 3D regions representing particles from the surrounding epoxy; this requires the selection of a threshold greyscale value. As the particle edges are characterised by a gradient (over $\sim 3 - 5$ voxels) rather than a sharp boundary, the choice of threshold is subjective and so we determined the sensitivity of particle volume and shape to this choice. From an original 3D greyscale image, of which we show a small region as a 2D slice in Figure 4.2a-c, we manually selected a best estimate threshold value of 98 from the range 0-255 (Figure 4.2b; regions defined as particles are highlighted in blue). We then increased and decreased the threshold by 10 (Figure 4.2c and 4.2a, respectively), which are our minimum and maximum estimates of the greyscale value which best defines particle boundaries. We calculate a maximum 6% error on mean d_v and 4% error on mean ψ_G arising from the selection of the particle boundaries.

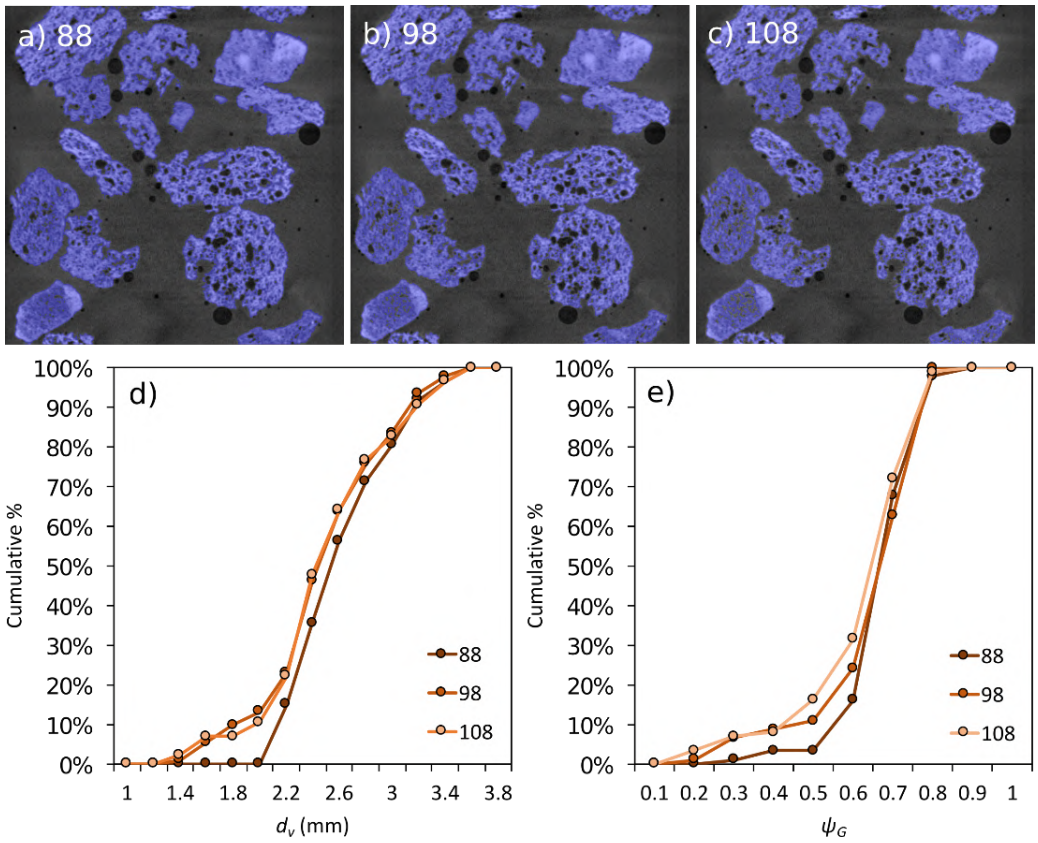

Figure 4.2: Sensitivity of d_v and ψ_G to the greyscale threshold used to define particle surfaces in Avizo analysis software. For this analysis we use the -1 φ fraction of sample HEK. Images a-c) show the definition of particle areas (highlighted in blue) resulting from greyscale thresholds of 88, 98 and 108 respectively; 98 is our best estimate. Panel d) shows the difference in the resulting d_v distributions and panel e) shows the difference in the resulting ψ_G distributions. Note that after thresholding we fill internal vesicles while reconstructing the outer surface of the particle.

Voxel size

To investigate the impact of voxel size on measured shape factors, we used X-ray CT data for 16 individual large particles from Sample Set 1. The original scans were conducted at the maximum resolution of the scanner (a voxel edge length of $\sim$ 3 µm, giving between 6.5×10^6 and 1.3×10^8 voxels per particle). We progressively resampled the scan data from 2 to 32 times the original voxel edge lengths, giving a maximum voxel edge length of $\sim$ 96 µm; after each resampling we recalculated A_{surf}, V, and the shape descriptors ψ_G, Ψ_D, e, and f. The results are shown in Figure 4.3. For a large, rough particle (KSM-9, Figure 4.3, inset) apparent surface area decreased by between 10 and 23% each time we doubled the voxel edge length; the mean for all particles at all scales is 12%. In contrast, volume measurements are relatively insensitive to imaging resolution;

when halving or doubling the resolution, the mean absolute volume change is 1.4%. This means the size parameter d_v is insensitive to resolution over this range. The shape descriptors vary in their sensitivity to resolution. Particles have higher apparent sphericity at low resolution: doubling the voxel edge length resulted in ψ_G increasing between 0.005 and 0.13 (3 – 32%, mean 14%). For most particles studied, both ψ_G and A_{surf} are sensitive to resolution for the whole resolution range, suggesting the particles exhibit surface irregularities at or below the scale of the 3 µm resolution limit. The exceptions are the Vedde ash particles KVE-1 and KVE-2, which are smooth glass shards (Figure 4.3, insets). For these particles, A_{surf} and ψ_G are almost constant above $\sim 10^5$ voxels / particle. Unlike ψ_G, which is a function of surface area, shape descriptors which are functions of principal axis lengths (Ψ_D, e, and f) are relatively insensitive to imaging resolution (Figure 4.3 d-f); on average, e, f and Ψ_D change by ± 1.2%, 1.6%, and 1.3% respectively when voxel edge length is doubled.

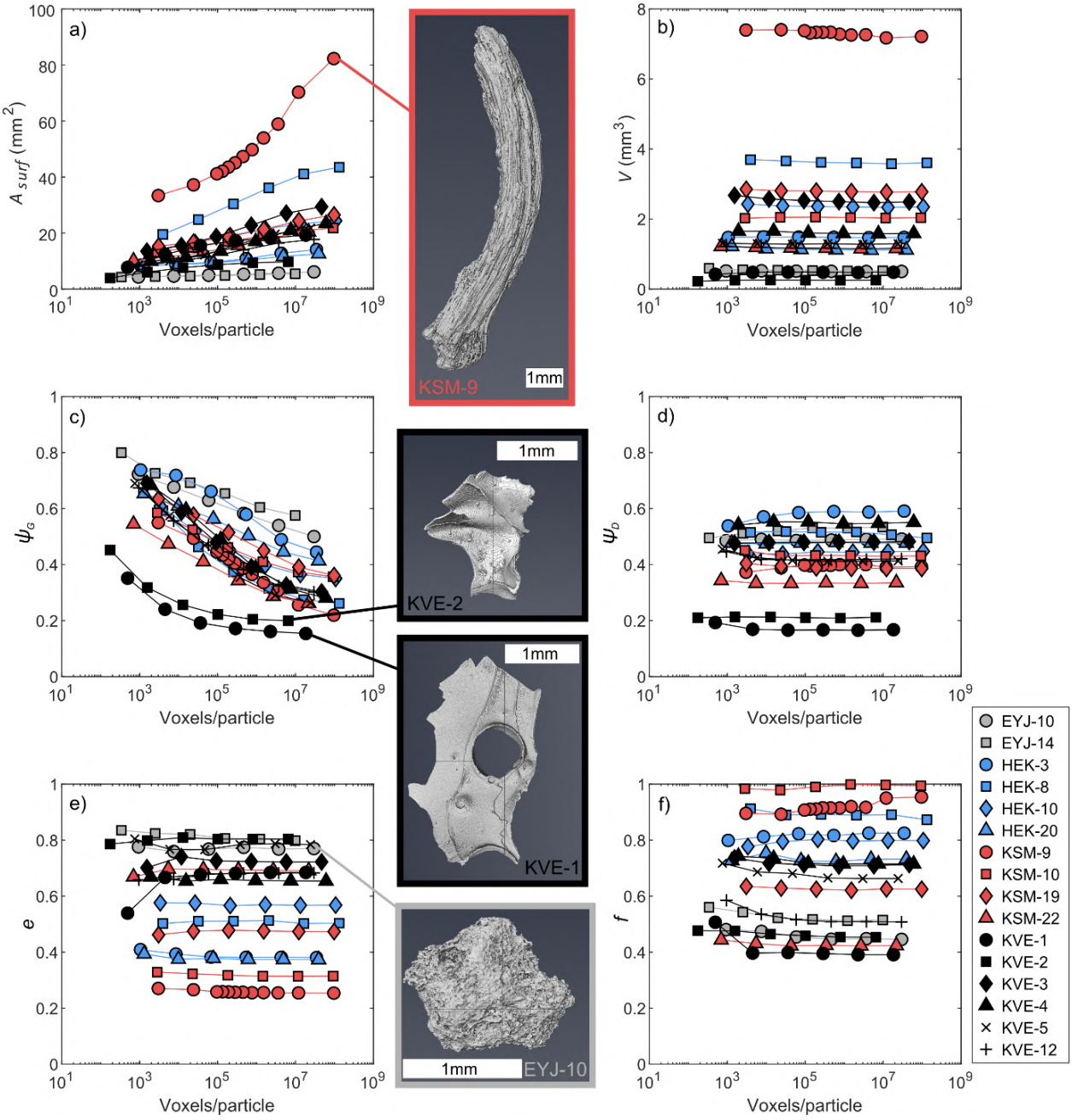

Figure 4.3: Sensitivity of particle measurements to CT imaging resolution. a) Surface area A_{surf}; b) volume V; c) sphericity ψ_G (Ganser, 1993); d) shape factor Ψ_D (Dioguardi et al., 2018); e) elongation e (Bagheri and Bonadonna, 2016b); f) flatness f (Bagheri and Bonadonna, 2016b).

4.5.2 Assessing the effectiveness of shape descriptors in representing the aerodynamic behaviour of volcanic ash

Measured median terminal velocities ($w_{t,\,rec}$) of particles dropped in the settling column range from 1.9 to 6.4 m s^{-1}. Minimum and maximum velocities deviate from the median by a maximum of 57%. We compare calculated fall velocities using the drag laws of Ganser (1993), Bagheri and Bonadonna (2016b) and Dioguardi et al. (2018) with our measured shape parameters, as well as a spherical particle drag law (White, 1974), to their measured terminal velocities to determine the most effective shape parameterisation. For the Ganser (1993) drag law, which uses the shape factor ψ_G which is very sensitive to imaging resolution, we first recalculate terminal velocity for every value of ψ_G obtained from resampling the CT data for the 16 high resolution scans (Figure 4.3c). A mean 14% reduction in ψ_G for each doubling of voxel edge length translates into an average reduction of 12% in calculated velocity ($w_{t,\,Ganser}$). Figure 4.4 shows these calculated velocities relative to $w_{t,\,rec}$. Importantly, we find that calculating ψ_G with high-resolution data results in calculated velocities which are much too low, as we overestimate the effect of very small-scale surface irregularities on drag. For example, using the original (high resolution) scan settings to calculate surface area results in the fall velocities predicted by the drag law of Ganser (1993) being between 1.2 and 2.3 times too slow. The best agreement between measured velocities and those calculated using the Ganser scheme occurs when we calculate ψ_G using a voxel edge length of 96 μm (resolutions between 10^2 and 10^5 voxels / particle). The results of our comparison between drag laws are shown in Figure 4.5. Using the analytical drag law of White (1974) for spherical particles overestimates terminal velocity with a mean absolute percentage error (MAPE) of 40% (Figure 4.5a); MAPE is calculated by: $\frac{100\%}{n}\sum_1^n|\frac{w_{t,rec}-w_{t,White}}{w_{t,White}}|$. Drag laws which include a shape factor (Ganser, 1993; Bagheri and Bonadonna, 2016b; Dioguardi et al., 2018) produce better agreements with measured velocities. The Bagheri and Bonadonna (2016b) scheme calculates velocity as a function of e and f, shape factors which do not significantly change with resolution; the scheme slightly overestimates terminal velocity, with a MAPE of 24% (Figure 4.5c). We calculate velocity after Dioguardi et al. (2018) using Ψ_D (equation 4.7); the MAPE is 22% (Figure 4.5b). Using the Ganser (1993) scheme with ψ_G calculated using a voxel edge length of 96 μm results in a MAPE of 19% (Figure 4.5d). However, we only show this best fit dataset; using the ψ_G data from the 16 high resolution scans increases the MAPE of the Ganser (1993) scheme to 69%, meaning the drag law performs worse than a spherical approximation if the impact of surface roughness is overestimated.

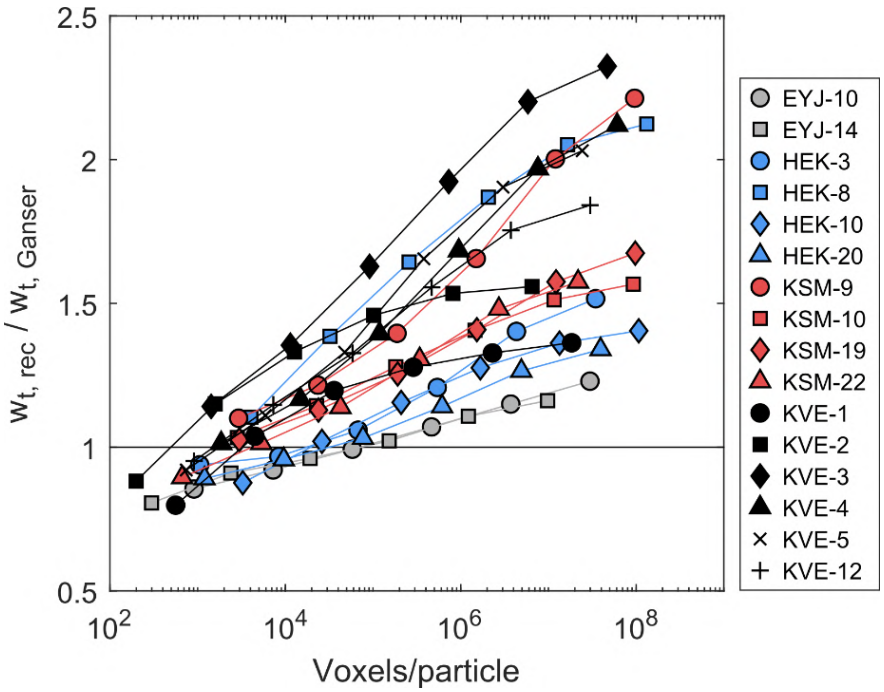

Figure 4.4: Measured velocity ($w_{t,\ rec}$) divided by velocity calculated after Ganser (1993); $w_{t,\ Ganser}$ with ψ_G calculated after progressive resampling of CT datasets to decrease resolution. Values of 1 indicate perfect agreement between $w_{t,\ rec}$ and $w_{t,\ Ganser}$.

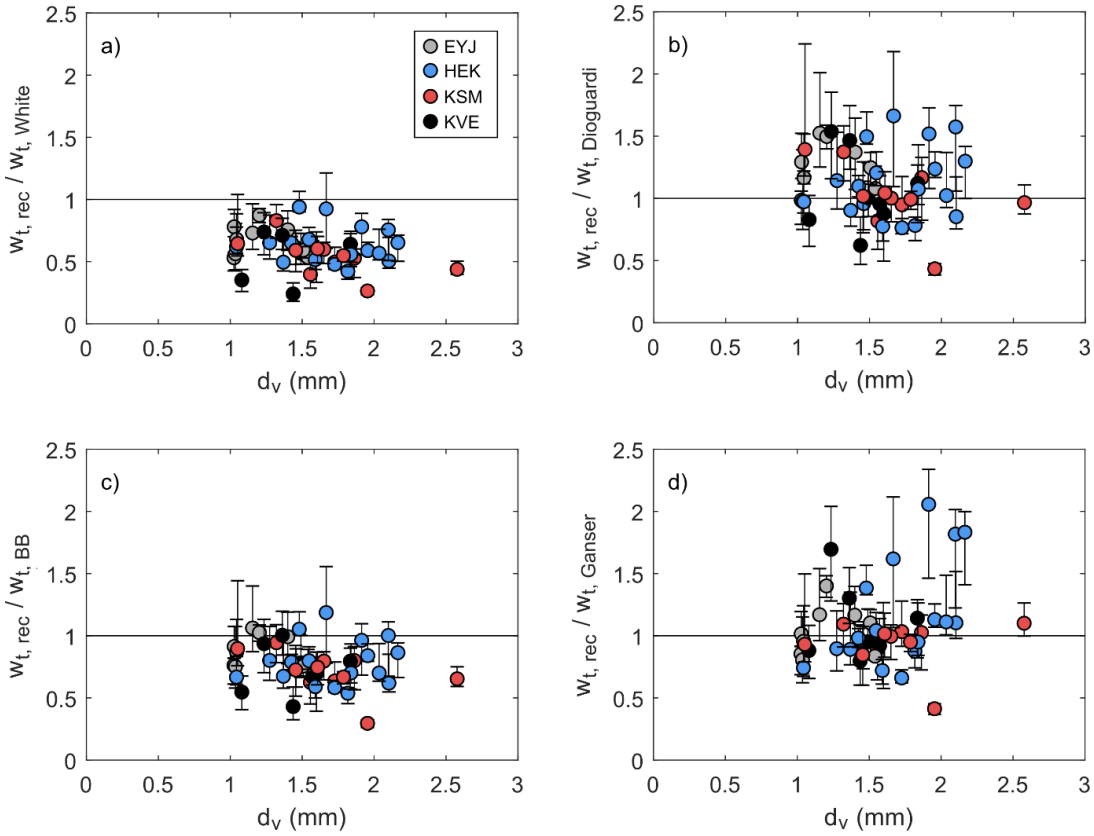

Figure 4.5: Measured velocity ($w_{t,\,rec}$) divided by velocity calculated by a) a spherical particle approximation (White, 1974), b) as a function of Ψ_D (Dioguardi et al., 2018), c) as a function of e and f (Bagheri and Bonadonna, 2016b), and d) as a function of ψ_G (Ganser, 1993) where ψ_G is calculated using CT scan resolutions of 96 µm voxel edge length. Note that the Ganser (1993) scheme performs worse than even a spherical particle approximation when ψ_G is calculated using much higher image resolutions.

4.5.3 A database of the shape of volcanic ash

We have determined that the drag laws of Ganser (1993), Bagheri and Bonadonna (2016b), and Dioguardi et al. (2018) produce reasonable estimates of terminal velocity for volcanic ash particles. In practice, when using shape-dependent drag laws to produce operational forecasts in real-time, information on particle morphology is not likely to be available. Therefore, the operational use of these schemes requires a database from which to choose the likely range of ash shape. Operationally, volcanic ash dispersion models typically use a particle size distribution (PSD); for most operational systems the bulk of the modelled erupted mass is restricted to particles with diameter < 100 µm (Hort, 2016); thus it is important to assess the relationship between particle shape and size, as well as obtain shape data for smaller particles. In addition, accurate calculation

of w_t using the Ganser (1993) scheme requires the shape factor ψ_G to be calculated from CT data with a resolution which gives between 10^2 and 10^5 voxels / particle, and so our database can only include ψ_G data in this resolution range. We obtain shape descriptors for every sieve fraction of samples KVE, KSU, HEK (Sample Set 2, Table 4.2), adjusting voxel size so that resolution is between 4728 and 20,000 voxels/particle for all sieve fractions. The resulting particle shape distributions are shown in Figure 4.6; we compare them in Figure 4.7 to published data from other eruptions that match our imaging resolution criteria. All data are available in supplementary material for the submitted paper version of this chapter. Sphericity ψ_G changes significantly with particle size for all eruptions in this study (Figure 4.6). Particles of $\sim$ 300 µm are the least spherical, with the lowest median sphericity of 0.27 and 0.36 respectively for the 2 φ (250 µm) sieve fractions of the HEK and KSU ash, and a lowest median sphericity of 0.17 for the 1.5 φ (350 µm) sieve fraction of the KVE ash. For all samples, sphericity is highly variable even within a single size fraction. The Dioguardi et al. (2018) shape factor Ψ_D shows a similar pattern, although with fewer extremely high or low values (and fewer outliers). The lowest median Ψ_D values are 0.34 (HEK, 3 φ), 0.21 (KVE, 1.5 φ), and 0.34 (KSU, 2 φ). Flatness f and elongation e, in contrast, do not show significant variation with particle size, and both shape factors are constrained to a narrower range, with median e and f between 0.56 and 0.81 for all samples and size fractions in this study. The KSU sample, chosen for its 'extreme' shape when viewed under an optical microscope, does not differ markedly from HEK in terms of mean values, although the percentage of particles with lower shape factors is higher for the KSU ash. The KSU ash has more elongated particles (24 % of particles have $e < 0.5$) than KVE (9 %) or HEK (6 %). However, the percentage of particles with $f < 0.5$ is low for all samples: 2 % for HEK, 3 % for KVE, and 4 % for KSU.

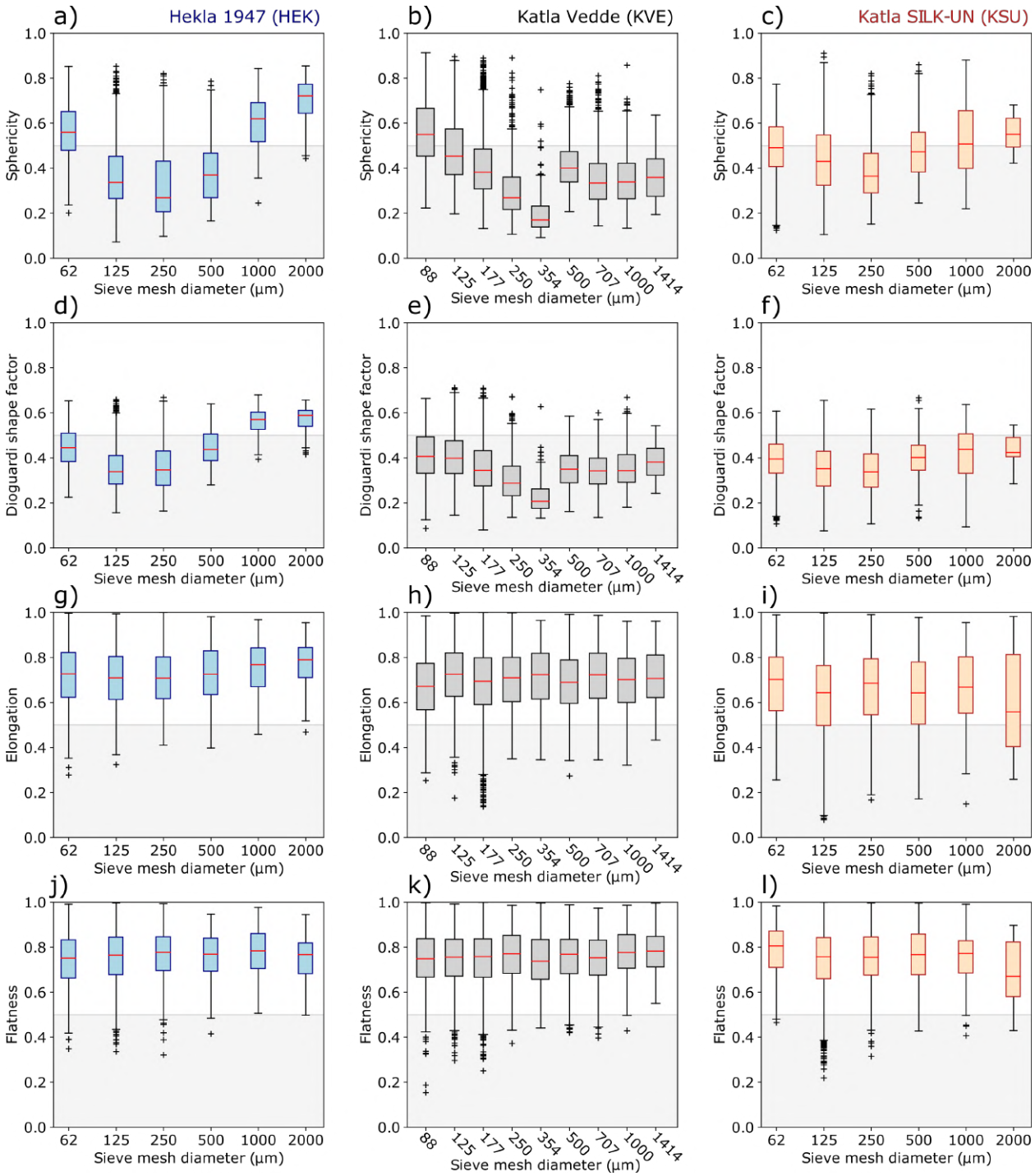

Figure 4.6: Variation in shape descriptors with particle size for (l-r) HEK, KVE and KSU. Shaded areas highlight shape descriptors < 0.5. Red lines indicate the median.

We compare our shape data to ash shape data from previous studies, to expand our morphology database to include different eruptions and particle size fractions, and to determine whether the eruptions studied here show a 'typical' range of volcanic ash shape. All ash shape data are given

in Figure 4.7. As data vary between studies, we plot only mean and standard deviation of shape for each sample. Some studies report the mean shape factor for each size fraction of a sample; others give the mean shape of a bulk sample; where the particles vary in size, we indicate the size range using the X-axis error bars in Figure 4.7. For the shape descriptor ψ_G, we include only data from studies that use CT data with a resolution of between 10^2 and 10^5 voxels/particle, which is our recommendation. Despite this limitation we still find a weak correlation between image resolution and ψ_G (Figure 4.7b). Because Ψ_D, e and f are not sensitive to imaging resolution, it is possible to directly compare our data to other studies measuring the same shape factors, regardless of experimental conditions, including CT scanning, optical microscopy, and caliper measurement of axis lengths. We calculated Ψ_D, e and f using equations 4.7, 4.8, and 4.9, where only axis lengths or ψ_e were reported. We also note that methods of measuring grain size differ between studies, and so the size ranges shown here should be considered approximate. All data sources and measurement specifics are available in supplementary material for the submitted paper version of this chapter.

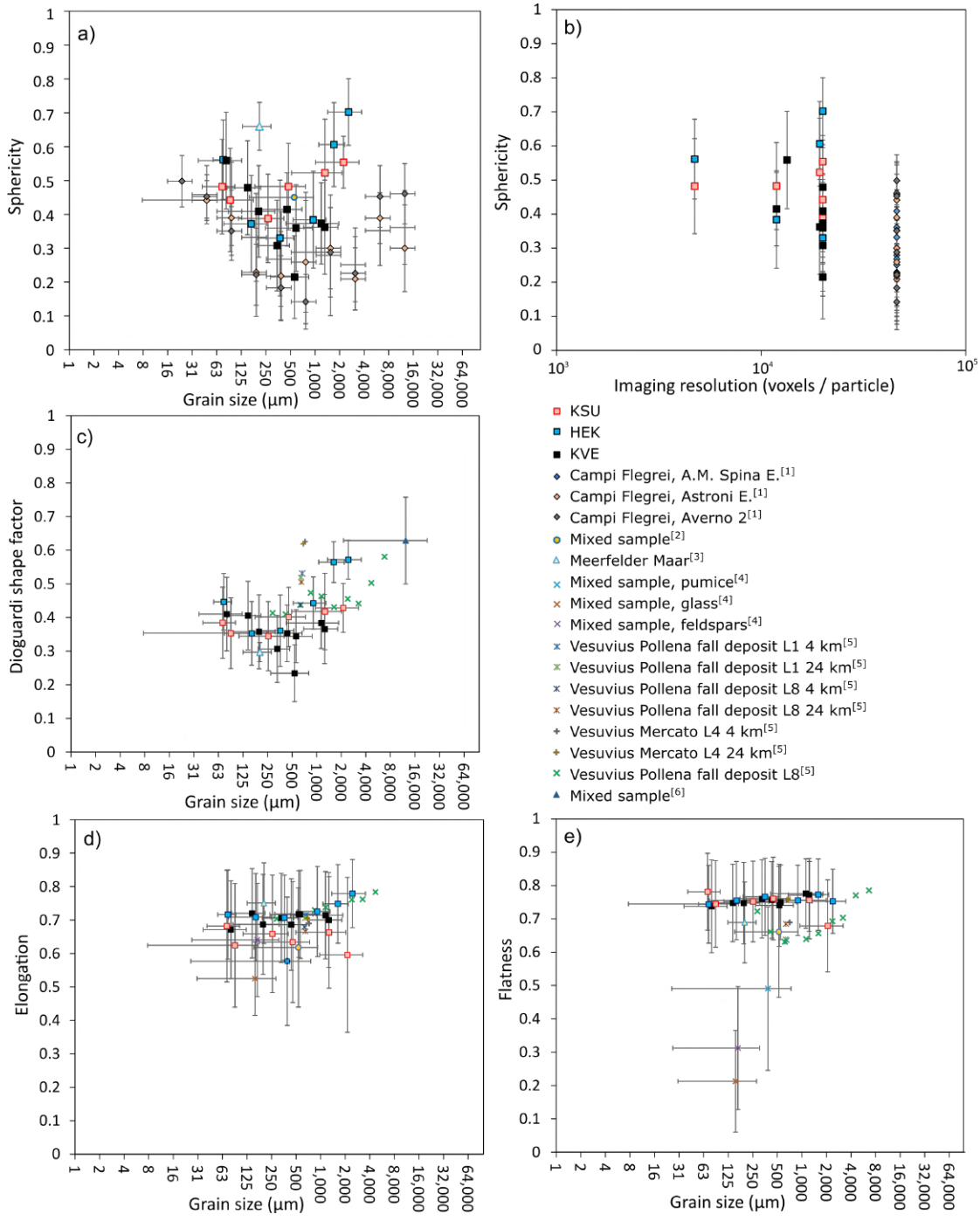

Figure 4.7: Shape measurements of volcanic ash particles from published literature: a-b) sphericity ψ_G (Ganser, 1993), c) shape factor Ψ_D (Dioguardi et al., 2018), d) elongation e and e) flatness f (Bagheri and Bonadonna, 2016b). X-axis error bars indicate the grain size range, with points plotted at the middle of the range; Y-axis error bars show one standard deviation of shape for each sample, with points indicating mean shape. Data sources: [1]Mele and Dioguardi (2018); [2]Bagheri et al. (2015); [3]Vonlanthen et al. (2015); [4]Wilson and Huang (1979); [5]Mele et al. (2011); [6]Dioguardi et al. (2018).

Figure 4.7a shows that ψ_G ranges from $\sim$ 0.1 to 0.8 for particles between 10^1 and 10^4 μm. Where multiple size fractions of the same sample are measured, the relationship between ψ_G and grain size is similar to samples from this study. Particles at the extremes of the size range are more spherical, with a pronounced low in sphericity occurring between 10^2 and 10^3 μm. A similar pattern can be observed for the Dioguardi et al. (2018) shape factor Ψ_D (Figure 4.7c). There is less variation in flatness; most samples have f between 0.5 and 0.9, using the ranges given by one standard deviation for all samples. The samples of Wilson and Huang (1979) are an exception, with mean flatness between 0.2 and 0.5. Mean elongation for all samples ranges between 0.4 and 0.9. The KSU data are more elongated (smaller e) than most other samples from the literature, as expected from visual inspection of the samples, which contain characteristic tube pumice 'needles'. However, neither the KSU or KVE samples, which were chosen for this study because of extreme ash shapes (elongated and flat, respectively) differ greatly from the other ash shape data in any mean shape factor.

4.6 Discussion

4.6.1 Measuring shape

X-ray CT is an accurate and efficient method of assessing particle size and shape in 3D, and allows imaging of hundreds of particles, and multiple shape factors, relatively rapidly. The analytic error resulting from manual selection of greyscale values is low (< 4 % on ψ_G, which is insignificant compared to its sensitivity to image resolution; and < 6 % on d_v). The high resolution makes it an invaluable tool for examining detailed structures in volcanic rocks. For shape quantification, however, high resolution surface area measurements result in very low ψ_G and therefore underestimate terminal velocity by the drag law of Ganser (1993). We recommend using a resolution between 10^2 and 10^5 voxels/particle to calculate ψ_G. The best agreement between $w_{t,\ rec}$ and $w_{t,\ Ganser}$ is reached at a range of image resolutions, which vary from particle to particle; we suggest this is due to the range of particle shapes as well as uncertainty on other parameters such as density, d_v, particle position in the settling column and the variability in $w_{t,\ rec}$ resulting from changing particle orientation (e.g., Saxby et al., 2018). Using shape parameters based on principal axis lengths is a more robust technique where imaging resolution cannot be kept constant. We conclude that above our lower resolution limit of $\sim 10^2$ voxels / particle, imaging resolution is not a concern for calculation of these shape descriptors, meaning that for calculation of e, f or Ψ_D it is practical to sacrifice higher resolution in favour of speed. As shape parameters based on axis lengths are more robust, we assess the accuracy of the Ganser (1993) drag law when

using the approximate sphericity of a smooth ellipsoid with equivalent axes to the particle (ψ_e; Equation 4.5) in place of a surface area based formula (ψ_G; Equation 4.2). Calculated velocities are accurate for the particles in this study (Figure 4.8), with MAPE of 23% (where MAPE is calculated by: $\frac{100\%}{n}\sum_1^n|\frac{w_{t,rec}-w_{t,Ganser}}{w_{t,Ganser}}|$) compared to MAPE of between 19% and 69% depending on image resolution for the surface area formulation. Therefore, it is valid to use the Ganser (1993) drag law with ψ_e in place of ψ_G for rough particles.

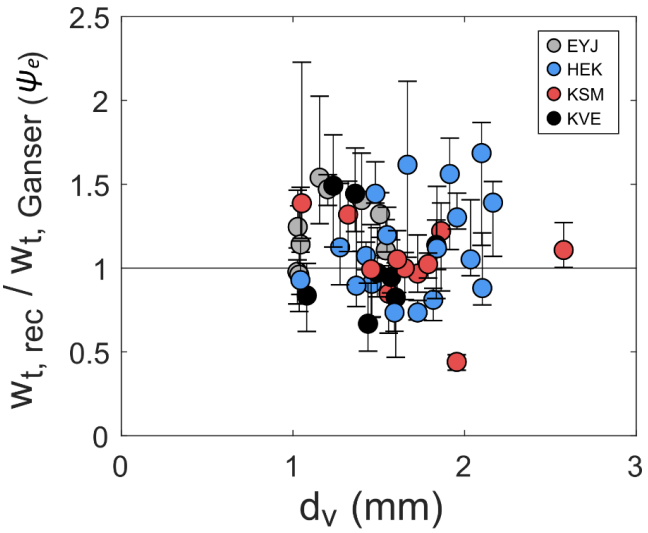

Figure 4.8: Measured velocity ($w_{t,\,rec}$) divided by velocity calculated according to the drag law of Ganser (1993) as a function of approximate sphericity ψ_e.

4.6.2 The shape range of volcanic ash

Particle sphericity ψ_G and shape factor Ψ_D are size-dependent: in our samples, and others from the published literature, particles of $\sim$ 250 to 500 µm have the lowest shape factors (i.e. are the most extreme-shaped). Although ψ_G is sensitive to image resolution, a similar trend seen in values of Ψ_D, which is insensitive to image resolution, suggests that it is not an artefact of CT scan parameters. A likely explanation for this pattern is that bubble size influences fragmentation (Liu et al., 2017). This means that bubble size distributions in volcanic ash particles often follow a similar trend, with modal values in the size range between 100 and 1000 µm (Rust and Cashman, 2011). Bubbles, along with crystals, control the surface irregularities of volcanic ash particles, meaning that similarity between the particle size and the bubble or crystal size can produce highly irregular particle surfaces. A recent X-ray CT study of volcanic ash particles (Mele and Dioguardi, 2018) found that surface irregularity increased as the particle size neared the bubble size; although we do not carry out bubble size analysis in this study, the similarity between our data and theirs (Figure 4.7) suggests bubble size could similarly be a primary control on shape for

our samples. Shape factors based on principal axis lengths (elongation e and flatness f) do not change significantly with particle size or between eruptions (Figures 4.6 and 4.7). The exceptions are three samples measured by Wilson and Huang (1979), with mean f as low as 0.2, whereas most other data are in the range 0.6 – 0.8 (Figure 4.7e). This may be partly because they separate the ash into components, with the lowest f from a sample of purely glass shards, whereas most of the other studies listed use bulk samples. Glass shards form from bubble wall fragments, and typically have a characteristic flat morphology. We do not include the Wilson and Huang (1979) data when assessing a default range of f to use in dispersion modelling; however, we note that some components of a volcanic ash sample can have much more 'extreme' shapes than the bulk. Our samples were chosen for their unusual shaped grains in order to provide a broad spectrum of ash shapes. Samples selected for the presence of 'extreme' shaped grains (KSU, KVE) do in fact contain a higher proportion of particles with shape descriptors < 0.5 (more extreme shapes) than the HEK sample (Figure 4.6). However, despite the presence of unusually shaped grains which give the samples a distinctive appearance under the optical microscope, mean shape values do not differ significantly from ash samples in other studies (Figure 4.7). This suggests that the range of values we observe for e, f, ψ_G and Ψ_D are valid as 'average' values for modelling purposes even for eruptions which produce unusual ash shapes.

4.6.3 Using shape in dispersion models

The drag laws of Ganser (1993), Bagheri and Bonadonna (2016b) and Dioguardi et al. (2018) produce reasonable estimates of terminal velocity for volcanic ash particles in the range 1.0 – 2.6 mm. The schemes are all valid for a wide range of flow regimes, and the Ganser (1993) and Bagheri and Bonadonna (2016b) drag laws are accurate for low-*Re* analogue particles (equivalent to volcanic ash from 1 μm to 1 mm in diameter; Saxby et al. (2018)). All are therefore suitable for use in atmospheric dispersion models used to produce operational forecasts of distal volcanic ash dispersion, which are usually initiated using a range of particle size classes. Of the three drag laws, the one chosen for inclusion in a dispersion model will most likely depend on the shape data available, as they are functions of different geometric shape descriptors. Although the Ganser (1993) law produces the lowest average error on w_t for our dataset (19%), it requires very specific conditions for surface area measurement, and we consider the Dioguardi et al. (2018) law equally accurate given its similar error on w_t (22%). In addition, if we calculate the Dioguardi et al. (2018) shape descriptor Ψ_D using the approximation given in Equation 4.7, it is solely a function of the three principal axis lengths of a particle and so results are independent of imaging resolution for the range investigated. The Bagheri and Bonadonna (2016b) drag law produces a similar error (24%) for the data in this study; it uses the shape descriptors e and f, which vary less between eruptions

and size classes than the shape descriptors of Ganser (1993) and Dioguardi et al. (2018). Therefore, we recommend the use of the Bagheri and Bonadonna (2016b) law where the shape of the ash is unknown, and it is convenient to assume a constant shape value across all size fractions of the PSD. It is important to note that benchtop X-ray CT cannot be used to accurately quantify the shape of the smallest diameter volcanic ash fractions relevant to aircraft hazard ($<$ 30 to 60 μm; Rose and Durant (2009) or respiratory health ($<$ 4 to 10 μm; Horwell et al. (2010)), due to constraints on imaging resolution. In our system the minimum voxel size is $\sim$ 3 μm, although synchrotron X-ray CT systems can achieve resolutions of 1 μm or less. Therefore, X-ray CT cannot give a full grain shape distribution for the range of sizes typically used to initiate dispersion models ($\sim$ 0.1 – 100 μm; Hort (2016)); this is especially pertinent for those shape descriptors which show a trend with grain size (sphericity ψ_G and shape factor Ψ_D). However, the terminal velocity of very small particles ($< \sim$ 30 μm) is low compared to atmospheric turbulence and vertical advection (Saxby et al., 2018), meaning that the dispersion of these particles (Class III fragments in the classification of Koyaguchi and Ohno (2001)) is insensitive to shape. It is therefore reasonable to apply the same shape factors for particles smaller than $\sim$ 30 μm despite the lack of available measurements.

The problem of parameterising shape in dispersion models is relevant for modelling the transport of other atmospheric particulates. One of the most abundant aerosol species is desert dust, which is non-spherical with a correlation between size and shape (Chou et al., 2008). The atmospheric dispersion of embers from wildfires is also sensitive to the shape of the model particles (Anthenien et al., 2006). Pollen and spores are mostly sub-spherical (Jarosz et al., 2004); Aylor (2002) found that it was reasonable to model corn pollen of 76 – 106 μm as spheres, although Schwendemann et al. (2007) found that the velocity of some spores is sensitive to surface area, warranting an investigation of the effects of roughness on dispersion. In a nuclear fallout event, a significant fraction of radionuclides could be associated with soil particles of tens to hundreds of microns in diameter, which are usually assumed to be spherical for modelling purposes (e.g., Rolph et al., 2014), but given their large size, we suggest that an investigation into particle shape is warranted. X-ray CT could be a useful tool in these applications. We have not found comparable work on non-volcanic atmospheric particulates, although X-ray tomography has been used to examine the internal structure of nuclear ejecta (Martin et al., 2019) and to quantify the shape of foraminifera specimens (Speijer et al., 2008; Jorry et al., 2006) in order to investigate intraspecific shape variations and transport mechanisms in water. Given the high porosity of test walls (Jorry et al., 2006), however, we suggest that caution should be taken when interpreting surface area measurements.

For volcanic ash we found that an imaging resolution of 10^2 - 10^5 voxels per particle is required for determining surface-area-dependent shape parameters for accurate drag calculation. This range

Table 4.4: Recommended shape descriptors to be used with shape-dependent drag laws in volcanic ash dispersion models in the absence of particle shape data for the eruption being modelled.

Drag law	Shape descriptor	Particle size fraction	Shape range
Ganser (1993)	ψ_G	$< 10^2$ µm	0.3 – 0.8
		10^2 µm – 10^4 µm	0.1 – 0.8
Bagheri and Bonadonna (2016b)	e and f	$< 10^4$ µm	e: 0.4 – 0.9
			f: 0.6 – 0.9
Dioguardi et al. (2018)	Ψ_D	$< 10^2$ µm	0.2 – 0.5
		10^2 µm – 10^4 µm	0.1 – 0.7

may extend to higher resolutions if particles are smoother.

4.7 Recommendations for including ash shape in dispersion models

Based on the above work we present a table of default shapes to be used with shape-dependent drag laws for modelling atmospheric ash concentrations where shape data are unavailable (Table 4.4). The shape ranges given are based on the mean and standard deviation of shape for the volcanic ash samples shown in Figure 4.7. Bagheri and Bonadonna (2016a) give the extremes of a shape range for volcanic ash: f = 0.07 – 1.0 and e = 0.24 – 1.0. Although we do not consider the full shape ranges, minimum shape in a sample will have an impact on the maximum travel distance of the ash particles (for a given size), as less spherical particles fall slower and therefore travel further. This means that even though the bulk of a size fraction may be deposited within a certain distance from source, a small proportion of extreme-shaped particles of the same size could travel much further. In the case of very far-travelled ash, including tephra preserved as non-visible horizons in sediment sequences (cryptotephra), the presence of unusual shapes can allow ash grains to travel significantly further than spherical equivalents. This partly explains a discrepancy between the measured and modelled travel distance of cryptotephra grains (Saxby et al., in revision; Chapter 3 of this thesis).

Chapter 5

Conclusions

5.1 Research aims

In this section, I return to the original research questions posed in the introduction and assess them given the data collected during the course of this PhD work.

5.1.1 What is the shape range of volcanic ash?

The shape range of volcanic ash primarily depends on the measurement technique used: 2D measurements are not a good approximation of 3D shape parameters (Chapter 2), and different parameters give very different values for the same particle. In addition, there can be a large range of shapes within a single sample or size fraction. For all the 3D shape descriptors we measure in Chapter 4, particles have a shape range from very close to zero, to very close to 1 (where 1 = an equant particle). Assigning default shape values for the purpose of producing ash concentration forecasts requires an assessment of average particle shape; ranges based on the mean shape of ash samples are given in Table 4.4. Even only considering mean shape, the ranges we give are broad, reflecting significant differences in mean shape between eruptions. The shape descriptors ψ_G and Ψ_D are size-dependent, whereas e and f do not show a trend with size for the volcanic ash size range we consider (10^1 – 10^4 μm).

Some samples were chosen due to the presence of extreme-shaped grains on initial visual inspection; the Katla SILK samples contain very elongated tube pumice fragments while the Vedde sample contains abundant flat, platy shards. Although particle shape varies between eruptions, these samples did not have a very different mean shape to the other samples studied.

In addition to eruptions producing different shapes, sorting by shape can occur during atmospheric transport, as very non-spherical particles fall slower and therefore can travel further. This means that a sample of very distal ash may contain less spherical particles than a proximal sample, as in the case of the Vedde ash (Chapter 3). In addition to sorting by atmospheric processes, it is important to recognise that ash shape may be modified during or after deposition, by breakage of particles upon landing or during reworking; or sorting by shape caused by fluvial or aeolian processes.

5.1.2 How well can current drag laws account for the aerodynamic behaviour of very non-spherical ash?

Both non-spherical analogue particles (Chapter 2) and volcanic ash particles (Chapter 4) fall slower than spheres of equivalent volume and density, as calculated by a drag law for spherical particles (White, 1974). In both cases, their aerodynamic behaviour is better accounted for by drag laws for non-spheres, as long as the laws are used with the correct shape parameters and within their range of applicability in terms of flow regime. The latter two caveats cannot be dismissed, as drag laws for non-spheres can perform worse than spherical assumptions if this advice is not followed. For example, the drag law of Wilson and Huang (1979) is a fully empirical correlation based on experiments with a Re range of $0.54 < Re < 79.1$, and a shape range of $F = 0.13$ to 0.86; extrapolating the law outside these ranges results in large errors on terminal velocity ($> 500\%$ for an elongate analogue particle with F of 0.06 at very low Re; Figure 2.5). The Ganser (1993) drag law uses the shape descriptor sphericity, a function of 3D surface area; in Chapter 2 I show that it gives worse results when a 2D approximation of sphericity is used, and in Chapter 4 I show that the results are highly sensitive to the imaging resolution used to calculate surface area when measuring shape in 3D. In Chapter 3, I show that there are multiple methods of measuring size and it is important to ensure consistency here in addition to measuring shape using the same parameters by which the drag law is calibrated

The drag laws I recommend for modelling the transport of non-spherical volcanic ash (Ganser, 1993; Bagheri and Bonadonna, 2016b; Dioguardi et al., 2018) are semi-empirical schemes which are valid for the whole Re range of volcanic ash falling in air and are calibrated using a wide range of particle shapes; they all perform better than a spherical approximation for velocity datasets used in this thesis, with mean absolute percentage errors on the order of 20% of terminal velocity.

5.1.3 How sensitive are ash concentration forecasts to particle shape?

The sensitivity of ash concentration forecasts to particle shape depends on several factors, including the size of the particles. Modelled volcanic ash total column mass loadings using the Hobbs et al. (1991) particle size distribution (PSD), the default at the London VAAC, are not very sensitive to particle shape. In Chapter 2 I modelled an eruption of Katla, Iceland, using spherical particles and particles with sphericity = 0.5; spatial agreement between plume locations for the two model setups exceeded 85% for the first 36 h after the modelled eruption start, when the London VAAC default PSD based on Hobbs et al. (1991) was used. The agreement between spherical and non-spherical models is worse if using a coarser PSD, and modelled air concentrations for thin vertical layers are more sensitive to shape than total column mass loadings.

The London VAAC default PSD is enriched in fine grained particles compared to other total grain size distributions, particularly for basaltic explosive eruptions. Therefore, it is worth considering shape as a parameter in operational dispersion modelling setups to ensure accuracy in cases where it is necessary to model larger grains, such as when particle size data are available during an eruption which produces a higher mass fraction of coarse particles. In addition, the current London VAAC PSD only considers particles of up to 100 μm in diameter, as larger particles are assumed to deposit close to the source; however, if we consider non-sphericity it may be advisable to model larger particles as a default. The travel distance of particles $\geq$ 100 μm is highly sensitive to shape, and I show in Chapter 2 that non-spherical particles of 200 μm can travel $>$ 500 km from the source, meaning they are relevant to regional ash hazard forecasts. It is important to note that the London VAAC assumes that size = d_v, the diameter of a volume-equivalent sphere, and therefore the default PSD represents particles which can be $>$ 100 μm according to other methods of measuring size (e.g. long axis). If the London VAAC were to adjust the default PSD to include $\geq$ 100 μm particles, ash concentration forecasts would be more sensitive to particle shape than they currently are.

5.1.4 How should we parameterise particle shape in operational dispersion modelling systems?

There are several aspects of parameterising particle shape to take into account when considering adapting operational systems. The conclusions here are tailored to the London VAAC and the NAME model, but should provide advice which is relevant to other forecasters.

Drag law

The first consideration is the accuracy of the drag law used to calculate terminal velocity for the conditions expected for distal ash clouds (Reynolds number *Re* of about 10^{-9} to 10^{2} assuming particles of 0.1 – 100 μm, the current default particle size distribution modelled by the London VAAC in the absence of particle size information during an eruption). I identify three drag laws which give accurate predictions of the terminal velocity of non-spherical ash (Ganser, 1993; Bagheri and Bonadonna, 2016b; Dioguardi et al., 2018). The laws give similar results, but in a case where only one law was needed, I would recommend the Ganser (1993) law. The law is a semi-empirical correlation which gives a solution for drag coefficient and terminal velocity over the whole range of flow regimes expected for distal volcanic ash clouds. It also works well for mm-sized volcanic ash particles falling in air (Chapter 4), and analogues with $Re < 10^{3}$, equivalent to particles of $<$ 1 mm falling in air (Chapter 2), meaning it is also valid for coarser particle size distributions. The Ganser (1993) law has been proven to produce velocity estimates which are accurate to within $\sim$ 20% over this *Re* range by multiple authors; a figure which is low compared to reported errors arising from using a spherical assumption to model the sedimentation of non-spherical particles. In this thesis, I report that the Ganser (1993) scheme gives a mean absolute percentage error of 19% on terminal velocity of analogue flat plates, cubes and rods (Chapter 2) and between 19 and 23%, depending on the sphericity equation used, on the terminal velocity of mm-sized volcanic ash particles falling in air (Chapter 4). Chhabra et al. (1999) compiled a large database of velocity measurements of smooth and irregular analogue particles from the published literature, with *Re* spanning nine orders of magnitude, and found the Ganser (1993) scheme to be accurate to within 16%. Bagheri and Bonadonna (2016b) report a 20% error on particle drag coefficient from using the Ganser (1993) scheme to predict the velocity of a mixed particle set including volcanic ash and analogues. The wealth of literature evaluating the performance of the Ganser (1993) scheme gives it an advantage over more recently published schemes whose limitations might not be known.

Another consideration is the shape descriptor used to calibrate the drag law. The Ganser (1993) scheme calculates velocity using the shape factor sphericity, a function of particle volume and surface area. Sphericity is a widely measured property of volcanic ash particles, although care must be taken when making or interpreting sphericity measurements of volcanic ash as surface area of irregular particles is highly dependent on imaging resolution (Chapter 4). However, we can resolve this issue by using the Ganser (1993) scheme with sphericity calculated using surface area measurements from data within a limited resolution range, or with sphericity calculated by approximating the particle as a smooth ellipsoid (Equation 4.5).

Another point in favour of the Ganser (1993) scheme is that it is currently used by the Buenos Aires VAAC, which uses the Fall3D model (Folch et al., 2009; Reckziegel et al., 2016); it would therefore be a good choice for allowing comparison of outputs by different VAACs worldwide.

Default sphericity value

As physical particle properties are not often available during an eruption, it is important to be able to choose a default sphericity value. I would recommend using non-spherical particles as the default; even in the absence of shape data, we know that volcanic ash particles are not spheres. Given that shape-dependent drag laws are available, and have been proven to be more accurate than spherical schemes, it is more reasonable to use an approximate shape than it is to model particles as spheres.

I would recommend sphericity = 0.5 as a default value, and sphericity = 0.3 as an extreme value, assuming use of the Ganser (1993) drag law. Given the low sensitivity of volcanic ash concentration forecasts to particle shape, compared to other factors such as size and density (Beckett et al., 2015), it is reasonable to assume an average value of shape for all particles in an eruption. Given the difficulty in obtaining accurate sphericity measurements during an eruption, it is also reasonable to base that value on an average taken from the literature. The values I recommend here are taken from Chapter 4, using only studies which use data in a limited resolution range (10^2 to 10^5 voxels/particle), which we found to give values of sphericity which produce accurate estimates of terminal velocity. These values are valid for particles of $\leq$ 100 μm in diameter; there is no lower limit on diameter, even though the data do not include particles $<$10 μm, due to difficulty in measuring the shape of very fine grained particles. Particles $<$10 μm have terminal velocities that are low compared to atmospheric motions (advection and diffusion) and therefore, their transport is dominated by atmospheric processes rather than physical particle properties, and so the transport of particles $<$10 μm is insensitive to the choice of shape value.

5.2 Practical implications

The work presented in this thesis has several practical outcomes which have important implications for measuring particle shape and using it as an input parameter in dispersion modelling. In the following sections, I describe the main practical outcomes of this work.

5.2.1 Volcanic ash shape database

The accuracy of volcanic ash forecasts depends on the accuracy of the model physics, the accuracy of the driving meteorological data, and the input parameters used to initialise dispersion; however, for modelling particle shape, there are many drag laws available and often shape data suitable for use with those drag laws are scarce because there is no standard way of measuring shape. I measure particle shape for bulk samples of Icelandic volcanic ash, and reanalyse data from the published literature to build a database of average volcanic ash shape values that can be used with drag laws I identify as producing accurate results (Ganser, 1993; Bagheri and Bonadonna, 2016b; Dioguardi et al., 2018). The database is presented in Chapter 4. All individual measurements are available in supplementary material for the submitted paper version of that chapter; in Chapter 4 I present a table of recommended average shape values for use where no data are available. As physical particle properties are not often measured during eruptions for ash forecasting purposes, this adds to the data available for use in the absence of measurements.

5.2.2 Changes to the London VAAC operational setup

Throughout the writing of this thesis, I have been involved in discussions with the Atmospheric Dispersion and Air Quality (ADAQ) group at the Met Office, UK, about parameterising particle shape in the London VAAC operational setup. While shape-dependent drag laws are already available in the NAME model, and have been used for research purposes, forecasters at the London VAAC do not have the option to use them operationally. Therefore, the ADAQ group is currently working on changes to the operational interface to incorporate particle shape as an operational parameter.

5.2.3 NAME on JASMIN User Guide

For the work in this thesis which used the NAME atmospheric dispersion model, I carried out the model runs on the JASMIN scientific analysis server (Lawrence et al., 2013) using a Windows PC and connecting to the server remotely via the utilities PuTTY and WinSCP. I put together an instruction manual as a quick start guide for Windows users wanting to run NAME on JASMIN. It includes instructions on how to apply for the necessary accounts, how to access all the data needed for an example NAME run, using one of my input files (a volcanic ash dispersion run for Katla volcano in Iceland), and how to plot the results. The User Guide is available on the Met Office Science Repository Service (MOSRS) and has been used as a quick start guide by students both at

the University of Bristol and elsewhere. I include the guide in this thesis as Appendix D.

5.3 Future directions

During the course of this project, I encountered several potentially interesting research questions which warrant further investigation. These are detailed in the sections below.

5.3.1 Modelling high plumes using the London VAAC operational setup

When modelling the 12.1 ka Vedde eruption of Katla volcano, Iceland (Chapter 3), I used 35 km as an upper bound on the plume height. However, Unified Model meteorological data set up for NAME only extend to the first 59 pressure levels ($\sim$ 29 km). This is the same number of levels used for operational London VAAC volcanic ash forecasts. Based only on recent eruptions, plume heights for explosive Icelandic eruptions range from $\sim$ 10-20 km (Mastin et al., 2009; Leadbetter and Hort, 2011); however, the 1362 eruption of Öræfajökull and the 1875 eruption of Askja are both estimated to have had plume heights of up to 34 km (Carey et al., 2010; Sharma et al., 2008), raising the possibility that the London VAAC may benefit from the capability to model plumes $>$ 29 km. For the VAAC to extend its met data to higher altitudes requires analysis of the computational cost of forecasts using greater volumes of met data, and model sensitivity analysis to determine the impact of the use of these data on ash forecasts.

5.3.2 The origin of the Katla SILK 'needles'

The SILK (silicic Katla) tephra is a series of distinctive light-coloured Holocene ash layers produced by large silicic eruptions of Katla volcano in Iceland. At least 12 SILK tephra units were erupted between ca. 6600 and 1675 years BP, with volumes ranging from 0.05 to 0.3 km^3 (Larsen et al., 2001). Within the SILK tephra are three distinctive horizons known as the 'needle layers', for their very distinctive fibrous grains, which in this thesis are referred to as SILK-LN (lower needle layer), SILK-MN (middle needle layer) and SILK-UN (upper needle layer) after Larsen et al. (2001). I used the samples of SILK tephra, collected during a field campaign in Iceland, as an example of 'extreme' shaped volcanic ash; shape distributions are given in Chapters 2 and 4. Questions remain concerning the origin of elongated fragments of tube pumice in the SILK tephra. Bubble textures in the pumice fragments could be analysed to indicate shear and

strain during fragmentation (Rust et al., 2003), in order to shed light on fragmentation processes during eruption.

5.3.3 Further shape data collection

As shape data collection methods become more efficient, and volcanic ash dispersion models become more sophisticated, there is likely to be a growing database of volcanic ash shapes available, and more of a demand to use them operationally. A useful exercise would be to examine the shape of ash from different regions and types of eruption, to determine whether there are any large-scale trends in shape. Forecasts could then progress from using one default shape value for all eruptions, to using a different shape value or range of values given information on the type of eruption (e.g. composition, phreatomagmatic versus magmatic) and the volcanic setting.

5.3.4 Settling of volcanic ash aggregates

The work presented here is focused on ash falling as single particles, and does not consider changes in shape, size and density of tephra particles due to the formation of aggregates (Brown et al., 2012). Aggregates often appear roughly spherical in form but can be have high surface roughness and be porous (Lane et al., 1993), qualities which act to increase drag. Therefore, the results presented here may also have implications for modelling the settling velocity of aggregates; a beneficial next stage would be to measure aggregate shape and conduct experiments on aggregate settling velocity. Porous objects permit the flow of fluid inside the object as well as around it, meaning that drag equations calibrated using solid particles can perform poorly for hollow objects or clusters (Lasso and Weidman, 1986; Chhabra et al., 1999). This means that drag equations identified here as being accurate for the settling of individual grains should also be evaluated against the measured settling velocity of volcanic ash aggregates.

References

Achenbach, E., 1974. The effects of surface roughness and tunnel blockage on the flow past spheres. Journal of Fluid Mechanics 65 (1), 113–125.

Alfano, F., Bonadonna, C., Delmelle, P., Costantini, L., 2011. Insights on tephra settling velocity from morphological observations. Journal of Volcanology and Geothermal Research 208, 86–98.

Anthenien, R. A., Tse, S. D., Carlos Fernandez-Pello, A., 7 2006. On the trajectories of embers initially elevated or lofted by small scale ground fire plumes in high winds. Fire Safety Journal 41 (5), 349–363.

Arason, P., Petersen, G. N., Bjornsson, H., 2011. Observations of the altitude of the volcanic plume during the eruption of Eyjafjallajökull, April-May 2010. Earth System Science Data 3, 9–17.

Aylor, D. E., 11 2002. Settling speed of corn (Zea mays) pollen. Journal of Aerosol Science 33 (11), 1601–1607.

Bagheri, G., Bonadonna, C., 1 2016a. Aerodynamics of Volcanic Particles: Characterization of Size, Shape, and Settling Velocity. Volcanic Ash, 39–52.

Bagheri, G., Bonadonna, C., 2016b. On the drag of freely falling non-spherical particles. Powder Technology 301, 526–544.

Bagheri, G., Rossi, E., Biass, S., Bonadonna, C., 11 2016. Timing and nature of volcanic particle clusters based on field and numerical investigations. Journal of Volcanology and Geothermal Research 327, 520–530.

Bagheri, G. H., Bonadonna, C., Manzella, I., Vonlanthen, P., 2015. On the characterization of size and shape of irregular particles. Powder Technology 270, 141–153.

Beckett, F. M., Kylling, A., Sigurardóttir, G., Von Löwis, S., Witham, C. S., 2017. Quantifying the mass loading of particles in an ash cloud remobilized from tephra deposits on Iceland. Atmospheric Chemistry and Physics 17, 4401–4418.

Beckett, F. M., Witham, C. S., Hort, M. C., Stevenson, J. A., Bonadonna, C., Millington, S. C., 2014. The sensitivity of NAME forecasts of the transport of volcanic ash clouds to the physical characteristics assigned to the particles. Tech. rep., Met Office, UK.

Beckett, F. M., Witham, C. S., Hort, M. C., Stevenson, J. A., Bonadonna, C., Millington, S. C., 2015. Sensitivity of dispersion model forecasts of volcanic ash to the physical characteristics of the particles. Journal of Geophysical Research.

Biass, S., Scaini, C., Bonadonna, C., Folch, A., Smith, K., Höskuldsson, A., 2014. A multi-scale risk assessment for tephra fallout and airborne concentration from multiple Icelandic volcanoes - Part 1: Hazard assessment. Natural

Hazards and Earth System Sciences Discussions 14 (8), 2265–2287.

Blockley, S. P., Lane, C. S., Lotter, A. F., Pollard, A. M., 2007. Evidence for the presence of the Vedde Ash in Central Europe. Quaternary Science Reviews 26, 3030–3036.

Blockley, S. P., Pyne-O'Donnell, S. D., Lowe, J. J., Matthews, I. P., Stone, A., Pollard, A. M., Turney, C. S., Molyneux, E. G., 2005. A new and less destructive laboratory procedure for the physical separation of distal glass tephra shards from sediments. Quaternary Science Reviews 24, 1952–1960.

Bonadonna, C., Genco, R., Gouhier, M., Pistolesi, M., Cioni, R., Alfano, F., Hoskuldsson, A., Ripepe, M., 2011. Tephra sedimentation during the 2010 Eyjafjallajökull eruption (Iceland) from deposit, radar, and satellite observations. Journal of Geophysical Research: Solid Earth 116.

Bonadonna, C., Phillips, J. C., 2003. Sedimentation from strong volcanic plumes. Journal of Geophysical Research: Solid Earth 108 (B7).

Bonadonna, C.; Scolllo, S. C. R. P. L. &. P. M., 2006. Determination of the largest clasts of tephra deposits for the characterization of explosive volcanic eruptions: IAVCEI Commission on Tephra Hazard Modelling. Tech. rep., IAVCEI.

Brenner, H., 1962. Effect of finite boundaries on the Stokes resistance of an arbitrary particle. Journal of Fluid Mechanics 12 (1), 35–48.

Brown, R., Bonadonna, C., Durant, A., 2012. A review of volcanic ash aggregation. Physics and Chemistry of the Earth, Parts A/B/C 45, 65–78.

Buckland, H. M., Eychenne, J., Rust, A. C., Cashman, K. V., 1 2018. Relating the physical properties of volcanic rocks to the characteristics of ash generated by experimental abrasion. Journal of Volcanology and Geothermal Research 349, 335–350.

Budd, L., Griggs, S., Howarth, D., Ison, S., 2011. A fiasco of volcanic proportions? Eyjafjallajökull and the closure of European airspace. Mobilities 6 (1), 31–40.

Burden, R. E., Phillips, J. C., Hincks, T. K., 2011. Estimating volcanic plume heights from depositional clast size. Journal of Geophysical Research: Solid Earth 116.

Carey, R. J., Houghton, B. F., Thordarson, T., 2010. Tephra dispersal and eruption dynamics of wet and dry phases of the 1875 eruption of Askja Volcano. Bulletin of Volcanology 72 (3), 259–278.

Carey, S., Sparks, R. S., 1986. Quantitative models of the fallout and dispersal of tephra from volcanic eruption columns. Bulletin of Volcanology 48, 109–125.

Cashman, K., Rust, A., 1 2016. Introduction. In: Volcanic Ash Hazard Observation. Elsevier, pp. 5–22.

Cheng, N.-S., 2008. Formula for the Viscosity of a Glycerol-Water Mixture. Industrial & Engineering Chemistry Research 47 (9), 3285–3288.

Chhabra, R. P., 1995. Wall effects on free-settling velocity of non-spherical particles in viscous media in cylindrical tubes. Powder Technology 85, 83–90.

Chhabra, R. P., Agarwal, L., Sinha, N. K., 1999. Drag on non-spherical particles: An evaluation of available methods. Powder Technology 101, 288–295.

Chhabra, R. P., Uhlherr, P. H. T., Richardson, J. F., 1996. Some further observations on the hindered settling velocity of spheres in the inertial flow regime. Chemical Engineering Science 51 (19), 4531–4532.

Chou, C., Formenti, P., Maille, M., Ausset, P., Helas, G., Harrison, M., Osborne, S., 12 2008. Size distribution, shape, and composition of mineral dust aerosols collected during the African Monsoon Multidisciplinary Analysis Special Observation Period 0: Dust and Biomass-Burning Experiment field campaign in Niger, January 2006. Journal of Geophysical Research: Atmospheres 113 (D23).

Chow, A. C., Adams, E. E., 11 2011. Prediction of Drag Coefficient and Secondary Motion of Free-Falling Rigid Cylindrical Particles with and without Curvature at Moderate Reynolds Number. Journal of Hydraulic Engineering 137 (11), 1406–1414.

Christiansen, E. B., Barker, D. H., 1965. The effect of shape and density on the free settling of particles at high Reynolds numbers. AIChE Journal 11 (1), 145–151.

Clarkson, R. J., Majewicz, E. J., Mack, P., 2016. A re-evaluation of the 2010 quantitative understanding of the effects volcanic ash has on gas turbine engines. Journal of Aerospace Engineering 230 (12), 2274–2291.

Clift, R., Gauvin, W. H., 1971. Motion of entrained particles in gas streams. The Canadian Journal of Chemical Engineering 49, 439–448.

Clift, R., Grace, J., Weber, M., 2005. Bubbles, drops, and particles. Courier Corporation.

Costa, A., Folch, A., Macedonio, G., Giaccio, B., Isaia, R., Smith, V. C., 2012. Quantifying volcanic ash dispersal and impact of the Campanian Ignimbrite super-eruption. Geophysical Research Letters 39 (10), 3–7.

Costa, A., Macedonio, G., Folch, A., 2006. A three-dimensional Eulerian model for transport and deposition of volcanic ashes. Earth and Planetary Science Letters 241, 634–647.

Cronin, S. J., Hedley, M. J., Neall, V. E., Smith, R. G., 4 1998. Agronomic impact of tephra fallout from the 1995 and 1996 Ruapehu Volcano eruptions, New Zealand. Environmental Geology 34 (1), 21–30.

Cullen, M. J. P., 1993. The unified forecast/climate model. Meteorological Magazine 122(1449), 81–94.

Dacre, H. F., Grant, A. L. M., Johnson, B. T., 2013. Aircraft observations and model simulations of concentration and particle size distribution in the Eyjafjallajökull volcanic ash cloud. Atmospheric Chemistry and Physics 13, 1277–1291.

D'Amours, R., Malo, A., Servranckx, R., Bensimon, D., Trudel, S., Gauthier-Bilodeau, J.-P., 2010. Application of the atmospheric Lagrangian particle dispersion model MLDP0 to the 2008 eruptions of Okmok and Kasatochi volcanoes. Journal of Geophysical Research Atmospheres 115.

Davies, S. M., 2015. Cryptotephras: The revolution in correlation and precision dating. Journal of Quaternary Science 30 (2), 114–130.

Dellino, P., Mele, D., Bonasia, R., Braia, G., La Volpe, L., Sulpizio, R., 2005. The analysis of the influence of pumice shape on its terminal velocity. Geophysical Research Letters 32.

Devenish, B. J., Thomson, D. J., Marenco, F., Leadbetter, S. J., Ricketts, H., Dacre, H. F., 2012. A study of the arrival over the United Kingdom in April 2010 of the Eyjafjallajökull ash cloud using ground-based lidar and numerical simulations. Atmospheric Environment 48, 152–164.

Di Felice, R., Gibilaro, L., Foscolo, P., 1995. On the hindered settling velocity of spheres in the inertial flow regime. Chemical Engineering Science 50 (18), 3005–3006.

Dietrich, W. E., 1982. Settling velocity of natural particles. Water Resources Research 18 (6), 1615–1626.

Dioguardi, F., Mele, D., Dellino, P., 2018. A new one-equation model of fluid drag for irregularly shaped particles valid over a wide range of Reynolds number: Aerodynamic drag of irregular particles. Journal of Geophysical Research: Solid Earth 123, 144–156.

Dioguardi, F., Mele, D., Dellino, P., Dürig, T., 2017. The terminal velocity of volcanic particles with shape obtained from 3D X-ray microtomography. Journal of Volcanology and Geothermal Research 329, 41–53.

Draxler, R. R., Hess, G. D., 1997. NOAA Technical Memorandum ERL ARL-224: Description of the HYSPLIT_4 Modelling System. Tech. rep., NOAA, Maryland.

Dufek, J., Manga, M., 2008. In situ production of ash in pyroclastic flows. Journal of Geophysical Research: Solid Earth 113.

Dugmore, A., 1989. Icelandic volcanic ash in Scotland. Scottish Geographical Magazine 105 (3), 168–172.

Dunbar, N. W., Iverson, N. A., Van Eaton, A. R., Sigl, M., Alloway, B. V., Kurbatov, A. V., Mastin, L. G., McConnell, J. R., Wilson, C. J. N., 2017. New Zealand supereruption provides time marker for the Last Glacial Maximum in Antarctica. Scientific Reports 7 (1), 12238.

Durant, A. J., Bonadonna, C., Horwell, C. J., 2010. Atmospheric and environmental impact of volcanic particulates. Elements 6, 235–240.

Elíasson, J., 2014. Katla volcano in Iceland, potential hazards and risk assessment. Natural Science 6 (3), 99–107.

Ersoy, O., Şen, E., Aydar, E., Tatar, I., Çelik, H. H., 2010. Surface area and volume measurements of volcanic ash particles using micro-computed tomography (micro-CT): A comparison with scanning electron microscope (SEM) stereoscopic imaging and geometric considerations. Journal of Volcanology and Geothermal Research 196, 281–286.

Folch, A., 2012. A review of tephra transport and dispersal models: Evolution, current status, and future perspectives. Journal of Volcanology and Geothermal Research 235-236, 96–115.

Folch, A., Costa, A., Macedonio, G., 2009. FALL3D: A computational model for transport and deposition of volcanic ash. Computers and Geosciences 35, 1334–1342.

Francis, P. N., Cooke, M. C., Saunders, R. W., 2012. Retrieval of physical properties of volcanic ash using Meteosat: A case study from the 2010 Eyjafjallajökull eruption. Journal of Geophysical Research: Atmospheres Atmospheres 117.

Gangale, G., Prata, A. J., Clarisse, L., 2010. The infrared spectral signature of volcanic ash determined from high-spectral resolution satellite measurements. Remote Sensing of Environment 114, 414–425.

Ganser, G. H., 1993. A rational approach to drag prediction of spherical and nonspherical particles. Powder Technology 77, 143–152.

Garboczi, E. J., Riding, K. A., Mirzahosseini, M., 2017. Particle shape effects on particle size measurement for crushed waste glass. Advanced Powder Technology 28, 648–657.

Giehl, C., Brooker, R. A., Marxer, H., Nowak, M., 2017. An experimental simulation of volcanic ash deposition in gas turbines and implications for jet engine safety. Chemical Geology 461, 160–170.

Gislason, S. R., Hassenkam, T., Nedel, S., Bovet, N., Eiriksdottir, E. S., Alfredsson, H. A., Hem, C. P., Balogh, Z. I., Dideriksen, K., Oskarsson, N., Sigfusson, B., Larsen, G., Stipp, S. L. S., 2011. Characterization of Eyjafjallajökull volcanic ash particles and a protocol for rapid risk assessment. Proceedings of the National Academy of Sciences 108 (18), 7307–7312.

Gooding, J. L., Clanton, U. S., Gabel, E. M., Warren, J. L., 11 1983. El Chichon volcanic ash in the stratosphere: Particle abundances and size distributions after the 1982 eruption. Geophysical Research Letters 10 (11), 1033–1036.

Grant, A. L., Dacre, H. F., Thomson, D. J., Marenco, F., 2012. Horizontal and vertical structure of the Eyjafjallajökull ash cloud over the UK: A comparison of airborne lidar observations and simulations. Atmospheric Chemistry and Physics 12, 10145–10159.

Guffanti, M., Casadevall, T. J., Budding, K., 2010. USGS Data Series 545: Encounters of Aircraft with Volcanic Ash Clouds: A Compilation of Known Incidents, 1953–2009. Tech. rep., USGS.

Haflidason, H., Regnéll, C., Pyne-O'Donnell, S., Svendsen, J. I., 2018. Extending the known distribution of the Vedde Ash into Siberia: occurrence in lake sediments from the Timan Ridge and the Ural Mountains, northern Russia. Boreas.

Haider, A., Levenspiel, O., 1989. Drag coefficient and terminal velocity of spherical and non-spherical particles. Powder Technology 58, 63–70.

Harvey, N. J., Huntley, N., Dacre, H., Goldstein, M., Thomson, D., Webster, H., 9 2018. Multi-level emulation of a volcanic ash transport and dispersion model to quantify sensitivity to uncertain parameters. Natural Hazards and Earth System Sciences Discussions, 1–50.

Higgins, M. D., Roberge, J., 8 2003. Crystal Size Distribution of Plagioclase and Amphibole from Soufriere Hills Volcano, Montserrat: Evidence for Dynamic Crystallization-Textural Coarsening Cycles. Journal of Petrology 44 (8), 1401–1411.

Hobbs, P. V., Radke, L. F., Lyons, J. H., Ferek, R. J., Coffman, D. J., Casadevall, T. J., 1991. Airborne measurements of particle and gas emissions from the 1990 volcanic eruptions of Mount Redoubt. October 96 (D10), 18735–18752.

Holmes, N. S., Morawska, L., 2006. A review of dispersion modelling and its application to the dispersion of particles: An overview of different dispersion models available. Atmospheric Environment 40, 5902–5928.

Hort, M. C., 2016. VAAC operational dispersion model configuration snap shot Version 2. Tech. Rep. March, NCEP, Washington.

Horwell, C. J., 2007. Grain-size analysis of volcanic ash for the rapid assessment of respiratory health hazard. Journal of Environmental Monitoring 9, 1107–1115.

Horwell, C. J., Stannett, G. W., Andronico, D., Bertagnini, A., Fenoglio, I., Fubini, B., Le Blond, J. S., Williamson, B. J., 2010. A physico-chemical assessment of the health hazard of Mt. Vesuvius volcanic ash. Journal of Volcanology and Geothermal Research 191, 222–232.

Iacovino, K., 2017. Glass Density Calc v3.2.

ICAO, 2012. Doc 9974: Flight Safety and Volcanic Ash. Tech. rep., International Civil Aviation Organisation.

Ingólfsson, Ó., Norðdahl, H., 1 2010. 4 Deglaciation and Holocene Glacial History of Iceland. Developments in Quaternary Sciences 13, 51–68.

James, M. R., Lane, S. J., Gilbert, J. S., 2003. Density, construction, and drag coefficient of electrostatic volcanic ash aggregates. Journal of Geophysical Research: Solid Earth 108 (B9).

Jarosz, N., Loubet, B., Huber, L., 10 2004. Modelling airborne concentration and deposition rate of maize pollen. Atmospheric Environment 38 (33), 5555–5566.

Jayaweera, K. O. L. F., Mason, B. J., 1965. The behaviour of freely falling cylinders and cones in a viscous fluid. Journal of Fluid Mechanics 22 (4), 709–720.

Jones, A., 2004. Atmospheric dispersion modelling at the Met Office. Weather 59 (11), 311–316.

Jones, A., Thomson, D., Hort, M., Devenish, B., 2007. The U.K. Met Office's next-generation atmospheric dispersion model, NAME III. In: Air Pollution Modeling and Its Application XVII. Springer, Boston, pp. 580–589.

Jones, A., Wellings, J., Bedwell, P., 2015. User Guide for NAME. Tech. rep., Met Office, UK, Exeter.

Jorry, S. J., Hasler, C.-A., Davaud, E., 5 2006. Hydrodynamic behaviour of Nummulites: implications for depositional models. Facies 52 (2), 221–235.

Komar, P. D., Reimers, C. E., 3 1978. Grain Shape Effects on Settling Rates. The Journal of Geology 86 (2), 193–209.

Koyaguchi, T., Ohno, M., 4 2001. Reconstruction of eruption column dynamics on the basis of grain size of tephra fall deposits: 2. Application to the Pinatubo 1991 eruption. Journal of Geophysical Research: Solid Earth 106 (B4), 6513–6533.

Kylling, A., Kahnert, M., Lindqvist, H., Nousianen, T., 2014. Volcanic ash infrared signature: porous non-spherical ash particle shapes compared to homogeneous spherical ash particles. Atmospheric Measurement Techniques 7 (4), 919–929.

Lacasse, C., 2001. Influence of climate variability on the atmospheric transport of Icelandic tephra in the subpolar North Atlantic. Global and Planetary Change 29 (1-2), 31–55.

Lacasse, C., Sigurdsson, H., Carey, S., Paterne, M., Guichard, F., 1996. North Atlantic deep-sea sedimentation of Late Quaternary tephra from the Iceland hotspot. Marine Geology 129 (3-4), 207–235.

Lacasse, C., Sigurdsson, H., Jóhannesson, H., Paterne, M., Carey, S., 1995. Source of Ash Zone 1 in the North Atlantic. Bulletin of Volcanology 57 (1), 18–32.

Lacasse, C., van den Bogaard, P., 2002. Enhanced airborne dispersal of silicic tephras during the onset of Northern Hemisphere glaciations, from 6 to 0 Ma records of explosive volcanism and climate change in the subpolar North Atlantic. Geology 30 (7), 623–626.

Lacis, A., Hansen, J., Sato, M., 1992. Climate forcing by stratospheric aerosols. Geophysical Research Letters 19 (15), 1607–1610.

Lane, C. S., Blockley, S. P., Mangerud, J., Smith, V. C., Lohne, Ø. S., Tomlinson, E. L., Matthews, I. P., Lotter, A. F., 2012. Was the 12.1ka Icelandic Vedde Ash one of a kind? Quaternary Science Reviews 33 (February), 87–99.

Lane, S., Gilbert, J., Hilton, M., 1993. The aerodynamic behaviour of volcanic aggregates. Bulletin of Volcanology 55 (7), 481–488.

Lange, A. R., Carmichael, I. S. E., 1990. Thermodynamic properties of silicate liquids with emphasis on density, thermal expansion and compressibility. Modern Methods of Igneous Petrology : Understanding Magmatic Processes, 25–64.

Larsen, G., 2000. Holocene eruptions within the Katla volcanic system, south Iceland: Characteristics and environmental impact. Jökull 49 (49), 1–28.

Larsen, G., Dugmore, A., Newton, A., 1999. The Holocene Geochemistry of historical-age silicic tephras in Iceland. The Holocene 9 (4), 463–471.

Larsen, G., Newton, A. J., Dugmore, A. J., Vilmundardóttir, E. G., 2001. Geochemistry, dispersal, volumes and chronology of Holocene silicic tephra layers from the Katla volcanic system, Iceland. Journal of Quaternary Science 16 (2), 119–132.

Lasso, I. A., Weidman, P. D., 1986. Stokes drag on hollow cylinders and conglomerates. Physics of Fluids 29 (12), 3921–3934.

Lawrence, B. N., Bennett, V. L., Churchill, J., Juckes, M., Kershaw, P., Pascoe, S., Pepler, S., Pritchard, M., Stephens, A., 10 2013. Storing and manipulating environmental big data with JASMIN. In: 2013 IEEE International Conference on Big Data. IEEE, pp. 68–75.

Lawson, I. T., Swindles, G. T., Plunkett, G., Greenberg, D., 2012. The spatial distribution of Holocene cryptotephras in north-west Europe since 7 ka: Implications for understanding ash fall events from Icelandic eruptions. Quaternary Science Reviews 41, 57–66.

Leadbetter, S. J., Hort, M. C., 2011. Volcanic ash hazard climatology for an eruption of Hekla Volcano, Iceland. Journal of Volcanology and Geothermal Research 199 (3-4), 230–241.

Leadbetter, S. J., Hort, M. C., Jones, A. R., Webster, H. N., Draxler, R. R., 2015. Sensitivity of the modelled deposition of Caesium-137 from the Fukushima Dai-ichi nuclear power plant to the wet deposition parameterisation in NAME. Journal of Environmental Radioactivity 139, 200–211.

Leith, D., 1987. Drag on nonspherical objects. Aerosol Science and Technology 6 (2), 153–161.

Liu, E. J., Cashman, K. V., Beckett, F. M., Witham, C. S., Leadbetter, S. J., Hort, M. C., Guðmundsson, S., 2014. Ash mists and brown snow: Remobilization of volcanic ash from recent Icelandic eruptions. Journal of Geophysical Research: Atmospheres 119.

Liu, E. J., Cashman, K. V., Rust, A. C., 2015. Optimising shape analysis to quantify volcanic ash morphology. GeoResJ 8, 14–30.

Liu, E. J., Cashman, K. V., Rust, A. C., Höskuldsson, A., 2017. Contrasting mechanisms of magma fragmentation during coeval magmatic and hydromagmatic activity: the Hverfjall Fires fissure eruption, Iceland. Bulletin of Volcanology 79 (10).

Liu, E. J., Oliva, M., Antoniades, D., Giralt, S., Granados, I., Pla-Rabes, S., Toro, M., Geyer, A., 2016. Expanding the tephrostratigraphical framework for the South Shetland Islands, Antarctica, by combining compositional and textural tephra characterisation. Sedimentary Geology 340, 49–61.

Lohne, Ø. S., Mangerud, J., Birks, H. H., 7 2014. IntCal13 calibrated ages of the Vedde and Saksunarvatn ashes and the Younger Dryas boundaries from Kråkenes, western Norway. Journal of Quaternary Science 29 (5), 506–507.

Loth, E., 2008. Drag of non-spherical solid particles of regular and irregular shape. Powder Technology 182 (3), 342–353.

MacKinnon, I. D. R., Gooding, J. L., McKay, D. S., Clanton, U. S., 1984. The El Chichón stratospheric cloud: solid particulates and settling rates. Journal of Volcanology and Geothermal Research 23 (1-2), 125–146.

Mangerud, J., Lie, S. E., Furnes, H., Kristiansen, I. L., Lømo, L., 1984. A Younger Dryas ash bed in western Norway, and its possible correlations with tephra in cores from the Norwegian Sea and the North Atlantic. Quaternary Research 21, 85–104.

Manzella, I., Bonadonna, C., Phillips, J. C., Monnard, H., 2015. The role of gravitational instabilities in deposition of volcanic ash. Geology 43 (3), 211–214.

Marchildon, E. K., Clamen, A., Gauvin, W. H., 1964. Drag and oscillatory motion of freely falling cylindrical particles. The Canadian Journal of Chemical Engineering 42 (4), 178–182.

Martin, P. G., Louvel, M., Cipiccia, S., Jones, C. P., Batey, D. J., Hallam, K. R., Yang, I. A. X., Satou, Y., Rau, C., Mosselmans, J. F. W., Richards, D. A., Scott, T. B., 12 2019. Provenance of uranium particulate contained within Fukushima Daiichi Nuclear Power Plant Unit 1 ejecta material. Nature Communications 10 (1), 2801.

Maryon, R. H., Ryall, D. B., Malcolm, A. L., 1999. The NAME 4 dispersion model: science documentation. Tech. rep., Met Office, UK.

Mastin, L. G., Guffanti, M., Servranckx, R., Webley, P., Barsotti, S., Dean, K., Durant, A., Ewert, J. W., Neri, A., Rose, W. I., Schneider, D., Siebert, L., Stunder, B., Swanson, G., Tupper, A., Volentik, A., Waythomas, C. F., 2009. A multidisciplinary effort to assign realistic source parameters to models of volcanic ash-cloud transport and dispersion during eruptions. Journal of Volcanology and Geothermal Research 186, 10–21.

Matthews, N. E., Smith, V. C., Costa, A., Durant, A. J., Pyle, D. M., Pearce, N. J., 2012. Ultra-distal tephra deposits from super-eruptions: Examples from Toba, Indonesia and Taupo Volcanic Zone, New Zealand. Quaternary International 258, 54–79.

Mele, D., Dellino, P., Sulpizio, R., Braia, G., 2011. A systematic investigation on the aerodynamics of ash particles. Journal of Volcanology and Geothermal Research 203, 1–11.

Mele, D., Dioguardi, F., 2018. The grain size dependency of vesicular particle shapes strongly affects the drag of particles. First results from microtomography investigations of Campi Flegrei fallout deposits. Journal of Volcanology and Geothermal Research 353, 18–24.

Meyer, P. S., Sigurdsson, H., Schilling, J.-G., 1985. Petrological and geochemical variations along Iceland's Neovolcanic Zones. Journal of Geophysical Research 90 (B12), 10043–10072.

Newhall, C. G., Self, S., 1982. The volcanic explosivity index (VEI): An estimate of explosive magnitude for historical volcanism. Journal of Geophysical Research 87 (C2), 1231–1238.

Norðdahl, H., Haflidason, H., 1992. The Skógar Tephra, a Younger Dryas marker in North Iceland. Boreas 21, 23–41.

Oakey, R. J., Green, M., Carling, P. A., Lee, M. W., Sear, D. A., Warburton, J., 11 2005. Grain-Shape Analysis–A New

Method for Determining Representative Particle Shapes for Populations of Natural Grains. Journal of Sedimentary Research 75 (6), 1065–1073.

Oberbeck, A., 1876. Ueber stationäre flüssigkeitsbewegungen mit berücksichtigung der inneren reibung. Journal für die Reine und Angewandte Mathematik 81, 62–80.

Ochs, F. A., Lange, R. A., 1999. The density of hydrous magmatic liquids. Science 283, 1314–1317.

Óladóttir, B. A., Larsen, G., Thordarson, T., Sigmarsson, O., 2005. The Katla volcano S-Iceland: Holocene tephra stratigraphy and eruption frequency. Jökull 55, 53–74.

Pettyjohn, E., Christiansen, E., 1948. Effect of particle shape on free settling rates of isometric particles. Chemical Engineering Progress 44 (2), 157–172.

Pilcher, J., Bradley, R. S., Francus, P., Anderson, L., 2005. A Holocene tephra record from the Lofoten Islands, Arctic Norway. Boreas 34, 1–21.

Ponomareva, V., Portnyagin, M., Davies, S. M., 2015. Tephra without Borders: Far-Reaching Clues into Past Explosive Eruptions. Frontiers in Earth Science 3.

Rasmussen, S. O., Vinther, B. M., Clausen, H. B., Andersen, K. K., 2007. Early Holocene climate oscillations recorded in three Greenland ice cores. Journal of Quaternary Science 26 (15-16), 1907–1914.

Reckziegel, F., Bustos, E., Mingari, L., Báez, W., Villarosa, G., Folch, A., Collini, E., Viramonte, J., Romero, J., Osores, S., 2016. Forecasting volcanic ash dispersal and coeval resuspension during the April-May 2015 Calbuco eruption. Journal of Volcanology and Geothermal Research 321, 44–57.

Riley, C. M., Rose, W. I., Bluth, G. J. S., 2003. Quantitative shape measurements of distal volcanic ash. Journal of Geophysical Research: Solid Earth 108 (B10), 1–15.

Rodger, H., 2018. An Investigation of Methods to Obtain 3D and 2D Physical Particle Parameters of Volcanic Ash Grains Which Could Affect Settling Velocity. Master's thesis, University of Bristol.

Rolph, G., Ngan, F., Draxler, R., 10 2014. Modeling the fallout from stabilized nuclear clouds using the HYSPLIT atmospheric dispersion model. Journal of Environmental Radioactivity 136, 41–55.

Rose, W. I., Bluth, G. J. S., Ernst, G. G. J., 5 2000. Integrating retrievals of volcanic cloud characteristics from satellite remote sensors: a summary. Philosophical Transactions of the Royal Society of London. Series A: Mathematical, Physical and Engineering Sciences 358 (1770), 1585–1606.

Rose, W. I., Bluth, G. J. S., Schneider, D. J., Ernst, G. G. J., Riley, C. M., Henderson, L. J., McGimsey, R. G., 11 2001. Observations of Volcanic Clouds in Their First Few Days of Atmospheric Residence: The 1992 Eruptions of Crater Peak, Mount Spurr Volcano, Alaska. The Journal of Geology 109 (6), 677–694.

Rose, W. I., Chesner, C. A., 1987. Dispersal of ash in the great Toba eruption, 75 ka. Geology 15, 913–917.

Rose, W. I., Durant, A. J., 2009. Fine ash content of explosive eruptions. Journal of Volcanology and Geothermal Research 186, 32–39.

Rust, A. C., Cashman, K. V., 2011. Permeability controls on expansion and size distributions of pyroclasts. Journal of Geophysical Research 116.

Rust, A. C., Manga, M., Cashman, K. V., 2003. Determining flow type, shear rate and shear stress in magmas from bubble shapes and orientations. Journal of Volcanology and Geothermal Research 122, 111–132.

Saxby, J., Beckett, F., Cashman, K., Rust, A., Tennant, E., 2018. The impact of particle shape on fall velocity: Implications for volcanic ash dispersion modelling. Journal of Volcanology and Geothermal Research 362.

Schumacher, R., 1994. A reappraisal of mount st. helens' ash clusters-depositional model from experimental observation. Journal of volcanology and geothermal research 59 (3), 253–260.

Schumann, U., Weinzierl, B., Reitebuch, O., Schlager, H., Minikin, A., Forster, C., Baumann, R., Sailer, T., Graf, K., Mannstein, H., Voigt, C., Rahm, S., Simmet, R., Scheibe, M., Lichtenstern, M., Stock, P., Rüba, H., Schauble, D., Tafferner, A., Rautenhaus, M., Gerz, T., Ziereis, H., Krautstrunk, M., Mallaun, C., Gayet, J. F., Lieke, K., Kandler, K., Ebert, M., Weinbruch, S., Stohl, A., Gasteiger, J., Groß, S., Freudenthaler, V., Wiegner, M., Ansmann, A., Tesche, M., Olafsson, H., Sturm, K., 2011. Airborne observations of the Eyjafjalla volcano ash cloud over Europe during air space closure in April and May 2010. Atmospheric Chemistry and Physics 11 (5), 2245–2279.

Schwendemann, A. B., Wang, G., Mertz, M. L., McWilliams, R. T., Thatcher, S. L., Osborn, J. M., 8 2007. Aerodynamics of saccate pollen and its implications for wind pollination. American Journal of Botany 94 (8), 1371–1381.

Scollo, S., Folch, A., Costa, A., 2008. A parametric and comparative study of different tephra fallout models. Journal of Volcanology and Geothermal Research 176 (2), 199–211.

Sharma, K., Self, S., Blake, S., Thordarson, T., Larsen, G., 2008. The AD 1362 Öræfajökull eruption, S.E. Iceland: Physical volcanology and volatile release. Journal of Volcanology and Geothermal Research 178 (4), 719–739.

Sigurdsson, H., 1990. Assessment of the atmospheric impact of volcanic eruptions. Global catastrophes in Earth history; An interdisciplinary conference on impacts, volcanism, and mass mortality; Geological Society of America Special Paper 247, 99–110.

Sparks, R., Bursik, M., Carey, S., Gilbert, J., Glaze, L., Sigurdsson, H., Woods, A., 1997. Volcanic plumes. John Wiley & Sons, Inc, United States.

Speijer, R. P., Van Loo, D., Masschaele, B., Vlassenbroeck, J., Cnudde, V., Jacobs, P., 8 2008. Quantifying foraminiferal growth with high-resolution X-ray computed tomography: New opportunities in foraminiferal ontogeny, phylogeny, and paleoceanographic applications. Geosphere 4 (4), 760.

Stevenson, J. A., Loughlin, S., Rae, C., Thordarson, T., Milodowski, A. E., Gilbert, J. S., Harangi, S., Lukács, R., Højgaard, B., Árting, U., Pyne-O'Donnell, S., MacLeod, A., Whitney, B., Cassidy, M., 2012. Distal deposition of tephra from the Eyjafjallajökull 2010 summit eruption. Journal of Geophysical Research 117 (6).

Stevenson, J. A., Loughlin, S. C., Font, A., Fuller, G. W., MacLeod, A., Oliver, I. W., Jackson, B., Horwell, C. J., Thordarson, T., Dawson, I., 2013. UK monitoring and deposition of tephra from the May 2011 eruption of Grímsvötn, Iceland. Journal of Applied Volcanology 2 (3).

Stevenson, J. A., Millington, S. C., Beckett, F. M., Swindles, G. T., Thordarson, T., 2015. Big grains go far: Understanding the discrepancy between tephrochronology and satellite infrared measurements of volcanic ash. Atmospheric Measurement Techniques 8 (5), 2069–2091.

Stohl, A., Prata, A. J., Eckhardt, S., Clarisse, L., Durant, A., Henne, S., Kristiansen, N. I., Minikin, A., Schumann,

U., Seibert, P., Stebel, K., Thomas, H. E., Thorsteinsson, T., Tørseth, K., Weinzierl, B., 2011. Determination of time-and height-resolved volcanic ash emissions and their use for quantitative ash dispersion modeling: The 2010 Eyjafjallajökull eruption. Atmospheric Chemistry and Physics 11 (9), 4333–4351.

Stull, R., 2012. An introduction to boundary layer meteorology. Springer Science & Business Media.

Svendsen, J. I., Mangerud, J., 1987. Late Weichselian and Holocene sea-level history for a cross-section of western Norway. Journal of Quaternary Science 2, 113–132.

Tennant, E., 2017. Settling velocity measurements of volcanic ash analogue particles with a non-uniform density distribution. Master's thesis, University of Bristol.

Thomson, D. J., Jones, A. R., Webster, H. N., 2009. NAME Technical Specification Document C01: Physical and mathematical constants and functions. Tech. rep., Met Office, UK.

Thordarson, T., Larsen, G., 2007. Volcanism in Iceland in historical time: Volcano types, eruption styles and eruptive history. Journal of Geodynamics 43, 118–152.

Thorsteinsdóttir, E. S., 2015a. Grain characteristics of tephra from the subglacial SILK-LN Katla eruption ˜3400 years ago and the subaerial Hekla eruption in 1947. Master's thesis, University of Iceland.
URL `https://skemman.is/handle/1946/20437`

Thorsteinsdóttir, E. S., 2015b. Grain characteristics of tephra from the subglacial SILK-LN Katla eruption ˜3400 years ago and the subaerial Hekla eruption in 1947. Master's thesis, University of Iceland.

Tomlinson, E. L., Smith, V. C., Albert, P. G., Aydar, E., Civetta, L., Cioni, R., Çubukçu, E., Gertisser, R., Isaia, R., Menzies, M. A., Orsi, G., Rosi, M., Zanchetta, G., 2015. The major and trace element glass compositions of the productive Mediterranean volcanic sources: Tools for correlating distal tephra layers in and around Europe. Quaternary Science Reviews 118, 48–66.

Turney, C. S., 1998. Extraction of rhyolitic component of Vedde microtephra from minerogenic lake sediments. Journal of Paleolimnology 19 (2), 199–206.

Unnikrishnan, A., Chhabra, R. P., 1991. An experimental study of motion of cylinders in newtonian fluids: Wall effects and drag coefficient. The Canadian Journal of Chemical Engineering 69 (3), 729–735.

Vonlanthen, P., Rausch, J., Ketcham, R. A., Putlitz, B., Baumgartner, L. P., Grobéty, B., 2015. High-resolution 3D analyses of the shape and internal constituents of small volcanic ash particles: The contribution of SEM micro-computed tomography (SEM micro-CT). Journal of Volcanology and Geothermal Research 293, 1–12.

Voth, G. A., Soldati, A., 2017. Anisotropic Particles in Turbulence. Annual Review of Fluid Mechanics 49, 249–276.

Wadell, H., 1933. Sphericity and roundness of rock particles. The Journal of Geology 41 (3), 310–331.

Wastegård, S., 2002. Early to middle Holocene silicic tephra horizons from the Katla volcanic system, Iceland: New results from the Faroe Islands. Journal of Quaternary Science 17 (8), 723–730.

Wastegård, S., Björck, S., Possnert, G., Wohlfarth, B., 1998. Evidence for the occurrence of Vedde Ash in Sweden: radiocarbon and calendar age estimates. Journal of Quaternary Science 13 (3), 271–274.

Watson, E. J., Swindles, G. T., Stevenson, J. A., Savov, I., Lawson, I. T., 2016. The transport of Icelandic volcanic ash: Insights from northern European cryptotephra records. Journal of Geophysical Research : Solid Earth 121,

7177–7192.

Watt, S. F., Gilbert, J. S., Folch, A., Phillips, J. C., Cai, X. M., 2015. An example of enhanced tephra deposition driven by topographically induced atmospheric turbulence. Bulletin of Volcanology 77 (35).

Webley, P. W., Stunder, B. J., Dean, K. G., 2009. Preliminary sensitivity study of eruption source parameters for operational volcanic ash cloud transport and dispersion models - A case study of the August 1992 eruption of the Crater Peak vent, Mount Spurr, Alaska. Journal of Volcanology and Geothermal Research 186, 108–119.

Webster, H. N., Carroll, E. B., Jones, A. R., Manning, A. J., Thomson, D. J., 12 2007. The Buncefield oil depot incident: a discussion of the meteorology. Weather 62 (12), 325–330.

Webster, H. N., Thomson, D. J., 2011. Dry deposition modelling in a Lagrangian dispersion model. International Journal of Environment and Pollution 47(1-4), 1–9.

Webster, H. N., Thomson, D. J., 2014. Forecasting Research Technical Report No. 584: The NAME wet deposition scheme. Tech. rep., Met Office, UK.

Webster, H. N., Thomson, D. J., Johnson, B. T., Heard, I. P., Turnbull, K., Marenco, F., Kristiansen, N. I., Dorsey, J., Minikin, A., Weinzierl, B., Schumann, U., Sparks, R. S., Loughlin, S. C., Hort, M. C., Leadbetter, S. J., Devenish, B. J., Manning, A. J., Witham, C. S., Haywood, J. M., Golding, B. W., 2012. Operational prediction of ash concentrations in the distal volcanic cloud from the 2010 Eyjafjallajökull eruption. Journal of Geophysical Research 117 (2).

Webster, H. N., Whitehead, T., Thomson, D. J., Webster, H. N., Whitehead, T., Thomson, D. J., 3 2018. Parameterizing Unresolved Mesoscale Motions in Atmospheric Dispersion Models. Journal of Applied Meteorology and Climatology 57 (3), 645–657.

Westbrook, C. D., Sephton, E. K., 2017. Using 3-D-printed analogues to investigate the fall speeds and orientations of complex ice particles. Geophysical Research Letters 44 (15), 7994–8001.

White, F. M., 1974. Viscous Fluid Flow. McGraw-Hill, New York.

Wilkins, K. L., Mackie, S., Watson, I. M., Webster, H. N., Thomson, D. J., Dacre, H. F., 2016. Data insertion in volcanic ash cloud forecasting. Annals of Geophysics 57.

Willmarth, W. W., Hawk, N. E., Harvey, R. L., 1964. Steady and unsteady motions and wakes of freely falling disks. The Physics of Fluids 7 (2), 197–208.

Wilson, L., Huang, T. C., 1979. The influence of shape on the atmospheric settling velocity of volcanic ash particles. Earth and Planetary Science Letters 44 (2), 311–324.

Wilson, T. M., Stewart, C., Sword-Daniels, V., Leonard, G. S., Johnston, D. M., Cole, J. W., Wardman, J., Wilson, G., Barnard, S. T., 1 2012. Volcanic ash impacts on critical infrastructure. Physics and Chemistry of the Earth, Parts A/B/C 45-46, 5–23.

Witham, C., Hort, M., Thomson, D., Leadbetter, S., Devenish, B., Webster, H., Beckett, F. M., 2017. Technical Summary (v1.4): The current volcanic ash modelling set- up at the London VAAC. Tech. rep., Met Office, UK.

Witham, C. S., Hort, M. C., Potts, R., Servranckx, R., Husson, P., Bonnardot, F., 2007. Comparison of VAAC atmospheric dispersion models using the 1 November 2004 Grímsvötn eruption. Meteorological Applications 14,

27–38.

Appendices

Chapter A

Supplementary Material for Chapter 2

A.1 Boundary wall correction

For particles settling in a finite fluid, boundary wall proximity can affect Stokesian resistance (Brenner, 1962). The magnitude of boundary effects diminishes with increasing tube diameter to particle diameter ratio, and increasing *Re* (Chhabra et al., 1996). This means that the size of the vessel used in particle settling experiments can affect the results, although that effect is not well-constrained for non-spherical particles (Chhabra, 1995). Studies of the terminal velocity of irregular shapes generally make no correction for boundary effects (Christiansen and Barker, 1965), account for wall effects by conducting experiments in a variety of vessel sizes (Unnikrishnan and Chhabra, 1991), or by applying an analytical correction for spherical particles (Pettyjohn and Christiansen, 1948).

The wall correction for spheres at high *Re* can be calculated by

$$k = \left(1 - \frac{A_s}{A}\right)\left(1 - \frac{A_s}{2A}\right)^{0.5} \tag{A.1}$$

where k is the ratio of w_t in the confined medium to w_t in an unbounded expanse, and A_s is the cross-sectional area of the sphere and A is the cross-sectional area of the tank (Di Felice et al., 1995; Chhabra et al., 1996). However, the wall factor is also a function of *Re* for a fixed A_S/A. Since experimental determination of wall factors is dependent on drag curves that are accurate to around 5% (Chhabra et al., 1996), a critical *Re* can be defined for each A_S/A, above which Equation A.1 is reliable. This critical value is that at which k is 95% of the value predicted by Equation A.1. Reference values based on experimental data are given by Chhabra et al. (1996).

For lower *Re* and irregular shapes, best fits can be calculated for each shape by assuming that $k = f(Re, d/D, shape)$ where d is particle diameter and D is tank diameter (Chhabra, 1995). *Re* is not a significant variable at 95% confidence intervals for most shapes. For flat plates (disks and

squares) and $d/D < 0.32$,

$$k = 1 - 1.7\left(\frac{d}{D}\right) \tag{A.2}$$

where d is diameter (disks) or diameter of an equal projected area circle (squares). For cylinders, the length to diameter ratio is important. For $0.03 < d_v/D < 0.5$,

$$k = 1 - 1.33\left(\frac{d_v}{D}\right) \qquad \left(\frac{L}{S}\right) < 10 \tag{A.3}$$

and

$$k = 1 - 3.58\left(\frac{d_v}{D}\right) \qquad \left(\frac{L}{S}\right) > 10 \tag{A.4}$$

where d_v is the diameter of a volume-equivalent sphere. For rectangular prisms the experimental scatter is greater, but error is around 10% at the 90% confidence level. For $0.16 < d_v/D < 0.6$,

$$k = 1 - 1.42\left(\frac{d_v}{D}\right) \tag{A.5}$$

With the exception of long cylinders ($L/S > 10$), all shapes show smaller wall effects than for a volume-equivalent sphere.

For the data in this study, boundary effects were corrected using Equations (A.1 - A.4). Boundary errors are similar to standard errors based on repeat measurements, with k ranging from 0.94 – 1.0 with a mean of 0.98. For particles in the Stokes regime, where boundary effects are greatest, k was calculated using Equations (A.2 - A.4). For particles in the intermediate and turbulent regimes, k values were calculated based on volume-equivalent spheres (Equation A.1), due to uncertainty inherent in extrapolating Chhabra (1995)'s shape-based corrections to higher *Re*. For these particles, k was consistently close to 1 with a mean of 0.99.

Chapter B

Supplementary Material for Chapter 3

B.1 Supplementary NAME deposition outputs and single-site met data

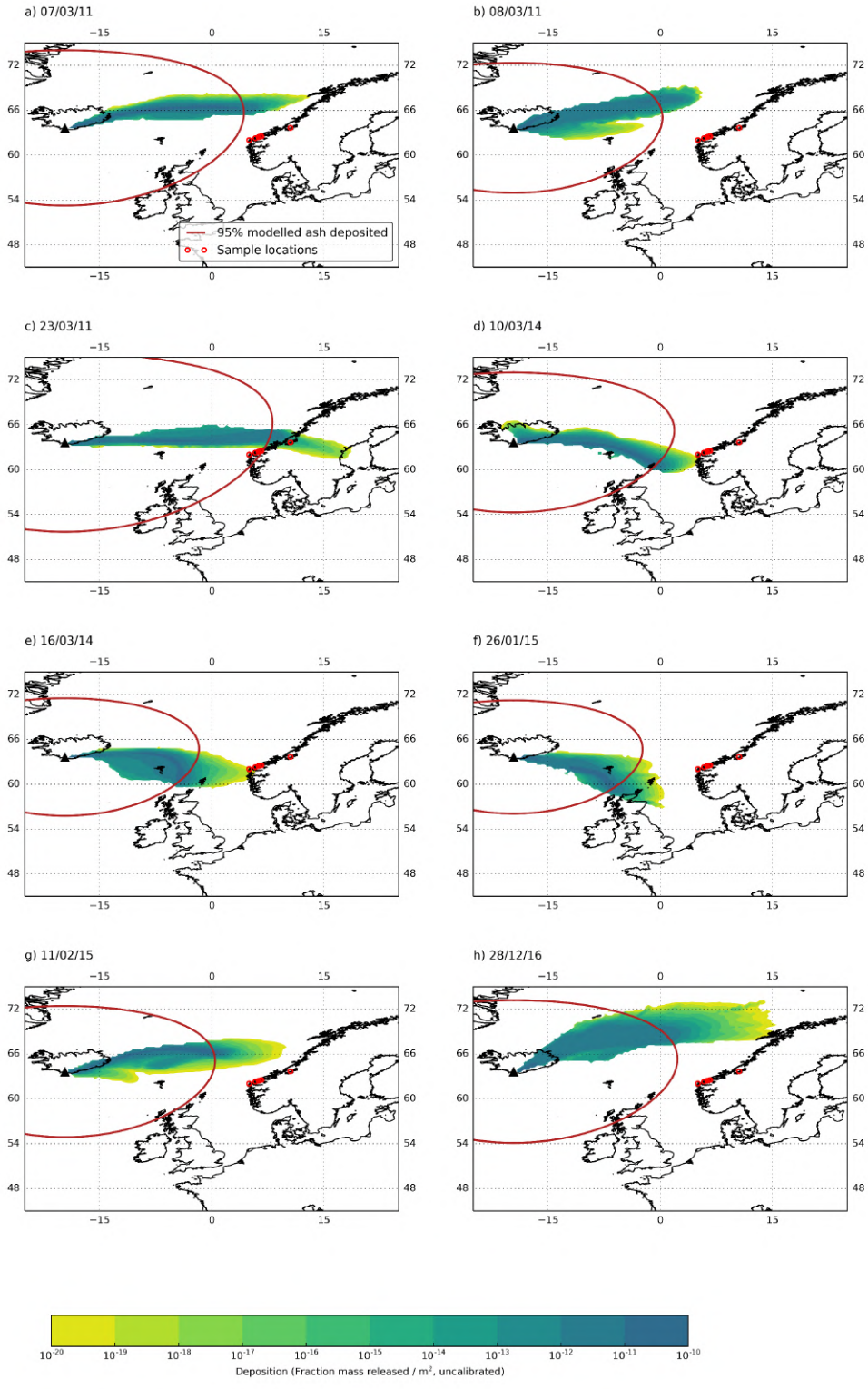

Figure B.1: Simulated isomass maps for a Vedde-like eruption of Katla volcano (black triangle), using the NAME model with the Ganser (1993) sedimentation scheme for non-spherical particles, d_v = 191 μm and ψ = 0.55. Sample locations (red circles) are given for sites KV1-6 to provide a reference for observed particle travel distances.

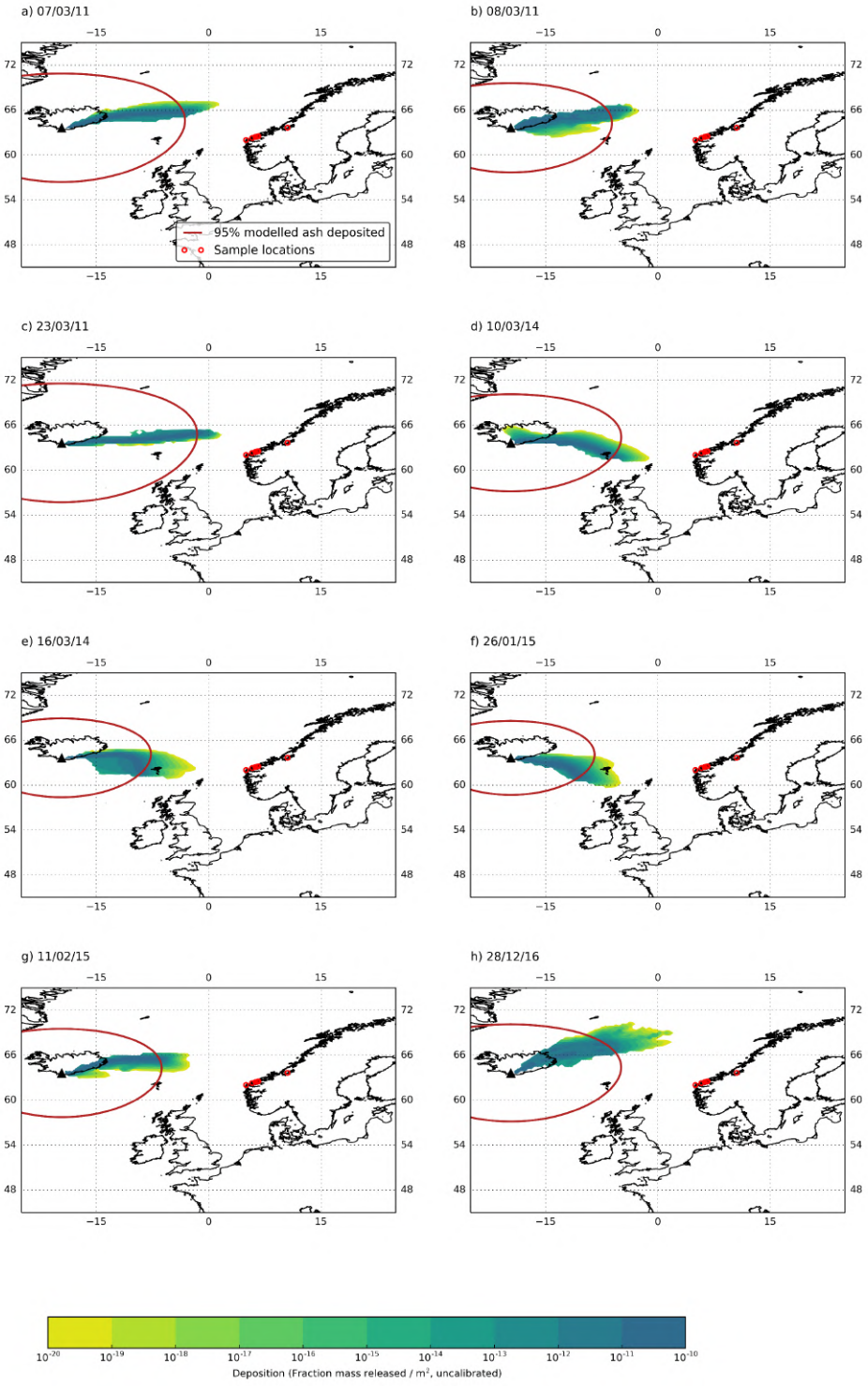

Figure B.2: Simulated isomass maps for a Vedde-like eruption of Katla volcano (black triangle), using the NAME model with the White (1974) sedimentation scheme for spherical particles and d_v = 191 µm. Sample locations (red circles) are given for sites KV1-6 to provide a reference for observed particle travel distances.

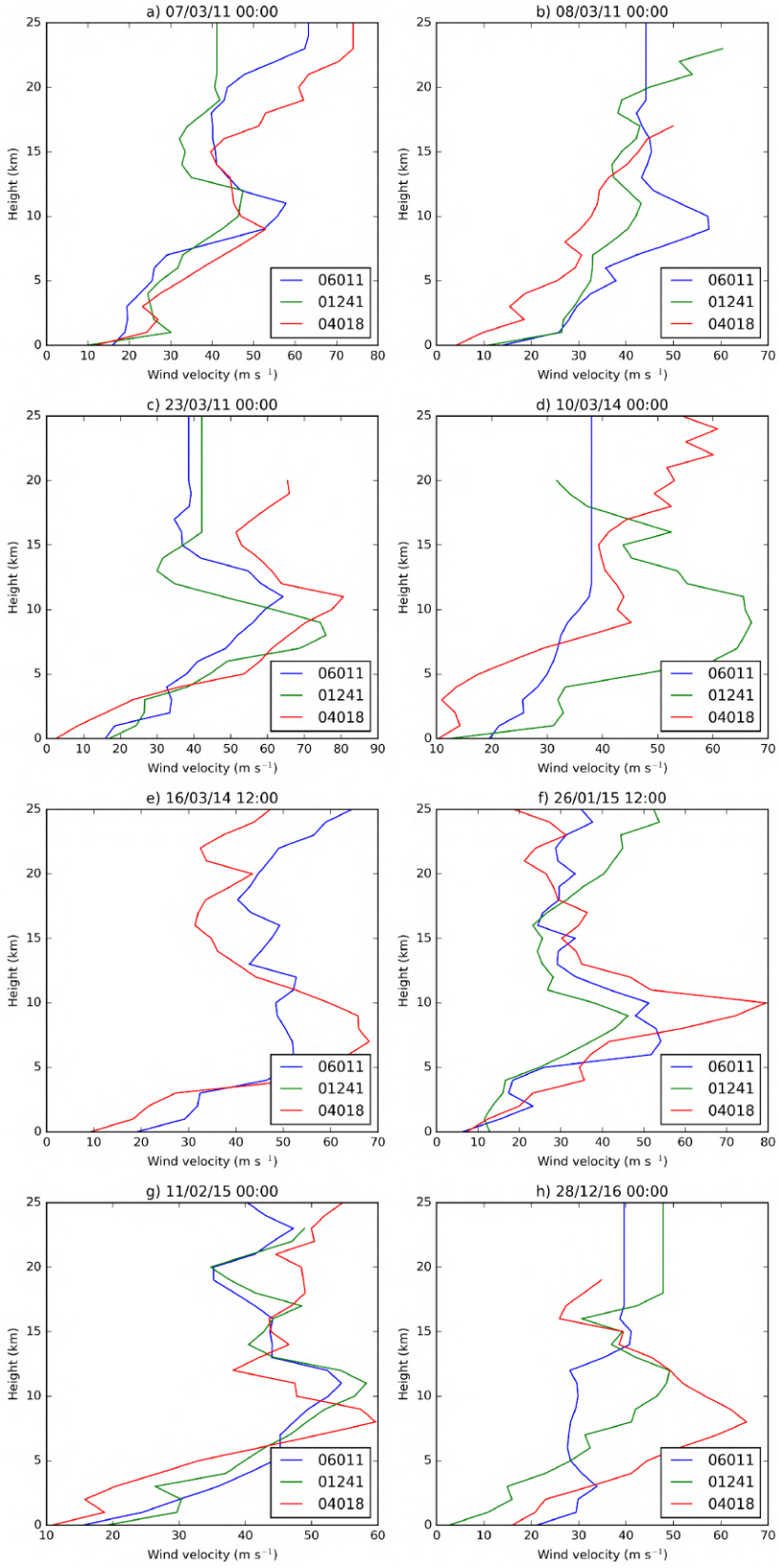

Figure B.3: Single-site met (radiosonde) data for the days in corresponding panels of Supplementary Figures B.1 - B.2. Line colours refer to the weather stations in the north Atlantic region; their locations are shown in Figure 3.2.

B.2 Calculation of terminal velocity

This section describes the calculation of terminal velocity used throughout this paper, using two alternative drag laws: a spherical approximation and a shape-dependent law. The same approach is used for the simple stratified atmosphere model and in NAME.

Terminal velocity w_t is given by:

$$w_t = (\frac{4}{3}\frac{d}{C_D}g\frac{\rho_P - \rho}{\rho})^{\frac{1}{2}} \tag{B.1}$$

where d is a characteristic particle dimension, g is 9.81 m s^{-1}, ρ is air density, ρ_P is particle density, and C_D is the drag coefficient.

We calculate C_D according to the analytical drag law for spheres (White, 1974):

$$C_D = C_1 + \frac{24}{\mathrm{Re}} + \frac{C_2}{1+\sqrt{\mathrm{Re}}} \tag{B.2}$$

where C_1 = 0.25 and C_2 = 6.0 for $Re < 5$ x 10^3. Reynolds number Re is given by:

$$Re = \frac{\rho w_t d}{\mu} \tag{B.3}$$

where μ is the dynamic viscosity of the fluid. As Re is a function of w_t (Equation B.1) the resulting equation system is nonlinear; we solve it iteratively using the terminal velocity of an equivalent-volume sphere in Stokes flow as an initial guess.

We also calculate C_D according to the Ganser (1993) drag law for non-spherical particles, where C_D is a function of the shape descriptor sphericity (ψ, Equation 3.1):

$$C_D = \frac{24}{\mathrm{Re}K_S}\left(1+0.1118\left[\mathrm{Re}\left(K_S K_N\right)\right]^{0.6567}\right) + \frac{0.4305K_N}{1+\frac{3305}{\mathrm{Re}K_S K_N}} \tag{B.4}$$

where K_N is a correction factor for turbulent flow:

$$K_N = 10^{1.84148(-Log\psi)^{0.5743}} \tag{B.5}$$

and K_S is a correction factor for laminar (Stokes) flow:

$$K_S = \frac{3}{1+2\psi^{-0.5}} \tag{B.6}$$

B.3 Choice of model input parameters: justification and sensitivity analysis

B.3.1 Persisted met approach

NAME runs for the 8 dates we examined used UM data from 59 pressure levels up to $\sim$ 29 km altitude, the limit for UM reanalysis data on the JASMIN server on which we carried out the model runs. The meteorological conditions higher in the stratosphere were taken to be the same as at 29 km altitude. To verify this 'persisted met' approach, we conducted sensitivity analysis to examine whether the transport of volcanic ash was sensitive to the choice of persisted versus 'real' met data above pressure level 59 ($\sim$ 29 km) up to pressure level 70 ($\sim$ 40 km), the highest level in the UM. We compared the sensitivity to persisted met with the sensitivity to plume height. Figure B.4a shows wind speed in the troposphere and stratosphere for 63.6467°N, 19.1303°W (Katla volcano, Iceland) on 2018/12/20; Figure B.4b shows the same profile but with the met conditions at pressure level 59 persisted above this point. Dotted lines at 25 km and 35 km illustrate the positions of the two plume top heights we used. For these NAME runs we released 2×10^{13} g of ash over 1 hour (2018/12/20 03:00 – 04:00) and then output deposition for the next 9 hours, by which time it had all been deposited. The particle size is 191 μm and particles were released in a uniform distribution from the vent height to the plume top height. Panels c-f in Figure B.4 show air concentration outputs at three vertical levels. There is a marked difference in air concentrations between the 25 km (panels c-d) and 35 km (panels e-f) plume cases. In comparison, the choice to use 70 level met data (panels c and e) or 59 levels (panels d and f) makes relatively little difference to the ash distribution in the atmosphere two hours after the eruption end time. We therefore determine that our use of persisted met data to model high plumes is robust.

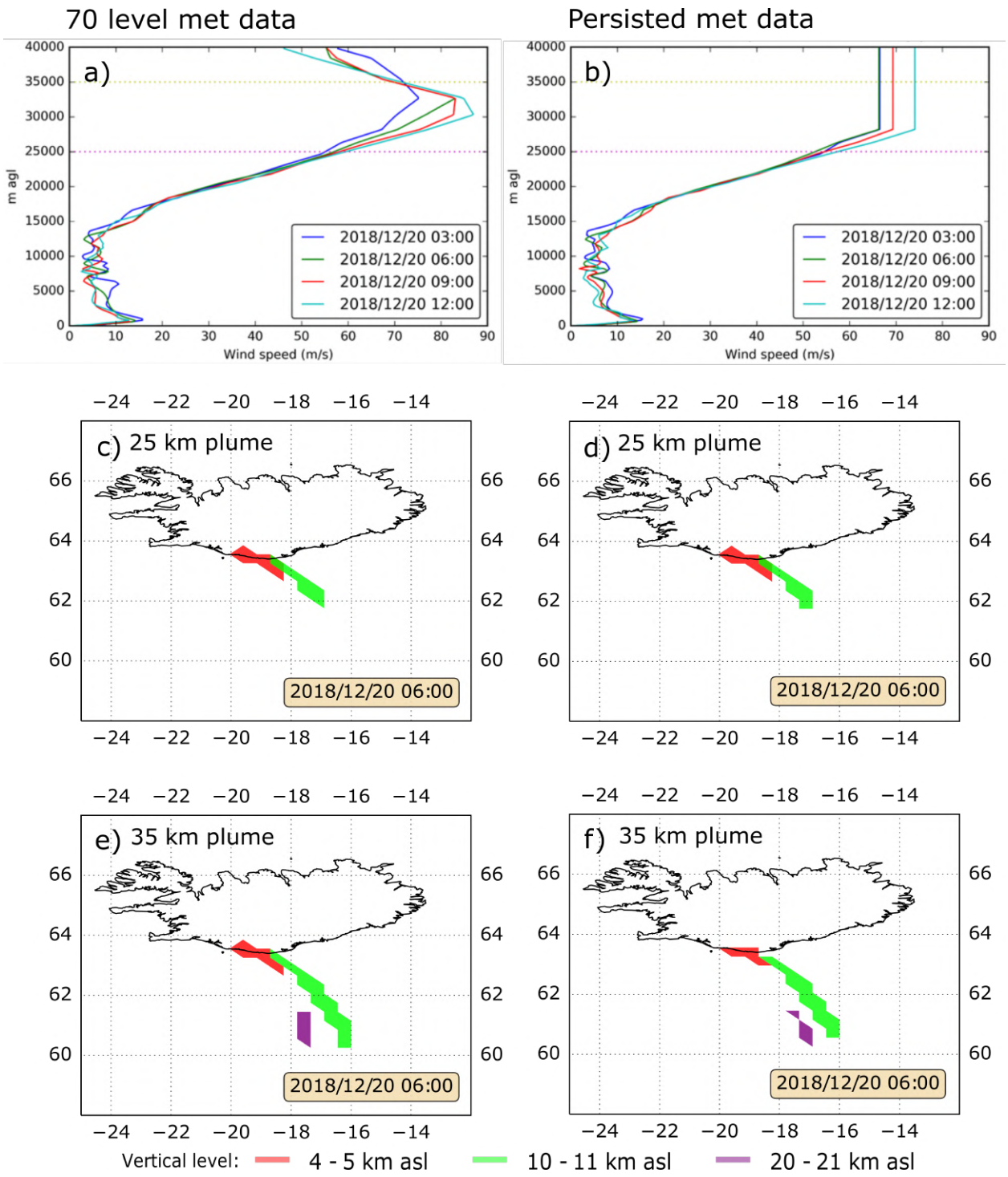

Figure B.4: Sensitivity of NAME modelled volcanic ash air concentrations to the choice of vertical UM model levels used and the plume height. a) Wind speed in the troposphere and stratosphere for 63.6467°N, 19.1303°W on 2018/12/20, using 70 UM model levels; b) Wind speed persisted above UM model level 59 for the same day; the remaining panels are air concentrations two hours after the eruption end, shown as a single contour with a threshold of 0.002 g m^{-3}: c) 25 km plume, 70 model levels; d) 25 km plume, 59 model levels; e) 35 km plume, 70 model levels; f) 35 km plume, 59 model levels.

B.4 Constraining input parameters

To constrain meteorological and eruptive conditions conducive to ash transport to Norway, we first modelled the travel distance of the largest shards from the Norwegian samples KV1-6 using a simple 2D stratified atmosphere model built in MATLAB. This allowed us to rapidly model multiple plume height and wind speed scenarios to inform inputs for modelling using NAME. In our simple model, particles move horizontally according to $\Delta t \times w_a$ where Δt = timestep (s) and w_a = wind velocity (m s^{-1}) and vertically according to $\Delta t \times w_t$ where w_t = particle terminal velocity. We use 80 m s^{-1}, an extreme value from our analysis of modern meteorological data, as an upper bound. We neglect turbulent diffusion and vertical advection as the vertical velocity of particles $\geq$ 100 μm is dominated by w_t (Saxby et al., 2018).

For the particle dimension d, we used 191 μm and 451 μm, d_{v5} and L_5, respectively, of sample KV4; runs with a shape parameter use ψ = 0.55, the mean ψ of those particles. C_D is calculated as a function of Reynolds number Re using the analytical formula of White (1974), which approximates particles as spheres, or as a function of Re and the shape parameter ψ using the empirical correlation of Ganser (1993). Both C_D correlations are described in Supplementary Material. The viscosity and density of air are calculated as a function of altitude according to the vertical temperature profile of the ICAO standard atmosphere (Thomson et al., 2009). We sample plume heights in 5 km intervals, using 35 km agl as an upper bound.

As meteorological conditions at the time of the Vedde eruption are unknown, we varied wind velocity W and plume height H within reasonable limits (H = 5 – 35 km and W = 5 – 80 m s^{-1} in increments of 5). For constant wind speed and atmospheric properties, the relationship between $H \times W$ and travel distance would be linear for a constant terminal velocity; the density stratification of the atmosphere means that terminal velocity is greater in the stratosphere, which causes the scatter in Figure B.5. We cannot account for the observed travel distance when we use L_5, but only when we use d_{v5} as the particle dimension. By modelling the particle as spherical, we can account for its travel distance only by invoking extreme meteorological conditions coupled with a large eruption (H = 35 km, W = 80 m s^{-1}). If we use a shape parameter (ψ = 0.55) we can account for its travel distance using a wider range of conditions (Figure B.5, inset; W = 55 m s^{-1} and H = 35 km to W = 75 m s^{-1} and H = 20 km). The results suggest that a plume height of $>$ 20 km was necessary to transport particles from Katla volcano to western Norway and that their shape and size are important factors in their distal transport.

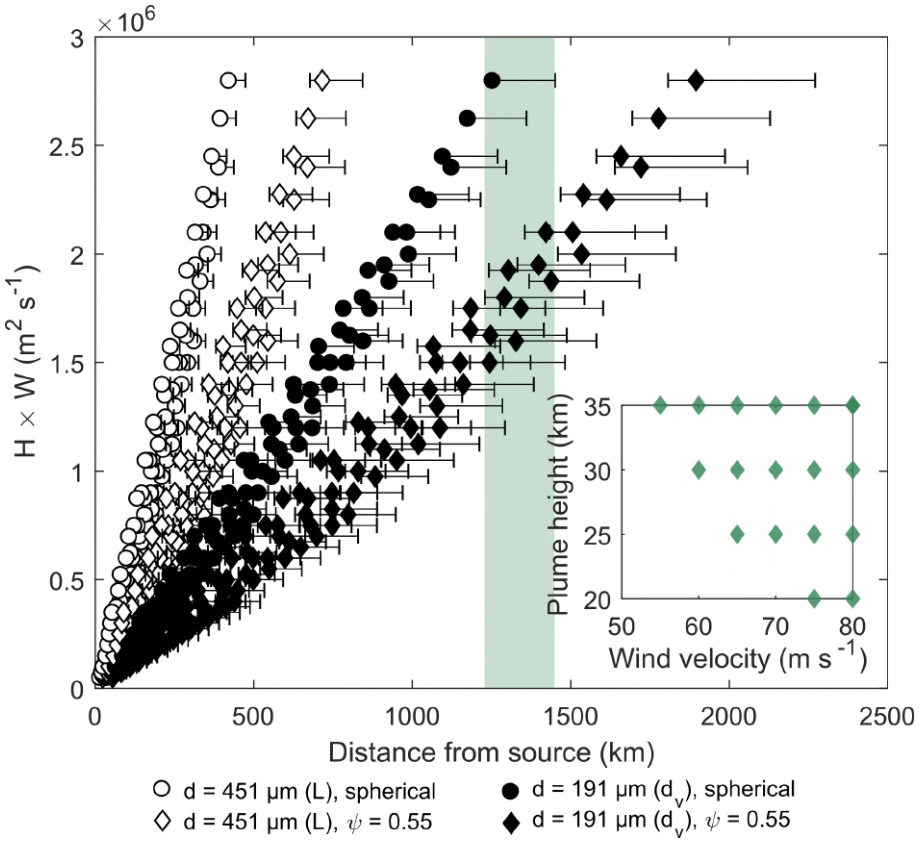

Figure B.5: Sensitivity of particle travel distances in a stratified atmosphere to altering the physical particle properties (d = 191 μm or d = 451 μm, and shape = spherical or ψ = 0.55), and transport conditions (plume height H and wind velocity W). For each of the four particles, 112 points are plotted, each for a different combination of H and W (see text for full ranges). The inset shows the range of H and W for which particles with d = 191 μm and ψ = 0.55 travelled as far or further than the great circle distance from Katla volcano to sample sites KV1-6 (green shading).

B.5 Uncertainty on physical particle properties

Uncertainty on the properties L, d_v, ψ and density could impact modelled travel distances. We translate our estimation of the uncertainties on these parameters into uncertainty on travel distance and show the uncertainty as horizontal error bars in Figure B.5. Uncertainty on travel distance is quantified by running an ensemble of three model scenarios: our measured particle properties; maximum size, shape and density; and minimum size, shape and density, the latter two cases using our calculated uncertainties. We determine that the uncertainty in travel distance caused by uncertainty in physical particle properties has a lesser impact than the choice of size and shape parameters used. The below sections explain how we quantified uncertainty for each physical parameter.

B.5.1 Particle size

Outliers in a size distribution can be due to inherent variability, measurement error or execution error (Bonadonna, 2006). In this study we account for these factors by taking a median of the 5 largest particles from each sample. The median is a robust parameter for dealing with outliers (Bonadonna, 2006). The number of largest particles taken for averaging does affect the result (Figure 3.8); consideration must therefore be given to the sample size. We find that for Sample KV3, for which we carried out the sample size analysis presented in Figure 3.8, increasing the number of particles averaged to 10 resulted in a decrease of 3.1% on L_5 and 3.4% on d_{v5}. We include particle sizes decreased by these percentages in our model ensemble (Figure B.5).

B.5.2 Particle shape

We quantified particle shape (sphericity ψ) by an optical microscopy method which approximates particles as flat plates. This method is associated with some error as it ignores particle surface roughness, which has however been shown to affect drag on a much lesser scale than particle shape (Bagheri and Bonadonna, 2016b). To estimate the uncertainty on ψ we took 2D approximate sphericity of volcanic ash particles from a mixed set of Icelandic eruptions (Rodger, 2018), which used the same optical microscopy method; we also scanned these particles in 3D using X-ray tomography (Saxby et al., in review) and so could directly compare 2D and 3D methods of measuring shape. We found a mean absolute discrepancy of 7% between the two methods and so we use $\pm$ 7% as upper and lower bounds on particle sphericity. This is likely to be an overly cautious estimation of error as the particles used in Rodger (2018) vary in shape, and are not all flat glass shards; higher surface roughness is expected to increase the discrepancy between ψ measured by the optical microscopy approximation and the tomography measurements.

B.5.3 Density

We calculated a best estimate particle density of 2456 kg m^{-3} using an average glass composition from measurements from Mangerud et al. (1984) and a glass density calculator (Iacovino, 2017). To determine a minimum and maximum density estimate to use as ensembles in the model (Figure B.5), we calculated the range of glass densities from all compositions for the silicic component of the Vedde ash in Mangerud et al. (1984). A major assumption is that there are no internal bubbles; we visually estimated using an optical microscope that the maximum bubble content was $\sim$ 10%. This maximum bubble volume, as well as the range in composition, gives a possible density range of 2186 – 2474 kg m^{-3}.

Chapter C

Supplementary Material for Chapter 4

C.1 Drag calculations

We calculate the drag coefficient C_D according to the analytical drag law for spheres (White, 1974):

$$C_D = C_1 + \frac{24}{\mathrm{Re}} + \frac{C_2}{1+\sqrt{\mathrm{Re}}} \tag{C.1}$$

where C_1 = 0.25 and C_2 = 6.0 for $Re < 5$ x 10^3. We also calculate C_D according to several semi-empirical schemes for non-spherical particles, where C_D is a function of one or more geometric shape descriptors (defined in the main text). In the drag law of Ganser (1993):

$$C_D = \frac{24}{\mathrm{Re}K_S}\left(1+0.1118\left[\mathrm{Re}\left(K_S K_N\right)\right]^{0.6567}\right) + \frac{0.4305K_N}{1+\frac{3305}{\mathrm{Re}K_S K_N}} \tag{C.2}$$

where K_N is a correction factor for turbulent flow:

$$K_N = 10^{1.84148(-Log\psi)^{0.5743}} \tag{C.3}$$

and K_S is a correction factor for laminar (Stokes) flow:

$$K_S = \frac{3}{1+2\psi^{-0.5}} \tag{C.4}$$

For the Bagheri and Bonadonna (2016b) drag law,

$$C_D = \frac{24K_S}{\mathrm{Re}}\left(1+0.125(\,Re\,K_N/K_S)^{2/3}\right) + \frac{0.46K_N}{1+\frac{5330}{\mathrm{Re}\,K_N/K_S}} \tag{C.5}$$

where:

$$K_S = (F_s^{\frac{1}{3}} + F_s^{-\frac{1}{3}})/2 \tag{C.6}$$

$$K_N = 10^{\alpha_2[-\log(F_N)]^{\beta_2}} \tag{C.7}$$

$$\alpha_2 = 0.45 + \frac{10}{\exp\left(2.5 \log\rho'\right) + 30} \tag{C.8}$$

$$\beta_2 = 1 - \frac{37}{\exp\left(3\log\rho'\right) + 100} \tag{C.9}$$

$$F_s = f\, e^{1.3}\, (\frac{d_v^3}{\mathrm{LIS}}) \tag{C.10}$$

$$F_N = f^2\, e\, (\frac{d_v^3}{\mathrm{LIS}}) \tag{C.11}$$

For the Dioguardi et al. (2018) drag law:

$$C_D = \frac{24}{\mathrm{Re}} \left(\frac{1-\Psi}{\mathrm{Re}} + 1\right)^{0.25} + \frac{24}{\mathrm{Re}} \left(0.1806\mathrm{Re}^{0.6459}\right) \Psi^{-\left(\mathrm{Re}^{0.08}\right)} + \frac{0.4251}{1 + \frac{6880.95}{\mathrm{Re}}\Psi^{5.05}} \tag{C.12}$$

Chapter D

NAME on JASMIN User Guide

Running NAME on JASMIN through Windows

Jen Saxby, Uni. Bristol, 2017

jennifer.saxby@bristol.ac.uk

** last updated 29/10/2018 (new JASMIN group workspace filepaths)

This is a step-by-step user guide designed for anyone who wants to get set up quickly on JASMIN and learn how to carry out a NAME run. It contains instructions on how to apply for all the necessary accounts and services, access the JASMIN virtual machines, carry out a NAME run, download the output and plot the results in Python. The example given is a volcanic ash dispersion run for Katla in Iceland.

1. Creating the required accounts

Step 1: Get a JASMIN account. Register as a new user at https://accounts.jasmin.ac.uk/. Your JASMIN account requires you to register a public SSH key (see section 2 for instructions). You may need to provide JASMIN with your IP address if you are not logging in from a known (.ac.uk) site.

Step 2: Go to https://accounts.jasmin.ac.uk/services/my_services/ and request access to the services you will need. These are:

- Login Services : jasmin-login
- Group Workspaces : name
- Project VMs : name
- Additional Services : nerctools

2. Creating an SSH key using PuTTY

The program PuTTY and related tools allow you to create SSH key pairs on Windows.

Step 1: Generate your key pair.

This uses the tool PUTTYgen (if you don't already have it, go to the PuTTY download page and select the link for puttygen.exe). Having installed PuTTYgen, start the application and a window should appear as follows:

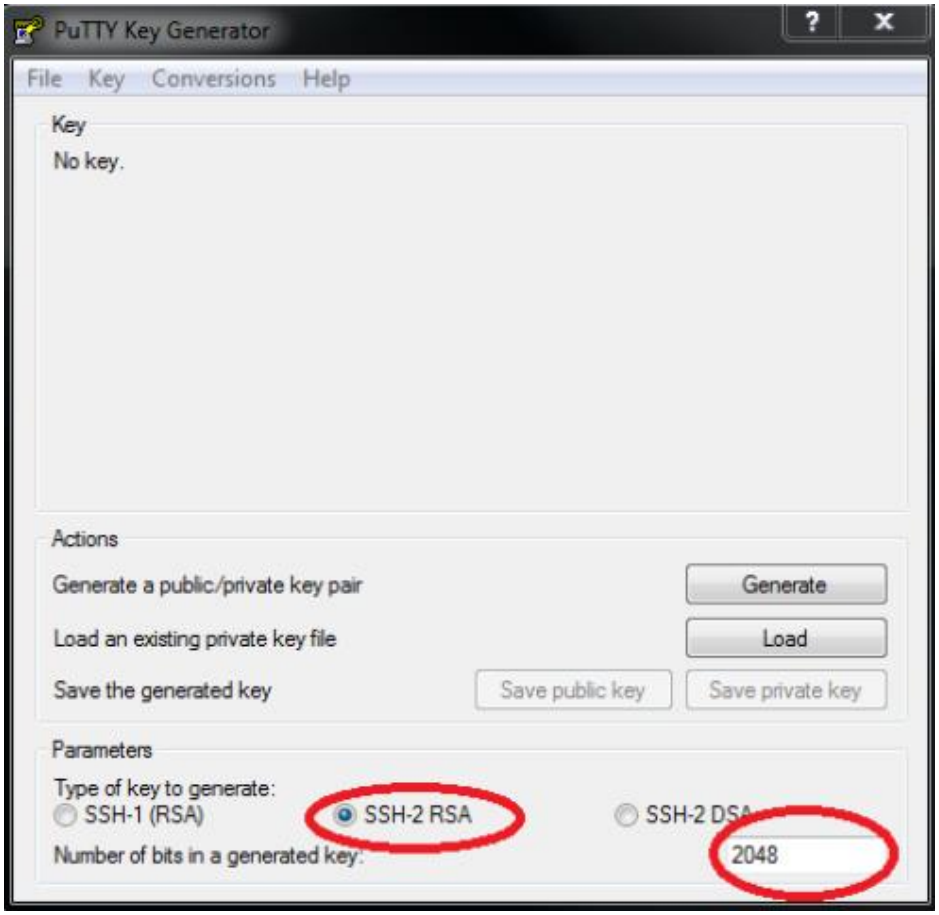

Please make sure that the type of key is set to "SSH-2 RSA" and the "number of bits in a generated key" is set to 2048 (see above).

Click on the **Generate** button and the window should show the following screen. Wiggle the cursor under the green bar to generate some randomness used to encrypt your private key. Once the green bar has filled up PuTTYgen will have created your key pair.

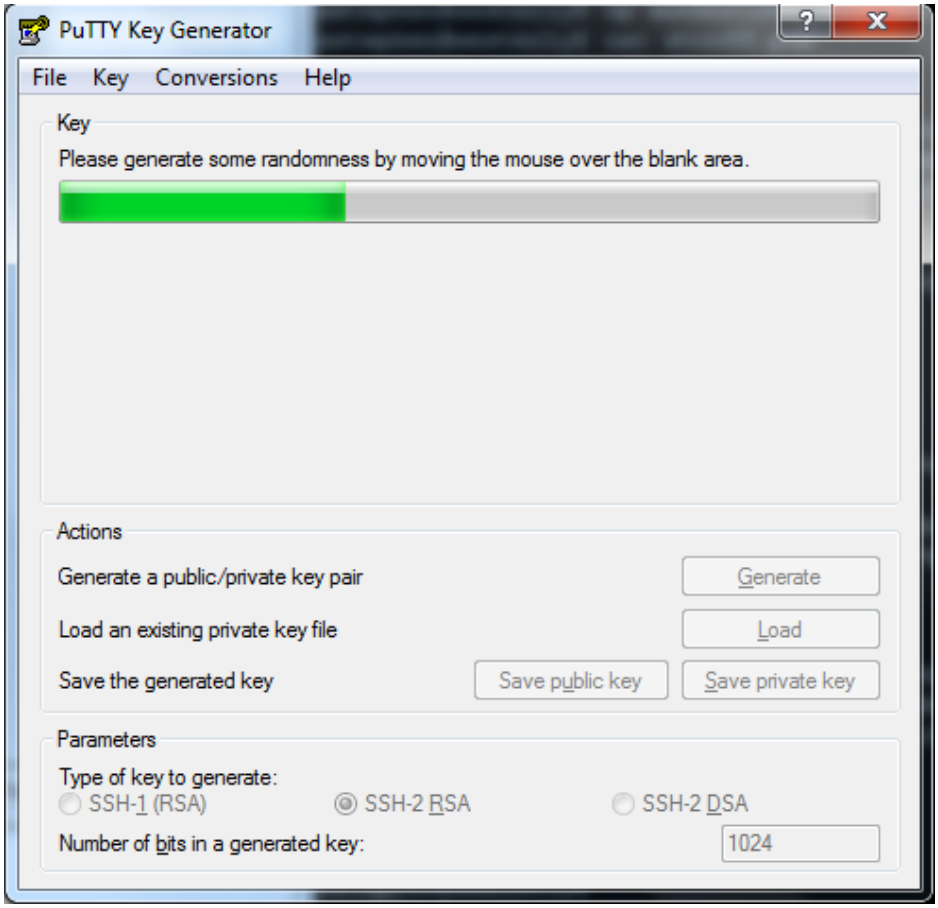

The following screen will appear which allows you to save your key pair. Firstly, make sure that you protect your private key with a suitable passphrase by typing it into the **Key passphrase** and **Confirm passphrase** inputs. You should then click **Save private key** button and save the key with a .ppk extension. Make a note of where you have saved the private key file.

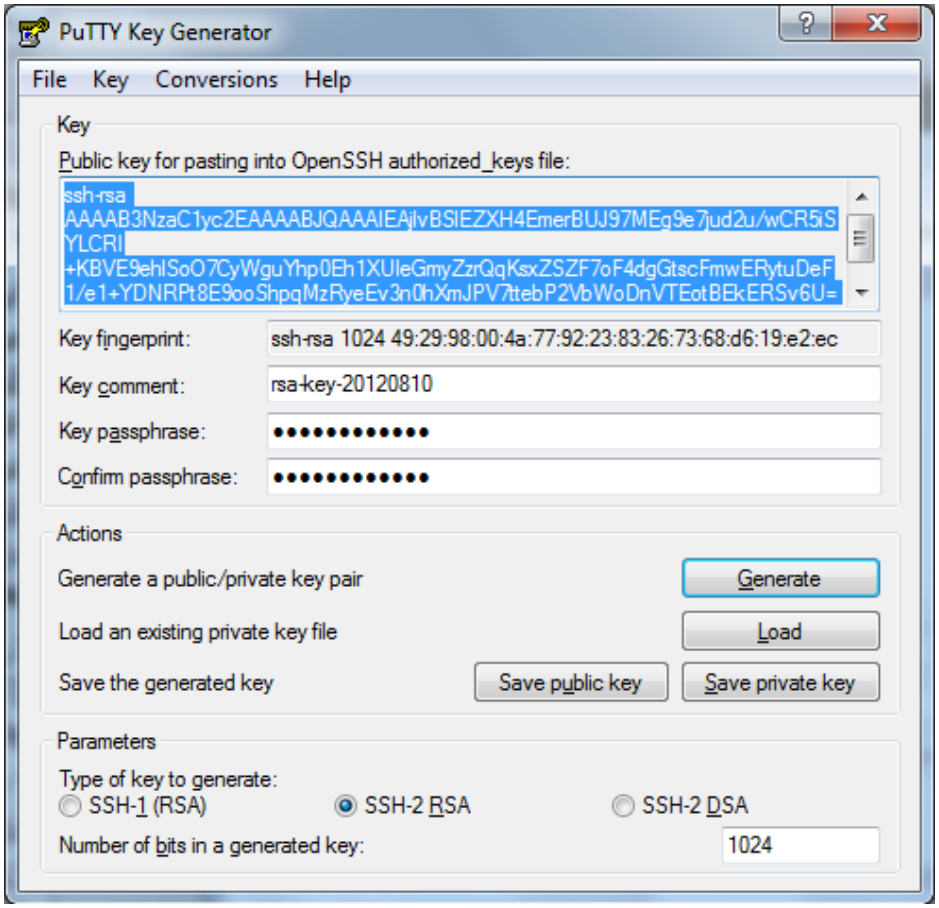

Step 2: Upload your public key file to JASMIN.

In order for you to be able to login to JASMIN servers using your public/private key pair your public key needs to be added to the JASMIN environment you wish to access. To do this, login at https://accounts.jasmin.ac.uk/ and click on **Update Key** next to **SSH Public Key**. Copy the text of your **public** key into the 'public key' box and press **Save**. Don't copy your **private** key, as this must never be disclosed to anyone. If the key is not valid or is less than the minimum length of 2048 bits then it will not be accepted. Note that only one key can be stored.

Step 3: Load your private key file into Pageant.

Open Pageant (a PuTTY authentication agent). The program may just appear as an icon in the bottom right of your taskbar. Right-click and click **Add Key**. Add your private key file (.ppk).

3. Logging onto JASMIN

Before logging in, your public key file must be uploaded to your JASMIN account and your private key file must be loaded into your Pageant session (as described in section 2).

Before logging onto any dedicated virtual machines, you must first access a JASMIN login gateway machine. The standard machine is jasmin-login1.ceda.ac.uk.

Open PuTTY (right-click on the icon, **New Session**) and connect to a JASMIN server using the address <your_username>@jasmin-login1.ceda.ac.uk (see image). The username you use will be the one you registered with JASMIN.

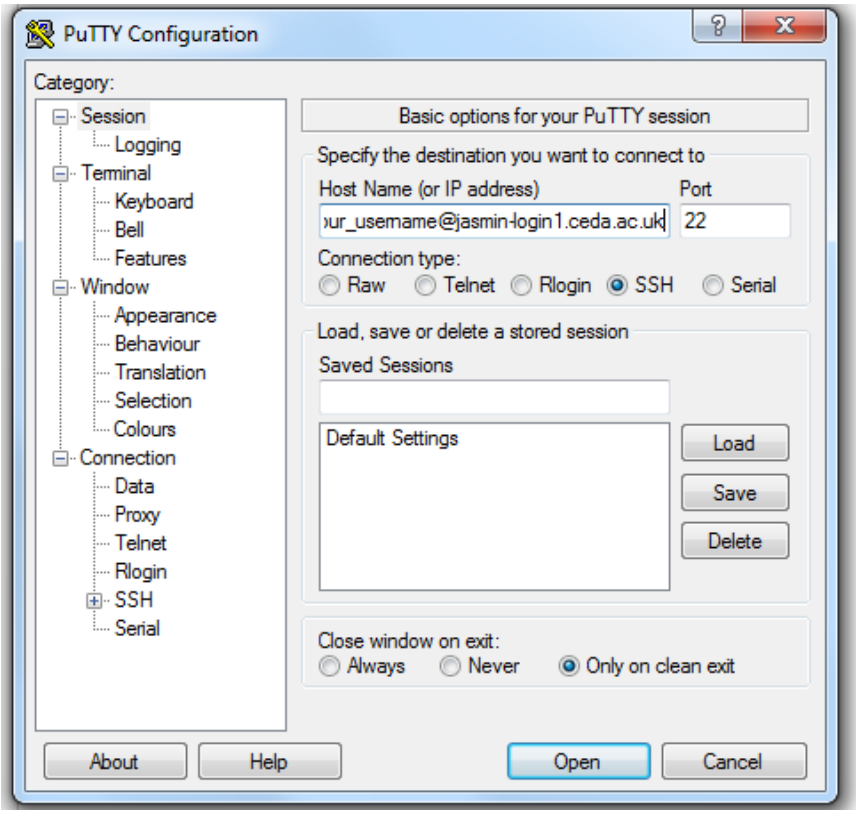

Make sure that '**Allow agent forwarding**' is checked (under **Connection** -> **SSH** -> **Auth**). This will allow you to hop to other machines using ssh without having to re-enter your key passphrase.

Logon to the remote server using the **Open** button.

When connected, you will see a black command window (see image) with some information about the JASMIN server, ending with the prompt:

```
[your_username@jasmin-login1 ~]$
```

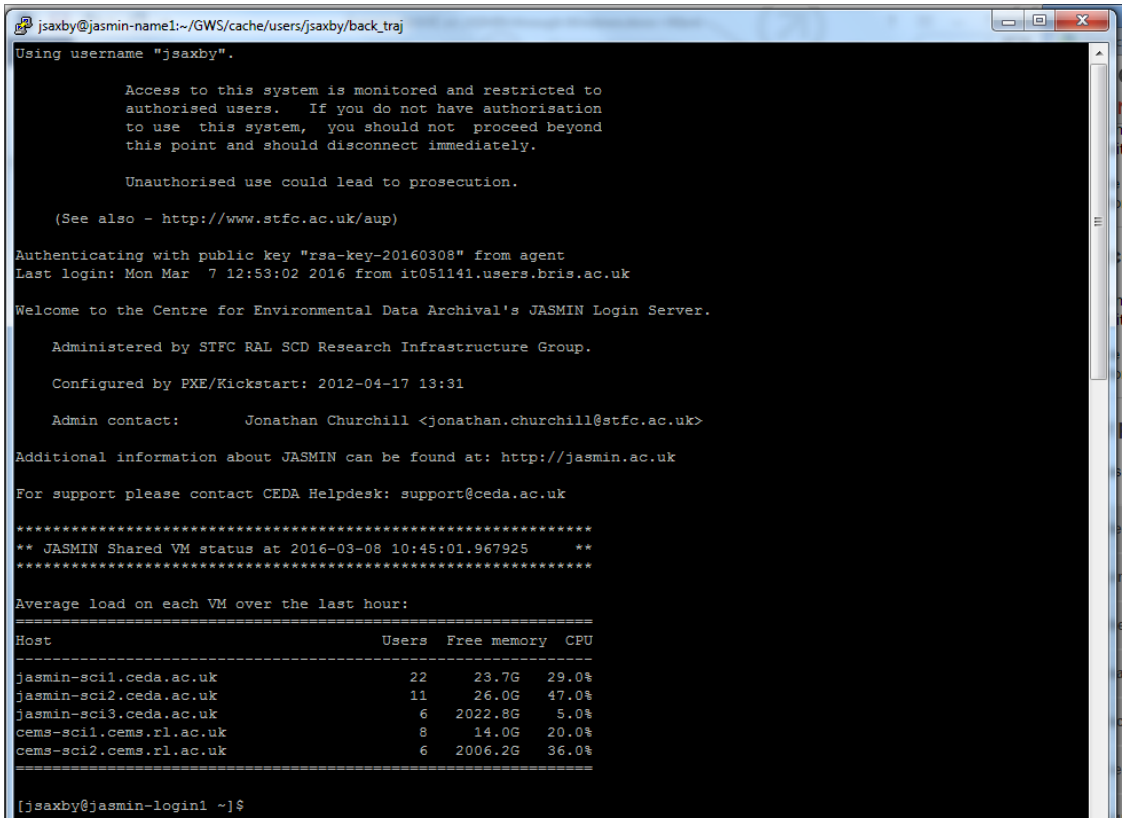

To port to a virtual machine from which you can run NAME, using ssh, type:

```
ssh jasmin-sci1.ceda.ac.uk
```

and press Enter. (You could also choose another one of the jasmin-sci servers based on the free memory shown, any of them will allow you to run NAME).

The prompt should change to:

```
[your_username@jasmin-sci1 ~]$
```

4. Getting started with NAME

Have a look in the NAME group workspace:

```
cd /gws/nopw/j04/name
```

(Type `ls` to list the files and subfolders contained). If this doesn't work, you'll need to go back to your JASMIN account and request access to the NAME group workspace resource.

Note that the `j04/name` folder is not visible until access is requested (e.g. by typing the whole filepath you want to access). This means that if you go to `/gws/nopw/j04/` and type `ls` the `name` folder will not appear.

The instructions for running NAME are located under the folder `"INSTRUCTIONS_ON_USAGE"` (versions v6.5 onwards are set up to run on the Lotus cluster, not on the NAME VMs themselves).

Your local working space is under `.../cache/users/[your-userid]` and the various code (NAME and example scripts) is under `.../code`

Hints:

`cd` = change directory (using it blank returns you to home)

`cd ../` = move up a level

`pwd` = prints your current working directory

`ls` = lists files and subfolders

Tip: You can access help for any command by typing `man` followed by the command, e.g. `man ls`. Press Enter to view more of the manual and press q to exit.

To transfer your own input files, you will need to use the dedicated transfer VM jasmin-xfer1.ceda.ac.uk. You can do all of the following via PuTTY by using ssh to access the transfer machine, but I prefer to use the Windows client WinSCP to upload files. It has the benefit of allowing easy navigation around the virtual machine using an interface similar to Windows Explorer, and it is also easier to open and edit text files. Login requires the host name (shown below). On clicking Login, it should prompt you for your username. Your private key must still be loaded in Pageant.

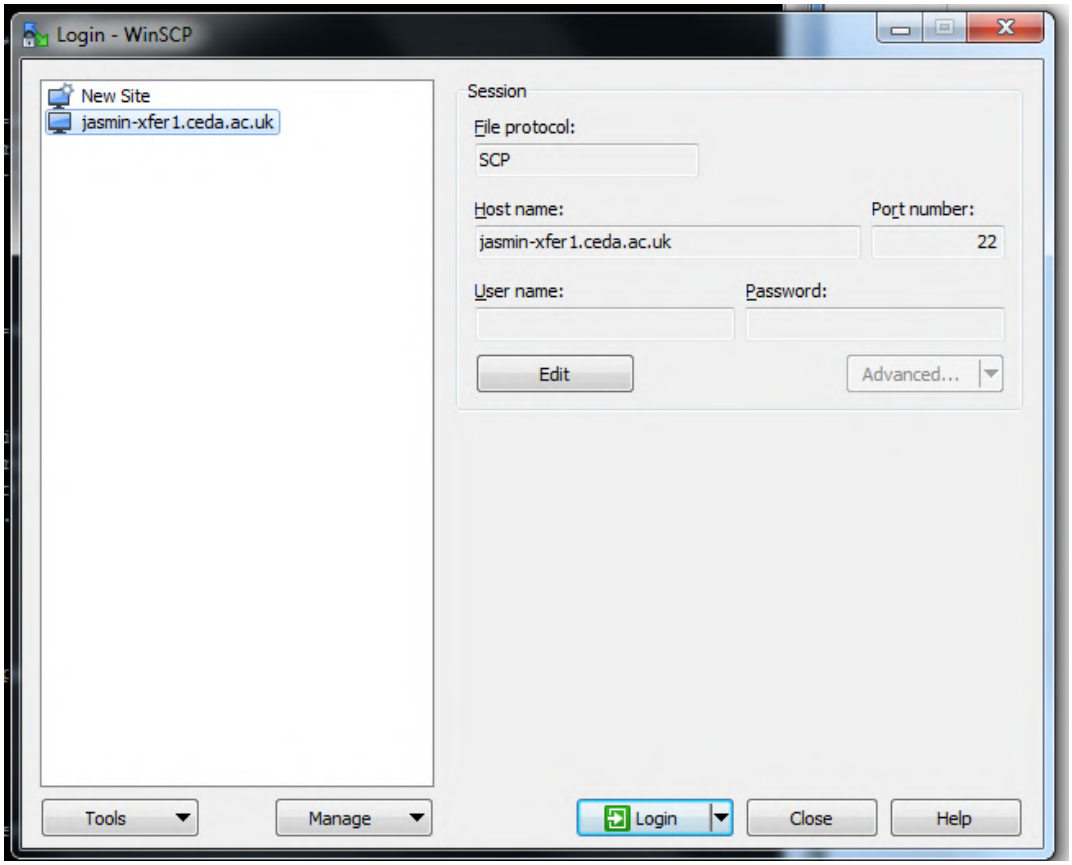

Go to / <root> (in the drop-down box, see below) and navigate to /home/users/[your-user-id]. This is where you will generally copy files you need to use. Drag and drop from your local directories in the left hand panel. Any files you copy here should be visible in the group workspace on any VM you then use, including the NAME VMs.

You could also navigate to /gws/nopw/j04/name/INSTRUCTIONS_ON_USAGE and download the running instructions for the latest version. The instructions for NAMEIII v6.5 are for an example back trajectory run.

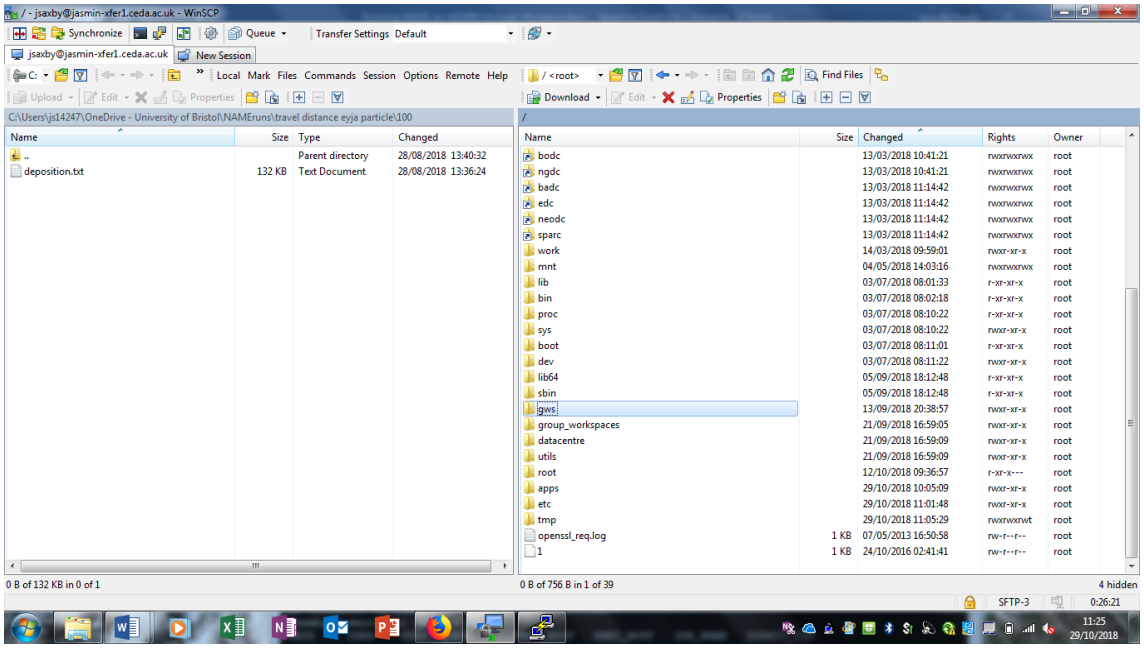

Navigate to your workspace on PuTTY by typing

```
cd /home/users/[your_username]
```

then type `ls` to check if the files you transferred are there.

You can store output files etc. on the NAME group workspace, at:

```
/gws/nopw/j04/name/cache/users/[your_username]
```

To run NAME:

The easiest way to run NAME is to type (NAME executable file) (your input file) into PuTTY, e.g.:

```
./nameiii_64bit.exe VolcanoRun_template_NAMEvn6.5.txt
```

An example volcanic ash dispersion run is set up under /gws/nopw/j04/name/cache/users/jsaxby/volcano_example. This example run contains the script katla_queue.scr, which submits the job to the Lotus queue; katla_run.scr, which submits the input file and runs the job (it's formatted the same as the command above); and the input file, KATLA_NAME_INPUT.txt. It also contains a script called MetRestore, which tells NAME how to deal with your met data, and a Python script which you'll use later for plotting. Copy the queue script, run script, input file, and met restore script to your own directory (/home/users/[your_username]). If you are not very familiar with bash, this is much easier to do on WinSCP than on PuTTY. Right click, 'Duplicate' and make sure to check 'Duplicate via local temporary copy'. Make sure to use *.* as a placeholder for the filenames being copied, so 'Target remote path' should be set to /home/users/[your_username]/*.*

Make sure you have permission to execute these files once they are in your user space. In WinSCP you can right-click, select 'Properties' and make sure R, W, and X (read, write, execute) are checked for 'Owner'.

When the files are in your local directory, you'll want to change the filepaths in **the input, queue, and run scripts** to reflect your own file setup. In the input file the filepaths you need to change are in the following blocks. You should just be able to replace my username with yours.

```
Output Options: Folder
NWP Met Module Instances: Restore Met Script, Met Folder
```

When you're ready to run, run the queue script by navigating to its directory in PuTTY and typing:

```
. katla_queue.scr
```

Type `bjobs` to see how the job is getting on. It will say 'pend' when your job is submitted to the queue; 'run' when it's running; and 'no unfinished job found' when done. When it's finished running take a look at the folder you set the outputs to save in. If you're looking on WinSCP you may have to refresh before they appear. Take a look at some of the text files just to check they're not empty. NAME will also produce 'error' and 'log' files associated with each job; you can check in these if your outputs don't appear or don't look right.

The run is an imaginary eruption of Katla volcano, Iceland in May 2010. The output covers the eruption and the next 72 hours of ash dispersion through the atmosphere.

Plotting your outputs:

When you've had a look at the outputs, download them from JASMIN along with the input file you've used to produce them (it is much easier if you save your outputs along with the input file which produced them every time!) Download the Python script ToTCol_Subplot.py from the volcano_example folder. This example plots six plots, one every twelve hours for three days, showing total column mass loading, i.e. how much ash is present in every 1m x 1m horizontal grid cell for the whole of the vertical model domain.

(N.B. Python is also available on JASMIN, and you may prefer to do your plotting remotely. These instructions detail how to do it locally on your own machine – I prefer this as it doesn't mean connecting to JASMIN if you want to plot something again).

If you are not familiar with Python plotting, I would recommend a Python distribution called Anaconda. It contains many scientific packages you'll need for plotting NAME outputs as well as a really useful development environment, Spyder, where you can edit and run scripts. The only extra package you'll need is the Met Office-developed set of plotting tools, Iris.

Download Anaconda from:

https://www.continuum.io/downloads

and choose the Python 2.7 version (it's older but has better functionality with Iris).

Anaconda comes with a package manager called conda that will download and install extra packages for you. You can use this from a Windows command prompt. Once Anaconda is installed, open your command prompt (Start > All Programs > Accessories > Command Prompt) and type

```
conda install -c scitools iris
```

Hit enter. It will ask you to approve the installation of new packages (see below) – type y and hit enter.

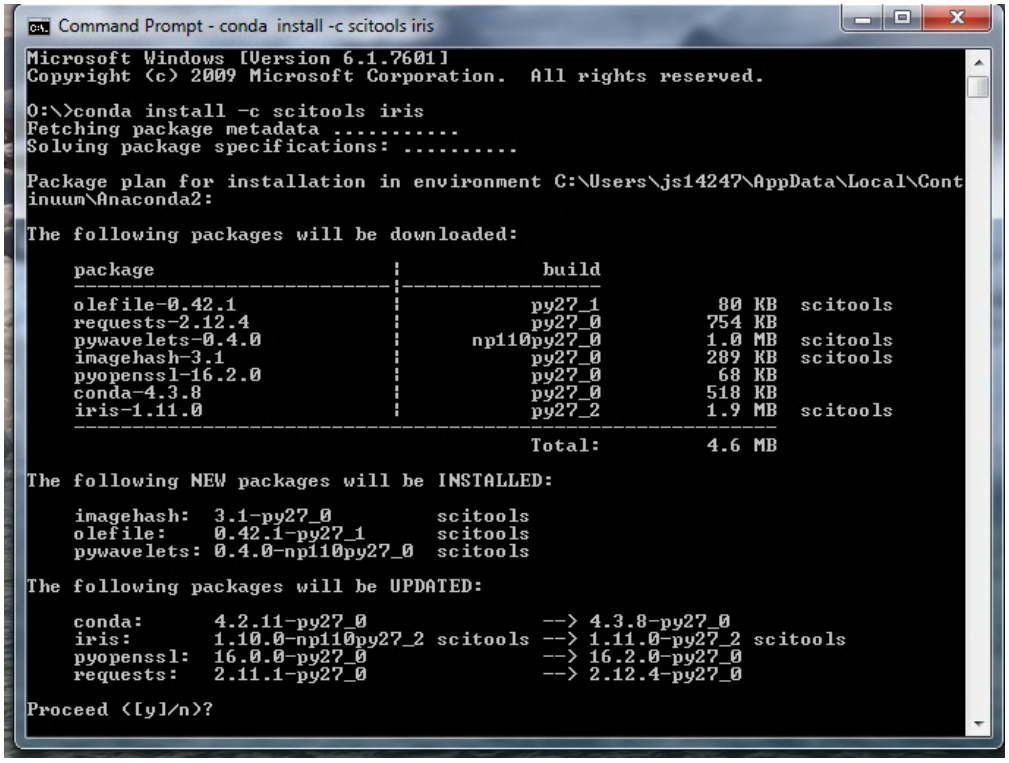

If there is an error installing one of the other packages which Iris depends on, try installing that package alone, e.g. `conda install -c scitools cartopy` if cartopy wouldn't install correctly – then try Iris again in the same way. Once you have Iris, open Spyder. You can type `import iris` into the command window in Spyder to check that Iris has installed successfully (if you don't get an error it's fine – see below)

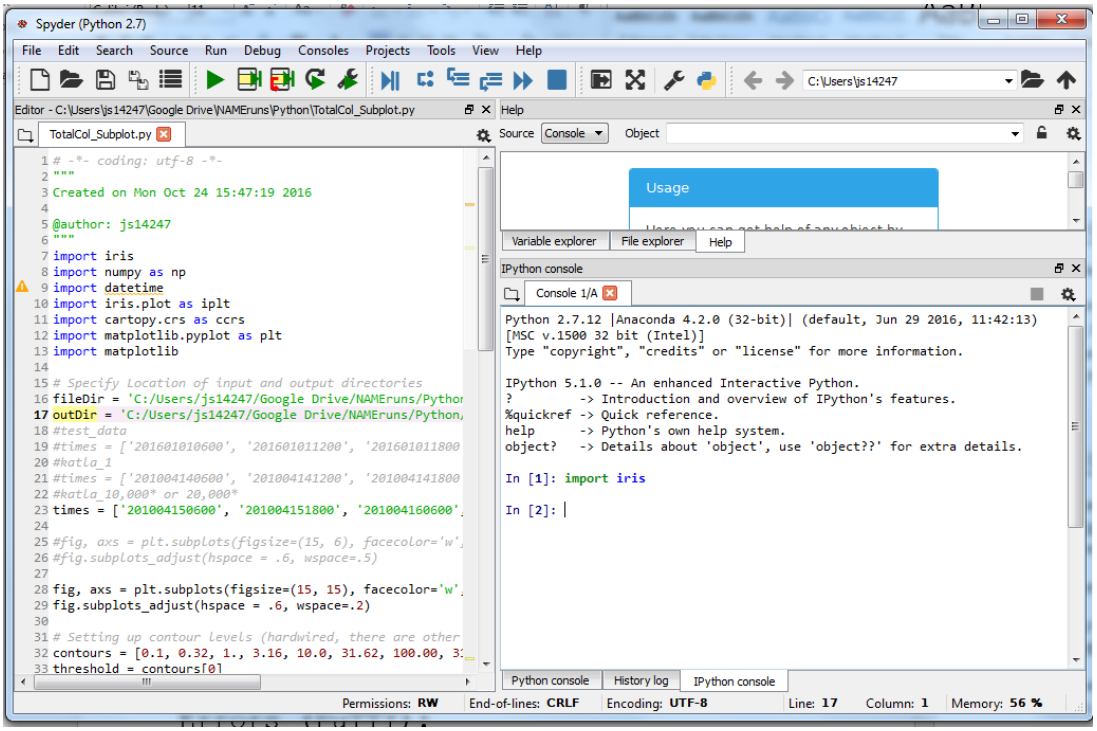

Open TotCol_Subplot.py in Spyder. You'll see that in the first few lines of code it names a file directory (fileDir) – this should be where your NAME output text files are stored. It also names an output directory (outDir) – this is where the code will save a pdf file of your output. (For my example, they are both set to the same directory). Modify the filepaths to suit your system, and then try plotting by pressing run (▶). It will take about 5 minutes to display an image in the command window because the files in this example are quite large. Check that the pdf has been created in your output directory. Your output should look like:

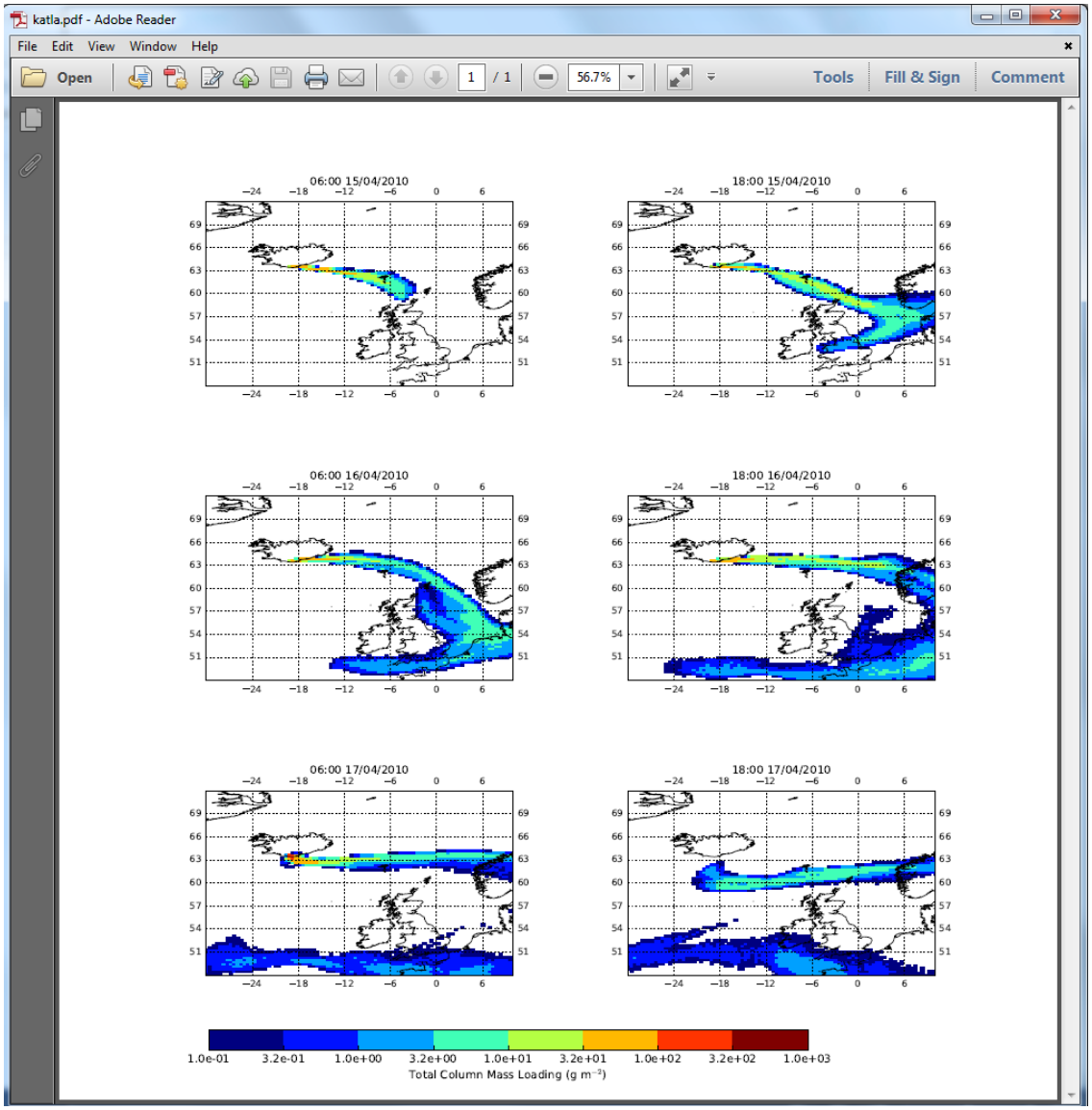
katla.pdf - Adobe Reader
File Edit View Window Help
Open
1 / 1
56.7%
Tools
Fill & Sign
Comment
06:00 15/04/2010
18:00 15/04/2010
06:00 16/04/2010
18:00 16/04/2010
06:00 17/04/2010
18:00 17/04/2010
−24 −18 −12 −6 0 6
69 66 63 60 57 54 51
1.0e-01 3.2e-01 1.0e+00 3.2e+00 1.0e+01 3.2e+01 1.0e+02 3.2e+02 1.0e+03
Total Column Mass Loading (g m⁻²)

Recompiling NAME on JASMIN

Most people will not need to recompile NAME – you only need to do this if you want to make changes to the code.

Firstly, copy NAME to your own directory (the whole NAMEIII_v7_2_lotus directory, or that for whichever version you are using). Make sure you have read/write/execute permissions for each file in that folder. Make whichever changes you need to make to your copy of the NAME code. Change directory so you're in the Code_Preprocessor folder before you move on (otherwise the preprocessing step will not work).

Input these commands into PuTTY (for lines 3 and 4, replace filepaths with your own, pointing to wherever your copied version of NAME is):

```
/bin/bash

module load intel/13.1

.
/home/users/jsaxby/volc_tests/NAMEIII_v6_5_lotus_white_minus/NAMEIII_v6_5/C
ode_Preprocessor/LinuxIntelRelease

cd
/home/users/jsaxby/volc_tests/NAMEIII_v6_5_lotus_white_minus/NAMEIII_v6_5/C
ode_NameIII

make clean

make
```

N.B. The NAME code is set up at the moment to compile the parallel executable. To setup your run to work with the parallel .exe, you need this text at the top of your run script (not queue script):

```
# setup for running with parallel executable

#/bin/ksh

# Set system variables

. /etc/profile

# Load Intel compiler module

module load intel/13.1
```

Also, just check that the parallel .exe has been updated (the file nameiii_64bit_par.exe in Executables_Linux).

Moving/copying met data from JASMIN

In this example I want to copy all the met data from April 2010 to my home directory, from which I can then download it.

```
cd /gws/nopw/j04/name/met_archive/Global/UMG_Mk6PT
```

```
cp MO201004*.UMG_Mk6_L59PT2.pp.gz /home/users/jsaxby
```

Errors (PuTTY):

'Permission denied'

On PuTTY, type chmod, then a three-letter code followed by the name of the file you don't have permission to read/write/execute, e.g. `chmod 777 nameiii_64bit.exe`.

(n.b. the code 777 will allow anyone to read, write and execute the file – look up a list of chmod codes if you're not sure which permissions you want to update)

Or, on WinSCP you can right-click the file, select 'Properties' and make sure R, W, and X (read, write, execute) are checked for 'Owner'.

'Segmentation fault (core dumped)'

The program is trying to access more memory than it is currently permitted to use. On PuTTY, type `ulimit -s unlimited` to increase the amount of memory Linux will use.

To logout:

Type 'logout', and hit Enter, twice to be logged out of the NAME VM and then the JASMIN server.

To cite the JASMIN team:

http://ieeexplore.ieee.org/xpl/articleDetails.jsp?arnumber=6691556

Lawrence, Bryan N., Victoria L. Bennett, J. Churchill, M. Juckes, Philip Kershaw, Stephen Pascoe, Sam Pepler, M. Pritchard, and Adrian Stephens. "Storing and manipulating environmental big data with JASMIN." In *Big Data, 2013 IEEE International Conference on*, pp. 68-75. IEEE, 2013.

Information sources:

NAME on JASMIN, http://collab.metoffice.gov.uk/twiki/bin/view/NAME/NAMEonJASMINGettingStarted (Ag Stephens, 2014)

SSH Keys (Windows), http://www.jasmin.ac.uk/workflow/ssh-keys/ssh-key-windows/

Logging onto JASMIN, http://www.jasmin.ac.uk/workflow/logging-on-to-jasmin/logon-windows/

PuTTY user manual, http://tartarus.org/~simon/putty-snapshots/puttydoc.txt (Simon Tatham, 1997-2016)

Basic vi Commands, https://www.cs.colostate.edu/helpdocs/vi.html

Andrew Jones (Met Office), pers. comm.

Chapter E

The effect of centre of mass on the aerodynamics of falling particles

This appendix is a summary of the main findings on particle centre of mass from the two Master's projects I supervised (Tennant, 2017; Rodger, 2018). The analysis presented here consists of my reanalysis of particle settling videos and 3D images collected by Hannah Rodger as part of her Master's thesis; and mine and Elly Tennant's reanalysis of data collected by Elly Tennant as part of her Master's project.

E.1 Motivations

Many shape-dependent drag laws are calibrated using regular analogue particles with uniform density (e.g., Ganser, 1993). Howevever, volcanic ash particles can contain bubbles or crystals of different density to the surrounding glass; this could cause the particle's centre of mass to be far removed from the geometric centre. An example of volcanic ash particles with irregular density distributions is shown in Figure E.1. This study tests the hypothesis that centre of mass displacement affects secondary motions, and that those secondary motions can affect terminal velocity.

E.2 Analogue particles

E.2.1 Methods

The settling column setup and image analysis was the same as reported in Chapter 2; additional experiments not reported in that chapter used PVC analogue particles with internal air voids created by drilling voids and then plugging the entrance with a PVC cap attached using glue. Voids were

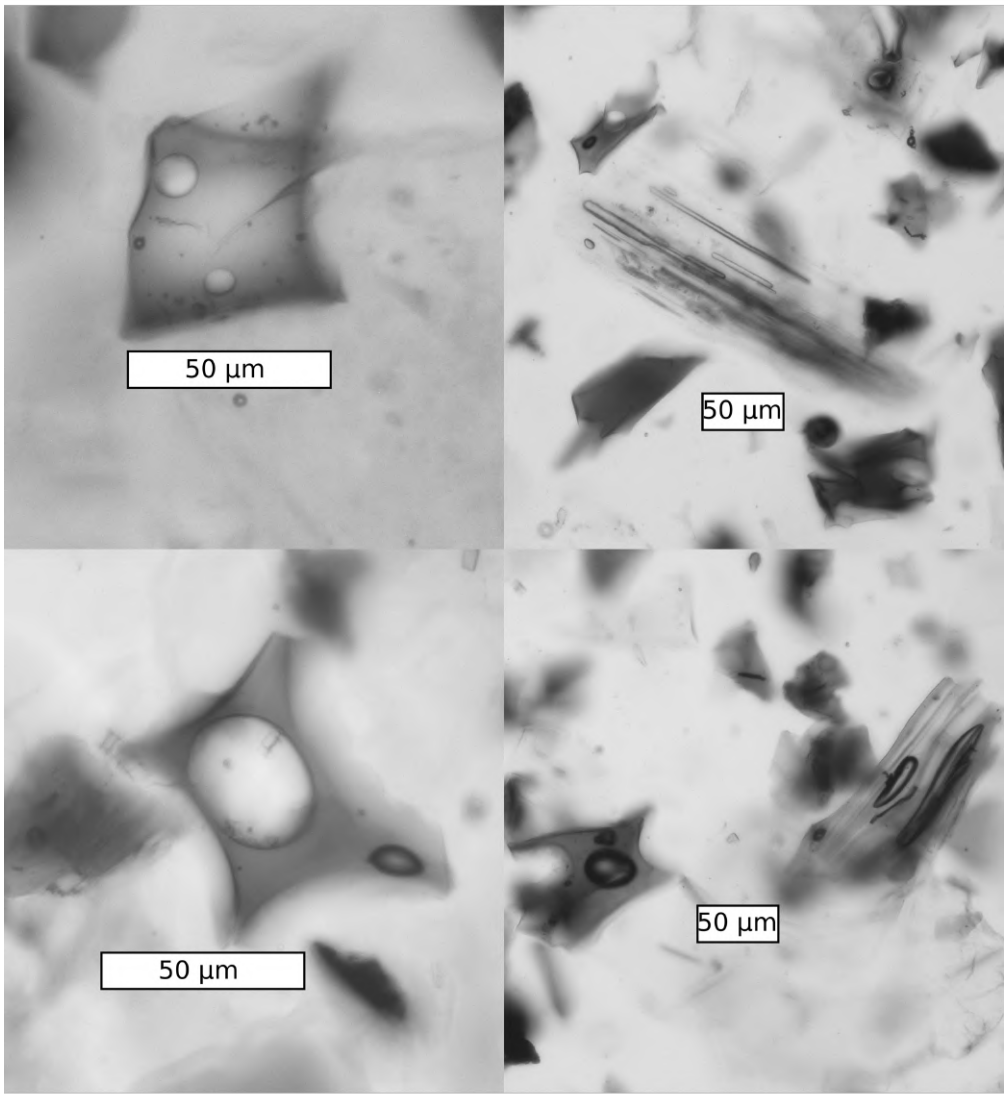

Figure E.1: Optical microscope images of ash particles with internal air bubbles. From the 12.1 ka BP Vedde ash (Mangerud et al., 1984), Katla volcano, Iceland.

placed on the extremities of particles (e.g. at one end of the long axis of elongated particles) in order to maximise the displacement of the centre of mass from the geometric centre. Particle geometries are given in Figure E.2. To check void dimensions after particle construction and to calculate centre of mass displacement, we reconstructed 3D volumes obtained by X-ray computed microtomography (CT) scans carried out using a Nikon XTH225ST scanner at the University of Bristol. Air voids have far lower X-ray attenuation than plastic or aluminium, meaning the resulting 3D datasets were easy to segment. We used Avizo 3D image analysis software to calculate the relative position of each particle's centre of mass; we then artificially filled the voids and recalculated centre of mass position. The difference in the two position measurements gives the absolute centre of mass displacement caused by the addition of the void. To convert to a dimensionless (particle size-independent) quantity we then divided absolute centre of mass displacement by the cube root of particle volume. The resulting dimensionless centre of mass displacements are given in Figure E.2. We refer to particles with a void as 'non-uniform' and particles without as 'uniform'.

The experiments were designed to create a Reynolds number (Re) range spanning the Stokes ($Re < 0.1$), intermediate ($Re \sim 0.1 - 1000$) and turbulent ($Re > 1000$) flow regimes, with particular focus on the intermediate regime as this is where secondary motions first develop (Pettyjohn and Christiansen, 1948; Jayaweera and Mason, 1965; Willmarth et al., 1964). Therefore, in addition to the fluids used in Chapter 2, Tennant (2017) also used glycerine solutions of 70% and 30% ($2 < Re < 349$). Densities and viscosities of glycerine-water solutions were calculated after Cheng (2008) and checked using the HAKKE Rheostress rheometer at the University of Bristol. All particles were dropped with their maximum projected area facing the direction of fall.

Theoretical velocities were calculated using the Ganser (1993) drag law for non-spherical particles; we used this to normalise the effect of density changes resulting from the inclusion of voids, and so isolate the impact of centre of mass.

E.2.2 Secondary motions and drag

Non-uniform particles settling in the Stokes regime generally have lower C_D than uniform particles; we suggest this is due to the positioning of the voids meaning that particles fall preferentially with minimum projected area in the fall direction (Figure E.3). Non-uniform particles also begin to exhibit secondary motions at lower Re than uniform particles; and they show a more diverse range of motions. While uniform particles oscillate about a downward trajectory, non-uniform particles also exhibit lateral gliding.

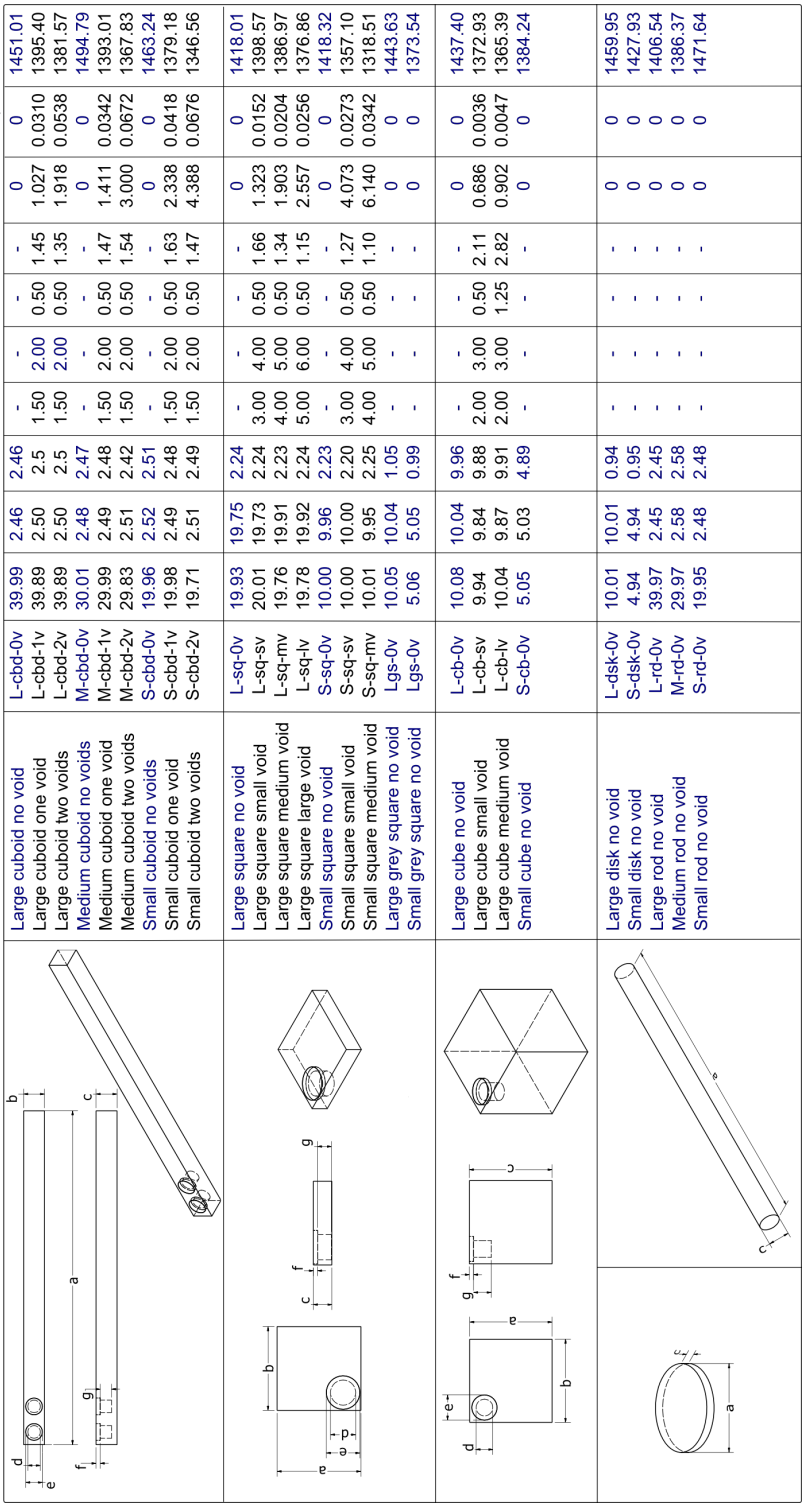

		Dimensions (mm)								Vol % voids	CoM disp	p (kg/m3)
		a	b	c	d	e	f	g				
Large cuboid no void	L-cbd-0v	39.99	2.46	2.46	-	-	-	-		0	0	1451.01
Large cuboid one void	L-cbd-1v	39.89	2.50	2.5	1.50	2.00	0.50	1.45		1.027	0.0310	1395.40
Large cuboid two voids	L-cbd-2v	39.89	2.50	2.5	1.50	2.00	0.50	1.35		1.918	0.0538	1381.57
Medium cuboid no voids	M-cbd-0v	30.01	2.48	2.47	-	-	-	-		0	0	1494.79
Medium cuboid one void	M-cbd-1v	29.99	2.49	2.48	1.50	2.00	0.50	1.47		1.411	0.0342	1393.01
Medium cuboid two voids	M-cbd-2v	29.83	2.51	2.42	1.50	2.00	0.50	1.54		3.000	0.0672	1367.83
Small cuboid no voids	S-cbd-0v	19.96	2.52	2.51	-	-	-	-		0	0	1463.24
Small cuboid one void	S-cbd-1v	19.98	2.49	2.48	1.50	2.00	0.50	1.63		2.338	0.0418	1379.18
Small cuboid two voids	S-cbd-2v	19.71	2.51	2.49	1.50	2.00	0.50	1.47		4.388	0.0676	1346.56
Large square no void	L-sq-0v	19.93	19.75	2.24	-	-	-	-		0	0	1418.01
Large square small void	L-sq-sv	20.01	19.73	2.24	3.00	4.00	0.50	1.66		1.323	0.0152	1398.57
Large square medium void	L-sq-mv	19.76	19.91	2.23	4.00	5.00	0.50	1.34		1.903	0.0204	1386.97
Large square large void	L-sq-lv	19.78	19.92	2.24	5.00	6.00	0.50	1.15		2.557	0.0256	1376.86
Small square no void	S-sq-0v	10.00	9.96	2.23	-	-	-	-		0	0	1418.32
Small square small void	S-sq-sv	10.00	10.00	2.20	3.00	4.00	0.50	1.27		4.073	0.0273	1357.10
Small square medium void	S-sq-mv	10.01	9.95	2.25	4.00	5.00	0.50	1.10		6.140	0.0342	1318.51
Large grey square no void	Lgs-0v	10.05	10.04	1.05	-	-	-	-		0	0	1443.63
Small grey square no void	Lgs-0v	5.06	5.05	0.99	-	-	-	-		0	0	1373.54
Large cube no void	L-cb-0v	10.08	10.04	9.96	-	-	-	-		0	0	1437.40
Large cube small void	L-cb-sv	9.94	9.84	9.88	2.00	3.00	0.50	2.11		0.686	0.0036	1372.93
Large cube medium void	L-cb-lv	10.04	9.87	9.91	2.00	3.00	1.25	2.82		0.902	0.0047	1365.39
Small cube no void	S-cb-0v	5.05	5.03	4.89	-	-	-	-		0	0	1384.24
Large disk no void	L-dsk-0v	10.01	10.01	0.94	-	-	-	-		0	0	1459.95
Small disk no void	S-dsk-0v	4.94	4.94	0.95	-	-	-	-		0	0	1427.93
Large rod no void	L-rd-0v	39.97	2.45	2.45	-	-	-	-		0	0	1406.54
Medium rod no void	M-rd-0v	29.97	2.58	2.58	-	-	-	-		0	0	1386.37
Small rod no void	S-rd-0v	19.95	2.48	2.48	-	-	-	-		0	0	1471.64

Figure E.2: Physical properties of non-uniform PVC analogue particles. Particle properties given are: a = particle long axis, b = intermediate axis, c = short axis, d = void diameter, e = cap diameter, f = cap thickness, g = void depth, CoM disp = particle centre of mass displacement (dimensionless). Uniform particles are shown in blue. Figure by Elly Tennant.

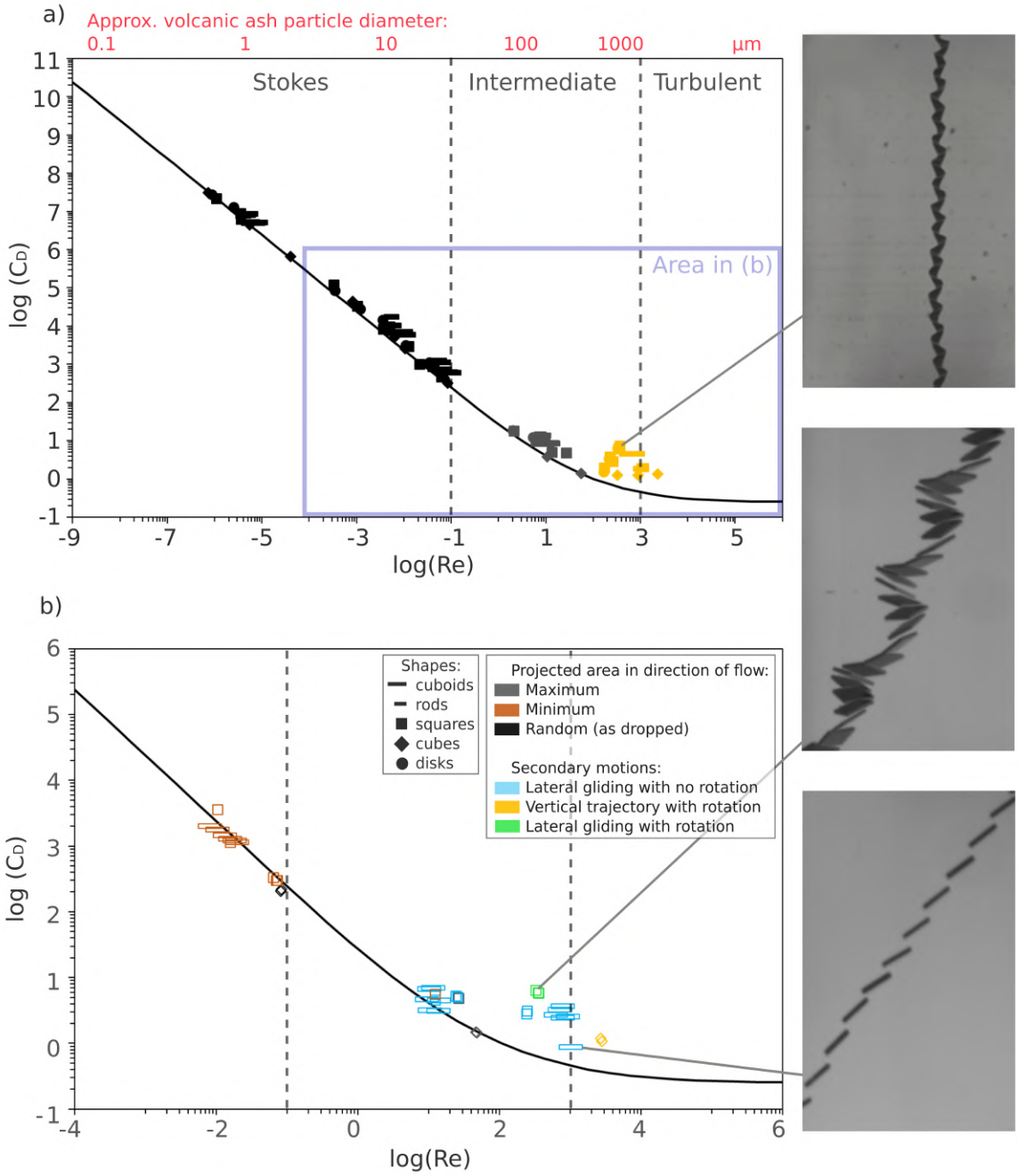

Figure E.3: $Re - C_D$ relationship for a) uniform particles (data from Chapter 2) and b) non-uniform particles (data from Tennant (2017)). Secondary motions are classified into several categories based on the presence or absence of lateral gliding and particle rotation; an example image-stacked trajectory for each category is shown. Where no secondary motions are observed the particles are categorised by their projected area in direction of flow.

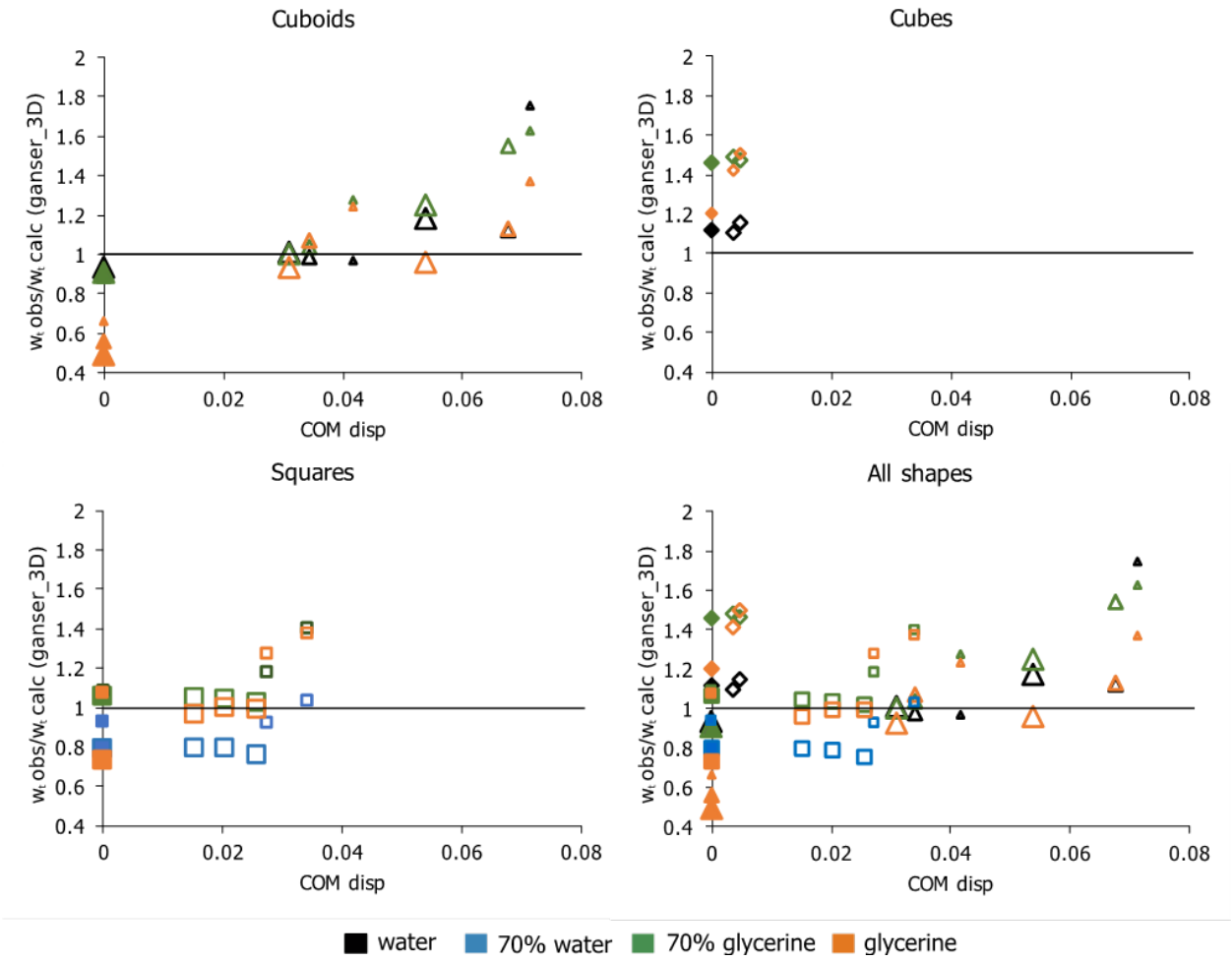

Figure E.4: Measured settling velocities (w_t obs) divided by settling velocities calculated using the drag law of Ganser (1993) (w_t calc (ganser_3D)), for uniform and non-uniform particles (data from Tennant (2017)). The solid line shows agreement between the Ganser (1993) law and the measured velocities; particles above the line have higher velocity than anticipated by Ganser (1993). Filled symbols indicate uniform particles; open symbols are non-uniform particles. Figure by Elly Tennant.

E.2.3 Effect on terminal velocity calculations

For the analogue particle set used, a higher centre of mass displacement results in higher settling velocities (normalised relative to velocities calculated using Ganser (1993)); relative velocities are shown in Figure E.4). The Ganser (1993) drag law produces an overall mean absolute percentage error of 23% on terminal velocity for the data presented in Figure E.4.

E.3 Volcanic ash particles

E.3.1 Methods

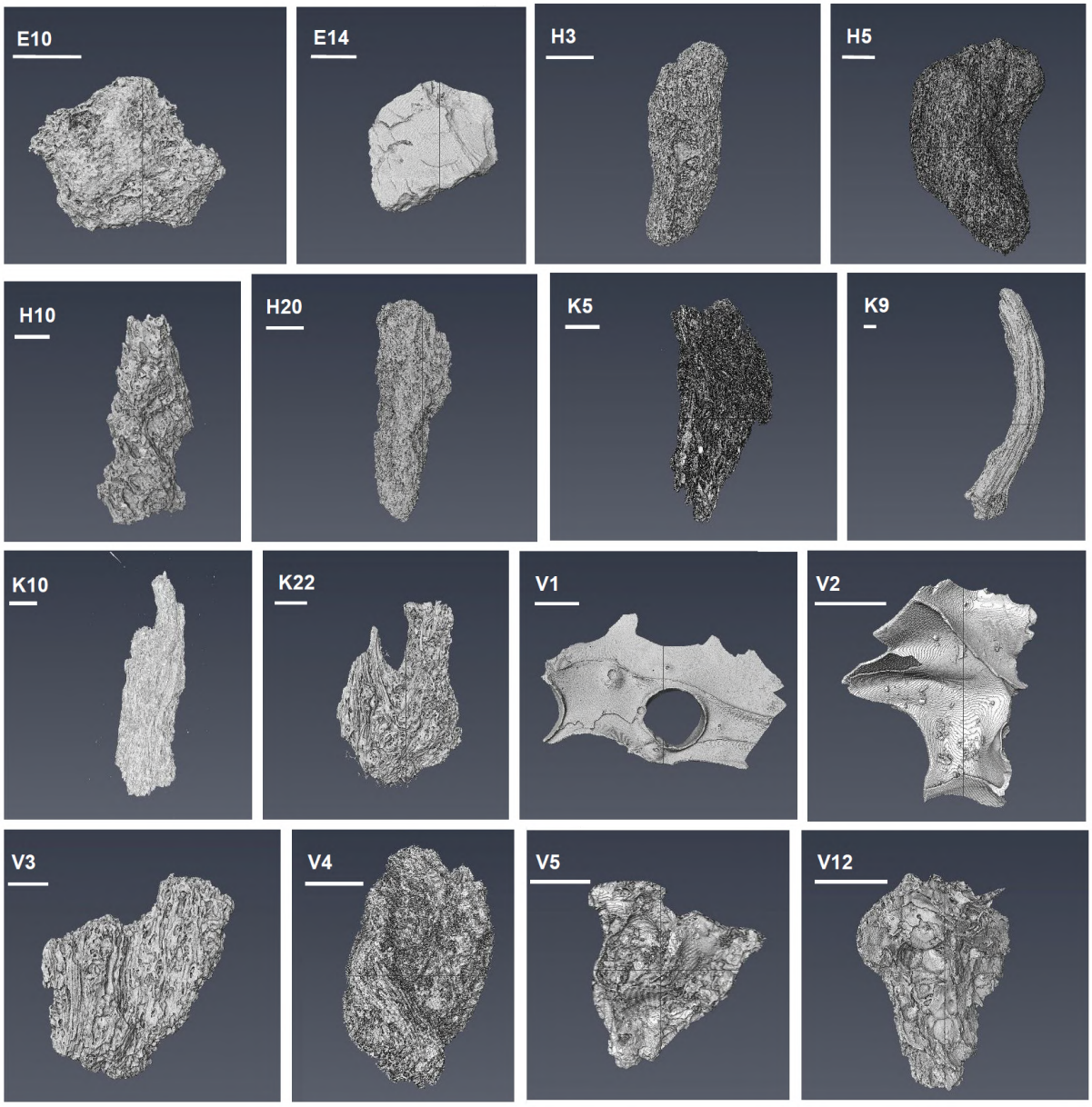

Figure E.5: X-ray CT images of volcanic ash particles scanned in high resolution (see Chapter 4 for details of scan parameters). Scale bar = 0.5 mm. Modified from Rodger (2018).

The volcanic ash particle results presented here (Figure E.6) used the same settling column setup and volcanic ash particles as reported in Chapter 4. The particles used are the 16 particles scanned at high resolution; reconstructions from the 16 scans are shown in Figure E.5. From the tomography data, we calculated centre of mass position for each particle, and then repeated the

calculation after artificially filling all internal voids (bubbles) using Avizo software. We calculated dimensionless centre of mass by the same calculation as for analogue particles. The results do not take into account the effect of crystal content on centre of mass; we expect this to be a lesser effect than bubble content as a) the ash particles are mostly poorly crystalline and b) the crystal-glass density ratio will be much lower than the bubble-glass density ratio.

E.3.2 Results

The particles have centre of mass displacements of 6×10^{-5} – 0.052. Within this range we found no correlation between centre of mass displacement and terminal velocity. Other factors affecting velocity (size, shape and density) are assumed to be accurately corrected for using the drag law of Ganser (1993). Measured velocities relative to Ganser (1993) are given in Figure E.6.

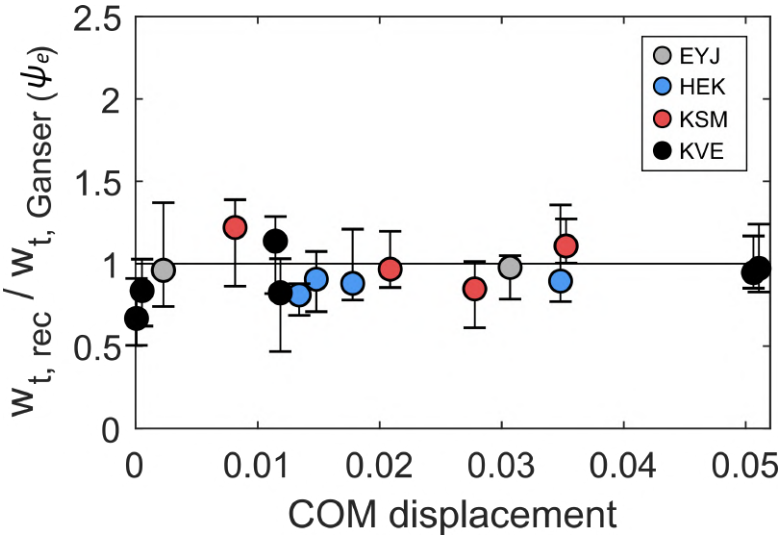

Figure E.6: Measured velocity ($w_{t,\,rec}$) divided by velocity calculated according to the drag law of Ganser (1993) using approximate ellipsoid sphericity (Equation 4.5, Chapter 4) as a function of centre of mass (COM) displacement. Sample codes refer to different eruptions: EYJ = Eyjafjallajökull 2010; HEK = Hekla 1947; KSM = Katla SILK-MN; KVE = Katla Vedde.

E.4 Conclusions and implications

For the analogue particles, particle centre of mass being displaced from a particle's geometric centre generally resulted in a more stable orientation during fall, and therefore a higher fall velocity. If centre of mass positioning affects fall velocity, it could therefore account for some of the variability in particle size observed in a single volcanic ash fall deposit. This is particularly relevant where centre of mass displacement causes particle trajectories to include a lateral motion component. However, within the range examined, centre of mass was found to have a small impact

compared to particle shape, as the shape-dependent drag law of Ganser (1993) was still effective for non-uniform analogue particles.

In addition, results using volcanic ash particles show no relationship between centre of mass and terminal velocity once other factors (shape, size, density) are corrected for. There are several explanations for this observation, including physical differences in the experimental conditions between the analogue experiments and the volcanic ash experiments. While the analogue particles had a range of centre of mass displacements of 0.0036 – 0.071, the centre of mass displacement we calculated for volcanic ash particles is slightly lower at 6×10^{-5} – 0.052. An important caveat of analogue experiments is that secondary motions and particle orientation are affected not only by *Re*, but also by particle-fluid density ratio (Marchildon et al., 1964; Bagheri and Bonadonna, 2016b); although the analogue experiments replicated the *Re* range of distal volcanic ash falling in air, the particle-fluid density ratios are much lower in our analogue experiments. In addition, since we found using analogue experiments that centre of mass has a lesser effect than shape, differences in terminal velocity caused by centre of mass could be too small to resolve given the experimental uncertainty in the volcanic ash study caused by factors such as uncertainty in the particle position in the settling column.